3Dwheel - Attitude Control of Small Satellites Using Magnetically Levitated Momentum Wheels

Jon Seddon

Submitted for the Degree of
Doctor of Philosophy
from the
University of Surrey

Surrey Space Centre
Faculty of Engineering and Physical Sciences
University of Surrey
Guildford, Surrey, GU2 7XH, U.K.

October 2011

Abstract

Momentum wheels are frequently used for the attitude control of satellites. Most existing momentum wheels support their spinning rotor using ball or roller bearings. These mechanical bearings are difficult to lubricate in the vacuum of space; they are prone to wear and so have a limited lifespan that can limit the useful lifespan of the satellite. Jitter in the bearings can generate microvibrations on the satellite that can affect its image quality; the noise level on the satellite platform is becoming increasingly important as the resolution of the cameras on small satellites approaches one metre ground resolution.

Replacing the mechanical bearings with active magnetic bearings, where the spinning rotor is suspended by electromagnets potentially offers many benefits. There will be no contact between moving parts, eliminating friction, stiction and wear. Because the rotor's position is actively controlled it can be controlled precisely generating very low levels of noise.

This thesis introduces a new concept - the 3Dwheel. The number of degrees of freedom that can be actively controlled in a magnetic bearing can be chosen. An engineering model of the 3Dwheel, a magnetically levitated momentum wheel with five degrees of freedom actively controlled, that has been designed, built and successfully tested is presented here. This design allows the rotor to be tilted generating a gyroscopic output torque; one 3Dwheel can therefore generate a torque about all three principal axes of the spacecraft. The electromagnets allow the wheel to be tilted with a high rate generating an output torque with a large magnitude and a bandwidth much greater than existing actuators.

In this thesis the theory behind magnetism is used to model and investigate the design of a magnetic bearing. From this, the design of the 3Dwheel is presented and explained. This process can be used to help design other magnetically levitated momentum wheel designs. The engineering model of the 3Dwheel was successfully levitated in the laboratory by four different controllers. The position of the rotor can be maintained within three standard deviations of the desired position within 11.6 μm. It has been tilted at a rate of 0.556 rads^{-1}, so generating a torque of 0.68 Nm while spinning at 5000 rpm. This resolution allows the 3Dwheel to have very low output noise levels. The 3Dwheel's bandwidth has been demonstrated to be two orders of magnitude greater than a conventional momentum wheel's.

Various techniques for improving the performance of controllers and allowing stable levitation of the rotor at spin rates exceeding the controller's bandwidth are presented. Simulations of the 3Dwheel fitted to a small satellite prove that from its demonstrated ability in the laboratory a single 3Dwheel is capable of providing 3-axis attitude control of a small satellite.

Key words: Magnetic bearings, Satellite control, Dynamic modelling, H∞ control, Non-linear systems.

Email: jon@jseddon.co.uk
WWW: http://www.ee.surrey.ac.uk/ssc

Acknowledgements

Completion of this thesis would not have been possible without the help and advice of many people.

I would like to thank my supervisor, Dr Alexandre Pechev for his enthusiasm, knowledge and guidance throughout the project.

Richard, Bob and the rest of the mechanical workshop staff for their skill, understanding and advice while producing the hardware used in this project. Dave Fishlock and his team in the Electronics Labs.

The rest of the students in the Control Systems Group for their enthusiasm for magnetic levitation, control systems and experimentation. The staff and students at the Surrey Space Centre for sharing their knowledge and enthusiasm of space and engineering with me during my studies.

Karen Collar for her support and advice throughout the PhD process.

Andrew Carrel, Nigel Phillips, Antje Deckert and the rest of the Mechanisms team at Surrey Satellite Technology Ltd for their advice and support on this project.

The Engineering and Physical Sciences Research Council for their financial support of this project through a Doctoral Training Grant.

Contents

Table of Symbols

$\mathbf{A}$	State space model gain matrix or direction cosine matrix
A	Cross section area, m^2
A_{Cu}	Cross section area of a conductor, m^2
A_{EM}	Cross section area of an electromagnet circuit, m^2
A_{PM}	Cross section area of a permanent magnet, m^2
$\mathbf{a}$	Translational acceleration, ms^{-2}
$\mathbf{B}$	State space model gain matrix
B	Magnetic flux density, T
B_{EM}	Flux density in an electromagnet's airgap, T
B_m	Operating flux density of a permanent magnet, T
B_r	Remanence of a permanent magnet, T
B_u	Useful flux density of a permanent magnet at its pole face, T
$\mathbf{C}$	State space model gain matrix
C	Capacitance, F
d	Diameter of a wire, m
e	Exponential constant, 2.71828
e	Radius of a point mass from the centre of geometry, m
$\mathbf{F}, f$	Force, N
$\mathbf{F_{SI}}$	Disturbance force due to the static imbalance, N
F_R	Reluctance force generated by an electromagnet, N
F_x, F_y, F_z	Force along the x, y and z axes, N
$G(s)$	Transfer function expressed in the Laplace domain
$\mathbf{H}$	Magnetic field strength, Am^{-1}
$\mathbf{H}$	Mapping function
$\mathbf{h}$	Angular momentum, Nms
$\dot{\mathbf{h}}$	Rate of change of angular momentum, or torque, Nm
$\mathbf{h_B}, \mathbf{h_I}$	Satellite angular momentum in the body and inertial reference frames, respectively, Nms
$\mathbf{h_0}$	Wheel angular momentum, Nms
H_c	Coercive magnetic field strength, Am^{-1}
$\mathbf{I}$	Moment of inertia, kgm^2
$\mathbf{I_{mw}}$	Momentum wheel moment of inertia, kgm^2
$\mathbf{I_{sat}}$	Satellite moment of inertia, kgm^2
I_{xx}, I_{yy}, I_{zz}	Moment of inertia components, kgm^2
I_{xy}, I_{xz}, I_{yz}	Products of inertia, kgm^2
i	Current, A
i_{drive}	Motor drive current, A
i_0	Bias current, A
j	$\sqrt{-1}$
K	Constant or gain
$K(s)$	Controller transfer function in the Laplace domain
K_i	Electromagnet current constant, NA^{-1}
K_l, K_D	Inertia and damping gains of an electric motor
K_x, K_R, K_{active}	Stiffness of an electromagnetic bearing, Nm^{-1}

K_α	Rotational stiffness of an electromagnetic bearing, Nm/$^\circ$
K_γ	Electromagnet force displacement constant, NA^{-1}
k	Iteration index number
$L(s)$	Loop transfer function
L	Inductance, H
l	Depth of an electromagnet, m
M	Mass, kg
N	Number of turns in a coil
$\mathbf{P}$	Covariance matrix
$\mathbf{p}$	State space model output vector
$\mathbf{Q}$	Noise estimate
$\mathbf{q}$	Quaternion attitude representation or state space model state vector
$\mathbf{R}$	Rotation matrix
R	Resistance, Ω
R_T/R_G	Useful flux ratio of a magnetic circuit
r	Radius, m
r_r	Outer radius of the rotor, m
r_T	Radius that a torque acts about (the lever arm length), m
r_u, r_i	Outer and inner radius of the rotor, respectively, m
$S(s)$	Sensitivity transfer function
s	Laplace Complex Variable
$\mathbf{T}$	Torque, Nm
$\mathbf{T_C}$	Output torque of a conventional momentum wheel, Nm
$\mathbf{T_{CI}}$	Disturbance torque due to the couple imbalance, Nm
$\mathbf{T_c}$	Torque command to achieve the desired attitude, Nm
$\mathbf{T_T}$	Output torque of a magnetically-levitated momentum-wheel generated by tilting the wheel, Nm
$T(s)$	Complimentary transfer function
T_x, T_y, T_z	Torque about the x, y and z axes, N
t	Time, s
$\mathbf{u}$	State space model input vector
V	Volume, m^3
$\mathbf{W}$	Measurement noise estimate
W	Work, J
x, y, z	Translation along the x, y and z axes, m
Z	Impedance, Ω
$\boldsymbol{\alpha}$	Rotor tilt angle, rad
$\alpha_x, \alpha_y, \alpha_z$	Rotor tilt angle about the x, y and z axes, rad
γ	Air gap width, m
γ_{min}	Minimum air gap width, m
γ_0	Default air gap width with the rotor in its central position, m
ε	Pole width, m
ζ	Damping Ratio
η	Height of the wheel, m
θ	Angle or Euler pitch angle, rad
μ	Permeability, Hm^{-1}
μ_r	Relative permeability

μ_0	Permeability of free space, $4\pi \times 10^{-7}$ Hm^{-1}
Ξ	Stator-rotor pole offset, m
π	Constant, 3.14159
ρ	Density, kgm^{-3}
σ	Electrical conductivity, Sm^{-1}
$\mathbf{\Phi}$	State transition matrix
Φ	Magnetic flux, Wb
ϕ	Euler roll angle, rad
χ	Angle between the principal axes of inertia and the geometrical axes, rad
ψ	Euler yaw angle, rad
$\boldsymbol{\omega}$	Angular velocity, rads^{-1}
ω_c	Corner frequency, rads^{-1}
ω_n	System bandwidth, rads^{-1}

Symbols in bold are vectors and symbols in italic type are scalar quantities. $\times$ is the vector cross product and $\cdot$ is the dot product. ^{T} is the vector transpose, $\dot{x}$ is the first differential of x with respect to time and $\ddot{x}$ is the second differential of x with respect to time.

Chapter 1

Introduction

1.1 Introduction

This thesis describes the design, optimisation and evaluation of a tilting magnetically levitated momentum wheel for use on satellites, particularly small satellites. Momentum wheels are a type of momentum exchange attitude actuator for satellites. Traditionally they consist of a rotor spinning around fixed roller or ball bearings. These mechanical bearings have several limitations. They are difficult to lubricate in the vacuum of space, with the lubricant either evaporating off, or they require a sealed pressure housing or the use of dry bearings, which may both have a limited lifespan. In all cases the bearing life limits the duration of the spacecraft's mission.

The mechanical bearings can be replaced with Active Magnetic Bearings (AMBs). In AMBs the spinning rotor is suspended by electromagnets. The rotor's position is monitored by contactless position sensors and a controller varies the currents through the electromagnet coils to keep the rotor in the desired position. Because the rotor's position is actively controlled the rotor can be spun very precisely, compensating for mass imbalance, generating a very low noise output torque.

The use of electromagnets offers the ability to gimbal or tilt the spinning rotor in a similar fashion to a Control Moment Gyro (CMG), generating a gyroscopic output torque about an axis perpendicular to the spin and tilt axes. Unlike in a CMG the tilt axis is not fixed and can be steered by the electromagnets to be anywhere on the plane normal to the spin axis of the wheel. Therefore a single tilting wheel can generate an output torque about all three principal axes of a spacecraft. This tilting wheel design has been called the 3Dwheel.

Because the 3Dwheel's rotor is tilted by electromagnets it can be tilted at a high rate generating a large output torque with a bandwidth greater than conventional actuators are capable of. The range of angles that the rotor can be tilted through is limited making the gyroscopic output torque ideally suited for damping microvibrations and high frequency disturbances, or for high bandwidth small angle manoeuvres such as in spacecraft rendezvous and docking. The 3Dwheel can still be operated conventionally about a single axis for spacecraft reorientation, with the added benefit of lower noise actuation, and so is no worse than a conventional wheel.

1.2 Example Mission

TopSat is a typical small satellite. It has a Image Motion Compensation (IMC) imaging mode, where the satellite pitches during image acquisition to maintain the camera pointing at one spot on the ground, improving the image resolution [1]. Figure 1.1 illustrates this imaging mode.

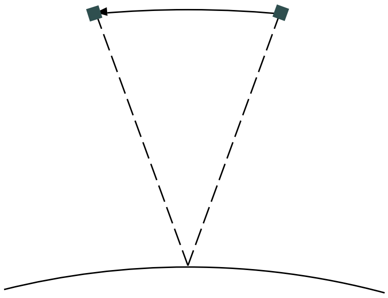

Figure 1.1: The TopSat small satellite's Image Motion Compensation mode, where TopSat has a constant pitch rotation rate during image capture to keep the camera pointing at the same location on the Earth's surface allowing for greater exposure times.

TopSat also has a requirement to be able to roll up to ±30° off track to image areas that are off to the side of its ground track. Coupled with the requirement to be able to counteract disturbances such as gravity gradient, aerodynamic, solar radiation and magnetic field disturbance, a three axis attitude control system is required. Three conventional reaction wheels can give three axis control or a single momentum wheel can provide gyroscopic stiffness about two axes and control about a third axis. A pyramidal configuration of four reaction or momentum wheels may be used to provide three axis active control with redundancy. A single 3Dwheel could be used instead of three conventional wheels to fulfil TopSat's attitude actuation requirements. With its spin axis aligned with the satellite's pitch axis it can pitch the satellite by operating conventionally and accelerating or decelerating the rotor. It can also use its gyroscopic torque output to roll the satellite for off track imaging when required and to remove any disturbances about the yaw axis.

Table 1.1 shows a comparison between an attitude control system for TopSat constructed from three magnetorquers [2], xenon resistojets [3][4] or conventional SSTL mini-satellite momentum wheels [5], and a single 3Dwheel. There is no redundancy in this configuration; if an actuator fails then one degree of freedom will become uncontrollable. The power consumption for the 3Dwheel has been taken from experimental data from the 3Dwheel hardware in the laboratory and is discussed in Section 8.3. The value is the control current required to stabilise the levitation of the wheel. It is assumed that the electrodynamic principle has been used with bias flux provided by permanent magnets and that the rotor is well balanced.

Table 1.2 shows a comparison between an attitude control system for TopSat constructed from four conventional wheels in a pyramidal configuration or two 3Dwheels to provide redundancy in case of the failure of a single actuator.

The mass and volume required by the 3Dwheel is less than the conventional wheel in both the redundant and non-redundant cases. The 3Dwheel's power consumption is almost twice that of the conventional wheel's. The power consumption can be reduced by decreasing the width of the air gaps at the expense of reducing the tilt range of the rotor and the time that the gyroscopic torque can be generated for. In the redundant case the 3Dwheel that is not being used can be spun down and cease to be levitated so that it requires no power. The 3Dwheel's output torque can be as great as 0.5 Nm about the two axes that are generated gyroscopically and 20 mNm about the wheel's spin axis.

Compared with the magnetorquer and resitojets both the conventional and 3Dwheel can generate larger torques but have a greater power consumption. The resistojet has the disadvantage that once its fuel has been expended then it will no longer be able to generate a torque. The accuracy of a resistojet depends on the smallest amount of fuel that it can expel. The accuracy of the conventional and 3Dwheels depends upon the accuracy that their rotational speed can be controlled with and the frequency that commands can be sent to the wheel control electronics at. A magnetorquer can only actively control the orientation of a satellite about two axes because of the shape of the Earth's magnetic field. Over the period of an entire orbit it will be able to control all three axes.

	Magnetotorquer	Xenon Resistojet	Conventional	3Dwheel
Mass, kg	5.4	20.5	9.6	~4
Power, W	3	15	42	~82
Volume, m^3	0.004	0.062	0.012	0.003
Torque, mNm	1.4	9	20	20 - 500
Accuracy [6], °	2	0.1 to 1	0.001 to 1	0.001 to 1

Table 1.1: Comparison between an attitude control system with no redundancy for TopSat constructed from three magnetorquers, resistojets or conventional SSTL mini-satellite momentum wheels, or a single 3Dwheel.

	Conventional	3Dwheel
Mass, kg	12.8	~8
Power, W	56	~164
Volume, m^3	0.015	0.006
Torque, mNm	20	20 - 1000

Table 1.2: Comparison between an attitude control system with redundancy for TopSat constructed from four conventional SSTL mini-satellite momentum wheels or two 3Dwheels.

Figure 1.2 shows a simulation of the 3Dwheel rolling TopSat through 29.3° in 45 seconds using its gyroscopic torque output while the rotor was spinning at a constant rate of 10,000 rpm. The rotor was tilted from its central position by $+2.8^\circ$ and then returned to its central position to stop the spacecraft from turning.

Figure 1.3 shows a disturbance that was seen on the UK-DMC spacecraft being damped by the 3Dwheel and a conventional momentum wheel. The disturbance was identified in an image [7] and so affects the image quality from the satellite. The magnitude of the attitude disturbance is over twenty times less when damped with a tilting momentum wheel than when it is damped by a momentum wheel operating conventionally. This improvement is due to the 3Dwheel's improved bandwidth.

The 3Dwheel concept provides additional benefits for other missions. The lack of friction gives the possibility of spinning the rotor faster than is possible with a conventional momentum

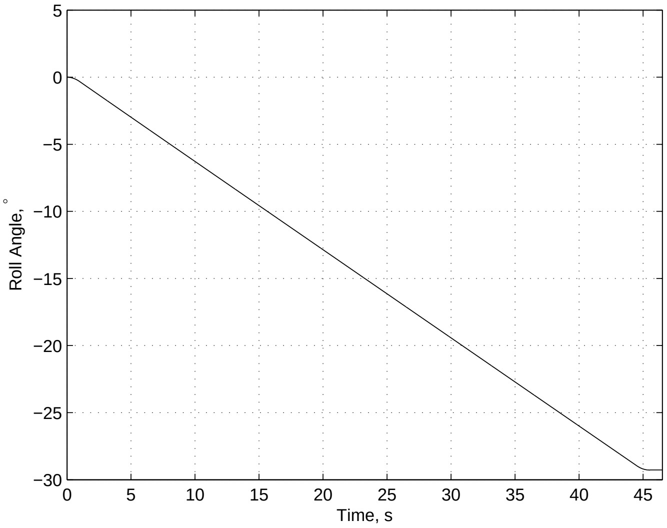

Figure 1.2: The 3Dwheel rolling the TopSat small satellite through 29.3° in a simulation using its gyroscopic torque output.

wheel. A higher spin rate gives the possibility of generating greater gyroscopic output torques, or means that the wheel will saturate less frequently. Higher spin rates also offer the facility of storing large amounts of angular momentum, making the 3Dwheel suitable for flywheel energy storage applications, which would be ideal for small satellite applications where a large current draw is occasionally required, such as in a Synthetic Aperture Radar (SAR) mission.

1.3 Thesis Structure

The work described in this thesis was split in to three main areas of work: modelling of the properties of active magnetic bearings using a numerical model based around the reluctance force equation and finite element techniques; dynamic models of the properties of the 3Dwheel; and the engineering model of the 3Dwheel. The engineering model of the 3Dwheel is a hardware model of the wheel designed to allow control algorithms and sensor configurations to be quickly and easily tested in hardware. The engineering model was designed for simplicity of construction and testing with no effort made to optimise its design for mass, volume, or any other variable. The dynamic model and engineering model were both used to develop and test the controllers to levitate the 3Dwheel's rotor.

Chapter 2 presents an overview of satellite attitude control actuators and the proposed tilting magnetically levitated momentum wheel. This chapter then reviews existing literature regarding magnetically levitated momentum wheels, magnetic bearings and control of active magnetic bearings.

Chapter 3 presents the theory that underpins all of the work in this thesis; magnetism, electromagnets and magnetic bearings are discussed. This knowledge of magnetism is then used to

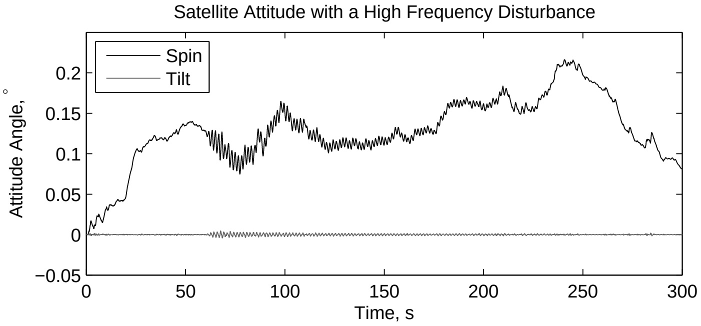

Figure 1.3: The satellite's attitude when applied with a high frequency disturbance torque that is being damped by a tilting momentum wheel (tilt in the legend) and a conventional momentum wheel (spin in the legend).

study the forces generated by electromagnets and the properties of different AMB configurations.

Chapter 4 builds on this knowledge of magnetisation to model and compare the design of three different magnetic bearing configurations that were developed for this thesis. An investigation of the AMB geometry is presented.

From this the design of the engineering model of the 3Dwheel that has been built and successfully tested is described in Chapter 5. A discussion of various components that are missing from the engineering model of the 3Dwheel but will be required in a flight-ready version is included.

Chapter 6 presents the dynamic model of the rotor's motion that was developed. Equations for the dynamics of the translational and rotational motion of the rotor are presented. Complete linearised and non-linear models of the rotor's motion are then produced from these equations. These models were used with the magnetic models to check and optimise the design before any hardware was produced. The mass imbalance of the rotor is also discussed along with methods for estimating the rate of change of motion from the position sensor data.

Chapter 7 combines the previous Chapters' work to discuss the development of the controllers to stabilise the levitation of the wheel. Results from simulations and the hardware engineering model of the wheel are presented during the discussion of the controllers as they influenced the choice of control techniques.

Chapter 8 presents further results from the engineering model of the 3Dwheel operating in the laboratory. Additional control techniques to improve its performance are discussed. Now that the 3Dwheel has been successfully demonstrated in the laboratory, simulation results are presented showing how it can be used on satellites.

Chapter 9 summarises the work undertaken and the conclusions reached during the project, and lists the novel aspects contained in this thesis. Suggestions for future work on the development of tilting magnetically levitated momentum wheels are made. A list of publications and awards is included.

Although the magnetics and the dynamics of motion are presented in separate chapters, the two topics were worked on simultaneously as one influences the other. The work has been presented in this order to make the thesis easier to follow.

Chapter 2

Context

2.1 Background

2.1.1 Satellite Attitude Control Devices

Attitude control is an important part of a modern satellite's functionality. For example, it allows satellites to keep their solar panels pointing at the Sun, and cameras and antennas pointed at their targets. There are two types of device used to orientate a spacecraft as part of an attitude control system: inertial and non-inertial.

Magnetic attitude control devices are a non-inertial device. A current is passed through a coil (called a magnetotorquer). The magnetic field generated interacts with the Earth's magnetic field and generates a torque on the satellite. Varying the current allows the spacecraft's attitude to be controlled. They have a typical accuracy of 2° and cannot be used for satellites in geostationary orbits because the Earth's magnetic field is too weak at that altitude.

Thrusters are the second type of non-inertial device. They expel mass to generate a torque about the centre of mass of the spacecraft. When launched, they carry a limited amount of propellant. When all of the propellant has been used then the spacecraft will no longer be able to control its attitude, ending its useful life. Thrusters can control the satellite with an accuracy of between 0.1 and 1° [6].

Reaction wheels and momentum wheels are inertial devices that generate a torque by changing their angular momentum. They consist of a spinning wheel. When the wheel is accelerated or decelerated a torque is imparted on to the satellite. Reaction wheels have a nominal angular velocity of zero while momentum wheels have an initial bias angular velocity that provides some gyroscopic stability to the satellite. Control Moment Gyros (CMGs) are a third type of inertial device and consist of a spinning wheel; the spinning wheel is gimballed to generate a torque perpendicular to the spin and gimbal axes as shown in Figure 2.1. Reaction wheels, momentum wheels and CMGs can all become saturated when the disturbance torque comes from a constant direction and they are rotating at their maximum velocity, or they are at their maximum gimbal angle. Another attitude control device, such as a thruster or magnetotorquer is then required to control the satellite while the wheel rotation velocity or CMG tilt angle is reduced. Reaction and momentum wheels, and CMGs can orientate a satellite with an accuracy of 0.001 to 1°.

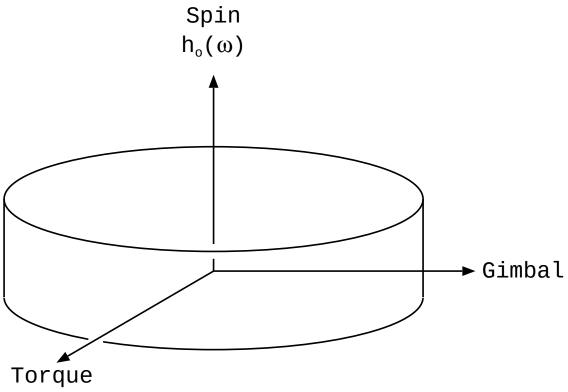

Figure 2.1: The relationship between the wheel spin axis, gimbal axis and output torque axis on a Control Moment Gyro (CMG) or on a tilting momentum wheel.

2.1.2 Tilting Momentum Wheel

This thesis proposes a novel magnetically levitated momentum wheel with four degrees of freedom actively controlled by electromagnets. With four degrees of freedom actively controlled it becomes possible to gimbal or tilt the spinning rotor, allowing a gyroscopic torque to be generated in the same way that a CMG does. Because the rotor is tilted using electromagnets it can be tilted at a high rate, generating a large output torque. Unlike in a CMG the tilt axis is not fixed and can be controlled so that an output torque can be generated about any axis on the plane normal to the rotor's spin axis. Therefore a single tilting magnetically levitated momentum wheel can generate an output torque about all three principal axes of a spacecraft, replacing three conventional momentum wheels, or two 3Dwheels can provide 3-axis control with redundancy.

The range of angles that the wheel can be tilted through is limited by the width of the air gap between the electromagnets and the rotor. As the air gap increases the resistance to the flow of magnetic flux increases and so the stiffness of the bearing decreases or the power consumption increases. Analytical and finite element simulations show that tilting through $\pm 5^\circ$ is feasible. Because the tilt range is limited and the tilt rate can be high then the gyroscopic output torque can only be generated for a limited period of time. Because of its large bandwidth, the gyroscopic torque is ideal for damping high frequency disturbances and microvibrations, or for high bandwidth small-angle manoeuvres, such as in spacecraft rendezvous and docking. However, it is still capable of reorientating a small satellite as shown in Figure 1.2.

An extension of the tilting magnetically levitated momentum wheel is the magnetically levitated momentum sphere, where a sphere is actively supported by a magnetic field. The sphere can be spun and when the direction of the spin is changed a gyroscopic output torque can be generated about any axis. Therefore a single magnetically levitated sphere can generate an output torque about any axis of a spacecraft. The maximum torque that can be generated, or the angular momentum that can be stored is the same about all three axes. To spin the sphere a type of brushless DC motor is required. Permanent magnets are placed around the sphere and coils generate a field that interacts with the permanent magnets. There are positions of the sphere where a singularity can occur because the arrangement of permanent magnets does not allow the sphere to be spun in the desired direction. The arrangement of the permanent magnets is therefore crucial. The reaction sphere is being actively researched by several groups [8][9] and will not be discussed further in this thesis.

A tilting momentum-wheel in the inertial reference frame is shown in Figure 2.2. The $\dot{\boldsymbol{\alpha}}$ tilt axis can be anywhere on the xy-plane of the inertial reference frame.

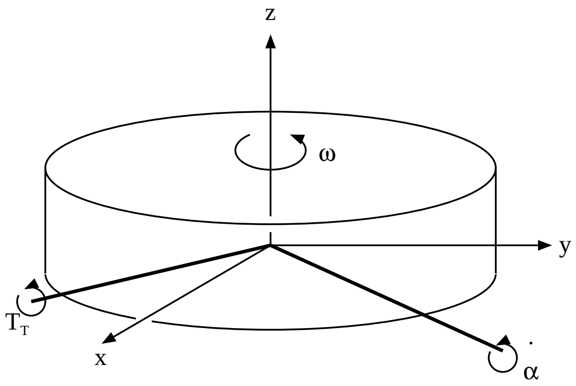

Figure 2.2: The tilting momentum wheel in the actuator reference frame.

The angular velocity of the spinning wheel in the actuator reference frame is given by:

$$\boldsymbol{\omega} = \omega_x \mathbf{i} + \omega_y \mathbf{j} + \omega_z \mathbf{k} \tag{2.1}$$

However, for a conventional momentum wheel, the spin axis is aligned with the z-axis of the inertial reference frame and the angular velocity is reduced to:

$$\boldsymbol{\omega} = \omega_z \mathbf{k} \tag{2.2}$$

The angular momentum of any spinning wheel is given by:

$$\mathbf{h} = \mathbf{I_{mw}} \boldsymbol{\omega} \tag{2.3}$$

where $\mathbf{h}$ is the angular momentum in Nms, $\mathbf{I_{mw}}$ is the moment of inertia of the wheel in kgm^2 and $\boldsymbol{\omega}$ is the angular velocity of the wheel in rads^{-1}.

The output torque $\mathbf{T_C}$ of a conventional momentum wheel, in Nm, is about the spin axis and is given by the rate of change of angular momentum:

$$\mathbf{T_C} = \frac{d\mathbf{h}}{dt} = \mathbf{I_{mw}} \frac{d\omega_z}{dt} \tag{2.4}$$

In comparison, the output torque $\mathbf{T_T}$ of a tilting momentum wheel, when tilting, is given by:

$$\mathbf{T_T} = \dot{\boldsymbol{\alpha}} \times \mathbf{h_0}(\boldsymbol{\omega}) = \dot{\boldsymbol{\alpha}} \times \mathbf{I_{mw}} \boldsymbol{\omega} \tag{2.5}$$

where $\mathbf{h_0}(\boldsymbol{\omega})$ is the wheel's angular momentum and $\dot{\boldsymbol{\alpha}}$ is the tilt rate of the wheel in rads^{-1}. $\times$ is the vector cross product, therefore the output torque is perpendicular to the spin and tilt axes as shown in Figure 2.2. The total output torque of a tilting wheel is therefore $\mathbf{T} = \mathbf{T_T} + \mathbf{T_C}$. A conventional momentum wheel can only generate an output torque about its spin axis ($\mathbf{T_C}$). Because in a tilting magnetically levitated momentum wheel the tilt axis is not fixed a single wheel can generate an output torque about all three principal axes of the spacecraft.

A tilting momentum wheel can generate torque and angular momentum in two ways: by changing the angular velocity of the wheel and by tilting the wheel. The angular momentum and torque vectors generated by accelerating the wheel will move as the wheel tilts. The angular momentum envelope for a tilting momentum wheel acting either as conventional wheel or a tilting wheel is shown in Figure 2.3. The rotor is assumed to be only able to spin in one direction; if the wheel can spin in either direction then the momentum cone will be mirrored below the xy plane. Angular momentum can be generated anywhere in a cone around the wheel's spin axis.

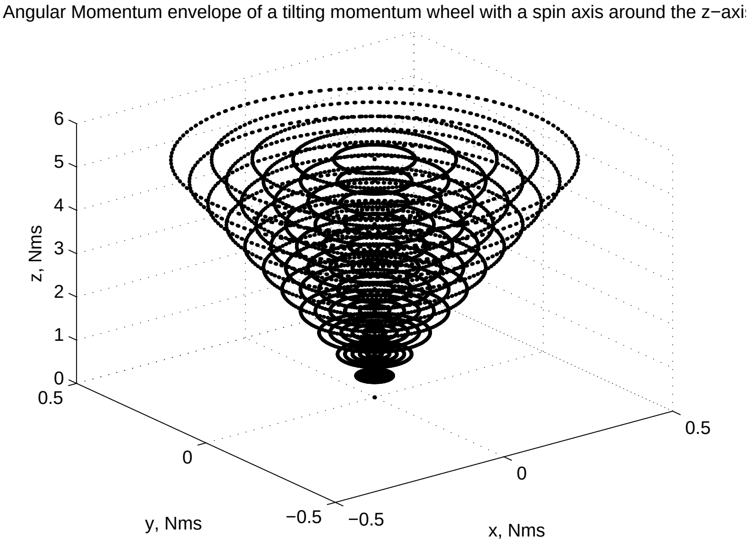

Figure 2.3: The angular momentum envelope of a tilting momentum wheel with its spin axis around the z-axis of the actuator reference frame.

The torque envelope of the proposed tilting momentum wheel is shown in Figure 2.4. It can generate a small torque for a long period of time in a cone around the spin axis. Or it can generate a much larger torque for a short period of time perpendicular to, and around the spin axis. Unlike in an array of control moment gyros a tilting momentum wheel will not suffer from singularities. There is no need to invert a matrix to calculate the tilt angle required to generate the desired output torque.

In a control moment gyro the torque generated is transferred to the spacecraft via the mechanical bearings. In a tilting magnetically levitated momentum wheel the stiffness of the magnetic bearings must be strong enough to not only tilt the spinning rotor, but also strong enough to transfer the gyroscopic torque generated to the spacecraft. Because of the cross-product in Equation 2.5 the output gyroscopic torque is perpendicular to the tilt axis. In a wheel with

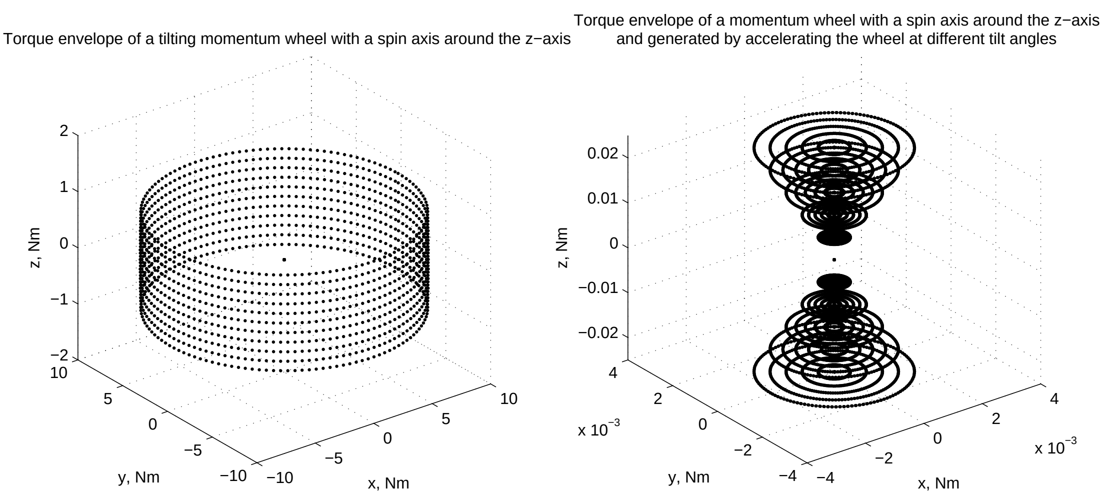

Figure 2.4: The torque envelopes of a tilting momentum wheel in the actuator reference frame. The plot on the left shows the torque that can be produced by tilting the wheel. The plot on the right shows the torque that can be generated by changing the angular velocity of the wheel at different tilt angles.

electromagnets arranged in four places around the wheel if the tilt axis is aligned with a set of electromagnets then these electromagnets will tilt the rotor and the electromagnets perpendicular to these will transfer the torque to the spacecraft. If the tilt axis is not aligned with the electromagnets then all of the electromagnets will have a component of their generated force tilting the rotor and a component transferring the torque to the spacecraft.

Figure 2.5 shows the rotor tilt rate necessary to generate given gyroscopic output torques at varying wheel spin rates for the proposed design. Also shown is the duration that the tilt can be generated for. The moment of inertia used in the calculation was the 3Dwheel's engineering model of 2.326×10^{-3} kgm^2. Higher rotor spin rates have the advantage of being able to generate a gyroscopic torque from lower tilt rates, which means that the torque can be generated for a longer period of time. Experiments presented later in the thesis achieved a tilt rate of 0.5 rads^{-1}.

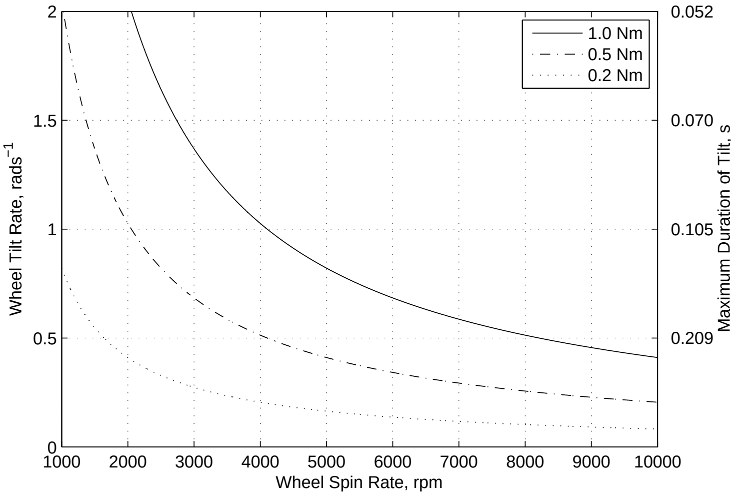

Figure 2.5: The relationship between tilt rate, spin rate and gyroscopic output torque. Also shown is the duration that the torque can be generated for.

2.2 Literature Review

2.2.1 Momentum Wheels

Chobotov [10], Sidi [11] and Wie [12] all describe the theory and provide an explanation of spacecraft momentum wheels. Manufacturers such as SSTL [5] and Rockwell Collins [13] provide datasheets for the small-satellite momentum-wheels that they manufacture. These wheels are typically available in sizes that can generate 0.5 mNm of torque and store 0.01 Nms of angular momentum, or generate 20 mNm of torque and store 4 Nms of angular momentum. These are suitable for micro-satellites of mass less than 60 kg and mini-satellites with a mass of less than 400 kg respectively.

Henrikson et al. [14] wrote one of the first papers about the use of Active Magnetic Bearings (AMBs) in satellite momentum wheels in 1974. The benefits of using AMBs were said to be the elimination of wear; no requirement for lubrication and so reduced sensitivity to temperature; and that they operate equally well in either air or vacuum and so are simple to test and do not require a heavy pressure-tight container. The wheel had a mass of 4 kg, rotated at 12,000 rpm and could store 33 Nms of angular momentum making it ideal for use on a large satellite.

Studer [15] discussed in 1977 the design of electrodynamic bearings for use on spacecraft. New magnetic materials such as Samarium Cobalt had recently been developed and made the design of such bearings practical for the first time.

Sindlinger [16] described in 1977 a commercial, tilting, magnetically-levitated momentum-wheel that had reached the pre-qualification stage. The high output torque produced by gimballing the wheel could be anywhere in the plane of the wheel. The output torque was more than sufficient to overcome any disturbance torques on the satellite and could slew the satellite at a rate of $2.5^{\circ}\mathrm{s}^{-1}$. The range of tilt was ± 10 mrad ($\pm 0.57^{\circ}$) achieved with an air gap width of about 0.7 mm. Modifications to the design to make it fully redundant against electronics or electromagnet failure were also discussed. The design used a controller built from analogue electrical components, but it was stated that future improvements in micro-computers would allow the controller to be built from a lighter digital processor in the future. The mass of the hardware and electronics was 12.6 kg and its steady state power consumption was 13 W.

Robinson [17] described in 1982 a small reaction wheel built with an AMB that was capable of storing 2 Nms of angular momentum. This design was no heavier, complex or expensive than equivalent wheels built with mechanical bearings. Robinson stated the same benefits for AMBs as Henrikson but also said that AMBs have a very low torque noise and transmission of vibrations. The power consumption of the electromagnets was stated as being 1 W.

Murakami et al. [18] described in 1984 a momentum wheel with an AMB that also had the ability to gimbal the wheel. The wheel was designed for a satellite that used roll-yaw exchange to remove the need for yaw sensing, which was considered difficult. The roll-yaw exchange was achieved by tilting the rotor by an angle whose amplitude was the angle between the spacecraft angular momentum vector and the orbital normal. This angle was limited by the gimbal range of the wheel, which was stated as being small. The wheel's gimbal capability was also used to counteract any wheel nutation. The levitation of the rotor was actively controlled in the axial direction and passively in the radial direction. The wheel had a mass of 5.5 kg, a radius of 300 mm, an angular momentum storage capability of 70 Nms and was designed for large communication satellites.

Tsuchiya et al. [19] analysed in 1991 the magnetic circuit and dynamics of a momentum wheel AMB. An analytical expression of the damping characteristics was developed. It was found theoretically and experimentally that the stiffness of the bearing affected the passive damping characteristics of the wheel. Tsuchiya's AMB was actively controlled in the axial direction and passively in the radial direction. Tsuchiya's method can be modified for other arrangements.

Gondhalekar et al. [20] described in 1991 a theoretical design of an AMB momentum wheel that could replace the mechanical bearing based Teldix DR-68 wheel. The aim was to have a maximum torque output of 600 mNm and an angular momentum storage capability of 68 Nms. Gondhalekar's emphasis while developing this wheel was to produce a low noise wheel by eliminating bearing noise and mass unbalance, which can be achieved by the AMB controller spinning the wheel around its centre of mass rather than its centre of geometry as a mechanical bearing does. The design of the magnetic bearing was not discussed, only the general configuration and the degrees of freedom to be actively and passively controlled.

Roland [21] discussed in 1991 the AMB reaction wheels that had been flown on the French SPOT 1, 2 and 3 satellites, each of which had a mass of 1800 kg. The very low levels of microvibrations and the independence of drag torques from temperature variations allowed these satellites to generate very sharp images. Roland then discussed the improvements that were made to the wheel design for the larger SPOT 4 satellite. He describes in detail the sources of microvibration in an AMB based reaction wheel and methods that can be used to reduce these microvibrations.

In his patent, Wittman [22] describes a tilting momentum wheel made from mechanical bearings. The wheel is tilted by three motorised screw-threads arranged in a triangle around the wheel. The patent claims that this tilting wheel can be used on spacecraft that contain only one wheel to counteract disturbances that are not about the same axis that the wheel rotates about. The patent also states that the design allows the wheel to be tilted to align it accurately with the spacecraft axes, when manufacturing tolerances do not allow this. The patent also claims that it can act as a double-gimbal Control Moment Gyro, although no mention is made of the tilt rate of the design.

Scharfe et al. [23] described in 1996 the design of a momentum wheel made from AMBs for the 400 kg AMSAT Phase 3-D satellite. The motivation for using AMBs was to improve the lifetime of the wheel compared with a ball-bearing based wheel. The design cycle was greatly reduced using Finite Element Analysis (FEA).

Samuel [24] in 1997 provided a summary of the AMB momentum wheels used on the SPOT 1 to 4, ERS 1 and 2, and HELIOS large imaging satellites.

Carabelli et al. [25] [26] [27] discuss the mechanical design, the design of a controller and the practical tests performed to characterise the performance for an AMB based momentum wheel. Levitation was not possible in [27] due to "...the low performances of the power electronic[s]". This was later corrected and the rotor was spun up through its first two critical frequencies. It was not possible to spin the rotor faster than its third critical frequency at 25300 rpm.

Scharfe et al. [28] [29] discuss how a momentum wheel that has been flown successfully on a large satellite [21][23] can be modified to become a practical wheel for a small 100 kg satellite and the design processes that can be used for this.

Zhou et al. [30] discussed in 2002 the theoretical design of an AMB based momentum wheel that used a combined set of motor and suspension electromagnets to reduce the mass and size of the wheel.

Bichler [31] and [32] discusses the design of an AMB based momentum wheel that also allows for vernier gimballing, or tilting, of the wheel. The wheel has an angular momentum storage capacity of up to 100 Nms and can generate torques of 3 Nm while tilting, and 100 mNm while operating as a conventional momentum wheel. The wheel can be tilted through a range of only 1°. The advantages of vernier gimballing are stated as being that the wheel can act as a control moment gyro, allowing the three axis attitude control of a spacecraft in a fine pointing range with only one wheel, suppression of unbalance vibrations and active damping of flexible spacecraft structures through fully controllable translational bearing forces. This design has been built and its low noise characteristics have been confirmed by practical measurements.

Bangcheng [33] discussed in 2008 how the geometry and design parameters of a magnetically-levitated momentum-wheel affect its performance.

Varatharajoo [34] describes an AMB based momentum wheel system that also uses the spinning wheels as a form of energy storage. The detailed design of an AMB based momentum wheel for a small satellite is presented.

Hosny [8] analytically described in 1997 a magnetically levitated sphere, where a single actuator can generate a torque about all three principal axes. Onillon [9] described in 2009 an engineering model of the reaction sphere. The sphere was able to be levitated, but required additional mechanical supports while the controllers initially levitated the wheel.

Siebert et al. [35] discuss the design and performance of a magnetically-levitated momentum-wheel constructed from a passive magnetic bearing. The stiffness of the bearing was a factor of ten less than similar active magnetic bearings [23]. The wheel was spun by compressed air against an impeller and so this design is not suitable for use on a spacecraft yet.

Privat et al. [36] and Bichler et al. [32] both describe different approaches to develop a launch locking device to securely hold an AMB based momentum wheel during launch.

Relationship to this Project Designs for momentum wheels built from AMBs have been previously proposed. However, they have mainly been for large satellites. There is little information about the measured performance of AMB based momentum wheels. Several authors have suggested that it is possible to tilt the rotor through a small angle to generate a gyroscopic torque, but no results demonstrating the gyroscopic torque have been presented nor has there been a discussion on how including the ability to tilt the rotor affects the design and properties of a wheel. There has been no mention of the optimisation of the magnetic geometry. The improved bandwidth obtained through the use of magnetic bearings has not been measured.

This project is novel because it will overcome these omissions from previous research and will also:

- discuss a scalable design methodology for momentum wheel magnetic bearings using numerical analysis methods such as finite element analysis and using analytical models;

- use the engineering model developed to evaluate the benefits and costs of including the ability to generate a gyroscopic torque;
- control the tilt of a magnetically levitated momentum wheel and the extra complexity that tilting introduces, namely that the tilt axis can be anywhere on the plane perpendicular to the wheel spin axis and the improved fault coverage and redundancy (allowing possible improvements in power and mass) that tilting provides.

All prior magnetically levitated momentum wheels for spacecraft apart from Sindlinger and Carabelli have used the electrodynamic principle, where permanent magnets generate bias flux in the magnetic bearing and actively controlled electromagnets generate a control flux to stabilise the system. This system has the advantage of having a linear relationship between the force acting on the rotor and the applied current [37][38]. The alternative approach taken in this project uses the electromagnetic principle where a purely attractive force acting on the rotor is generated by electromagnets. This approach has the benefit of being able to generate larger forces, increasing the stiffness of the bearing if required [16].

2.2.2 Satellite Microvibrations

Bamber et al. [7] identified, from satellite images, microvibrations in a satellite's attitude that started when a momentum wheel with a mechanical bearing was accelerated. These vibrations were at a higher frequency than could be seen in the telemetry data. The microvibrations were affecting the image quality.

Using data from a satellite to ground station laser communications link, Toyoshima et al. [39] measured the microvibrations on a satellite. Vibrations were present at frequencies greater than the attitude sensors on current satellites can measure and higher than momentum wheels with mechanical bearings can counteract.

Privat [40] characterised the microvibrations generated by a magnetically-levitated momentum-wheel and on the SPOT 4 satellite on the ground before launch and also on-orbit.

2.2.3 Active Magnetic Bearings (AMBs)

Allaire et al. [38] described in 1991 a radial AMB with permanent magnets to provide bias flux. The stiffness of the bearing was calculated and a controller for it was described.

Pang et al. [41] describes the procedure used to design an AMB that includes bias flux from permanent magnets.

Zayadine [42] provides a complete description of the modelling and design of an AMB. A detailed numerical model of the magnetic flux and the forces generated by the AMB is developed.

Walsh et al. [43] discussed in 1997 the design of a flywheel built with AMBs to provide energy storage for satellites. To maximise the storage capacity of the wheel it is spun at a speed of 671000 rpm.

D'Arrigo et al. [44] describe a numerical model for a simple active magnetic bearing and compares the accuracy of the model with the results of Finite Element Analyses.

Murphy et al. [45] describe the design of a flywheel built with an AMB. The design and choice of materials are discussed in detail along with the high levels of hysteresis drag that were found in the final design.

2.2.4 Controllers for AMBs

Lange [46] described in 1983 a method for designing an optimal AMB momentum wheel controller. The system performance was optimised with respect to the output noise. Cross-coupling additionally damped the satellite open loop nutation oscillation.

Williams et al. [47] described in 1990 a digital controller for an AMB. The use of second-order derivative feedback extended the bandwidth of the controller and integral feedback reduced the rotor position error when the bearing was supporting a static load.

Bichler [31] described a controller for an AMB based momentum wheel that rotated the wheel about its axis of inertia rather than its geometrical centre to minimise noise. No details of the algorithm were given. A double integrator was also included in the control loop to suppress vibrations from the wheel. This was implemented by feeding back the current command, which is linearly proportional to the force and so the rotor's position.

Higuchi et al. [48] presented in 1990 a method using a model based observer to estimate imbalance. A synchronous signal is then fed back spinning the rotor about its centre of mass and principal axes to prevent any imbalance disturbances from being generated.

Herzog et al. [49] described in 1996 an approach for compensating for couple imbalance that uses a notch filter, with its stopband centred on the rotor's spin rate. This prevents the controller from trying to compensate for the imbalance and allows the rotor to spin around its principal axes of inertia. Practical results demonstrate the method's effectiveness.

Lum et al. [50] described in 1996 a method using an adaptation algorithm that estimates the centre of mass position and inertia matrix's products of inertia. The controller can use these values to spin the rotor about its centre of mass and principal axes. This method is independent of the rotor's spin rate; once the imbalance parameters have been estimated the estimator can be stopped. This is useful when the rotor is accelerated through its critical frequencies. However it is only valid for rigid rotors and so will not work on flexible high-speed rotors.

Namerikawa et al. [51] described in 1997 the modelling, uncertainty description and robustness analysis of an AMB. The linearization of the model was discussed as one of the uncertainties. The robustness of the controllers derived from the models was discussed.

Shafai et al. [52] described single-input single-output and multi-input multi-output digital controllers to control AMBs. Techniques such as H_∞, Quantitative Feedback Theory and LQG/Loop Transfer Recovery were discussed. A novel technique to spin the rotor around its centre of inertia rather than its centre of geometry to overcome mass imbalance was also developed.

Trumper [53] described in 1997 how feedback linearisation could be used to linearise the reluctance force equations in a one degree of freedom magnetic suspension system. The method only works when the state space equations can be written in the companion form.

Scharfe et al. [29] discussed a controller for an AMB based momentum wheel. He used two independent control loops to control the radial position of the wheel, but stated that additional complexity was required to compensate for cross-coupling effects between the two directions controlled and also undesired tilt modes. Analogue controllers were used as the components in them were already radiation hardened, but this did limit the flexibility of the design.

Tsiotras et al. [54] described in 2000 the simulation of a controller for an AMB based flywheel that minimised the bias current in the electromagnets of an AMB to minimise the eddy current losses.

Lindlau et al. [55] described in 2002 a feedback linearization controller to control the voltage for a single degree of freedom AMB. Together with μ-synthesis this technique provided the high performance control for a nonlinear plant independent of the disturbance force level or displacement.

Lanzon et al. [56] described in 2002 a hybrid H_∞ and μ-synthesis controller for an AMB. The rotor speed was treated as an uncertainty to reduce the computational complexity of the designs and the order of the synthesised controllers. Experiments confirmed the stability and performance characteristics of this approach.

Gerlach [37] described in 2005 how the analogue controller in the Teldix magnetically levitated momentum wheel [31] was replaced by a digital controller implemented on a Digital Signal Processor (DSP). The performance of a filter to allow the wheel to spin around its centre of mass is discussed and the microvibrations generated by the wheel are presented.

Control techniques such as proportional, integral and derivative (PID) are well discussed in textbooks such as Dorf [57] and D'Azzo [58]. Dorf also covers the lead lag technique that has been widely used in previous projects by this research group. H∞ control has been used extensively within the research group and so was well understood [59][60]. Other authors have used H∞ control for the levitation of magnetic bearings [52] along with PID [47], Loop Transfer Recovery [52] and μ-synthesis [55]. No control technique seems to be preferred in literature over others and so using the techniques that the research group has most experience with is a sensible engineering choice.

Relationship to this Project Section 2.2.2 presents results showing the microvibrations that have been seen on satellites. These microvibrations occur at a frequency that is too great for actuators such as conventional momentum wheels, control moment gyros, thrusters or magnetotorquers to damp down. The microvibrations do affect the images obtained from small satellites [7]. Because the 3Dwheel uses electromagnets to tilt its rotor it will have sufficient bandwidth to damp such microvibrations.

Section 2.2.3 presents several systems other than satellite momentum wheels that have used active magnetic bearings to suspend a spinning rotor. The papers describing these systems contain useful information on the modelling of AMBs. They also discuss other applications that the 3Dwheel could be used for, such as flywheel energy storage.

Section 2.2.4 describes some techniques used to control AMB systems. Most of the literature presents novel techniques to improve the levitation controller in terms of minimising the error in the rotor's position from the desired position when the rotor has mass imbalance. There is little discussion available comparing the performance of different types of controller. Some of the literature describes analogue controllers from before the time that digital controllers implemented on microprocessors became commonly used.

2.3 Conclusions

Chapter 1 introduced the proposed 3Dwheel design. This Chapter has provided further details of the design and the torque outputs possible from the novel design proposed. The review of prior literature has shown that the 3Dwheel concept is feasible. The proposed work is state of the art as it uses the electromagnetic principle to provide the possibility for larger forces and greater stiffnesses than existing designs and can tilt through a wider range of angles than existing designs providing the capability of 3-axis attitude control of a spacecraft from a single actuator. Chapter 3 will provide an introduction to electromagnetism that allows the materials to be used in the design to be chosen and the forces generated to be modelled. Chapter 4 builds on this to discuss and compare possible design configurations. Chapter 5 then goes on to introduce the design of the 3Dwheel hardware that was built and successfully tested in the laboratory.

Chapter 3

Magnetism and Electromagnets

Magnetism is a form of electromagnetism, one of the four fundamental forces of nature along with gravity and the strong and weak nuclear forces. However, for the rest of this project electromagnetism will refer not to the fundamental force but to a magnetic field generated by an electric current.

This Chapter discusses magnetic materials and how their structure affects their properties and their suitability for use in the various components of a magnetic bearing. Electromagnets are then introduced and their geometry and the forces generated by them are derived. This will be used in the next Chapter to derive models of the behaviour of different geometries and to optimise the 3Dwheel's geometry.

3.1 Magnetic Materials

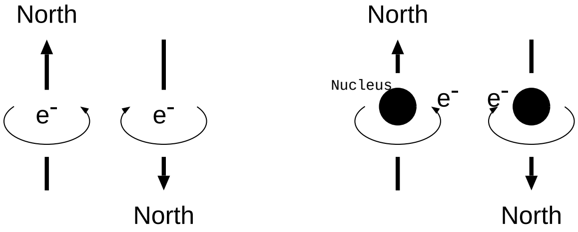

Figure 3.1: Magnetic moments are caused by the direction of rotation of an electron and by the direction of the orbit of an electron about an atom's nucleus [61].

Every electron in the atom of a material has two magnetic moments [61]. The magnetic moments are caused by the motion of the electron as it orbits around the atom's nucleus and also by the electron spinning around its own axis as illustrated in Figure 3.1. Each energy level in an atom can contain two electrons, each with an opposite spin direction. The magnetic moments of each electron pair in an energy level oppose each other. Therefore, when an energy level is full the magnetic moments cancel each other out. The unpaired valence electron in most elements that have an odd atomic number interacts with the valence electron in other atoms, again resulting in no net magnetic moment. Certain elements, such as the transition metal elements (scandium to copper) have an unfilled inner electron energy level. They therefore have a permanent magnetic moment and each atom behaves as a magnetic dipole.

An atom responds to an applied magnetic field in different ways depending upon how its magnetic dipole reacts to the field. In most transition metal elements the sum of an atom's magnetic moments is zero. However, nickel, iron and cobalt have an exchange interaction where the orientation of the dipole in one atom influences surrounding atoms to have the same dipole orientation. This results in a desirable amplification of the effect of the magnetic field.

The magnetic field strength H in Am^{-1} inside a coil of N turns and l m long with a current i A flowing through it is given by:

$$H = \frac{Ni}{l} \tag{3.1}$$

In a vacuum the magnetic flux density B measured in T is related to the magnetic field strength by:

$$B = \mu_0 H \tag{3.2}$$

where μ_0 is the permeability of free space with a value of $4\pi \times 10^{-7}$ Hm^{-1}. When a core with a relative permeability μ_r is inserted into the coil then the flux density becomes:

$$B = \mu_0 \mu_r H \tag{3.3}$$

If $\mu_r > 1$ in a material then the magnetic field is amplified because the magnetic moments reinforce the applied field. However, if $\mu_r < 1$ then the magnetic moments oppose the field.

Several types of behaviour can be seen in different materials depending on a material's relative permeability. Materials can be classified according to this behaviour:

Antiferromagnetic $\mu_r = 0$ manganese, chromium, MnO and NiO. The magnetic moments in neighbouring dipoles always oppose each other. These materials have no magnetisation.

Diamagnetic $\mu_r \approx 0.99995$ copper, silver, gold and alumina at room temperature. Superconductors must be diamagnetic. They lose their superconductivity when other magnetic effects such as paramagnetism start and permit the field to enter the material.

Paramagnetic $1 < \mu_r < 1.01$. Paramagnetic material has unpaired electrons, and each atom has a net magnetic moment due to electron spin. An applied magnetic field causes the dipoles to line up with the field. The dipoles do not interact and so a large magnetic field is required to cause this. The effect is also lost when the magnetic field is removed.

Ferromagnetic $\mu_r \gg 1$ (it can be as high as 10^6). Ferromagnetic behaviour is caused by unfilled energy electron levels in the 3d level of iron, nickel and cobalt. It is also seen in a few materials, including gadolinium. Permanent unpaired magnetic dipoles align easily with an applied magnetic field as one atom influences neighbouring atoms. Large magnetisations are obtained even with small magnetic fields.

Ferrimagnetic $\mu_r \gg 1$. Ceramic material with different ions having different magnetic moments. The dipoles of one ion may align with an applied magnetic field but those of a different ion oppose the field. But because each ion has a different dipole strength a net magnetism results. Ferrimagnetic materials can be produced that generate a good amplification of an applied magnetic field.

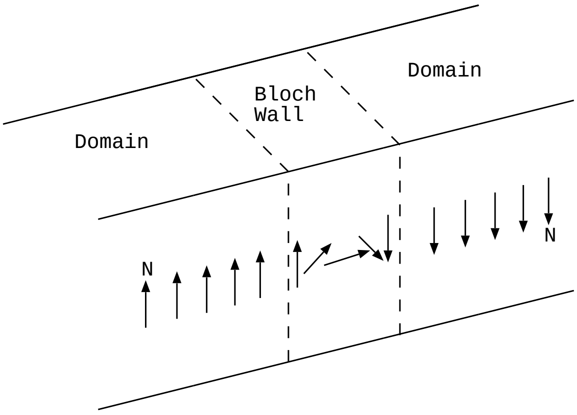

Figure 3.2: The arrangement of domains and Bloch Walls in a ferromagnetic material that has not been exposed to a magnetic field [61].

3.1.1 Ferromagnetic Materials

In ferromagnetic materials domains exist within the material as shown in Figure 3.2. All of the magnetic dipoles in one domain are aligned. Before exposure to a magnetic field the dipole direction of each domain is random and so the material has no net magnetisation. The boundaries between domains are called Bloch Walls. These boundary areas are narrow and the direction of the magnetic dipole moment continuously and gradually changes within them. Domains are typically around 0.05 mm in size and the Bloch Walls are about 100 nm thick.

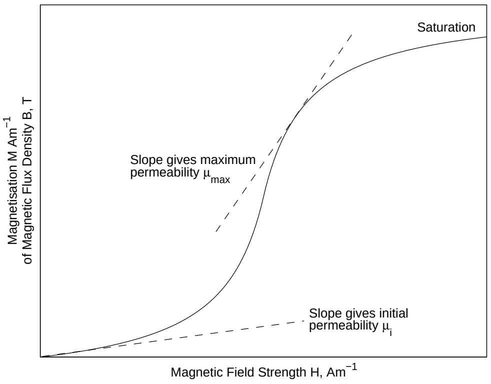

Figure 3.3: The magnetisation generated in a material by an applied magnetic field.

When a magnetic field is applied to a ferromagnetic material, domains with a magnetic moment nearly aligned with the magnetic field grow in size. The applied field provides the force required to move the Bloch Walls to allow the domains to grow. At first a large force is required to move the Bloch Walls. Therefore a large applied magnetic field is required to provide only a small magnetisation of the material. This is shown in Figure 3.3 by the shallow initial slope of the curve which gives the initial permeability of the material μ_i. As the field increases, domains orientate with the field more easily and so the gradient of the curve and the permeability increases. Eventually all of the domains are orientated with the applied field and so the material is saturated. This gives the maximum permeability μ_{max} and the saturation magnetisation that the material can have.

When the field is removed the Bloch Walls' resistance to movement prevents the material from having a random orientation of dipoles again. Many of the dipoles will remain orientated with the direction that the applied field had leaving a residual magnetisation or remanence B_r. The material is now acting as a permanent magnet. When a field with an alternating direction is applied Figure 3.4 is produced; this plot for a material is commonly called a BH curve. When the direction of the field is reversed the domains aligned with the newly applied field begin to grow. A coercive field H_c is required to force the domains to be randomly orientated and for there to be no net magnetisation.

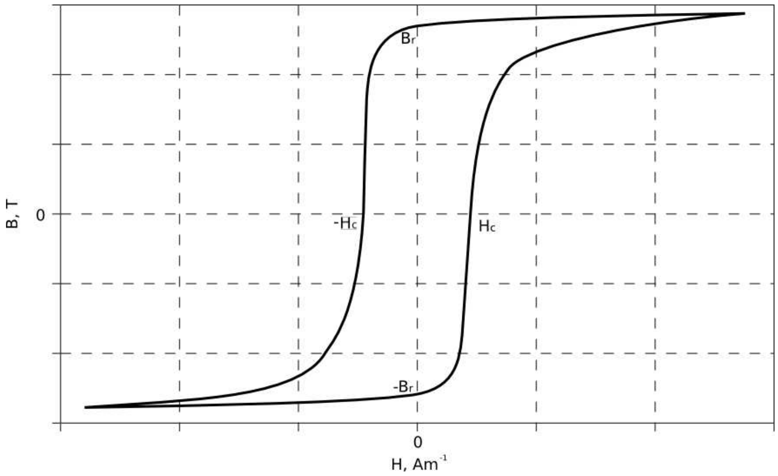

Figure 3.4: The magnetic flux density in a material when subject to an applied magnetic field [62].

3.1.2 Material Properties for Electromagnets

Ferromagnetic materials in a coil's core amplify the magnetic field produced when a current flows through the coil. When an alternating field is used the core is continuously moving through the hysteresis of the material's BH curve as shown in Figure 3.5. From this curve we can deduce that a soft magnetic material to be used in an electromagnet should have the following properties:

- a high saturation flux density to allow the material to do work;

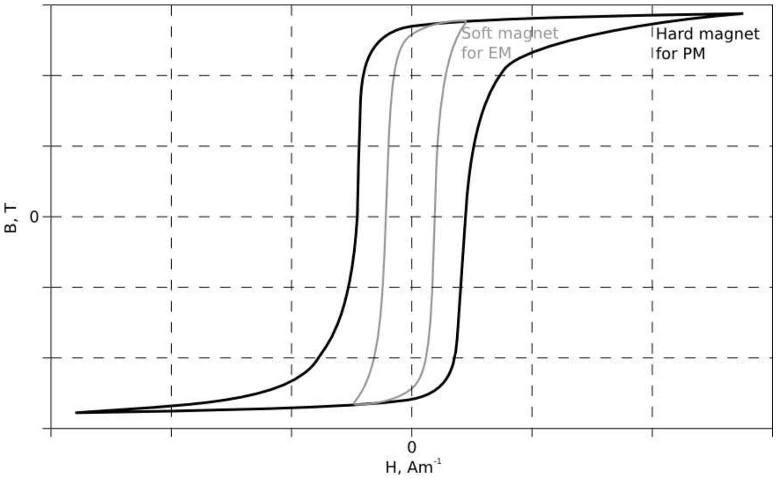

Figure 3.5: The ideal material BH curves for different applications [62].

- a high permeability to allow the saturation point to be reached with only a small applied field;
- a small coercive field to allow reorientation of the domains with only a small applied field;
- and a small remanence so that little magnetisation remains when the external field is removed.

This results in a small hysteresis loop and minimises energy losses in operation. If the frequency of the applied field is high enough that the domains cannot be realigned in one cycle then the material may heat due to dipole friction. Higher frequencies also cause the hysteresis loop to be moved through more often resulting in higher energy losses and more heating. Some materials allow the dipoles to be reorientated at higher rates than other materials.

Table 3.1 shows the permeability, saturation flux density and coercive field for different materials commonly used in the cores of electromagnets. Pure iron has a low permeability requiring a low applied field, but the addition of silicon can improve this and also reduce the coercive field. Silicon steel can be either unorientated, which has similar magnetic properties in all directions, or grain-orientated, which has an improved permeability in the rolling direction, making it ideal for use in transformer and electromagnet laminations. Alloys such as permalloy can be produced with improved permeabilites, but at the expense of a reduced saturation flux density. Such alloys can be used in some electromagnets and are also commonly used in magnetic tape recording heads.

3.1.3 Material Properties for Permanent Magnets

Conversely, materials used as permanent magnets should have the following properties:

- a high remanence so that the domains are stable and a large flux density remains when the applied field is removed;

Material	μ_{max}	Saturation B, T	H_c, Am^{-1}
99.95% Iron	5000	2.14	71.60
Fe-3% Si (grain-orientated)	50000	2.01	7.16
Fe-3% Si (unorientated)	8000	2.01	55.70
45 Permalloy (55% Fe 45% Ni)	25000	1.60	19.89
Supermalloy (79% Ni 16% Fe 5% Mo)	800000	0.80	0.48

Table 3.1: Comparison of the properties of different ferromagnetic materials [61].

- a high permeability leaving a large residual magnetic field;
- and a high coercive field so that the material retains its magnetism.

All of which result in a large hysteresis loop. Also good is a high power (or BH product), which is related to the power required to demagnetise the permanent magnet. A large remanence and coercive field gives a high power. This is the largest rectangle that can be drawn in the second or fourth quadrant of the material's BH curve.

Table 3.2 shows the properties of several permanent magnet materials. Steel can act as a permanent magnet, but modern alloys have much improved properties with the best being NdFeB permanent magnets, which are now relatively affordable.

Material	B_r, T	H_c, Am^{-1}	max BH
Steel (0.9% C 1.0% Mn bal. Fe)	1	4000	1600
Alnico 1 (21% Ni 12% Al 5% Co bal. Fe)	0.71	35000	11100
Alnico 5 (24% Co 14% Ni 8% Al 3% Cu bal. Fe)	1.31	50900	47700
Alnico 12 (35% Co 18% Ni 8% Ti 6% Al bal. Fe)	0.58	75600	12700
Cunife (60% Cu 20% Fe 20% Ni)	0.54	43800	11900
Co_5Sm	0.95	756000	200000
$BaO \cdot 6Fe_2O_3$	0.40	191000	20000
$SrO \cdot 6Fe_2O_3$	0.34	263000	29000
Nd_2Fe_12B	1.20	875000	360000

Table 3.2: Selected properties of permanent magnet materials [61].

3.1.4 Eddy Current Losses

High electrical resistivity is also desirable in soft magnet materials for use in electromagnets. An applied time varying magnetic flux to a material induces an electromotive force (emf) around a ferromagnetic material. If the material's conductivity is not zero than the emf will induce an eddy current around the material. These eddy currents produce ohmic (or i^2R) heating and so a low conductivity and hence high resistance reduces these losses. Ceramic or ferrite materials therefore suffer less from heating than solid steel materials. The induced emf is proportional to the cross sectional area of the material, but the resistance is proportional to the length of the material's perimeter [63]. Therefore, by splitting the material into thin laminations separated by an insulating varnish the eddy current losses will be reduced. There will be a reduction in the core's permeability because of the cross-sectional area is occupied by the insulating material, but this is considered to be a much smaller loss than the benefit of reduced eddy current losses.

3.2 Electromagnets

It is important to use our knowledge of magnetism and materials to optimise the design of the electromagnets that will be used. An optimum design will generate large forces and a high stiffness for the minimum current input and hence power consumption. An optimum design will minimise the size of the electromagnets to reduce the design's mass and volume.

To achieve this optimisation in this Section the force generated by an electromagnet is derived and the concept of stiffness introduced. The different electromagnet configurations possible are then discussed.

3.2.1 Electromagnets

The reluctance force F_R generated in an electromagnet is given by:

$$F_R = -\frac{\mu_0 N^2 \varepsilon l i^2}{4\gamma^2} \tag{3.4}$$

where the negative sign indicates that the force is attractive. F_R has units of newton, μ_0 is the permeability of free space with a value of $4\pi \times 10^{-7}$ henry per metre, N is the number of turns in the electromagnet's coil, εl is the cross sectional area of the air gap measured in square metre, i is the current flowing through the coil in ampere and γ is the width of the air gap in metre. The reluctance force equation is derived in Appendix A.

3.2.2 Stiffness

The stiffness of a bearing is its resistance to movement when a force is applied on the bearing. It is defined as:

$$K_x = \frac{\triangle F_x}{\triangle x}_{\text{as } \triangle x \rightarrow 0} \tag{3.5}$$

where K_x is the stiffness with units of newton per metre where δx is the displacement produced with units of metre when a force F_x is applied.

The stiffness K_R of a magnetic bearing can be calculated as:

$$\begin{aligned} K_R &= \frac{\partial F_R}{\partial \gamma} && (3.6) \\ &= \frac{\mu_0 N^2 \varepsilon l i^2}{2\gamma^3} && (3.7) \end{aligned}$$

The stiffness of the bearing is an important term when the reluctance force is linearised when deriving controllers. If an integral term is included in a magnetic bearing's controller then the stiffness will be increased because as the integral term works to remove steady-state error it also maintains the rotor's position, increasing the stiffness.

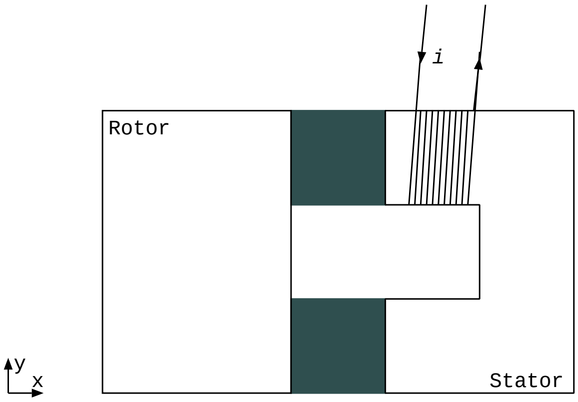

Figure 3.6: A flat rotor aligned with the stator.

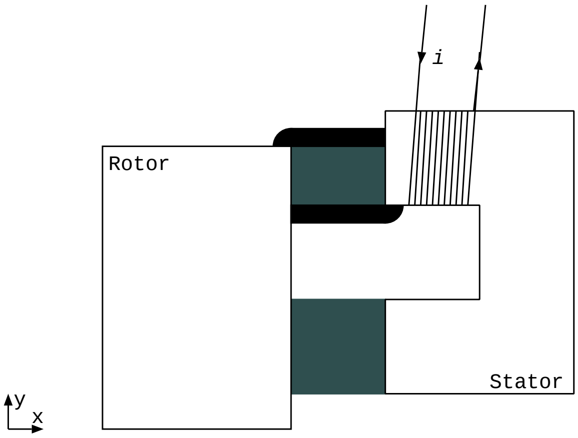

Figure 3.7: A flat rotor offset from the stator.

3.2.3 U-Shaped Electromagnets

With a simple rectangular rotor, when the rotor and stator are aligned as shown in Figure 3.6 the magnetic flux flowing from the electromagnets in the stator through the rotor and back to the stator will generate a force only in the x-direction. When the rotor is offset from the stator as shown in Figure 3.7 the flux in one air gap flows directly between the rotor and the stator, while in the other air gap, part of the flux will flow directly between the two poles (the mean reluctance - shown in grey) and the rest of the flux takes two slightly curved paths (the fringe reluctances - shown in black). The mean reluctance generates a suspension force only in the x-direction, while the fringe reluctances generate a force in the x-direction and also a smaller one in the y-direction. The y-component of the force will bring the stator and rotor into alignment again. When a u-shaped rotor is used, as shown in Figure 3.8, both poles have a fringe reluctance and so a greater restoring force is generated [44]. A u-shaped configuration will give improved control over the rotor because the increased fringe reluctances will generate an increased restoring force in the y-direction.

Equation 3.4 provides the magnitude of the force produced by an electromagnet. The following simplified numerical model gives the magnitude and direction of the force [42][44]:

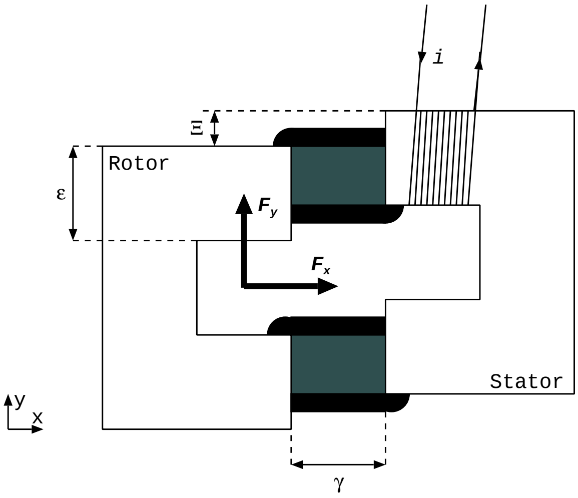

Figure 3.8: A u-shaped rotor offset from the stator.

$$F_x\left(\Xi,\gamma,i\right)=\frac{1}{4}N^2\mu_0\left(-\frac{\varepsilon-\Xi}{\gamma^2}-\frac{4\Xi}{4\gamma^2+\pi\gamma\Xi}\right)li^2 \tag{3.8}$$

$$F_y\left(\Xi,\gamma,i\right)=\frac{1}{4}N^2\mu_0\left(-\frac{1}{\gamma}+\frac{4}{4\gamma+\pi\Xi}\right)li^2 \tag{3.9}$$

The dimensions are defined in Figure 3.8. Where F_x is the strong attractive force and F_y is the guidance force that tries to bring the rotor and stator back into alignment, both in newtons. γ is the width of the air gap between the rotor and stator, Ξ is the offset between the rotor and stator, ε is the width of the poles, l is the depth of the poles, all with units of metres. N is the number of turns in the electromagnet's coil. i is the current flowing through the coils in amperes. μ_0 is the permeability of free space.

Figure 3.9 compares the forces generated in a simple electromagnet as calculated by an FEA simulation and Equations 3.8 and 3.9. The electromagnet is similar to Figure 3.8. It had an air gap width γ of 1.3 mm, pole width ε of 5 mm, depth l of 40 mm, one coil with $N = 300$ turns and a current i of 3 A in the coil. For the FEA simulation the FEMM software package was used with a triangular mesh and the mesh size set to 0.5 mm. The accuracy was set to 1×10^{-8} in FEMM's arbitrary units. The force on the rotor was calculated using FEMM's weighted stress tensor method.

For Figure 3.9 the rotor was initially aligned with the stator ($\Xi = 0$ mm) and was shifted in the y-direction by 0.5 mm, until there was no overlap between the rotor and stator poles. There is a good agreement between the two models until the rotor has been shifted to the side by almost the pole width ε. The restoring force F_y from the numerical model then continues to grow, in reality this force will begin to decrease as the offset Ξ approaches the pole width ε; the FEA simulation models this well. In the central position the difference between the attractive force in the x direction from the FEA simulation and the numerical method is 5.6% of the force predicted. No measurements were taken from the experimental hardware of the actual forces generated. It is therefore hard to calculate the accuracy of the FEA and numerical methods.

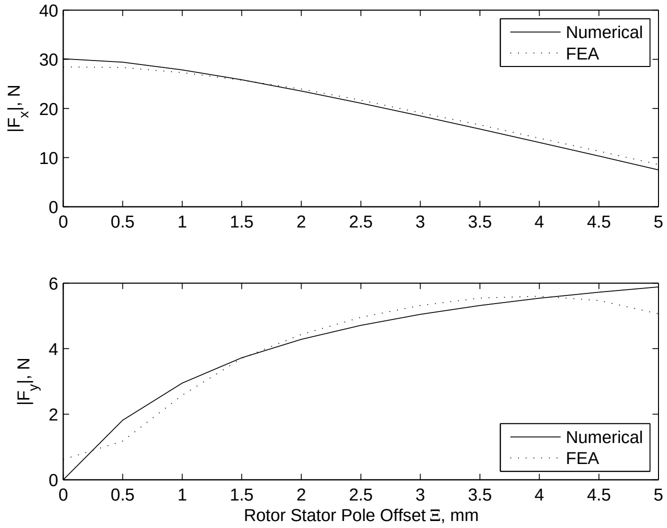

Figure 3.9: A comparison of the forces generated by an electromagnet calculated by the simple numerical and an FEA model.

Because the shape of the two method's responses agree then there is confidence that the two methods produce results that are good enough for designing magnet geometries that produce the greatest force possible.

U-shaped rotor pieces will be used to provide passive control of the rotor in the axis perpendicular to the actively controlled axis.

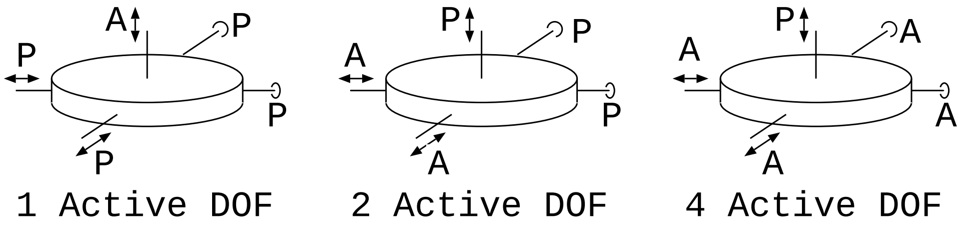

Figure 3.10: The Degrees Of Freedom (DOF) Actively (A) and Passively (P) controlled in active magnetic bearings [28].

3.3 Magnetic Bearings

Conventional, or mechanical, bearings have two solid objects in contact, and moving relative to each other. To reduce the friction between the two objects, and to prevent heating or damage to the objects, lubrication, or additional moving components, such as ball or roller-bearings are used. An alternative to the mechanical bearing is the magnetic bearing, where the moving part is held in place with a magnetic field. The simplest form of magnetic bearing is the passive magnetic bearing where the moving parts are suspended and their position determined passively by permanent magnets [35]. Active Magnetic Bearings (AMBs) combine electromagnets and position sensors. The current through the electromagnets' coils are varied to control the position of the moving part using feedback from the position sensors. Permanent magnets can be used in addition to electromagnets to generate part of the magnetic flux. Depending upon the arrangement of the electromagnets a number of degrees of freedom of the moving part can be controlled actively and the remainder passively as shown in Figure 3.10.

In a bearing with one degree of freedom actively controlled this will generally be the axial position. It will often have simple control electronics and mechanical construction but the passive damping of radial oscillations will be poor. A design with two degrees of freedom actively controlled will generally have the radial positions actively controlled. The design and the control system will still be relatively simple and the design will have a low axial height. A design with four degrees of freedom actively controlled has a much more complex mechanical and control system design but offers the facility to gimbal the moving parts [23].

3.3.1 Permanent Magnet Bias Flux

A combination of electro and permanent magnets is used in some magnetic bearings to generate the magnetic field from each electromagnet position. The flux density in the air gap of the bearing determines the characteristics of the bearing. The flux density in the air gap is limited by the saturation flux-density of the iron part of the magnetic circuit. If the saturation flux-density is exceeded then the efficiency of the system will decrease and it may become uncontrollable. Careful design is required to prevent this from happening while generating the best bearing characteristics possible.

The flux density in the air gap of an electromagnet, modified to our geometry is [41]:

$$B_{EM} = \frac{\mu_0 N i}{2\gamma} \tag{3.10}$$

where B_{EM} is the flux density in the air gap in tesla, N is the number of turns in the coil, i is the current in the air gap in Amps and γ is the air gap width in metres. This numerical solution for the air gap flux density has been confirmed by FEA simulations.

Molenaar [64] suggests that if bias flux from permanent magnets is required, an optimal design will have half of the air gap flux coming from the permanent magnets. The size of the permanent magnet required can be calculated from:

$$A_{PM} = \frac{B_u \varepsilon l}{B_r} \frac{R_G}{R_T} \frac{B_r}{B_m} \tag{3.11}$$

Where A_{PM} is the cross-section area of the permanent magnet in m^2; B_u is the useful flux density of the permanent magnet at the pole face, in tesla, which should be half of B_{EM}; εl is the cross-section area of the pole face in m^2, B_r is the remanence of the permanent magnet, with a value of 1.2 T being common for a neodymium (NdFeB) rare earth magnet; R_T/R_G is the useful flux ratio of the circuit and can be approximated to 40%. The maximum energy output from a permanent magnet can be obtained with the operating flux density being half the magnet's remanence; B_r/B_m is therefore two.

Simulations of circuits with the FEMM FEA package, which is described in Appendix B.2, have produced a lower flux density in the air gap than predicted by Equation 3.11. Further simulations and experimental investigations are necessary in this area.

3.4 Conclusions

A good understanding of the physics behind magnetism is essential when working with magnetic bearings. It allows the bearing's properties to be modelled and optimised and it allows the results from finite element simulations to be interpreted. Knowledge of magnetism allows the effects of eddy currents to be understood and means that laminated steel can be used to minimise losses from eddy currents.

The number of degrees of freedom actively controlled in a magnetic bearing is fundamental to that bearing's properties. The number of degrees of freedom to be actively controlled is the first thing to be decided when designing an active magnetic bearing. The 3Dwheel has to have four degrees of freedom actively controlled by electromagnets to allow it to generate its tilting torque. A fifth degree of freedom is actively controlled by a motor and the sixth degree of freedom is passively controlled by the electromagnets.

The next Chapter uses the reluctance force equation and stiffness to derive models for various electromagnet geometries. This knowledge can then be used to choose which geometry to use and to investigate the chosen geometry.

Chapter 4

Magnetic Bearing Design

There are many potential geometries that can be used in an active magnetic bearing. The final bearing design must be able to generate sufficient force to control the rotor's position and its stiffness must be great enough to transfer the gyroscopic torque generated to the spacecraft.

An analytical model of the forces generated by an electromagnet is therefore developed in this Chapter. The analytical model and numerical finite element simulations are then used to examine the properties of three different geometries that were generated for this thesis. The forces generated and the stiffness of each geometry is calculated to determine the suitability of each geometry for use in a tilting magnetically levitated design. The finite element software used is discussed in Appendix B.

The analytical model and finite element simulations are then used to identify how individual dimensions in a magnetic bearing affect the bearing's properties. These results can be used to optimise the chosen geometry to maximise its performance.

4.1 Radial and Axial Electromagnets

Figure 4.1 shows a tilting magnetically levitated momentum wheel. The rotor spins about its spin axis. Tilting the rotor about the tilt or gimbal axis produces a gyroscopic torque about the torque axis. Assuming that electromagnets are used in four positions around the wheel; to tilt the wheel electromagnets are required in the positions marked with a G. The electromagnets in positions marked with a T are required to transfer this torque to the spacecraft. Electromagnets are required in a minimum of three positions around the wheel. Electromagnets in four positions were chosen for this project to simplify the control logic required. Three is the minimum number of positions required to control the wheel, but will result in a reduced stiffness.

When a magnetically levitated momentum wheel is tilted, a relatively small force from an electromagnet generates a torque that can accelerate the rotor quickly, generating a large gyroscopic output torque. This output torque will have a tendency to rotate the rotor about an axis normal to the spin and tilt axes. Instead it is desired that the electromagnets hold the rotor steady, transferring the output torque to the spacecraft. The stiffness of the electromagnets determine the maximum torque that can be transferred from the wheel to the spacecraft. This is different to a Control Moment Gyro where the mechanical bearings transmit the output torque to the spacecraft.

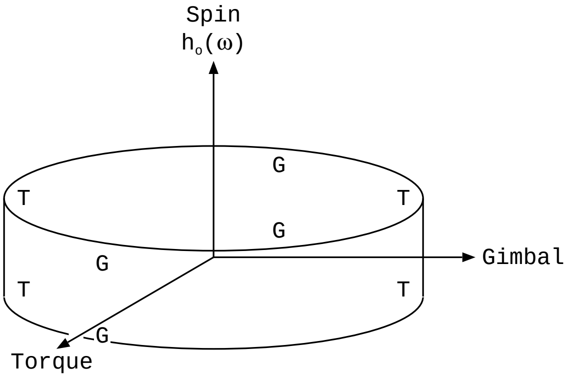

Figure 4.1: The electromagnet positions around a tilting magnetically levitated momentum wheel. The electromagnets to tilt the wheel are in the positions G and the magnets to transfer the resulting torque to the spacecraft are in positions T.

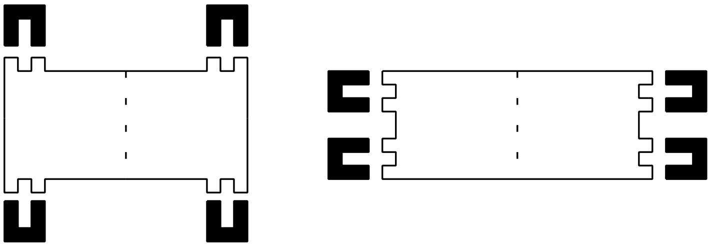

(a) Axial Electromagnets (b) Radial Electromagnets

Figure 4.2: Possible arrangements of the electromagnets in a cross-section of a tilting momentum-wheel. The electromagnets are shown in black. The spin axis of each wheel is indicated by the dotted line.

4.1.1 Axial Electromagnets

Electromagnets arranged axially above and below the rotor are shown in Figure 4.2(a). The axial translational position of the wheel and the two rotational axes are actively controlled. The radial position of the wheel is passively controlled. The tilting torque that an axial electromagnet exerts on the wheel is given by:

$$T_x = F_R r_T \tag{4.1}$$

where r_T is the distance from the centre of the wheel to the point that the electromagnet's force acts through; r_T is discussed in Section 4.4.2. When transferring a torque to the satellite the axial electromagnets' stiffness K_R depends upon the distance δz the rotor moves in the axial direction during the transfer:

$$K_R = \frac{T_{xfer}}{r_T \delta z} \tag{4.2}$$

Equating this to the reluctance force stiffness from Equation 3.7, allows the axial displacement to be predicted for different magnet designs or for the electromagnets to be optimised for torque transfer. The pole face area εl of the electromagnet depends upon the radius of the pole face. An example axial electromagnet pole face is shown in Figure 4.3. The angle of the arc that the pole face extends over can vary but was initially set at 45°. The inner pole face area will be used when calculating the stiffness as it is the smallest, which is given by:

$$\varepsilon l = \frac{45^\circ}{360^\circ}(\pi(r_i + \varepsilon)^2 - \pi r_i^2) \tag{4.3}$$

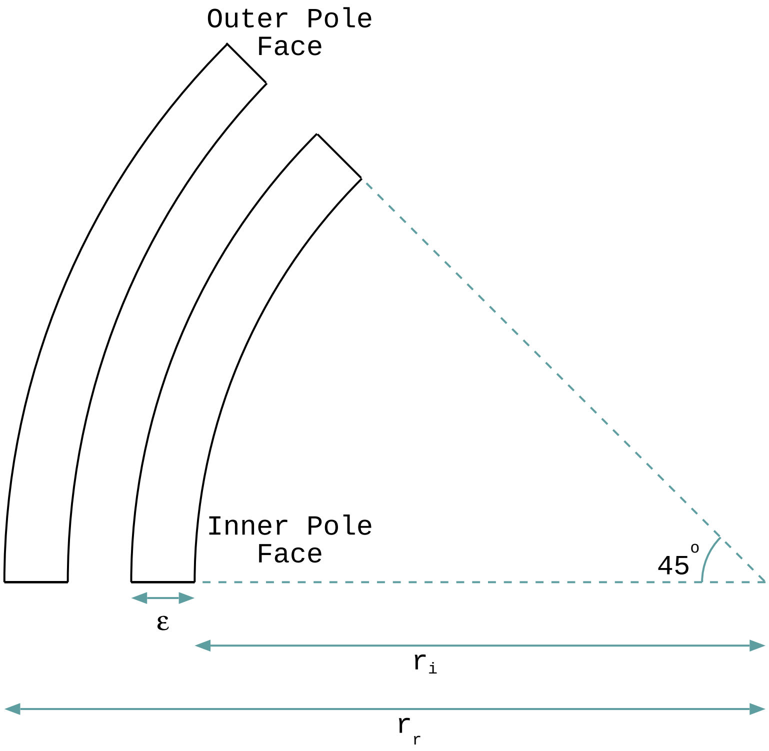

Figure 4.3: A plan view of the pole face of an axial electromagnet spanning an arc of 45°.

where r_i is the inner radius of the inner pole face.

The minimum width of the electromagnet air gap required to allow rotation through a set angle depends upon the magnet's distance from the axis of rotation. If the axial height of the rotor is η and the radius of the rotor is r_r, then using the rotation matrix:

$$\begin{bmatrix} x' \\ y' \end{bmatrix} = \begin{bmatrix} \cos\theta & -\sin\theta \\ \sin\theta & \cos\theta \end{bmatrix} \begin{bmatrix} x \\ y \end{bmatrix} \tag{4.4}$$

the minimum air gap width is then:

$$\gamma_{min} = r_r \sin \alpha_{max} + \eta/2 \cos \alpha_{max} - \eta/2 \tag{4.5}$$

where α_{max} is the maximum tilt angle of the wheel.

4.1.2 Radial Electromagnets

Electromagnets arranged radially around the wheel are shown in Figure 4.2(b). The rotor's position along both radial translation axes and its rotational position about both tilt axes is actively controlled. Its axial translational position is passively controlled.

For the case of radial electromagnets the minimum air gap to tilt the rotor through the maximum tilt angle α_{max} is given by:

$$\gamma_{min} = r_r \cos(-\alpha_{max}) - \eta/2 \sin(-\alpha_{max}) - r_r \tag{4.6}$$

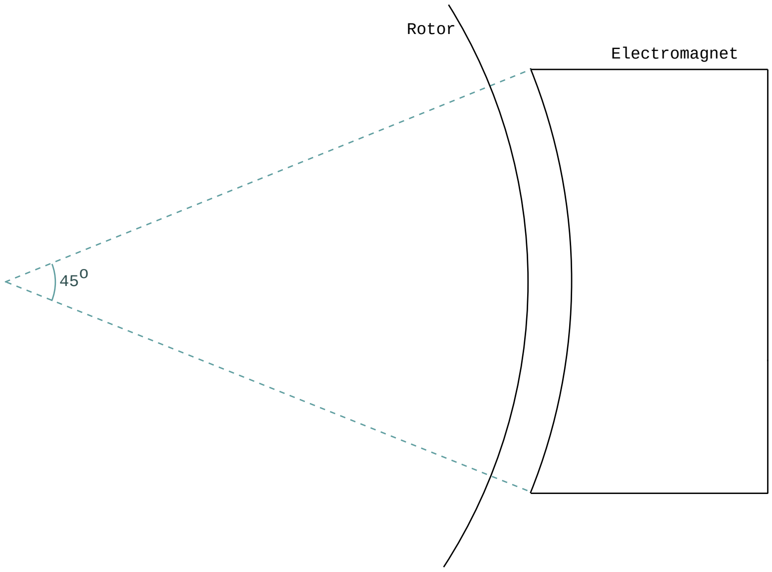

Figure 4.4: A plan view of a radial electromagnet spanning an arc of 45°.

The poles have initially been assumed to spread over an arc of $45°$ again as shown in Figure 4.4. The cross sectional area of the air gap is given by:

$$\varepsilon l = \varepsilon \frac{45°}{360°} 2\pi (r_r + \gamma) \tag{4.7}$$

4.1.3 Radial and Axial Electromagnets Comparison

Section 4.4 discusses the optimum geometry for the rotor of a satellite momentum wheel and how it will tend to have the largest possible radius to maximise its moment of inertia and generate a large output torque while minimising its height so that it has a low mass. The engineering model of the 3Dwheel built for this project has a radius of 50 mm, an axial height of 56 mm and is capable of tilting through $\pm 3^\circ$. For this configuration the minimum air gap width with axial electromagnets is 2.6 mm and 1.4 mm with radial electromagnets. The reluctance force produced by an electromagnet is inversely proportional to the square of its air gap. Therefore, for a rotor with these dimensions, the radial configuration will tend to produce a larger force and have a greater stiffness than the axial configuration.

4.2 Principal Geometry Options

Section 4.1 provided an overview of the different ways that electromagnets could be arranged around a rotor. More detailed models and comparisons between these configurations will now be developed. Each design will be primarily analysed for the force and stiffness that it can generate. Force is important for torque generation. Stiffness is important for torque generation and also for transferring the gyroscopic torque generated to the spacecraft. For use on a spacecraft then it is important to minimise the mass and volume of the electromagnets. For the engineering model then ease of construction and maintenance are also important to consider.

Two radial and one axial configuration have been developed for this thesis. These designs will now be compared.

4.2.1 External Radial

Figure 4.5 shows the External Radial design. U-shaped electromagnets are arranged in two layers around the outside of the rotor to provide active control of two radial translation and two rotation axes. The axial translational position is controlled passively. The electromagnets can easily be made from laminated steel to minimise eddy current losses.

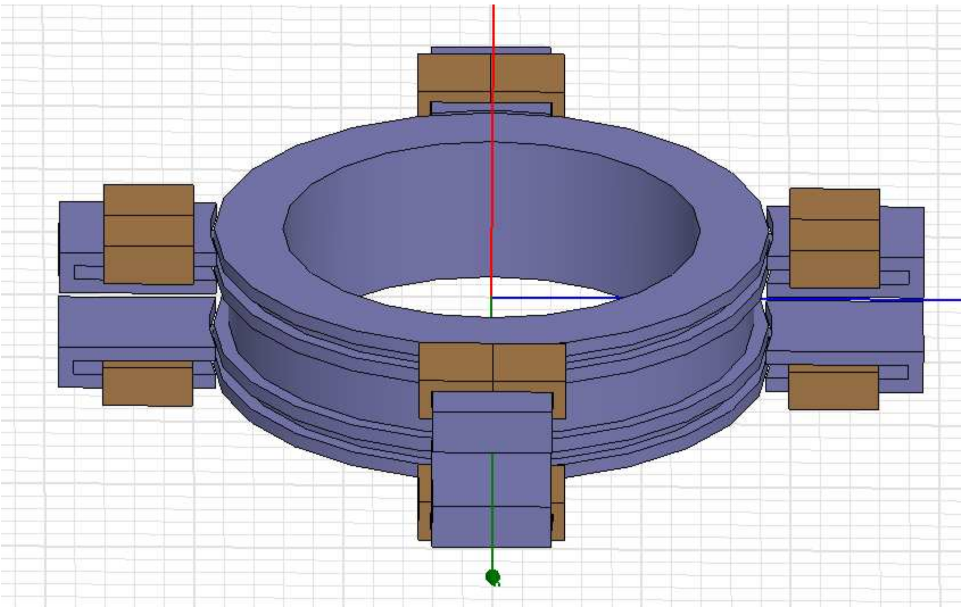

Figure 4.5: The External Radial design with u-shaped electromagnets arranged around the outside of the rotor.

4.2.2 Planar Radial

Figure 4.6 shows the Planar Radial design and Figure 4.7 shows the magnetic flux density vectors when all of the Planar Radial design's electromagnets are energised. Both poles of an electromagnet are in the same plane normal to the rotor's spin axis' central position. Two radial translation and two rotation axes are actively controlled; the axial translational position is passively controlled. Figure 4.7 shows a simplified version of the design; the mass of this design could be reduced by removing the steel between poles that has no flux flowing through it. This design could be easily manufactured from laminated steel.

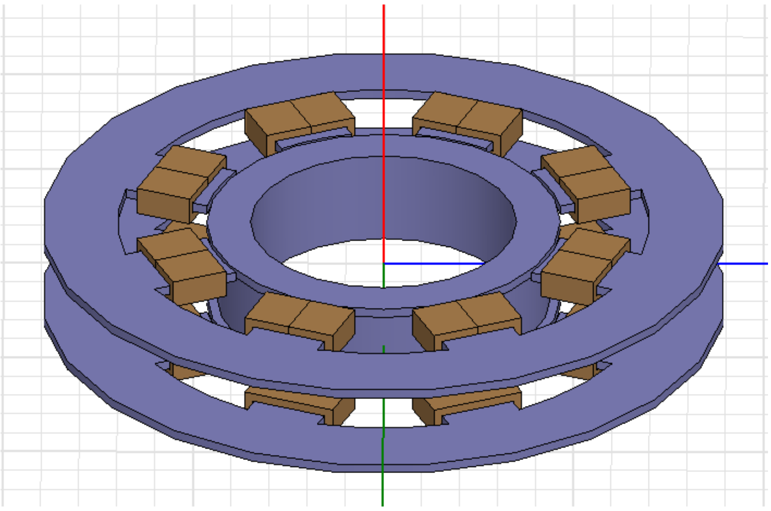

Figure 4.6: The Planar Radial design with the electromagnets arranged in a plane.

4.2.3 Axial

Figure 4.8 shows the Axial design. The axial translational position and rotational axes are actively controlled; two radial translation axes are passively controlled. This design could be difficult to make from laminated steel, making the design susceptible to eddy current losses. Each lamination in an electromagnet would have to be wedge shaped, which would be too costly to manufacture using traditional techniques.

4.2.4 Design Comparison

Each of the designs was modelled in the 3D Maxwell FEA package, which is described in Appendix B.2. The force generated by an electromagnet is given by the reluctance force equation:

$$F_R = -\frac{\mu_0 N^2 \varepsilon l i^2}{4\gamma^2} \tag{4.8}$$

To allow each of the designs to be compared with the others the cross sectional area of each design's air gap εl was made the same. For the Axial and External Radial designs each electromagnet had 100 turns with 3 A flowing through each one. For the Planar Radial design, each electromagnet requires two coils to control the flux and so each coil has 50 turns and 3 A flowing through it, giving a total of 300 ampere-turns per electromagnet again.

For each of the designs two rotor radii that could each tilt through 3° were compared:

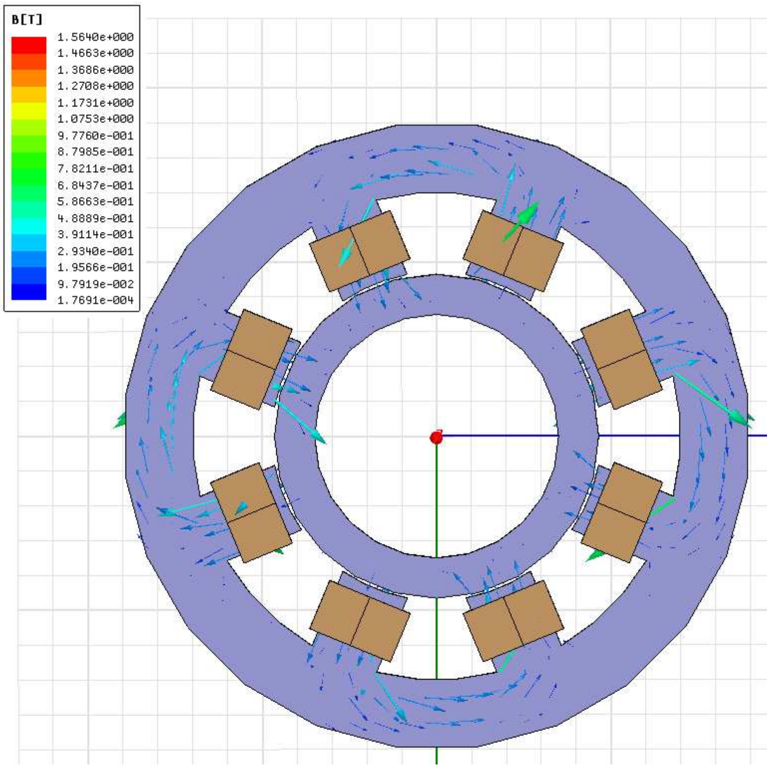

Figure 4.7: The Planar Radial design showing the lines of magnetic flux calculated in a magnetostatic finite element simulation.

1. a rotor of radius 93 mm and height 50 mm. The External Radial and Radial Planar designs having an air gap width of 1.2 mm, pole height ε of 5.0 mm and a pole width of 40 mm, giving a pole face length l of 40.3 mm. The Axial design had an air gap width of 4.9 mm, the pole height was 5.0 mm and the arc that each pole spread around was 29° so that the area of the inner pole face was the same as the product εl for the radial designs to give a good comparison;

2. a rotor of radius 50 mm and height 50 mm. The two radial designs having an air gap width of 1.3 mm, pole height ε of 5.0 mm, pole width of 38 mm giving a pole face length of 38.9 mm. A pole width of 38 mm was the largest that could be used that fitted all eight of the Planar design's poles around the rotor. The Axial design required an air gap width of 2.6 mm, a pole height ε of 5.0 mm and a pole arc of 60° to give the same pole face area εl as the radial designs.

The axial, radial and rotational stiffness of each of the three designs was calculated analytically and using a 3D finite element analysis (as described in Appendix B. For each design some translational axes will be actively controlled and others passively, which is summarised in Table 4.1. The tilt axes are actively controlled in all designs. The electromagnets that need to be energised to calculate the translational forces vary and are included in the table; “all” means that all electromagnets had current flowing through them, “+x” means that only electromagnets on the positive x-axis were energised (electromagnets 1 and 2 in Figure 6.2), “top” means the four electromagnets above the rotor and “+y top” means that the electromagnet on the +y axis

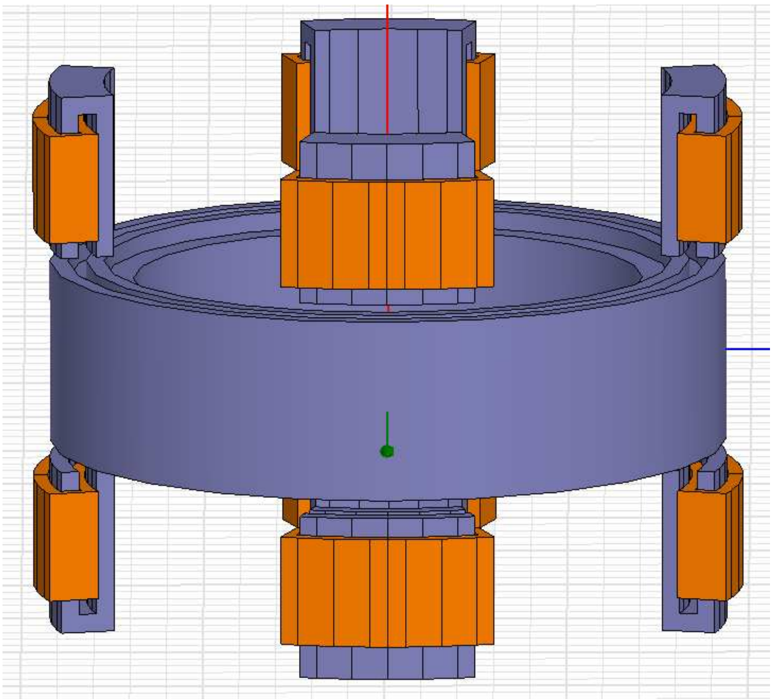

Figure 4.8: The Axial design with the electromagnets arranged axially.

above the rotor had a current through it. Where an active force is being measured, the forces on the rotor were calculated with the rotor in its central position and shifted along the appropriate axis by 0.1 mm, e.g. for the axial stiffness, shifted by 0.1 mm in the +z direction. The active stiffness is then:

$$K_{active} = \frac{F_R(\delta z = 0.1 \text{ mm}) - F_R(\delta z = 0)}{1 \times 10^{-4}} \tag{4.9}$$

where the stiffness is calculated by finding the change in force on the rotor when the rotor is shifted in the z direction by 0.1 mm divided by the distance that the rotor was shifted by. The magnitude of the passive stiffness, from Equation 3.9, depends on the offset Ξ between the rotor and stator poles. Therefore, the passive stiffness was calculated by finding the passive restoring force at $\Xi = 0.5$ and 0.6 mm, which is 10% of the pole width when $\varepsilon = 5.0$ mm. For example, for calculating the axial stiffness of the External Radial design, the axial force was calculated with the rotor shifted along the +z axis by 0.5 and 0.6 mm. The magnitude of the active force was found analytically using the standard reluctance force equation, Equation 4.9, ignoring the effect of the offset Ξ between the rotor and stator poles. Ξ could have been accounted for by using Equation 3.8. However, with the geometry of the 50 mm radius rotor, there is only a 2.3% difference in the values from Equations 4.9 and 3.8, which is less than than the 5.6% difference between Equation 4.9 and the finite element simulation value from Figure 3.9.

Analytically, in addition to calculating the stiffness by finding the force or torque acting on the rotor in two positions, the stiffness can also be calculated by differentiating the active or passive reluctance force equation with respect to the the air gap width γ in the active case or pole offset Ξ in the passive case:

	Axial Stiffness	Radial Stiffness	Rotational Stiffness
External Radial	Passive, all EMs $\delta z = 0.5, 0.6$ mm	Active, +x EMs $\delta x = 0.0, 0.1$ mm	Active, -y top & +y bot $\delta\alpha = 0.0, 0.1°$
Radial Planar	Passive, all EMs $\delta z = 0.5, 0.6$ mm	Active, +x EMs $\delta x = 0.0, 0.1$ mm	Active, -y top & +y bot $\delta\alpha = 0.0, 0.1°$
Axial	Active, top EMs $\delta z = 0.0, 0.1$ mm	Passive, all EMs $\delta x = 0.5, 0.6$ mm	Active, +y top & -y bot $\delta\alpha = 0.0, 0.1°$

Table 4.1: The source (active or passive) of the force along this axis, the electromagnets (EMs) required to test this force and the positions in which the force was calculated when evaluating the stiffness.

$$\begin{aligned} F_z(\Xi, \gamma, i) &= \frac{1}{4} N^2 \mu_0 l i^2 \left(-\frac{1}{\gamma} + \frac{4}{4\gamma + \pi \Xi} \right) \\ \frac{\partial F_z}{\partial \Xi} &= -\frac{N^2 \mu_0 l i^2 \pi}{(4\gamma + \pi \Xi)} \end{aligned} \tag{4.10}$$

Similarly in the active case:

$$\begin{aligned} F_z(\gamma, i) &= \frac{\mu_0 N^2 \varepsilon l i^2}{4\gamma^2} \\ \frac{\partial F_z}{\partial \gamma} &= -\frac{\mu_0 N^2 \varepsilon l i^2}{2\gamma^3} \end{aligned} \tag{4.11}$$

The rotational stiffness was calculated with two electromagnets energised so that a torque was exerted on the rotor that had a direction to rotate the rotor in the positive (anti-clockwise looking from the positive axis towards the origin) direction about the +x axis. The torque was measured with the rotor central and when tilted by $0.1°$ about the x-axis.

	93 mm Radius			50 mm Radius		
	Radial	Planar	Axial	Radial	Planar	Axial
F_z at δz_1, N	-1.22	-0.911	1.003	-1.18	-0.765	3.37
F_z at δz_2, N	-1.45	-1.07	1.051	-1.40	-0.907	3.57
K_z, Nm^{-1}	2.28×10^3	1.56×10^3	475	2.20×10^3	1.42×10^3	2.06×10^3

Table 4.2: The designs' axial stiffnesses calculated using finite element analysis simulations.

Table 4.2 shows the designs' axial stiffness calculated using finite element simulations and Table 4.3 shows the axial stiffnesses calculated analytically.

Table 4.4 shows the designs' radial stiffness calculated using finite element simulations and Table 4.5 shows the radial stiffnesses calculated analytically.

The rotational stiffness was calculated for all three designs and the results are shown in Table 4.6.

	93 mm Radius				50 mm Radius			
	External Radial		Axial		External Radial		Axial	
	Force	∂F/$\partial\Xi$	Force	∂F/$\partial\gamma$	Force	∂F/$\partial\Xi$	Force	∂F/$\partial\gamma$
F_z at δz_1, N	-1.87		0.922		-1.57		3.05	
F_z at δz_2, N	-2.14		0.960		-1.80		3.29	
K_z, Nm^{-1}	2.69×10^3	2.82×10^3	380	392	2.31×10^3	2.41×10^3	2.39×10^3	2.53×10^3

Table 4.3: The External Radial and Axial designs' axial stiffnesses calculated analytically.

	93 mm Radius			50 mm Radius		
	Radial	Planar	Axial	Radial	Planar	Axial
F_x at δx_1, N	7.42	5.52	-0.0464	5.41	3.83	-0.188
F_x at δx_2, N	8.60	6.28	-0.0579	6.14	4.30	-0.277
K_x, Nm^{-1}	1.18×10^4	7.61×10^3	115	7.25×10^3	4.68×10^3	894

Table 4.4: The designs' radial stiffness calculated using finite element analyses.

The volume occupied by each design was found by drawing the smallest rectangular box possible around each design. The results are shown in Table 4.7. This is not the most accurate comparison of the volumes of each design because:

(i) these models were drawn to provide a comparison of the electro-magnetic properties of each design and so are not optimised for size;

(ii) the volume was calculated by drawing a rectangular box around each design; the External Radial design contains much empty volume between the electromagnets and the Planar Radial design has a smaller volume when surrounded by a cylinder (6.1×10^{-3} m^3). The design of the Planar Radial configuration will also offer the most room for volume reduction, with large amounts of steel used around the outside of this early design.

4.2.5 Conclusions

Because of the 93 mm radius axial design's large air gap width it has a poor radial and axial stiffness, although its rotational stiffness is comparable with the other designs.

An actively controlled force is always greater than a passively controlled force, with an increase in stiffness of between 5.2 and 2.3 times observed.

The design with the best axial and radial stiffness was the External Radial design with a radius of 93 mm. This design had a greater stiffness than the equivalent 50 mm radius design. The External Radial design had a consistently higher stiffness than the Planar Radial design. This is possibly due to shorter path length of the iron part of the magnetic circuit that the flux flows through in the External Radial design, because the pole face cross section area was identical in both designs.

The axial stiffness of the 50 mm radius Axial design is comparable to the axial stiffness of the other 50 mm radius designs despite its larger air gap width because it is an active force while

	93 mm Radius				50 mm Radius			
	External Radial		Axial		External Radial		Axial	
	Force	∂F/$\partial\gamma$	Force	∂F/∂Ξ	Force	∂F/$\partial\gamma$	Force	∂F/∂Ξ
F_x at δx_1, N	7.91		-0.0676		6.51		-0.209	
F_x at δx_2, N	9.42		-0.0799		7.64		-0.245	
K_z, Nm^{-1}	1.50×10^4	1.32×10^4	125	123	1.13×10^4	1.00×10^4	364	354

Table 4.5: The External Radial and Axial designs' radial stiffnesses calculated analytically.

	93 mm Radius			50 mm Radius		
	Radial	Planar	Axial	Radial	Planar	Axial
T_x at 0.0°, Nm	8.84×10^{-2}	8.85×10^{-2}	4.34×10^{-2}	9.10×10^{-2}	8.33×10^{-2}	7.32×10^{-2}
T_x at 0.1°, Nm	9.25×10^{-2}	9.03×10^{-2}	4.60×10^{-2}	9.28×10^{-2}	8.51×10^{-2}	7.73×10^{-2}
$K_{\alpha x}$, Nm/°	4.08×10^{-2}	1.79×10^{-2}	2.53×10^{-2}	1.76×10^{-2}	1.81×10^{-2}	4.12×10^{-2}

Table 4.6: The designs' rotational stiffness calculated using finite element analyses.

the axial force of the Radial designs is passive. The axial forces generated by this Axial design are in fact greater than the axial forces in the other designs. However, the radial stiffness of the Axial design is poor because it is generated passively by electromagnets with large air gaps. Radial stiffness is important to counteract static mass imbalance.

The force predicted analytically was greater than the finite element force in all cases except for the axial force in the 93 mm radius Axial design and the radial force in the 50 mm radius Axial design. The magnitude of the difference between the analytical and finite element methods varies between designs. These simulation values ideally need to be compared with experimental data to determine their accuracy.

The stiffest design that can generate the greatest force will always be the design that has the smallest air gap width. The minimum air gap required is determined by the range of angles that the rotor is designed to tilt through. During the design process there must be a trade off between these two variables.

For a tilting magnetically levitated wheel stiffness is important so that the gyroscopically generated torque can be transferred to the spacecraft. For use on a spacecraft the most important factors to optimise are the power consumption so that the actuator fits with in the spacecraft's available power budget. Volume and mass are also important factors as there is limited space available on a spacecraft and mass needs to be minimised for the launch.

	93 mm Radius			50 mm Radius		
	Radial	Planar	Axial	Radial	Planar	Axial
Volume, m^3	5.0×10^{-3}	7.8×10^{-3}	5.7×10^{-3}	2.2×10^{-3}	9.4×10^{-3}	9.8×10^{-4}

Table 4.7: The volume occupied by a rectangular box surrounding the initial, non-optimised designs for the External Radial, Planar Radial and Axial designs.

4.3 Electromagnet Induced Disturbances

As well as producing the desired restoring forces, two situations have been identified where the electromagnets can generate unwanted disturbance torques.

4.3.1 Non-Parallel Pole Faces

The reluctance force exerted on a rotor by an electromagnet is given by:

$$F_R = -\frac{\mu_0 N^2 \varepsilon l i^2}{4\gamma^2} \tag{4.12}$$

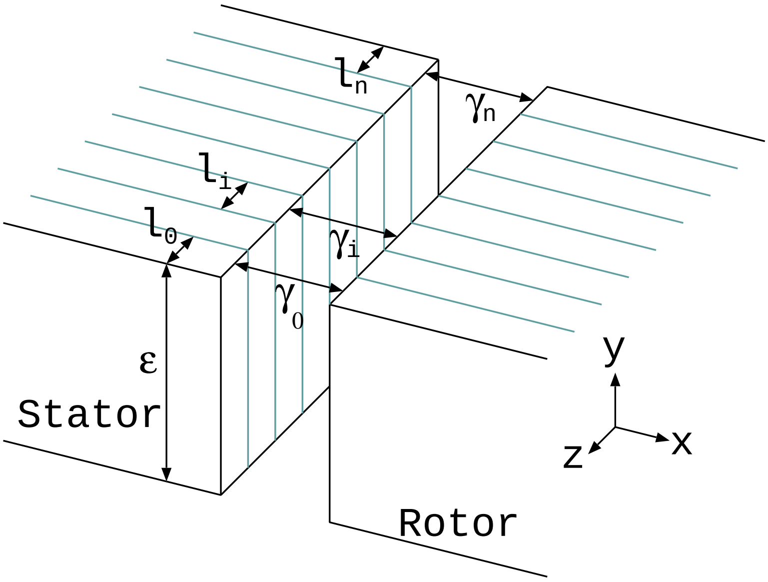

Figure 4.9: How the magnetic flux in one pole of an electromagnet can be divided into smaller sections.

This assumes that the pole faces on the rotor and stator are parallel, and hence the air gap has a constant width across the entire pole face. If the pole faces are not parallel then an additional rotational force will be generated that will have a direction that makes the pole faces even more non-parallel. Figure 4.9 shows the pole faces of one of the air gaps in an electromagnet. Equation 4.12 can be re-written as:

$$F_R = -\frac{\mu_0 N^2 \varepsilon i^2}{4} \sum_{i=0}^{n} \frac{l_i}{\gamma_i^2} \tag{4.13}$$

This means that if the rotor is rotated about the +y axis then $\gamma_n < \gamma_0$. The attractive force generated at the γ_n end of the pole face will be greater than the force at the γ_0 end. This will result in the usual reluctance force acting on the rotor in the -x direction, but also a torque about the +y axis. The direction of this torque will cause the rotor to rotate further about the +y axis. This positive feedback system is therefore unstable in this respect.

This phenomenon was first observed in the beam hardware described in Section 5.1. The beam hardware was a tilting magnetically levitated beam where one translational and one rotational axis was actively controlled. The phenomenon was then confirmed through analytical and finite element simulations. Finite element simulations have confirmed this behaviour as shown in Table 4.8. For this simulation: $\varepsilon = 5$ mm, $l = 40$ mm, $\gamma = 1.3$ mm, $N = 100$ and $i = 3.0$ A. The rotor was rotated by 1° about the +y axis. The axes are as defined in Figure 4.9.

	Parallel Pole Faces	1° Rotor Rotation about +y
F_x, N	3.70	3.96
T_y, Nm	0.000	0.014

Table 4.8: The forces acting on the rotor in an electromagnet with parallel pole faces and with the rotor rotated through 1°.

Designs must have all six degrees of freedom controlled, either actively or passively. The levitated beam has two rotational degrees of freedom uncontrolled and one actively controlled; it has one translational degree of freedom actively controlled, one passively and one uncontrolled and is therefore unstable.

4.3.2 Rotated Pole Faces

When the rotor is tilted about the gimbal axis in Figure 4.1 then the rotor at positions marked T will be at an angle to the stator electromagnets. Figure 4.10 shows this situation for one of the electromagnets marked as T in Figure 4.1 with the stator electromagnet shown in dark blue in the background and is viewed through the semi-transparent rotor in the foreground.

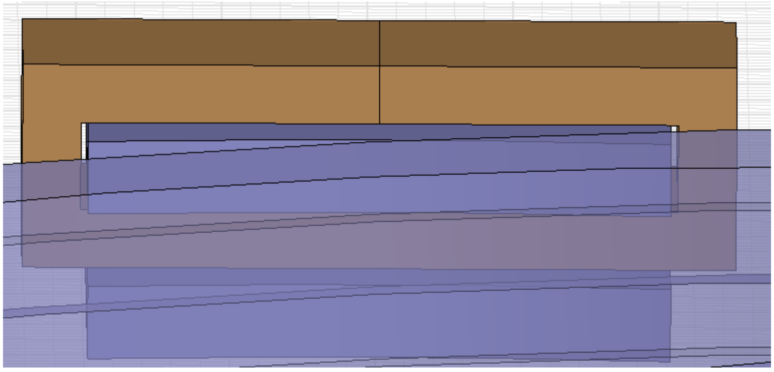

Figure 4.10: A 3D rendering of one electromagnet in a tilting magnetically-levitated momentum-wheel. The stator electromagnet is in the background and is viewed through the semi-transparent rotor.

For a positive rotation about the gimbal axis in Figure 4.1 there will be an active reluctance force attracting the rotor to the stator. There will also be a passive restoring force that has a direction that tries to rotate the rotor to oppose the applied rotation.

A finite element simulation of this phenomenon was performed. The system had the usual properties of: $\varepsilon = 5$ mm, $l = 40$ mm, $\gamma = 1.3$ mm, $N = 100$ and $i = 3.0$ A. The results are shown in Table 4.9. This disturbance torque is almost two orders of magnitude less than the torque applied to tilt the wheel in Table 4.6. This disturbance can be ignored.

	Parallel Pole Faces	1° Rotor Rotation about +x
F_x, N	3.70	3.68
T_x, Nm	-2.0×10^{-5}	-1.0×10^{-3}

Table 4.9: The forces acting on the rotor in an electromagnet with the rotor at an angle of 1° to the stator.

4.4 Geometry Investigation

The effect of varying a magnetic bearing's geometry on its force and stiffness has been studied by varying one dimension at a time. This knowledge can be used to obtain the best bearing properties possible.

4.4.1 Cross Sectional Electromagnet Area

Figure A.1 in Appendix A shows the model of an electromagnet used when deriving the equation giving the reluctance force generated by an electromagnet. From the derivation of this equation, the magnetic flux Φ in the circuit is given by:

$$\Phi = \frac{Ni}{\dfrac{\gamma_{rotor} + \gamma_{stator}}{\varepsilon l \mu_{iron}} + \dfrac{2\gamma}{\varepsilon l \mu_{air}}} \tag{4.14}$$

However in a vacuum $\mu_{air} \approx \mu_0$ and $\mu_{iron} \gg \mu_{air}$, therefore Φ is approximated to:

$$\Phi = \frac{Ni\varepsilon l \mu_0}{2\gamma} \tag{4.15}$$

where εl is the cross-sectional area of the air gap. Therefore, reducing the cross-sectional area of the rotor or stator iron sections away from the pole face should have only a minimal effect on the magnetic flux and hence the reluctance force generated. The pole face area of the steel sections must still be kept at εl as this defines the air gap cross-sectional area and the reluctance force generated.

These assumptions were confirmed using the Finite Element simulations shown in Figure 4.11. For this simulation, $\varepsilon = 5$ mm, $l = 40$ mm, $\gamma = 1.3$ mm, $N = 100$ and $i = 3.0$ A. In the lower design of Figure 4.11 the width of the iron part of the stator has been halved in thickness to 2.5 mm.

The results are shown in Table 4.10. These finite element results confirm the theory above. The results show that reducing the cross-sectional area of part of the steel away from the pole faces in an electromagnet has a minimal effect on the force generated by that electromagnet. This result is useful because iron can be removed from parts of an electromagnet to reduce the mass and volume of a design without affecting the force generated. With all designs it is important to check that the magnetic flux is not saturating the steel. When steel is removed from a design it is particularly important to check that the magnetic flux is not saturating the thinner sections of the material.

4.4.2 Coil Position on an Electromagnet

Figure 4.12 shows two electromagnets with identical steel parts, but with their coils mounted in different sections of the steel part. The top symmetrical electromagnet has its coil mounted on

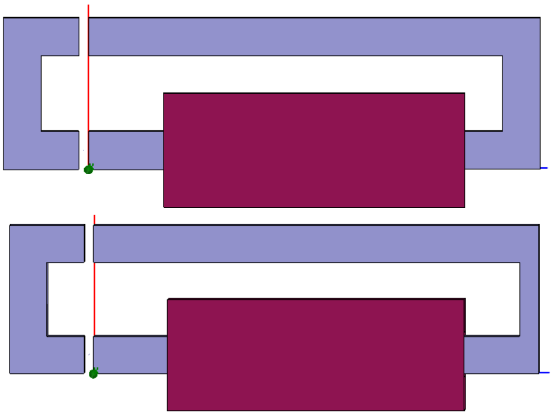

Figure 4.11: A finite element simulation of two simple electromagnets, the bottom one of which has a reduced cross-section area in the right-hand steel part of the stator.

Design	Force, N
Constant εl	3.72
Thinner	3.70

Table 4.10: The reluctance force generated by two electromagnets, one of which has a reduced cross-sectional area in part of stator.

the back edge and the bottom asymmetric design has its coil mounted on the bottom edge, where it is often more convenient to wind the coil. These designs were simulated in the Maxwell FEA package. Their properties were, using our standard notation: $\varepsilon = 5.0$ mm, $l = 40$ mm, $\gamma = 1.3$ mm, $N = 100$ and $i = 3.0$ A.

The magnetic flux density plotted through the centre of the two air gaps of each electromagnet is shown in Figure 4.13. The electromagnet with the coil on its back edge has the same flux density in both air gaps. The electromagnet with the coil on the bottom edge has the same total flux density but is 5.2% greater in the air gap closest to the coil than in the other air gap. This difference in flux density generates a similar attractive force on the rotor and a small additional force in a perpendicular direction. The forces acting on the rotor in the two cases are shown in Table 4.11. The negligible value was 2.5×10^{-5} N, which is less than the accuracy of the simulation and so can be taken to be 0 N. The direction of the perpendicular force in the electromagnet with the coil on the bottom edge was to move the rotor towards the air gap closest to the coil.

	Back Edge	Bottom Edge
F_y, N	3.70	3.72
F_z, N	negligible	-0.02

Table 4.11: The forces acting on the rotors with their coils on the back and bottom edges.

Although the forces are small in this case, they will increase in electromagnets generating a larger magnetic flux. The passive restoring forces generated by electromagnets are also much smaller than the main active forces. The passive forces are along the same axis as the force

Figure 4.12: A finite element simulation of identical electromagnets with their coils mounted in different locations. The top electromagnet has a coil on its back edge and the bottom magnet has the coil on its bottom edge.

from the electromagnet with the coil on its bottom pole and so there will be constructive or destructive interference with the passive force. The effects of this asymmetric force from the electromagnet with the coil on the bottom edge can be minimised in the External Radial Design of a momentum wheel by always placing the coils on the outside of the electromagnets as shown in Figure 4.5. These asymmetric forces will not occur in the Planar Radial design.

	Bottom Pole	Top Pole
F_x, N	0.531	0.529
F_y, N	7.46×10^{-3}	-7.50×10^{-3}
T_0, Nm	-1.57×10^{-2}	-1.82×10^{-2}
r_T, m	3.0×10^{-2}	3.4×10^{-2}

Table 4.12: The forces, torques and lever arms generated by the two designs shown in Figure 4.14.

Figure 4.14 shows two alternative positions for the coil on asymmetric electromagnets. In both cases the bottom of the electromagnet is 20 mm above the origin, the height of each pole is 8.0 mm and there is a gap of 8.0 mm between the arms of the poles . The forces along the positive x and y axes and the torque about the origin were calculated in a 2D finite element simulation and are shown in Table 4.12. A torque T_0 about point $(0, 0)$ can be defined by:

$$T_0 = r_T F \tag{4.16}$$

where F is the force acting on an object a distance r_T from the point that the object is pivoting about (the lever arm length). Table 4.12 shows that the horizontal force on the rotor of both designs in Figure 4.14 is similar but the torque produced is different. Rearranging Equation 4.16

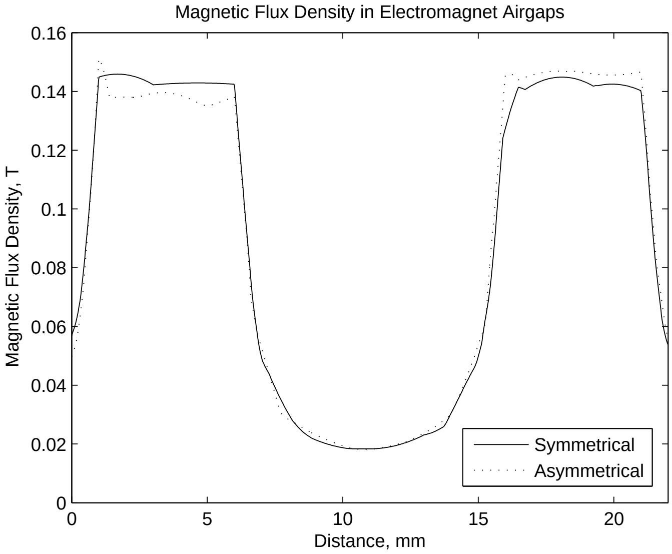

Figure 4.13: A finite element simulation of the magnetic flux density plotted through the centre of the two air gaps of two electromagnets. The symmetrical plot has the coil on the electromagnet's back edge and the asymmetric plot has the coil on its bottom edge.

allows the lever arm length r_T to be calculated for both designs, with the results being included in the bottom row of Table 4.12.

The lever arm length of a u-shaped electromagnet used to tilt a rotor can be assumed to be in the centre of an electromagnet, between the two poles. The torque generated by such an electromagnet can be maximised by placing the coil on the pole furthest from the centre of rotation.

4.4.3 Passive and Active Force Contribution

Figure 4.15 shows the forces acting on the rotor to generate a torque T_t that tilts the rotor. Figure 4.15 shows an external radial design, but the axial design has the same configuration, only rotated; therefore the following discussion is applicable to both the axial and radial designs. When the electromagnet is energised by current i_t the torque has the direction shown in the Figure. The active force F_x generated by the electromagnets acts at a distance r_y to generate T_t. Once the rotor has been tilted the rotor and stator poles are not aligned and a passive restoring force F_y will be generated that has a direction that tries to bring the rotor and stator poles back into alignment. This passive restoring force acts at a distance r_x and the torque component generated will have a direction that opposes the tilting torque. However, as shown by Figure 3.9, $F_x \gg F_y$ and so the net torque on the rotor will tilt the rotor. Increasing the height of the rotor will increase the magnitude of the torque that tilts the rotor. Decreasing the radius of the rotor will increase the tilting torque.

Figure 4.16 shows the forces acting on the rotor to generate a restoring torque T_r that brings a tilted rotor back into alignment with the stator. Both the active force F_x and the passive restoring force F_y now have directions that try to bring the rotor back into alignment.

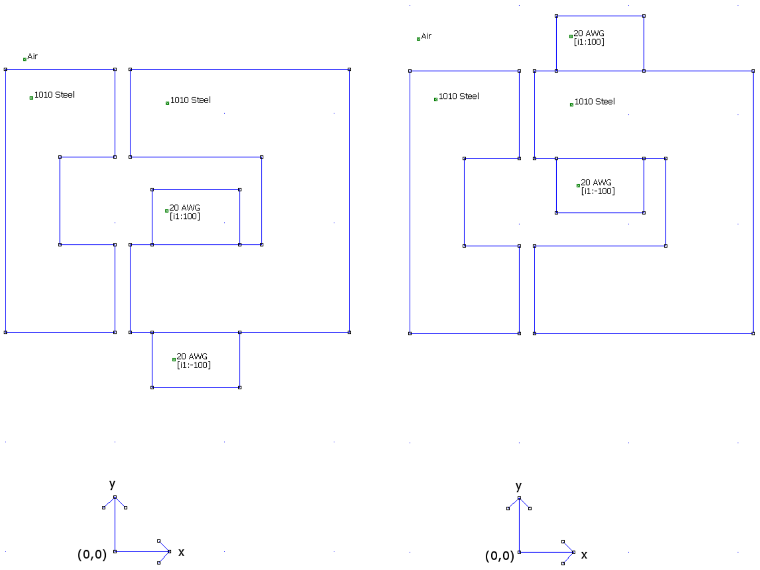

(a) Coil on the bottom electromagnet pole. (b) Coil on the top electromagnet pole.

Figure 4.14: Different positions for the coil on an electromagnet.

4.4.4 Air Gap Width

From Section 4.1.2 the minimum air gap width required when radial electromagnets are being used is:

$$\begin{aligned}\gamma_{min} &= r_r \cos(-\alpha_{max}) - \eta/2 \sin(-\alpha_{max}) - r_r \\ &= (\cos(\alpha_{max}) - 1)\, r_r - \eta/2 \sin(-\alpha_{max}) \end{aligned} \tag{4.17}$$

Because $\cos \alpha_{max} < 1$ then the minimum air gap width is proportional to $-r_r$ and the air gap required will decrease for an increasing radius, which is not intuitive.

For maximum force generation the air gap should be as small as possible. Therefore the radius should be maximised and the height minimised. Figure 4.17 shows how the minimum air gap required to tilt through $\pm 3°$ varies with different rotor heights and radii.

The suggestion from this Section that the radius be maximised and the height minimised is the opposite of the results from the previous Section, Section 4.4.3. The force generated by the electromagnets is inversely-proportional to the square of the air gap width. Maximising the radius and minimising the height will therefore have the greatest desirable effect on the 3Dwheel's properties. Ideally an optimisation procedure should be developed to determine the rotor's dimensions.

4.4.5 Mass

The mass of a hollow ring shaped rotor is:

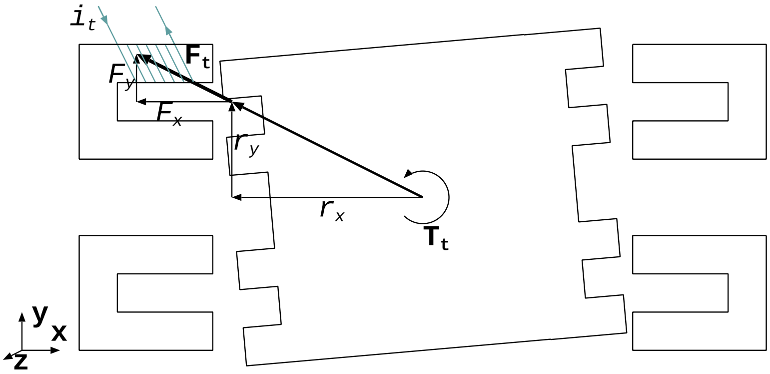

Figure 4.15: The two force components that the top-left electromagnet exerts on the momentum wheel in the electromagnet reference frame to tilt the wheel.

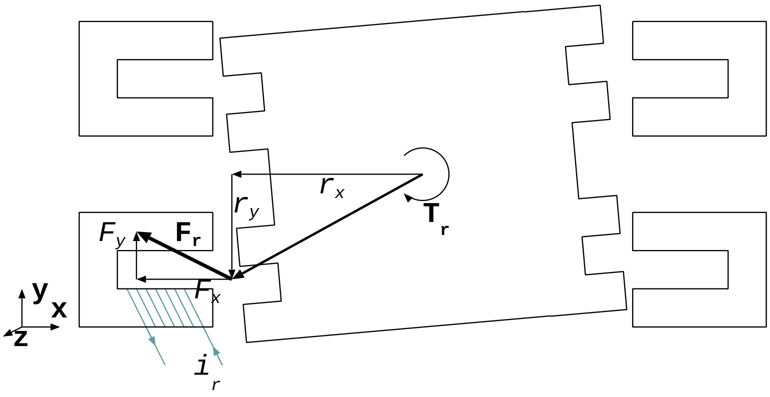

Figure 4.16: The two force components that the top-left electromagnet exerts on the momentum wheel in the electromagnet reference frame to tilt the wheel.

$$M = \rho\eta\pi(r_r^2 - r_i^2) \tag{4.18}$$

where r_r is the outer radius of the rotor and r_i is the radius of the hollow centre. This assumes that the rotor has smooth vertical faces, which will not be the case as the pole faces will be u-shaped to improve the stiffness. For Figure 4.18 it was assumed that $r_i = r_r - 20$ mm. Therefore:

$$M = \rho\eta\pi(0.04r_r - 4 \times 10^{-4}) \tag{4.19}$$

Therefore the mass is proportional to wheel radius r_r and height η, with the radius having a greater effect on the mass. The mass of the wheel for various rotor heights and radii with the assumptions mentioned here is shown in Figure 4.18.

4.4.6 Moment of Inertia

The moment of inertia of a hollow rotor about its hollow axis is given by:

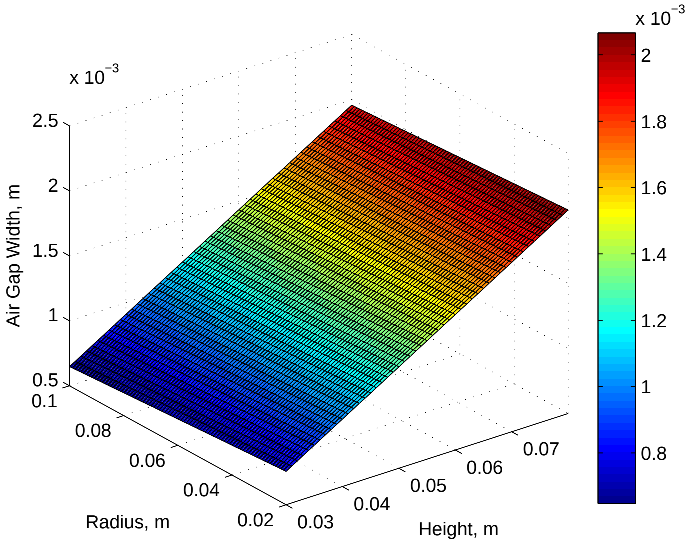

Figure 4.17: The minimum air gap width required for different rotor heights and radii.

$$I_{mw(3,3)} = \rho\eta\frac{\pi}{2}(r_u^4 - r_i^4) \tag{4.20}$$

For Figure 4.19 it was again assumed that $r_i = r_r - 20$ mm. Therefore the moment of inertia is proportional to r_r^3 and to height η.

The moment of inertia of the wheel for various rotor heights and radii is shown in Figure 4.19.

4.4.7 Conclusions

Because the moment of inertia is proportional to the cube of the wheel radius, then the radius should be made as large as possible while keeping the height small to save mass that does not contribute to the moment of inertia. Maximising the moment of inertia maximises the wheel's angular momentum and torque generation capability. Maximising the radius and minimising the height also minimises the width of the air gap width, increasing the force generated or reducing the power consumption. However generating a large torque is pointless if it cannot be transferred to the spacecraft. Therefore, if it is found that the required torque cannot be transferred to the spacecraft then the height of the wheel should be increased.

Richie [65][66] discusses the numerical optimisation of the rotor design for a combined energy storage and attitude control CMG. A Nonlinear Programming Problem technique was developed to choose the rotor dimensions that gave the optimum performance in terms of mass, torque generation and energy capacity. A similar optimisation for the 3Dwheel would choose the rotor geometry that gives the optimum torque generation, mass and power consumption.

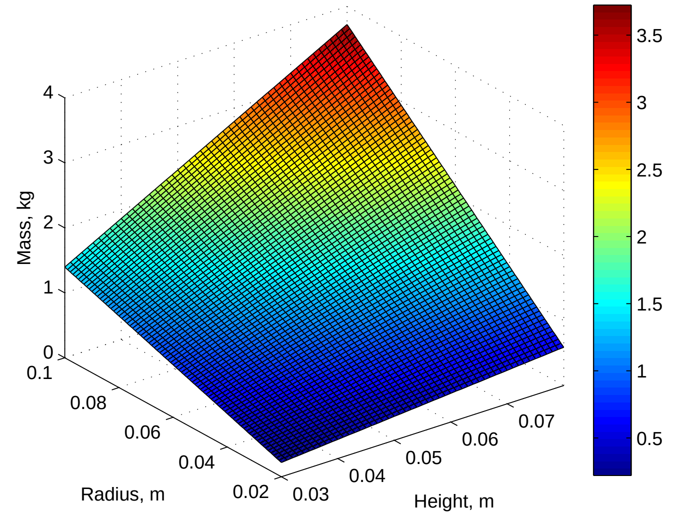

Figure 4.18: The rotor mass for different rotor heights and radii.

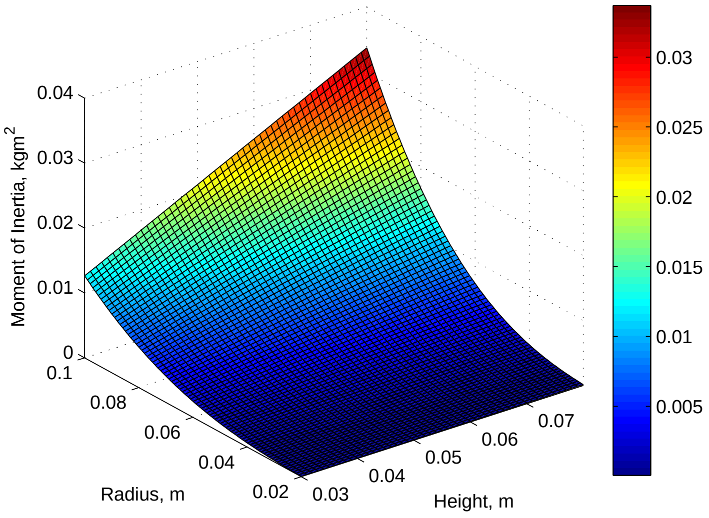

Figure 4.19: The rotor moment of inertia for varying rotor heights and radii.

4.5 Controllability

It was found that in certain circumstances a tilting magnetically levitated momentum wheel cannot exert a torque in the desired direction on the rotor in all rotor positions.

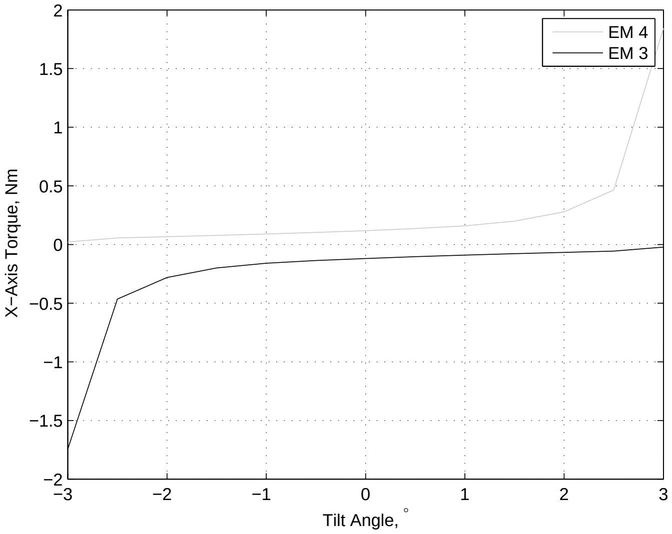

Figure 4.20: The torque generated about the rotor's x-axis by the top (EM 3) and bottom (EM 4) electromagnets on the positive x-axis.

Figure 4.20 shows the torque that an electromagnet can exert on the rotor at all tilt angles calculated by a three dimensional finite element simulation for the engineering model of the 3Dwheel. For rotations about the x-axis, electromagnet three when producing an attractive force will cause a negative rotation about the x-axis. The electromagnet numbering scheme is illustrated in Figure 6.2. Figure 4.20 shows that this torque can be generated at all tilt angles. Similarly, electromagnet four can generate a positive torque at all tilt angles. Therefore this design is fully controllable.

Figure 4.21 shows the torques that can be generated about an axis of rotation midway between the positive x and y axes for the engineering model of the 3Dwheel. Electromagnets one and three were used to generate the negative torques. Again this design is fully controllable at all tilt angles.

Several initial attempts at optimising the geometry resulted in designs that were not controllable. Figure 4.22 shows an early design that is not controllable at all tilt angles. This drawing is from the FEMM finite element simulation software. The two stator electromagnets on the left of the figure are made from a single piece of steel. Due to the symmetry of design, to make the finite element analysis quicker, only half of the design is drawn; the design is mirrored about the right hand edge of the drawing. Coils are placed on all of the stator poles. The top two coils are connected in series and form one electromagnet; the bottom two coils are also connected in series to form the second electromagnet. Figure 4.23 shows the torque exerted on the rotor by each of the electromagnets. Between $-4.3°$ and $-1.3°$, and between $+1.3°$ and $+4.3°$ the torque exerted on the rotor is in the same direction from both electromagnets. Therefore the

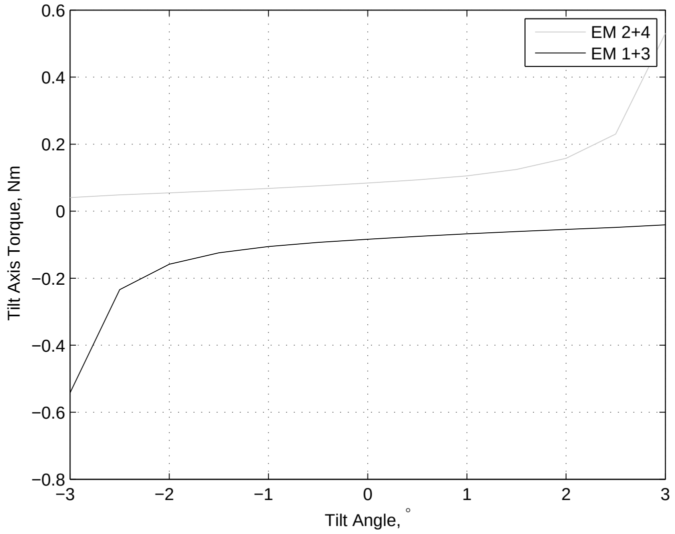

Figure 4.21: The torque generated about the axis between the positive x and y axes of the rotor by the top (EM 1 and EM 3) and bottom (EM 2 and EM 4) electromagnets.

rotor is not controllable between these angles and the maximum angle that the rotor can be tilted through while maintaining control is $\pm 1.3°$. This design would require mechanical stops to prevent the rotor from being tilted further than this.

Figure 4.24 shows an attempt to increase the tilt range of this design where the stator poles are brought closer together. Figure 4.25 shows how the maximum tilt angle increases as the stator poles are brought closer together, but at the expense of axial and radial stiffness.

The 3Dwheel engineering model hardware was stable through all tilt angles due to its small air gap width. If the air gap had been made wider to allow for a greater tilt angle then it would have become uncontrollable.

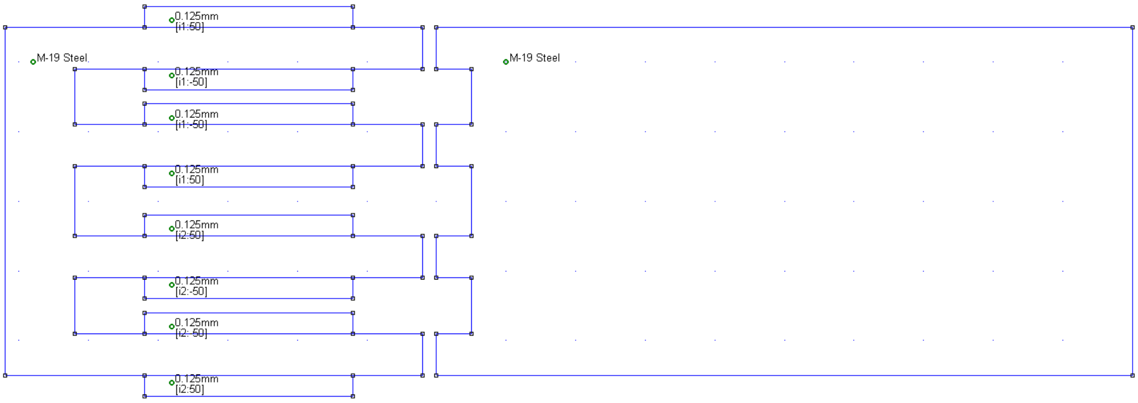

Figure 4.22: A drawing in the FEMM finite element simulation software of an early design that is not controllable at all tilt angles. The two stator electromagnets on the left are made from a single piece of steel. Due to the symmetry of design, to make the finite element analysis quicker, only half of the design is drawn; the design is mirrored about the right hand edge of the drawing.

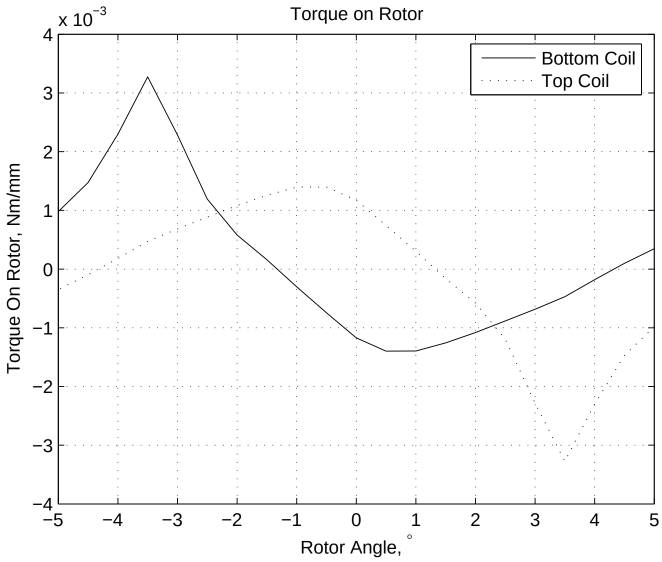

Figure 4.23: The torque on the rotor in the simulation shown in Figure 4.22 when one coil is energised at a time.

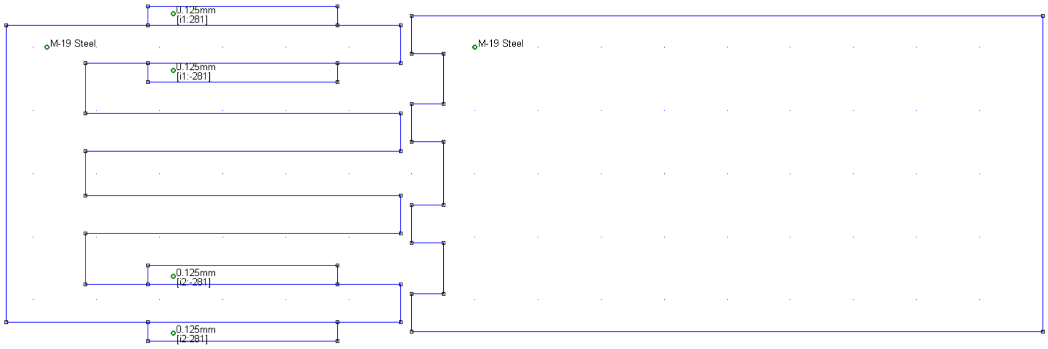

Figure 4.24: A wheel with the stator poles shifted towards the centre by 1.5 mm to increase the angle that the rotor can be tilted through.

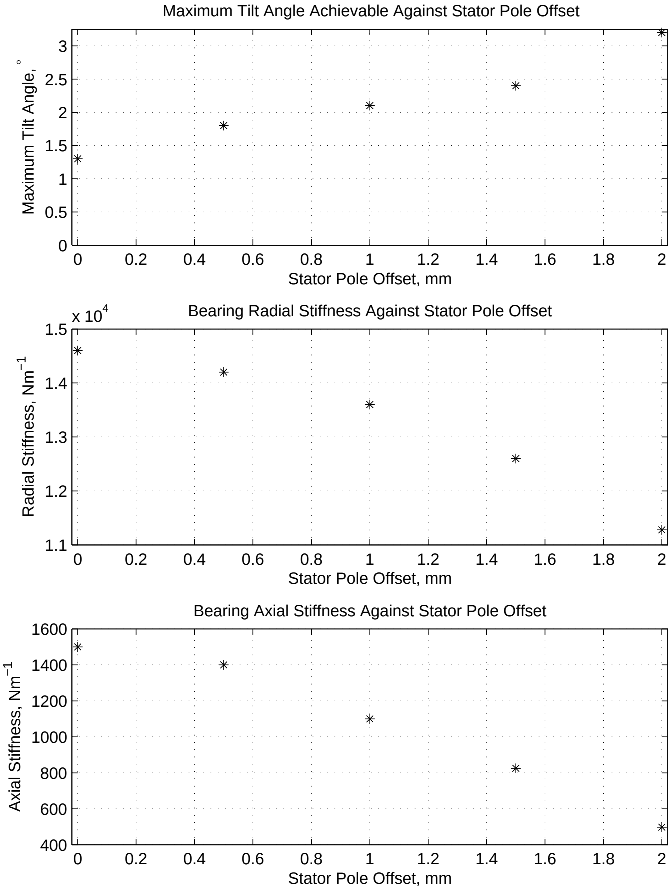

Figure 4.25: How the bearing's properties change as the stator pole offset is increased.

4.6 Pole Face Length

The cross sectional area of an electromagnet's air gap affects the force that it can generate. Initially there was some confusion about the correct way to determine the cross sectional area to use when the air gap was curved.

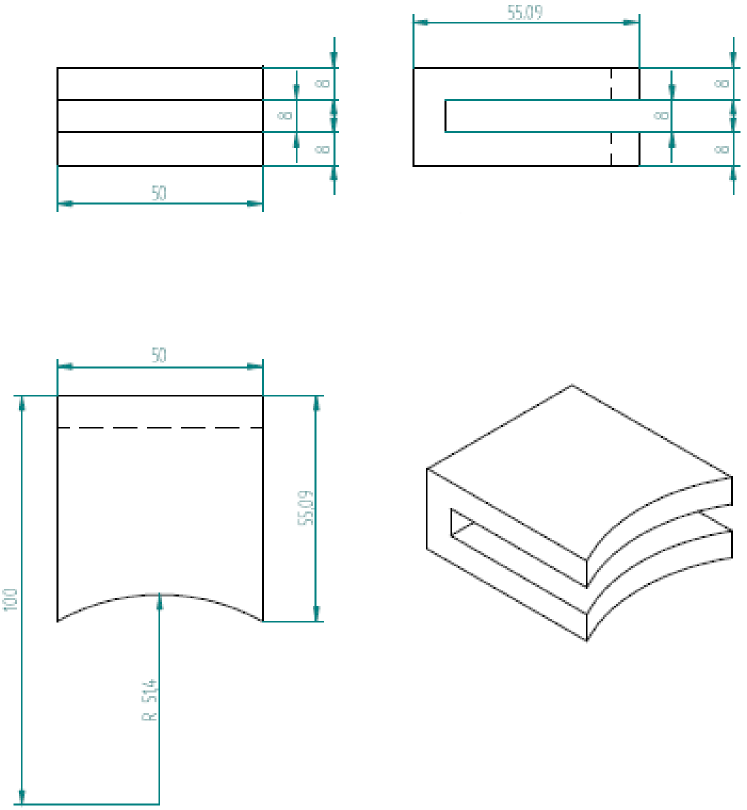

Figure 4.26: An isometric representation of a typical electromagnet in a radial design of a magnetically levitated momentum wheel.

Figure 4.26 shows a typical electromagnet steel piece for use in a radial magnetic bearing with the stator electromagnets being arranged around the outside of the rotor. The attractive force generated by such an electromagnet is given by the familiar reluctance force equation:

$$F_R = -\frac{\mu_0 N^2 \varepsilon l i^2}{4\gamma^2} \tag{4.21}$$

where l is the length of the pole face. The length of the pole face determines the amount of flux that can flow through the steel and air gap of the magnetic circuit. From the derivation of the reluctance force equation in Appendix A, because the relative permeability of the air gap is very much less than that of the iron part of the magnetic circuit, the width of the air gap determines the force generated.

After a quick glance at Figure 4.26 the width of the air gap might be assumed to be 50.0 mm. However the pole face is curved and so the actual width is greater. The length of the pole face of the rotor is less than the pole face length of the stator electromagnets. For system shown in the Figure the rotor radius was 50.0 mm, the air gap width was 1.4 mm and so the radius of the stator pole face was 51.4 mm. It is assumed that the length of inner pole face determines the pole length of the electromagnet as this is the smallest pole face.

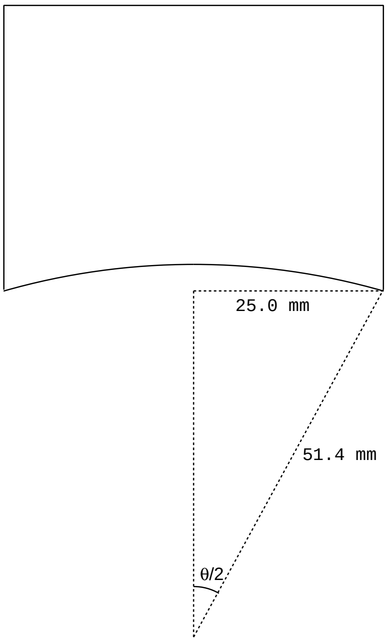

Figure 4.27: The geometry of the electromagnet.

Figure 4.27 shows the geometry of the electromagnet. The angle θ spanned by the electromagnet is given by:

$$\begin{aligned} \sin\frac{\theta}{2} &= \frac{25}{51.4} \\ \frac{\theta}{2} &= 29.1^\circ \\ \theta &= 58.2^\circ \end{aligned}$$

Therefore the length of the stator's pole face is $(58.2/360)2\pi 51.4 = 52.2$ mm. If the pole face length l in the reluctance force equation had been incorrectly assumed to be 50.0 mm then the reluctance force calculated would have been underestimated by $\frac{52.2-50}{52.2} \times 100 = 4.2\%$.

This geometry was simulated in a three dimensional finite element simulation to see the effect of using the wrong value of l. The geometry used has dimensions given in Table 6.2. Analytically an incorrect value of l of 50.0 mm gave a force of 5.77 N, a correct value of l of 50.8 mm from the inner rotor pole face length gave 6.02 N and the finite element simulation gave 6.77 N. Therefore using the wrong assumption about the pole face length l when calculating the reluctance force produces an error that is less than total error from all assumptions made.

Unfortunately the difference between the electromagnet's width and its pole face width was only spotted late in the project. During the development of the controllers for the 3Dwheel hardware a value of $l = 50.0$ mm was used. However the actual path taken by the flux is unknown and so the different values of l should have a minimal effect when combined with all other assumptions made.

4.7 Conclusions

The use of analytical and finite element models means that the properties of the bearing design can be understood and optimised before any hardware is made. Three electromagnet designs were developed for this thesis and have been compared.

Understanding the properties allows controllers to be designed in advance. Together with the dynamic model of the bearing the properties of the bearing are well known before it is built and levitation can be rapidly achieved once it has been built. Not all designs will be controllable through their entire tilt range and so careful modelling is required to check that the design will function as intended.

Investigations of the factors that affect a bearing's performance show that there are many variables that affect its properties. Therefore a final flight-ready optimal design requires some form of optimisation such as a nonlinear programming technique [65][66].

The lessons learnt during the modelling work in this Chapter will be used in the next Chapter to present the hardware built for the laboratory investigations.

Chapter 5

Hardware Design

Chapter 3 provided the theory behind magnetism and the forces generated by an electromagnet. Chapter 4 then went on to use this to model and compare three different electromagnet configurations that had been developed for this thesis.

This Chapter will now use these models and knowledge to present the mechanical and magnetic design of two pieces of hardware developed and built for this thesis. Initially a levitated beam with only two degrees of freedom actively controlled was built to allow controllers to be tested in a simplified environment. Results from the beam then influenced the design of the engineering model of the 3Dwheel that was built to demonstrate the tilting magnetically levitated momentum wheel concept and to allow different controllers to be tested.

5.1 Levitated Beam

To simplify the development of the 3Dwheel it was decided to build a 2D tilting magnetically levitated beam. One translational axis and one rotational axis would be actively controlled and the vertical translational axis overcoming gravity would be passively controlled. Figure 5.1 shows the beam hardware that was built. Drawings of the design of the beam are shown in Appendix D. The beam allowed the sensitivity of the sensors and amplifiers to be studied.

Stable levitation of the beam was not possible because only three degrees of freedom were controlled. This work should reinforce the engineering concept that all degrees of freedom have to be controlled to have a stable system. However, a great deal was learnt about sensors, amplifiers and system dynamics, which allowed the final 3Dwheel to be built and levitated in a short space of time.

Non-Parallel Pole Faces

The main discovery from the 2D beam was of the positive feedback that occurs when straight pole faces become non-parallel as described in Section 4.3.1. This is not a problem for the 3Dwheel because the pole faces are not straight and all degrees of freedom are controlled.

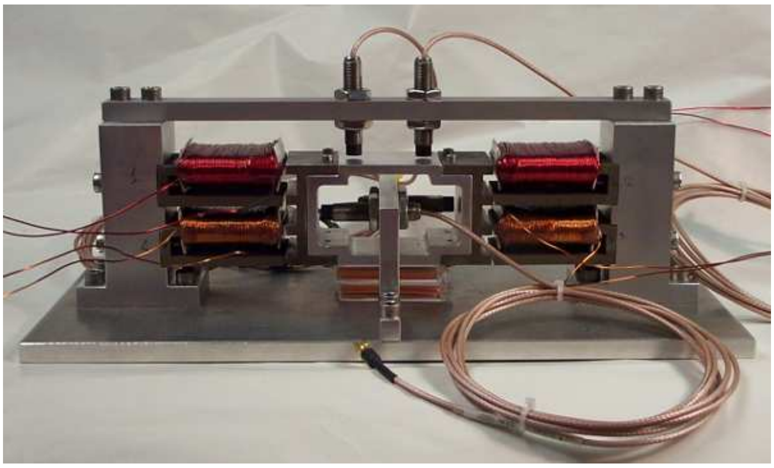

Figure 5.1: The 2D beam hardware that was built.

Switching Amplifiers

For maximum efficiency switching amplifiers built around the SA60 amplifier IC [67] from Apex, now Cirrus Logic Inc. were tried. An active feedback circuit is necessary to stabilise the SA60. Apex provide software that suggests component values for the feedback circuit. The complete amplifier system once built was found to have several problems. The design was very susceptible to noise and so close attention had to be paid to the Printed Circuit Board (PCB) design for the amplifier. Analysis of the suggested circuit showed that it had a poor phase margin. The gain of one of the stages in the feedback circuit was reduced by a calculated amount which resulted in an improved phase margin of the overall system and stability.

The final circuit was very dependent on the electrical properties of the coils that it was driving, with small changes to the coils making it unstable again. To allow the rapid development of the 3Dwheel hardware an existing linear amplifier design developed by Delft University of Technology [64] was used with their assistance instead of the SA60 based amplifier.

Inductance Effect on Controller Design

It was found that the inductance of the coils in the electromagnets also has a strong influence on the performance of the controllers. The transfer function of the electrical part of the system is:

$$G_{elect}(s) = \frac{1}{Ls + R} \tag{5.1}$$

and through the use with the experimental system of the Digital Signal Analyser (DSA) tool described in Appendix B where a white noise signal was injected into the loop and the frequency response of response was found, the transfer function was refined to:

$$G_{elect}(s) = \frac{12}{2Ls + 1.7R} \tag{5.2}$$

R was measured as 0.9 Ω for 240 turns and then estimated to be 0.38 Ω for 100 turns. The inductance L is given by:

$$L = \frac{\mu_0 N^2 \varepsilon l}{2\gamma} \tag{5.3}$$

The mechanical dynamics of the system were calculated in a similar fashion to Equation 6.43 as:

$$G_{mech}(s) = \frac{-\frac{K_i}{M}}{s^2 - \frac{K_z}{M}} \tag{5.4}$$

DSA also showed that there was a low pass filter included in the dynamics with a cut-off frequency of 600 rads^{-1}:

$$G_{filt}(s) = \frac{-1}{\frac{1}{600}s + 1} \tag{5.5}$$

Therefore the plant system is given by:

$$G(s) = \frac{12}{2Ls + 1.7R} \frac{-\frac{K_i}{M}}{s^2 - \frac{K_z}{M}} \frac{-1}{\frac{1}{600}s + 1} \tag{5.6}$$

This system has four poles: one from the filter, one from the electrical part and a conjugate pair from the mechanical part. The frequencies that these poles will occur at for systems with 100 and 240 turns are shown in Table 5.1 (ε=5$\times$10^{-3} m, l=40$\times$10^{-3} m and γ=1$\times$10^{-3} m,).

Pole Source	100 turns	240 turns
Mechanical	$\pm$58 rads^{-1}	$\pm$139 rads^{-1}
Filter	-600 rads^{-1}	-600 rads^{-1}
Electrical	-257 rads^{-1}	-106 rads^{-1}

Table 5.1: Pole frequencies for systems with 100 and 240 turns.

System	100 turns	240 turns
Inductance, mH	1.26	7.24
Cross-over Frequency, rads^{-1}	98	169
Phase Margin, $^\circ$	46	29

Table 5.2: Properties of the systems with 100 and 240 turns.

The Bode plot of the plant is shown in Figure 5.2 and the derived controller response is shown in Figure 5.3. When there are 240 turns the pole from the electrical part of the system occurs at a similar frequency to the negative pole from the mechanical part, leading to a large phase loss at the cross-over frequency. This produces a combined controller and plant with a high-bandwidth and a high gain, which then requires a large current and is noisy. For the system

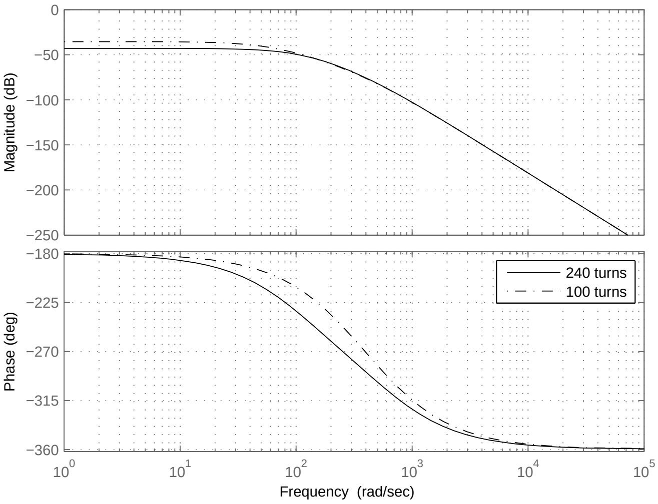

Figure 5.2: Bode plot of the responses of the beam plant.

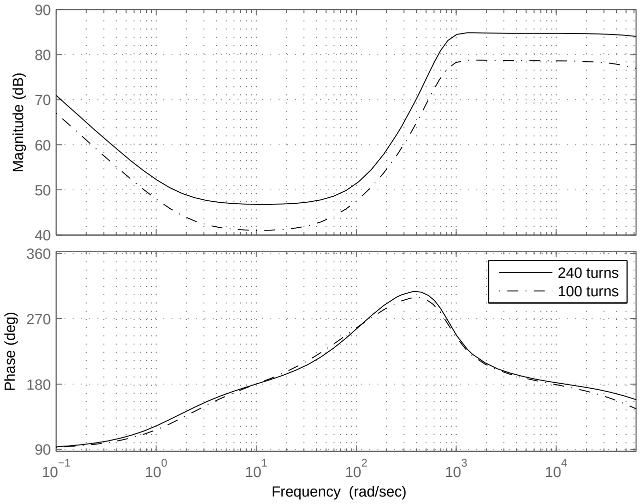

Figure 5.3: Bode plot of the H∞ controllers synthesised for different numbers of coil turns.

with 100 turns the pole from the electrical part is at a much higher frequency and so the system has an improved phase margin at the cross-over frequency and is more likely to be controllable.

It is therefore important to consider the predicted overall system response during the design stage. Increasing the number of turns in a coil to reduce the current required can have unintended consequences. 240 turns was chosen in this case so that there was enough passive stiffness to support the weight of the beam against gravity.

5.2 3Dwheel Engineering Model

The engineering model of the 3Dwheel was designed and built to allow the development and testing of different controllers on real hardware and to compare the simulation models against actual hardware. The engineering model was designed for ease of manufacture and adjustment during testing; the hardware was not optimised for mass, volume, or any other variable. The design of the engineering model and the reasoning behind the design choices are discussed here. Similar logic can be followed when designing the hardware for a 3Dwheel ready for flight on a spacecraft.

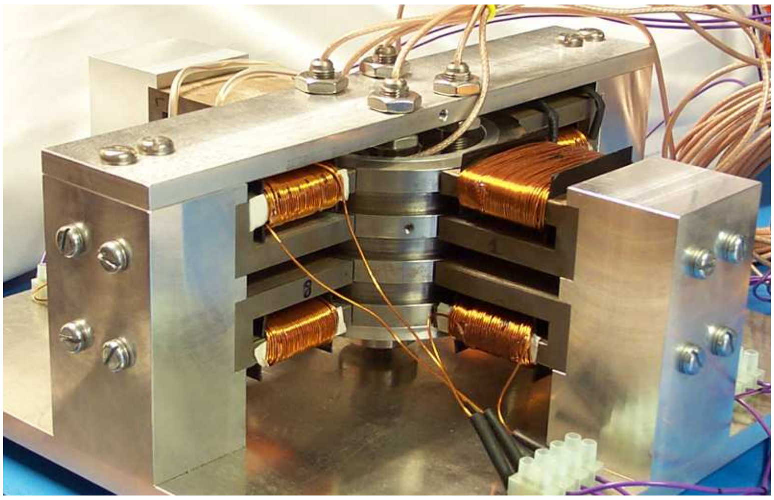

Figure 5.4: The 3Dwheel that was built and successfully tested.

Figure 5.4 shows the 3Dwheel hardware that was built and successfully levitated. The aim of the project was to design a tilting magnetically-levitated momentum-wheel for a small satellite, e.g. as a replacement for SSTL's Minisatellite reaction wheel[5], which was designed in 2002 and was their main reaction/momentum wheel at the start of this project in 2006. It had a total mass of 3.2 kg, an outer case size of $190 \times 190 \times 110$ mm, a maximum output torque of 20 mNm, momentum 4.2 Nms, maximum angular velocity of ± 5000 rpm and a momentum of inertia about its spin axis of 0.008 kgm^2.

It was decided that the 3Dwheel should also be capable of generating a conventional output torque of 20 mNm. Figure 5.5 shows how the stiffness required to transmit a gyroscopic torque of 1 Nm to the spacecraft varies with rotor radius with the rotor being allowed to move no more than 0.5 mm axially when transferring the output torque to the spacecraft. It also shows

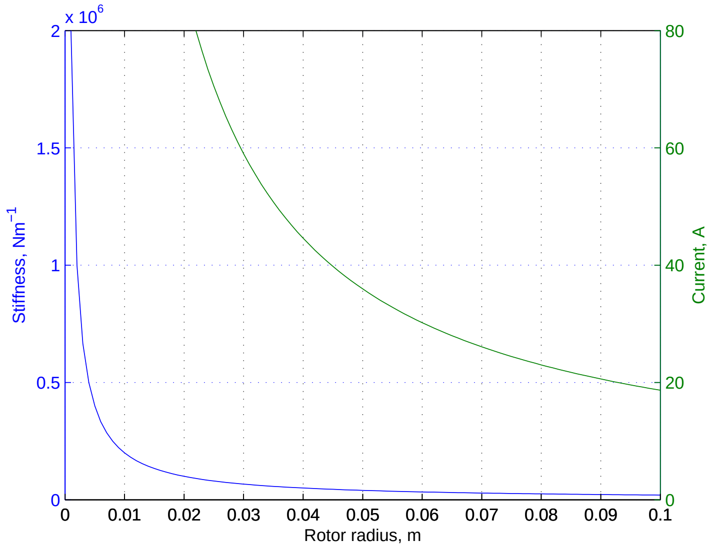

Figure 5.5: The stiffness and current required to transfer a torque of 1 Nm to the spacecraft using radial electromagnets around a wheel of varying radius.

the total current required to generate this stiffness at this radius if each electromagnet has 100 turns and was calculated by rearranging Equation 4.10. The air gap width is calculated using Equation 4.6. Rotor radii of between 100 and 50 mm have only a small increase in stiffness and current requirement. A torque of 1 Nm is very high and will be discussed and relaxed in the next Section. To save on material costs and produce a compact demonstration to illustrate the concept, a rotor radius of 50 mm was chosen for the 3Dwheel engineering model. Later discussions show that a rotor of this radius still has a sufficiently large moment of inertia to generate a conventional output torque of 20 mNm.

The External Radial geometry from Section 4.2 was chosen because this geometry requires the electromagnets with the smallest air gap widths and so has the greatest stiffness and generates the largest forces. For the engineering model it also has the benefit of being simple to construct.

Rotor Dimensions

Existing Sensonics PRS04 eddy current sensors had to be used as there was insufficient money available to buy new sensors. The PRS04 has a measurement range from 1 to 4 mm. The rotor can move one air gap width in both a positive and negative direction from its central position. Therefore to use only one eddy current sensor to measure the rotor's position along each translational axis then the air gap width must not be greater than half of the eddy current sensor's measurement range. Therefore the air gap width will be constrained to less than 1.5 mm.

From Equation 4.17 and Figure 4.17, if the radius of the wheel is 50 mm then the maximum height η of the wheel must be less than 59 mm to satisfy the air gap width constraint at a maximum tilt angle of 3°. Maximising the height of each pole face increases the force that can be generated by the system for a given current according to the reluctance force equation. Therefore a pole face height of 8 mm was chosen as shown in Figure 5.6 to make the largest possible pole face height while maintaining the air gap constraint. The dimensions of the interior hollow section were then chosen to provide an adequate moment of inertia. These dimensions left sufficient room for the sensors to be placed inside of the rotor. Table 5.3 shows the final properties of the rotor calculated from the CAD software. The steel rotor, the upper and lower aluminium liners and the permanent magnet for gravity compensation were included in this calculation; the permanent magnet for spin rate measurement and the motor's magnet ring were not included.

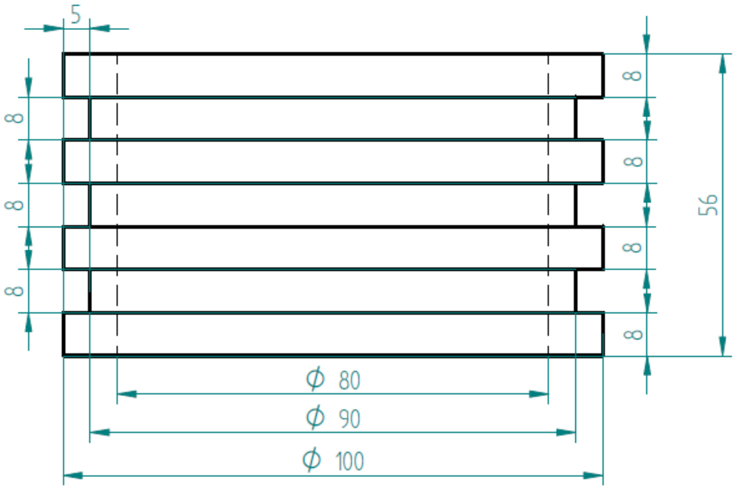

Figure 5.6: The cross section of the steel part of the rotor with dimensions.

Mass, kg	1.301
Moment of Inertia, kgm^2	$I_{xx} = I_{yy}$ =0.001594 I_{zz} = 0.002326

Table 5.3: Properties of the rotor calculated by the CAD software.

Coil Design

The stiffness, and hence torque capability, of the design is controlled by the dimensions of the pole face, the number of turns in the coils and the current flowing through the coils. These three variables were optimised using the analytical equations in Section 3.2 and 2D and 3D finite element simulations. To check that the the final version of the 3Dwheel's electromagnets had enough stiffness to transfer the gyroscopic output torque to the spacecraft the following method was used. A 3D finite simulation of the 3Dwheel was performed with the rotor already tilted about the x-axis by 1° to simulate the generation of the gyroscopic torque. This would result in an output gyroscopic torque about the y-axis, which would require the electromagnets two and five (from Figure 6.2) along the x-axis to transfer the torque to the spacecraft. Therefore these two electromagnets were energised with a current of 3.0 A through 100 turns in each coil. In this position the FEA simulation showed a torque of -0.2386 Nm acting on the rotor about the y-axis. The rotor was then rotated about the y-axis by +0.1° and the torque acting on the rotor about the y-axis was -0.2336 Nm. The rotational stiffness of the system for torque transfer is

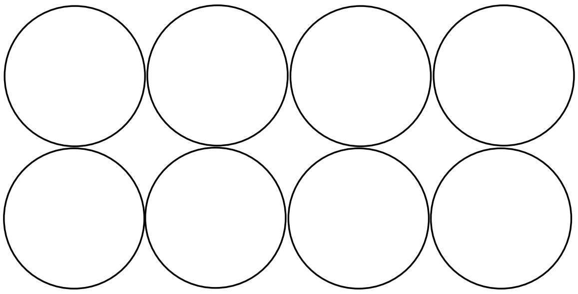

Figure 5.7: The typical arrangement of wires after being wound into a coil.

therefore:

$$K_\alpha = \frac{-0.2386 - -0.2336}{0.1} = -49.6 \text{ mNm}/^\circ \tag{5.7}$$

If it is assumed that the maximum acceptable axial movement of the rotor while transferring this torque is 1 mm (13% of the pole face height), which would be generated by a rotation of 1.2° using Equation C.2 then the maximum torque that can be transferred is $0.0496 \times 1.2 = 60$ mNm, which is too low. From Equation 3.7 stiffness is proportional to i^2 and so doubling the current to 6.0 A will result in a maximum torque that can be transferred of 238 mNm, or 9.0 A will transfer a torque of 536 mNm, which is acceptable. The torques calculated here are greater than those in Table 4.6 because here the rotor is tilted by 1° and so there are additional passive restoring components in the force generated. A current of 3.0 A in an electromagnet results in a predicted peak flux density of 0.4 T in each electromagnet from 3D finite element simulations. A current of 6.0 A resulted in a flux density of 1.0 T and 9.0 A was just beginning to reach the saturation point of the steel with a flux density of 1.5 T.

The cross-sectional area of a coil is given by:

$$A_{Cu} = N(1.1^2 d)^2 \tag{5.8}$$

where A_{Cu} is the cross-section area of the wire in m^2, N is the number of turns in the coil and d is the diameter of the wire in metres. The 1.1^2 term allows for the insulation thickness and irregularities during the winding process. When wound the wire will tend to sit as shown in Figure 5.7 [68].

The diameter of the wire is determined by the average and maximum current that will flow through the coils. A current density in the coil of 10 Amm^{-2} will result in the heating of the coils by several tens of degrees and will not damage the wire [64]. 20 AWG enamelled copper wire was chosen, which has a conductor diameter of 0.80 mm and hence a maximum current of 5.0 A. The depth of the electromagnets was then set so that there was sufficient room for the coils according to Equation 5.8. For operation in a vacuum the conduction of the heat away from the coils must also be considered during the thermal design process. It had been anticipated that if the initial system development went smoothly and quickly enough then the u-shaped electromagnets could be modified to insert a permanent magnet into them as shown in Figure 5.8 to test the 3Dwheel under the electrodynamic principle. Time was not

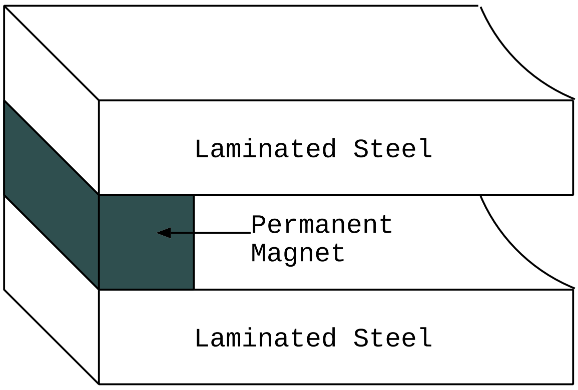

Figure 5.8: A possible design for the inclusion of bias flux from a permanent magnet in an electromagnet.

available to complete this task. This would also be costly due to the requirement for custom sized permanent magnets to be manufactured.

Electromagnet Construction

To minimise eddy current losses the electromagnets should be made from laminated steel. Ideally the steel part of the rotor would be too, however because of its shape and because it rotates, this would be expensive to manufacture and probably weaker due to the laminations.

To reduce costs there was a brief investigation into machining the electromagnet shapes from old transformers. This was not feasible due to there being no suitable sized transformers available and also fears that the machining process would be likely to break apart some of the laminations.

The most cost effective way found to produce the electromagnets was using photo or chemical etching; this process works using the following steps:

1. a photosensitive resist is applied to the material to be etched;
2. a printed mask is then laid over the resist layer and both are exposed to UV light. Areas of the resist exposed to the UV light harden;
3. soft areas of resist that were masked from the UV light are then chemically developed away leaving only the areas that were exposed.
4. the material passes through a tank of etchant. Areas of material not protected by resist are etched away;
5. a stripping solution is then applied to remove the remaining resist, leaving just the etched material.

Each electromagnet is 50 mm thick and each layer of lamination is 0.35 mm, requiring 142 laminations per electromagnet if the thickness of the adhesive is ignored. Photo etching allows this large number of laminations to be produced efficiently by a machine, requiring little human intervention and minimising costs. The tolerance of the process is ±0.0525 mm. The individual parts can then be placed in a former and laminated together. The steel used is Transil 330, an unorientated low-loss silicon steel, which has a core loss of 3.3 Wkg^{-1} at a flux density of 1.5 T at a switching frequency of 50 Hz.

To cut the curved face in the laminated electromagnets, the traditional approach would be to place them on a turntable on a milling machine. To prevent the separation of laminations a clamp could be placed around the laminations. There was concern that this approach would still have the risk of damaging the end laminations in each stack. Therefore the curves were cut into the electromagnets using wire erosion. This process used for the electromagnets achieves a tolerance of 30 μm with a surface finish of 1.2 μm.

The electromagnets were sent directly from the photo etching to the wire erosion company. At some stage in the manufacturing processes an error occurred, possibly that they were not mounted in a machine perfectly square. Figure 5.9(b) shows a photograph of two of the wound electromagnets sat back to back on a perfectly flat optical bench. Figure 5.9(a) shows a drawing of the requested magnet shape in dotted line and the actual in solid line. The fault was not spotted until after the coils had been wound onto the steel. The two companies involved could not agree when during manufacture the fault had occurred. As time and finances were limited, a 51.4 mm radius circular aluminium block was fabricated. The electromagnets were loosely mounted in their supports and the supports were loosely attached to the base plate. The circular block was placed in the centre of the electromagnets and everything was tightened, leaving the electromagnets in the correct place once the aluminium block had been removed. Because of the electromagnets' parallelogram shape, if two magnets were mounted in the correct orientation they would have the same shape; if one of the magnets in Figure 5.9(b) were to be rotated through 180° then they would have the same shape and the curved surfaces aligned.

The intention had been to have the coils wound around the top most pole of the electromagnets in the top layer of magnets and around the bottom most pole of the bottom layer of electromagnets to achieve the best performance as described in Section 4.4.2. Because the coils had been wound around the electromagnets before the problem had been discovered the arrangement of the electromagnets around the rotor had to be modified so that the curved surfaces aligned. It was only possible to have all eight electromagnets' curved faces aligned when two of the coils were not wound around the intended poles as shown in Figure 5.4. The system worked well and so it was decided not to rewind the coils on the correct poles.

Coil winding machines exist that will wind coils automatically and precisely by rotating the object to be wound. Because the electromagnets are u-shaped it is not possible to wind the turns directly on to the steel pieces with a coil winding machine. An alternative is to wind the turns around a plastic bobbin that can then be placed over the steel pole. Bobbins are available for common transformer sizes, but none of these had the same dimensions as the electromagnets. There was not sufficient funding available to have custom plastic bobbins fabricated.

Therefore the coils were wound around the electromagnets by hand. The following steps were found to produce the best results:

1. with a file round off the edges of the steel that the coils are to be wound around;
2. cut one edge off, and trim to size, plastic triangular paper binders;

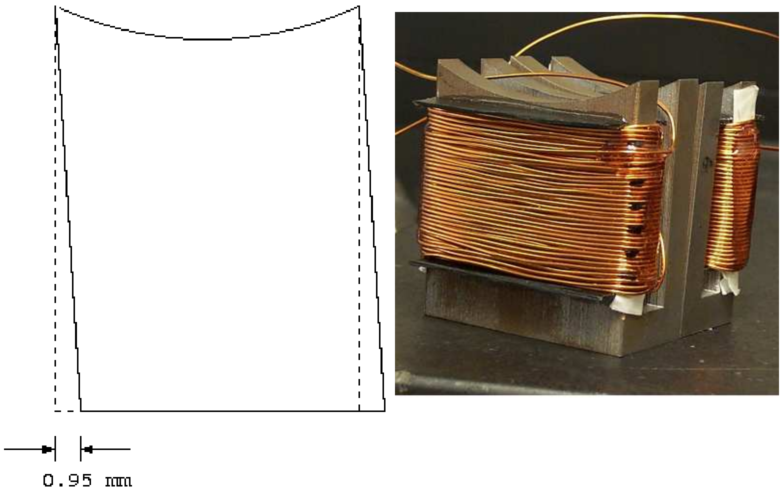

(a) The intended and actual shape (b) The wound electromagnets

Figure 5.9: The misformed electromagnets. The intended shape is shown by the dotted line and the actual shape by the solid line.

3. glue four of these plastic parts to the steel using high-temperature epoxy adhesive;
4. wrap five layers of transformer or greaseproof paper around the steel to provide insulation;
5. bolt the steel piece to the bench and secure the free end of the copper wire;
6. wind the enamelled copper wire around the steel as tightly as possible with fingers
7. stop every few turns and push the coils towards the end of the steel to ensure that they are tightly packed together.;
8. when all of the turns have been wound, secure the ends using high-temperature epoxy;
9. measure the resistance between the wire and the steel to ensure that the wire's insulation has not been damaged and measure the inductance and resistance of the coil.

It is necessary to round off the corners of the steel as the pressure of the wire against the sharp right-angled edge of the steel will cut through both the paper and the enamel insulation, shorting the coil to the steel. The transformer paper provides additional protection. The plastic end pieces allow the ends of each layer of turns to be finished neatly and for subsequent layers to sit neatly as shown in Figure 5.7. The completed coil measurements are shown in Table 5.4. During the winding process it was difficult to keep track of the number of turns that had been wound. There was a suspicion that only 95 turns had been wound around electromagnet 7 and this was confirmed by these measurements. An additional gain of $100/95$ was added in the software for channel 7 to increase the gain and compensate for this decrease in the number of turns. This approach worked well and so there was no need to rewind the coil. The average resistance of the seven good coils was 0.906 Ω and the inductance was 2.756 mH.

Coil	Resistance, Ω	Inductance, mH
1	0.890	2.765
2	0.915	2.796
3	0.914	2.790
4	0.920	2.792
5	0.900	2.711
6	0.905	2.743
7	0.850	2.532
8	0.897	2.690

Table 5.4: The resistance and inductance of the eight electromagnets' coils.

Sensor Integration

The Sensonics PRS04 eddy current sensors that were available for this project have the properties described in Table 5.5 [69]. The sensors had been calibrated for use with an aluminium target. The steel rotor therefore had to be lined with aluminium. However, from Section 4.4.6, material in the centre of a rotor contributes little to its moment of inertia, but does affect its mass. Therefore material providing structural support or a sensing surface in the centre of the rotor should be made from a low density material such as aluminium.

Tip Diameter	8.0 mm
Sensitivity	4 mV$/\mu$m
Linear Range	1 to 4 mm
Resolution	0.002 mm
Temperature sensitivity	$<$5% at 150°C
Frequency Range	0 to 10 kHz
Effect of Target Curvature	+2% for $\phi 150$ mm +5% for $\phi 25$ mm
Effect of Target Magnetism	Less than 1% at 11 mT

Table 5.5: Eddy current sensor properties.

Eddy current sensors have their output affected when measuring a curved surface. The data sheet states that for a curved surface of diameter 150 mm there will be an effect of $+2\%$; meaning that the target object will appear 2% closer than the point directly beneath the sensor. The data sheet additionally specifies an effect of 5% at 25 mm diameter. The effect of target curvature is likely to be related to the diameter of the curvature and the distance between the sensor and the object to be measured by a square law. The target material also has an effect [70]. If one is available, further tests with a laser interferometer should be conducted to confirm this behaviour.

The sensors have a 3.0 mm measurement range. They can therefore measure the axial position of an object that moves at most 1.5 mm axially from its central position. The axial movement of an object will increase as its radius from the centre of the rotor increases. Using Equation 4.5, but placing the surface that the sensors measure on a plane in the centre of the rotor means that $\eta = 0$ and so the sensor's air gap width becomes $\gamma_{min} = r_r \sin\theta$. Therefore for the air gap to be less than 1.5 mm at a maximum tilt angle of $3°$, the sensor must be less than 28.7 mm from the centre of the rotor. The diameter of the sensor's tip is 8.0 mm and the area of the target that the sensor requires to see in order to obtain an accurate measurement is twice the diameter of the tip. The sensor support and the aluminium liner in the centre of the wheel was dimensioned to meet these two requirements.

To calculate the tilt angle of the rotor from the three vertically mounted eddy current sensors:

1. the positions in 3D of three points on the rotor directly underneath three of the axial sensors are formed. The x and y components of their positions are known and the z component is formed by the sensor's output. The points are called $\mathbf{A}$, $\mathbf{B}$ and $\mathbf{D}$. Two vectors are formed: $\overrightarrow{\mathbf{BA}} = \mathbf{A} - \mathbf{B}$ and $\overrightarrow{\mathbf{DA}} = \mathbf{A} - \mathbf{D}$;
2. unit vectors are formed from these two vectors and the vector to form an orthogonal right-hand co-ordinate system is found using the vector cross-product: $\hat{\overrightarrow{\mathbf{BA}}} \times \hat{\overrightarrow{\mathbf{DA}}}$;
3. these three orthogonal vectors are formed into a direction cosine matrix $\mathbf{DCM}$ and the tilt angles are found by assuming a 3-1-3 Euler rotation order $\alpha_y = -\arcsin(\mathbf{DCM}(1,3))$ and $\alpha_x = \arcsin(\mathbf{DCM}(1,3))/\cos(\alpha_y)$.

Because the initial position of the translation and tilt sensors is not known measurements must be taken to calibrate their position. To do this the gravity compensation permanent magnet was placed in its lowest position, plastic shims were placed under the rotor so that its poles were level with the electromagnet poles. Paper shims were then placed between the electromagnets and rotor poles so that the rotor appeared by eye to be central in the system. The sensor voltages measured by the real-time control system data acquisition cards were then recorded. The Simulink data acquisition block was then modified to subtract these "central" positions from the sensor values so that the block outputs positions from the central position. This is not the best method of determining the centre of the inertial reference frame as it was only done by eye (although the available alternative was to use a vernier caliper, which is difficult to use in the curved area between the rotor and stator poles) and it takes no account of the air gap between the motor's rotor and stator. If the air gap between the motor's rotor and stator is not constant then the motor will add a disturbance force to the system. Ideally an accurate survey of the system, such as with a laser interferometer, would be performed during its construction so that the position of the motor and centre of geometry and sensor offsets is accurately known. There was not sufficient finances available during this project to have the system surveyed this accurately.

The two horizontally mounted sensors that measure the x and y translational position of the rotor are offset from the centre position of the rotor, with the x-axis sensor being below the centre line and the y-axis sensor being above the centre line. With low bias currents and hence low controller gains and without the motor magnets fitted this offset did not affect the control loop. However with the magnets fitted and with higher controller gains then this offset had to be compensated for to achieve stable levitation. The position of the sensors can be calculated using the following method; the geometry of the problem is shown in Figure 5.10. The sensor measures a point on the tilted rotor (y'_m, z'_m). The axial height of the sensor is known and so $z'_m = 20 \times 10^{-3}$ m. For a rotation by angle α_x about the x-axis the following rotation matrix exists:

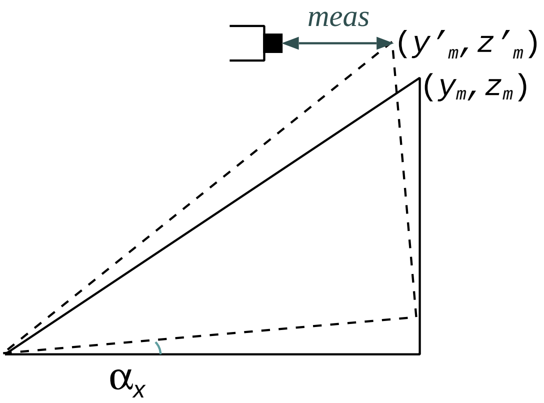

Figure 5.10: The geometry of the translation sensor compensation method.

$$\begin{bmatrix} y'_m \\ z'_m \end{bmatrix} = \begin{bmatrix} \cos\alpha_x & -\sin\alpha_x \\ \sin\alpha_x & \cos\alpha_x \end{bmatrix} \begin{bmatrix} y_m \\ z_m \end{bmatrix} \tag{5.9}$$

Therefore the axial position of the measured point can be found if the rotor was not tilted:

$$\begin{aligned} z'_m &= y_m \sin\alpha_x + z_m \cos\alpha_x \\ z_m &= \frac{z'_m - y_m \sin\alpha_x}{\cos\alpha_x} \end{aligned} \tag{5.10}$$

The radius of the rotor gives the radial position of the measured point when the rotor is not tilted. Therefore $y_m = 35 \times 10^{-3}$ m and the radial position of the measured point can be found:

$$y'_m = y_m \cos\alpha_x - z_m \sin\alpha_x \tag{5.11}$$

The y-axis translational position of the rotor, corrected for tilt, is therefore: $y = meas + (y_m - y'_m)$. The measured sensor values for the x-axis translation can be similarly compensated.

Electrical Interfacing

The LM3886 linear audio amplifiers used have a poor power efficiency compared to a class-D switching amplifier and so would not be used in a flight model of the 3Dwheel, but they provided a low noise amplifier that allowed the rapid development of the 3Dwheel system. They were built into a rack mount system to allow their use with other magnetic levitation projects under development by the research group. The LM3886 is designed to drive speakers with an impedance of 4 to 8 Ω. The average coil's impedance, using $|Z| = \sqrt{R^2 + (\omega L)^2}$ is 0.91, 0.95 and 2.9 Ω at 1, 100 and 1000 rads^{-1} respectively. The amplifier had a tendency to oscillate when higher currents were being drawn because the coils' impedances were lower than it was designed to drive. 3.3 Ω 50 W resistors were added in series with the coils and were mounted on each current amplifier channel's heat sink and no further instabilities were encountered.

Anti-aliasing filters were added to the inputs and outputs of the data acquisition and output cards. First order resistor-capacitor (RC) filters were found to provide sufficient filtering.

Gravity Compensation

For testing of magnetically levitated wheels on Earth, the system must be strong enough to support the mass of the rotor against gravity. The approach taken in the magnetically levitated beam was to have the passive stiffness of the beam great enough to support its mass. This complicated the design of the controllers as described in Section 5.1. The alternative approach taken with the 3Dwheel is to place circular permanent magnets on the base of the rotor and on the base plate and orientate them to repel, or place attractively orientated permanent magnets on the top of the rotor and above the rotor.

3D finite element simulations were used to determine the size of permanent magnets to use and their location. The data sheet for the chosen permanent magnets gave the remanence B_r as 1.3 T and the coercive field H_c as 923 kAm^{-1}. No value for bulk conductivity was available from the manufacturers and so the default value of 625,000 Sm^{-1} from the default FEA NdFeB magnet was used. Figure 5.11 shows a cross section of the FEA simulation. Each permanent magnet had a radius of 9.5 mm and a height of 5.0 mm. Table 5.6 shows the results of this simulation for repulsive magnets being rotated about their x-axis and Table 5.7 shows the results for attractive magnets. The suspension force is comparable for both orientations as is the disturbance force along the y-axis and the disturbance torque about the x-axis. Table 5.8 shows the repulsive magnets being offset along the x-axis and Table 5.9 shows the offset of attractive magnets. Therefore the attractive gravity compensation permanent magnets will try and resist any displacement whereas repulsive magnets will amplify any offset between magnets, trying to force them further apart.

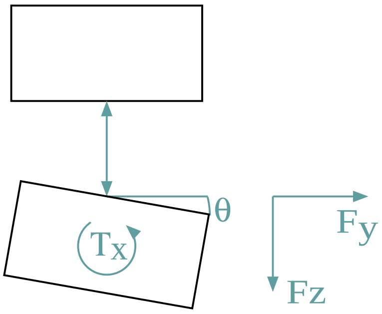

Figure 5.11: A cross section of the 3D FEA simulation of the repulsive permanent magnets.

The magnitude of the disturbances generated by the repulsive and attractive modes can both be compensated by the electromagnets. The repulsive mode is easier to tune because of its inherent stability; if the attractive magnets are too close together then the positive feedback of the system will increase the attractive force between them. The repulsive configuration was therefore chosen to compensate for gravity. The magnet on the base plate was housed in

Angle θ, °	F_z, N	T_x, mNm	F_y, N
0	15.6	0.0	0.0
1	15.6	-3.4	0.23
2	15.7	-6.6	0.46
3	15.7	-9.8	0.58

Table 5.6: The results of the 3D FEA simulation of the repulsive permanent magnets being tilted about the x-axis.

Angle θ, °	F_z, N	T_x, mNm	F_y, N
0	-16.7	0.0	0.0
1	-16.7	3.3	-0.25
2	-16.7	6.2	-0.42
3	-16.6	9.6	-0.66

Table 5.7: The results of the 3D FEA simulation of the attractive permanent magnets being tilted about the x-axis.

a threaded support, allowing its distance from the rotor's permanent magnet to be adjusted, hence controlling the force that is generated.

The use of attractive electromagnets to compensate for gravity was also investigated. Although working in the unstable attractive mode, closed loop control is available with electromagnets and position sensors. Table 5.10 shows the axial force exerted on the rotor at various tilt angles through various tilt axes. The force varies considerably, but will be under closed loop control and so this can be compensated for. Table 5.11 shows the torque exerted about the tilt axis as the rotor is tilted through various angles through several tilt axes. The magnitude of the torque when the rotor is at its maximum tilt angle is likely to exceed what the levitation electromagnets can generate. Because of this and the additional complexity of using electromagnets compared with the permanent magnets it was decided to use repulsive permanent magnets for gravity compensation.

The forces predicted by the FEA simulation were found to match the forces experienced in the final hardware. Initially the magnets were not mounted centrally in their holders causing a disturbance as predicted by the FEA simulations. When the magnets were mounted as precisely as possible with the aid of shims the disturbance forces were minimised and the levitation system reached equilibrium rapidly during the tuning of the controllers.

Motor Integration

A brushless DC motor is ideal for use in a magnetically levitated momentum wheel as there is no physical contact between the rotor and the stator because the coils are fitted to the stator. Brushless DC motor design is a complex but well understood process. A custom motor is required for a flight ready wheel to achieve mass, power, volume and torque requirements. For the engineering model of the 3Dwheel it was decided to modify an existing motor. A motor with sufficient air gap between the stator poles and the rotor magnets was identified to allow the rotor to be tilted through $\pm 3^\circ$. Because the rotor is at the centre of rotation, for a given angular

x-axis offset, mm	F_z, N	F_x, N
0	15.6	0.0
1	15.4	1.5
2	14.8	3.0

Table 5.8: The results of the 3D FEA simulation of the repulsive permanent magnets undergoing a translation offset along the x-axis.

x-axis offset, mm	F_z, N	F_x, N
0	-16.7	0.0
1	-16.5	-1.6
2	-16.0	-3.1

Table 5.9: The results of the 3D FEA simulation of the attractive permanent magnets undergoing a translation offset along the x-axis.

rotation the minimum air gap width is less than at the electromagnets, which are further from the centre of rotation.

Figure 5.12 shows the motor's stator poles and coils mounted between the two translation eddy current sensors. The cable for the bottom eddy current sensor has to pass through the centre of the stator. Sacrificial adhesive tape has been placed around the stator poles in case the rotor and stator collide during testing. Figure 5.13 shows the motor's rotor and permanent magnets mounted inside the aluminium liner of the 3Dwheel's rotor. The motor's rotor was attached to the liner using epoxy adhesive.

Brushless DC motor controllers need to know the rotor's angular rate to switch the current between coils. This information can come from either a Hall sensor mounted on the rotor or by observing the voltage induced in the coils by the permanent magnets. The motor chosen used the second method, which made the integration of the motor into the 3Dwheel easier as no Hall sensor was necessary. Interface electronics and software were developed to control the motor using its I^{2}C interface from the system's real time control environment. The motor's controller was unable to provide reliable control of the rotor's angular velocity, possibly because of the increase in inertia of the 3Dwheel rotor compared to the rotor that it was designed to drive. A small permanent magnet was attached to the rotor and a Hall sensor was mounted on the baseplate. A proportional-integral (PI) controller was implemented and manually tuned in the real-time control environment to provide closed-loop control of the rotor's speed as shown in Figure 5.14.

Commands to the motor control electronics are sent over an I^{2}C interface, using a “bit banging” technique over a digital i/o line. The real time operating system runs at 1 kHz, hence only a bit rate of 500 Hz is achievable over the I^{2}C bus and so commands can only be sent to the motor at a maximum rate of 2 Hz due to the number of bits in the command.

Mechanical Support

During initial testing it was found that the 3.0 mm diameter support between the brackets holding the x and y-axis translation sensors was not strong enough and was bending if the

Rotor Tilt Angle, °	F_z, N Rotor = $0°$	F_z, N Rotor = $45°$	F_z, N Rotor = $90°$
0.0	14.4	14.4	14.4
1.5	16.9	16.4	15.7
3.0	31.7	47.4	21.8

Table 5.10: FEA results showing the axial force generated on the rotor by gravity compensation electromagnets at various tilt angles about various axes.

Rotor Tilt Angle, °	T_x, mNm Rotor = $0°$	T_x, mNm Rotor = $45°$	T_x, mNm Rotor = $90°$
0.0	0.04	0.04	0.04
1.5	122	88.3	0.06
3.0	453	772	0.19

Table 5.11: FEA results showing the tilting torque exerted on the rotor by gravity compensation electromagnets at various tilt angles about various axes.

motor rotor came into contact with the motor stator, resulting in a positive feedback system that applied a stronger force and bent the support further. The diameter of the support between the sensor holders was therefore increased and the hole in the centre of the motor's stator was enlarged. The method used to secure the top translation sensor bracket to the frame over the base plate was also improved.

Control System Implementation

The system was modelled using the Simulink modelling environment that is part of the Matlab mathematics software package by The Mathworks Inc. The Real-Time Workshop toolbox was used to convert the Simulink model into C code that was suitable for use with a real-time operating system. A further toolbox, xPC Target, was used for the real-time operating system. This set of tools had the advantage that the same model could be used to simulate the wheel and to then control the hardware with only minimal changes being required.

The xPC Target operating system ran on standard PC hardware. A National Instruments PCI-6703 analogue output card was used, which has sixteen 16-bit analogue voltage outputs. Voltages were sampled using the National Instruments sixteen channel 12-bit PCI-6023E analogue input card. Financial constraints prevented the use of other cards. The 12-bit range of the input card was not ideal. One bit corresponds to $20/2^{11} = 9.8$ mV (1-bit is required for the sign and so only 11-bits are available for the magnitude). The sensors have a sensitivity of 4 mVμm^{-1} and so 1-bit corresponds to a movement of 2.5 μm.

Linear voltage amplifiers were built to convert the voltage output range of the sensors and the input range of the current amplifiers to use the full voltage range of the i/o cards to make full use of the cards' resolution. The gain of each amplifier was found using a calibrated 4-digit meter. The amplifiers were not temperature compensated as the temperature in the lab remained fairly constant. Temperature compensated amplifiers would need to be considered for use on a flight model of the wheel.

Figure 5.12: The brushless DC motor's stator mounted between the two translation eddy current sensors.

Conclusion

An engineering model of a tilting magnetically levitated momentum wheel has been designed and built. The design was chosen for ease of manufacture. No efforts to optimise the design for minimum mass or for structural strength; the design has been over engineered. The structural modes of the rotor were not calculated. A full design of a flight ready wheel should optimise the mass of the wheel against strength, while considering the effect of the design's fundamental frequencies on the control of the spinning rotor. Table 5.12 summarises the properties of the engineering model hardware.

Rotor radius	50 mm
Rotor height	56 mm
Rotor mass	1.3 kg
Moment of inertia	2.326×10^{-3} kgm^2
Angular velocity	5000 rpm, 524 rads^{-1}
Angular momentum	1.22 Nms
Tilt range	$\pm3.0°$
Radial stiffness	1.6×10^4 Nm^{-1}
Axial stiffness	3.6×10^3 Nm^{-1}

Table 5.12: Summary of the engineering model design.

Figure 5.13: The brushless DC motor's rotor and permanent magnets mounted on the 3Dwheel's aluminium liner.

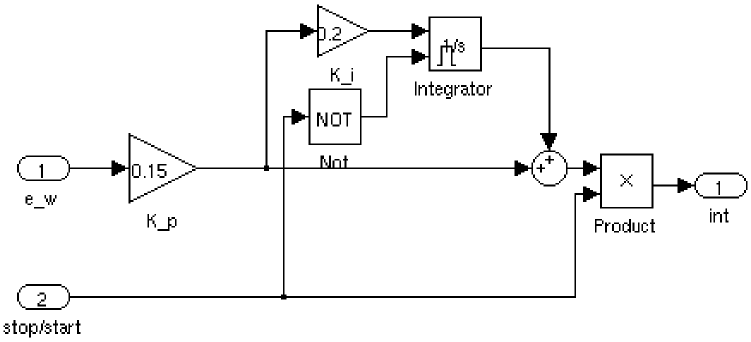

Figure 5.14: The Simulink PI controller to control the rotor's spin rate.

5.3 Additional Design Aspects

This project has concentrated on the magnetic design and control of a tilting magnetically levitated momentum wheel using the electromagnetic principle. To turn this 3Dwheel into a system ready for flight on a spacecraft several additional items of research need to be performed. During launch the spacecraft will not have any electrical power and so the rotor cannot be levitated using the electromagnets. Additionally during launch the entire spacecraft is subject to strong forces and so all moving parts must be restrained. Therefore a launch lock mechanism is required to secure the rotor during its ride to orbit. The electromagnets' coils generate large magnetic fields. Various other components on a spacecraft interact with the Earth's relatively weak magnetic field, such as magnetotorquers for attitude control and magnetometers for attitude determination. Additionally the spacecraft contains sensitive electronic components as part of its bus and payload that could potentially suffer from interference from the electromagnets. Therefore the extent of any stray magnetic fields from the electromagnets must be understood and appropriate shielding devised. For testing of the 3Dwheel during spacecraft assembly, integration and test, gravity compensation of the rotor against gravity must be considered.

5.3.1 Launch Lock Mechanism

Traditionally large communication satellites have used pyrotechnic releases to release securing straps or devices after launch. Pyrotechnic releases can generate large shocks during their operation [6], are sensitive to electromagnetic disturbances, may leave debris behind and can be expensive because of their inherent dangerousness.

Alternative, safer and cheaper, releases have been developed for small satellites. Aramid or dyneema straps are used to secure the spacecraft's mechanisms. The straps pass over an electrically-heated thermal-knife. When current is applied to the knife it slowly melts through the strap. A spring gently applies pressure to push the knife against the strap. As the strap is cut through pressure is gradually released resulting in no shock force. The system is not susceptible to electromagnetic disturbances; the knife can be tested on the ground before launch. The temperature of the knife is designed to cleanly melt and seal the strap leaving behind no debris [71].

It is envisaged that such a strap and thermal-knife system could be used as a launch lock mechanism for the 3Dwheel by having the strap securing the rotor to the stator's base plate during launch. Once on orbit the strap would be cut and springs would pull the strap clear of the rotor.

An alternative approach would be to use a Shape Memory Alloy (SMA). SMAs can be deformed into a low temperature shape, but will recover their original shape when heated. They are commonly made from a nickel-titanium based alloy [72]. Combined with mechanical springs, lightweight release mechanisms can be developed that are able to apply forces of up to 1500 N, but will release in five seconds with an applied electrical power of 60 W [73].

On the magnetically levitated momentum wheel fitted to the SPOT 4 satellite the launch lock system consisted of a metallic bellows filled with nitrogen gas [36]. An pyrotechnic device fractured a pipe releasing the gas after launch. The manufacture and testing of this system was likely to be complex and not appropriate for use on a small satellite.

A magnetically levitated momentum wheel that was built and tested on Earth, but not knowingly flown was fitted with a rubber bellows that held the rotor in place during launch [31]. Gas was released from the bellows using a magnetic actuator. This design had the advantage of being refillable and so the system could be tested several times and refilled between tests. This design is more appropriate for use on small satellites. Care must be taken to vent the gas to a suitable location on the spacecraft to avoid contaminating camera lenses. The release of the gas will act as a thruster on the spacecraft; on small satellites with a low mass and moment of inertia the thrust and torque generated must be carefully evaluated. Until the gas is released the momentum wheels will not be operational and so the attitude control capabilities of the satellite will be limited; the direction of the venting thrust may not be able to be controlled and could have an adverse effect on the satellite's orbit or tumble rate.

A third approach for a launch lock mechanism mentioned in the literature uses a DC motor and a worm gear to drive a plate down, trapping the rotor [29].

5.3.2 Magnetic Shielding

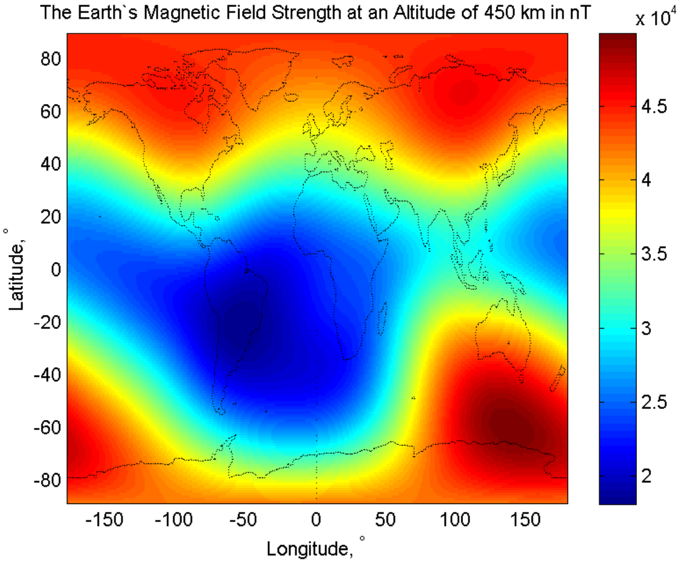

Figure 5.15: The Earth's magnetic field intensity at an altitude of 450 km [74].

With a bias current of 3 A the magnitude of the magnetic field strength 100 mm from the engineering model of the 3Dwheel is 7.3×10^{-5} T and 2.2×10^{-6} T at a distance of 200 mm according to a 2D FEMM magnetostatic finite element analysis. Figure 5.15 shows the intensity of the Earth's magnetic field at an altitude of 450 km above the Earth [74]. At this typical low Earth orbit altitude the magnitude of the Earth's magnetic field varies between 1.8 and 5×10^{-5} T. Surrounding the wheel with a 1.0 mm thick ferromagnetic cover reduces this field to 7.0×10^{-7} T and 1.2×10^{-8} T at 100 and 200 mm distance respectively. A shield of this thickness will have a volume of 3.71×10^{-5} m^3 if the electromagnets are placed in the centre of the rotor. Using steel with a density of 7900 $\mathrm{kgm^{-3}}$ such a case will have a mass of 0.293 kg. Figure 5.16 [5] shows SSTL's mini-satellite momentum wheel and the aluminium case around it. A shield will be necessary to protect the rest of the spacecraft from debris in case of a loss of levitation at a high angular rate [75].

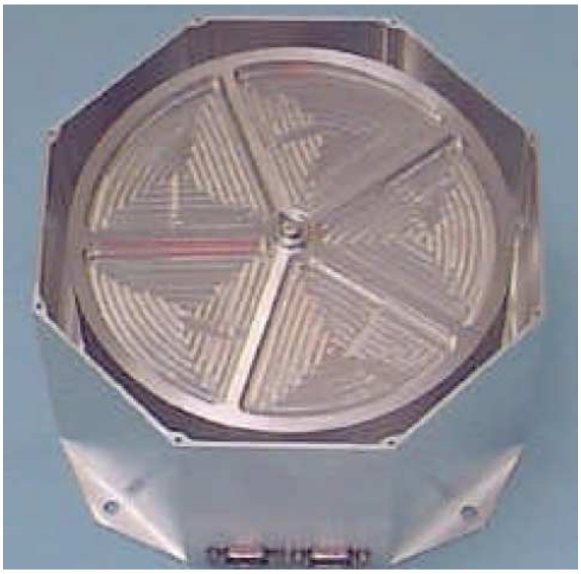

Figure 5.16: SSTL's mini-satellite momentum wheel [5].

5.3.3 Gravity Compensation

To test the 3Dwheel engineering model in the lab repulsive permanent magnets underneath the rotor were used to compensate for gravity. All testing of the wheel was done with the wheel horizontal (with the rotor's spin axis pointing vertically out from the centre of the Earth). 3Dwheels cannot be assumed to be in this orientation during spacecraft assembly, particularly as there may be several wheels mounted orthogonally to each other or in a pyramidal configuration. Once away from the Earth's surface this pair of repulsive magnets will try and displace the rotor axially with only the electromagnets' passive restoring force acting against the permanent magnets. If the permanent magnet in the base plate of the engineering model was in a certain position the rotor could be made to oscillate axially because of a lack of damping in the permanent magnet system. Additional repulsive permanent magnets above the rotor could be used to prevent these two problems. Additional permanent magnets could not be fitted during this project as the sensor mount in the centre of the rotor did not allow enough room for additional permanent magnets. A complete dynamic model of the permanent magnet gravity compensation system needs to be developed. Increasing the passive force generated by the electromagnets to compensate for gravity is not the best solution for reasons described in Section 5.1 and because of the thermal dissipation of additional heat generated in the coils, and the increase in mass and ohmic losses due to any additional turns required in the coils.

5.3.4 Rotor Critical Frequencies

The critical frequencies of the 3Dwheel engineering model's rotor have not been calculated as mechanical finite element software was not available. The rotor will increasingly vibrate and suffer from instabilities as its spin rate passes each of its critical frequencies. The complete levitation system must have sufficient stiffness to support the rotor through these frequencies if they occur in the wheel's operating range. The rotor's critical frequencies on the wheel designed for the AMSAT 3D satellite were said to be above its maximum operating speed of 3000 rpm [23]. The composite rotor developed for an energy storage application had its first critical frequency at 46019 rpm [34].

5.3.5 Touch Down Bearings

If electrical power to the controller or electromagnets' amplifier is lost, the rotor will cease to be levitated. Mechanical touch down bearings need to be provided to allow the rotor to gracefully lose its angular momentum without the rotor and stator being damaged. Such bearings must prevent the rotor or stator from coming into contact with each other but must not limit the rotor's movement during normal operation. Designing touch down bearings for the tilting wheel is more complex than standard wheels because its greater air gap width allows the rotor a greater range of movement. Bearings such as roller or ball bearings, or plastic solid bearings could be used. The bearing must be designed to cope with the maximum angular velocity of the wheel and the touch down bearing design could even limit the wheel's maximum spin rate [23].

An additional solution proposed by several authors is to use the motor as a generator if power to the electromagnets is lost. This would maintain levitation of the rotor and dissipate the rotor's kinetic energy in a controlled fashion until the touchdown bearings are able to support the rotor. The 3Dwheel's rotor spinning at 5000 rpm has a kinetic energy of $\frac{1}{2}I_{zz}\dot{\alpha}_z^2 = \frac{1}{2} \times 0.002326 \times 524^2 = 319$ J. Assuming that levitation can be achieved with a power consumption of 10 W [1] then if the generator has a 100% conversion efficiency then the rotor can be levitated for 32 seconds, or 9.6 seconds at 30% conversion efficiency.

5.3.6 Redundancy

In the engineering model of the 3Dwheel there is no redundancy; a failure of a single amplifier or sensor would prevent the rotor from being levitated. For use on spacecraft the lifetime and likelihood of each component failing must be calculated. Additional redundant components can be added if necessary to provide redundancy and an improved lifetime, albeit with a mass penalty. This is an advantage of a magnetically-levitated momentum-wheel. The mechanical bearings in a conventional wheel are one of the components most likely to fail and it is not possible to include redundant or spare mechanical bearings.

---

[1] The AMSAT Phase 3-D wheel's bearings have a stated power consumption of 5 W [23]

5.4 Conclusions

The knowledge acquired during these investigations has been combined to produce the engineering model of the 3Dwheel hardware. The engineering model has been designed to demonstrate that a tilting magnetically levitated momentum wheel suitable for use on small satellites is feasible. The engineering model has been designed for ease of manufacture and so is quite different from a flight-ready wheel.

Finally, the aspects of a tilting magnetically levitated momentum wheel that were not considered during this project have been briefly introduced. These aspects must be fully developed for a flight-ready wheel.

The next Chapter will develop a model of the dynamic motion of the 3Dwheel's rotor. This model will allow the response of the rotor to be modelled and will be used to derive controllers to stabilise the levitation and motion of the 3Dwheel's rotor.

Chapter 6

Dynamic Modelling

In the previous Chapters the magnetic properties of a tilting magnetically levitated momentum wheel were discussed and modelled analytically and numerically. This work was used to design the hardware for the engineering model of the 3Dwheel. As well as having magnetic properties a magnetically levitated rotor has dynamic properties in its translational and rotational motion. In this Chapter analytical models of these motions are developed. The models will be used to predict the dynamics of the rotor's motion and again in the next Chapter to derive controllers to stabilise the 3Dwheel's levitation and motion.

The models initially assume a perfect rotor with no mass imbalance. This is later extended to discuss a rotor that is not perfectly balanced. The sensors used in the engineering model and in a flight-ready model measure only the rotor's position. Many control techniques require knowledge of the rates that the rotor is moving at. Calculating these rates by differentiating the sensor values also differentiates noise in the values. Therefore Kalman filters were developed to estimate the rotor's rate of movement. A method to tune the Kalman filters to the actual dynamics of the engineering model is presented.

6.1 Dynamic Equations

The motion of the rotor can be separated into translational and rotational components:

6.1.1 Dynamics of Translational Motion

The dynamic behaviour of the rotor for translational motion is given by Newton's Second Law:

$$\mathbf{F} = M\mathbf{a} \tag{6.1}$$

where $\mathbf{F}$ is the force acting on the rotor in the fixed inertial frame $\mathbf{N}$, $\mathbf{a}$ is the acceleration of the rotor in the inertial frame and M is the mass of the rotor. The acceleration is given by:

$$\mathbf{a} = \ddot{x}\mathbf{\hat{n}_x} + \ddot{y}\mathbf{\hat{n}_y} + \ddot{z}\mathbf{\hat{n}_z} \tag{6.2}$$

where x is the translational position along the x-axis and $\ddot{x}$ is the second derivative of the translational position, or acceleration, along the x-axis.

6.1.2 Inertia Matrix

In translational motion, the object's mass determines its acceleration when a force is applied. Mass is a scalar quantity. In rotational motion the equivalent of mass is the moment of inertia. For three dimensional motion the tensor inertia matrix is used.

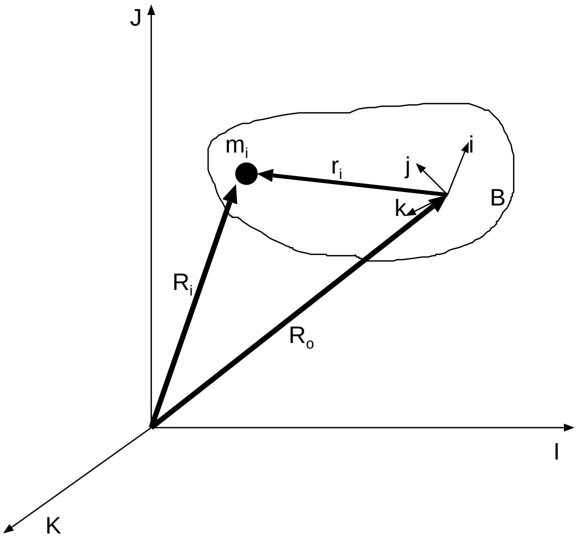

Figure 6.1: The body and inertial reference frames.

The derivation of the inertia matrix of a body B is described in many texts, for example [11] and [12].

I, **J** and **K** form the fixed inertial reference frame. **i**, **j** and **k** form the body reference frame.

For a particle m_i in the body its position is given by:

$$\mathbf{R_i} = \mathbf{R_0} + \mathbf{r_i} \tag{6.3}$$

From Euler's Moment Equation the velocity of m_i is given by:

$$\dot{\mathbf{R}}_\mathbf{i} = \dot{\mathbf{R}}_\mathbf{0} + \dot{\mathbf{r}}_\mathbf{i} + \boldsymbol{\omega} \times \mathbf{r_i} \tag{6.4}$$

where $\boldsymbol{\omega}$ is the angular velocity of the body frame with respect to the inertial frame.

The angular momentum of particle m_i is then:

$$\begin{aligned} \mathbf{h_i} &= \mathbf{r_i} \times \mathbf{m_i}\dot{\mathbf{R}}_\mathbf{i} \\ &= \mathbf{r_i} \times \mathbf{m_i}(\dot{\mathbf{R}}_\mathbf{0} + \dot{\mathbf{r}}_\mathbf{i} + \boldsymbol{\omega}\times\mathbf{r_i}) \end{aligned} \tag{6.5}$$

As we have a rigid body then $\dot{\mathbf{r_i}} = 0$ and so:

$$\begin{aligned}
\mathbf{h_i} &= \mathbf{r_i} \times \mathbf{m_i}(\dot{\mathbf{R_0}} + \boldsymbol{\omega}\times\mathbf{r_i}) \\
&= \mathbf{r_i} \times \mathbf{m_i}\dot{\mathbf{R_0}} + \mathbf{r_i} \times \mathbf{m_i}(\boldsymbol{\omega}\times\mathbf{r_i}) \\
&= -\dot{\mathbf{R_0}} \times \mathbf{m_i}\mathbf{r_i} + \mathbf{r_i} \times \mathbf{m_i}(\boldsymbol{\omega}\times\mathbf{r_i}) \qquad (6.6)
\end{aligned}$$

To find the angular momentum of the whole body we sum the angular momentum of all the particles:

$$\begin{aligned}
\mathbf{h} &= \sum_{m_i} -\dot{\mathbf{R_0}} \times \mathbf{m_i}\mathbf{r_i} + \sum_{m_i} \mathbf{r_i} \times (\boldsymbol{\omega}\times\mathbf{r_i})\mathbf{m_i} \\
&= -\dot{\mathbf{R_0}} \times \sum_{m_i} \mathbf{m_i}\mathbf{r_i} + \sum_{m_i} \mathbf{r_i} \times (\boldsymbol{\omega}\times\mathbf{r_i})\mathbf{m_i} \qquad (6.7)
\end{aligned}$$

Because the motion is about the centre of mass $\sum_{m_i} \mathbf{m_i}\mathbf{r_i} = 0$, therefore:

$$\mathbf{h} = \sum_{m_i} \mathbf{r_i} \times (\boldsymbol{\omega}\times\mathbf{r_i})\mathbf{m_i} \qquad (6.8)$$

The position of each particle is given by:

$$\begin{aligned}
\mathbf{r_i} &= x_i\hat{\mathbf{i}} + y_i\hat{\mathbf{j}} + z_i\hat{\mathbf{k}} \\
&= \begin{bmatrix} x_i & y_i & z_i \end{bmatrix}^T \qquad (6.9)
\end{aligned}$$

and:

$$\boldsymbol{\omega} = \begin{bmatrix} \omega_x & \omega_y & \omega_z \end{bmatrix}^T \qquad (6.10)$$

Therefore:

$$\mathbf{r_i} \times (\boldsymbol{\omega}\times\mathbf{r_i}) = \begin{bmatrix} -\omega_z x_i z_i + \omega_x z_i^2 - \omega_y x_i y_i + \omega_x y_i^2 \\ -\omega_z y_i z_i + \omega_y z_i^2 + \omega_y x_i^2 - \omega_x x_i y_i \\ \omega_z y_i^2 - \omega_y y_i z_i + \omega_z x_i^2 - \omega_x x_i z_i \end{bmatrix} \qquad (6.11)$$

Defining:

$$\begin{aligned}
I_{xx} &= \sum_{m_i}(y_i^2 + z_i^2)m_i \\
I_{yy} &= \sum_{m_i}(x_i^2 + z_i^2)m_i \\
I_{zz} &= \sum_{m_i}(x_i^2 + y_i^2)m_i \\
I_{xy} &= I_{yx} = \sum_{m_i} x_i y_i m_i \\
I_{xz} &= I_{zx} = \sum_{m_i} x_i z_i m_i \\
I_{yz} &= I_{zy} = \sum_{m_i} y_i z_i m_i \qquad (6.12)
\end{aligned}$$

Now, the angular momentum of the body is:

$$\begin{aligned}
\mathbf{h} &= \begin{bmatrix} I_{xx} & -I_{xy} & -I_{xz} \\ -I_{yx} & I_{yy} & -I_{yz} \\ -I_{zx} & -I_{zy} & I_{zz} \end{bmatrix} \begin{bmatrix} \omega_x \\ \omega_y \\ \omega_z \end{bmatrix} = \mathbf{I}\boldsymbol{\omega} \\
&= \hat{\mathbf{i}}(\omega_x I_{xx} - \omega_y I_{xy} - \omega_z I_{xz}) + \\
&\quad \hat{\mathbf{j}}(\omega_y I_{yy} - \omega_x I_{yx} - \omega_z I_{yz}) + \\
&\quad \hat{\mathbf{k}}(\omega_z I_{zz} - \omega_x I_{zx} - \omega_y I_{zy}) \qquad (6.13)
\end{aligned}$$

I_{xx}, I_{yy} and I_{zz} are called the principal moments of inertia and the remaining, off diagonal elements, are called the products of inertia.

6.1.3 Dynamics of Rotational Motion

The body frame $\mathbf{B}$ is fixed to, and rotates with, the body. $\mathbf{B}$ rotates with angular velocity $\boldsymbol{\omega}^{\boldsymbol{B/N}}$ with respect to the inertial frame $\mathbf{N}$. This angular velocity can be written as:

$$\begin{aligned}
\boldsymbol{\omega}^{\boldsymbol{B/N}} &= \omega'_x \hat{\mathbf{n}}_{\mathbf{x}} + \omega'_y \hat{\mathbf{n}}_{\mathbf{y}} + \omega'_z \hat{\mathbf{n}}_{\mathbf{z}} \\
&= \omega_x \hat{\mathbf{b}}_{\mathbf{x}} + \omega_y \hat{\mathbf{b}}_{\mathbf{y}} + \omega_z \hat{\mathbf{b}}_{\mathbf{z}} \\
&= \dot{\alpha}_x \hat{\mathbf{b}}_{\mathbf{x}} + \dot{\alpha}_y \hat{\mathbf{b}}_{\mathbf{y}} + \dot{\alpha}_z \hat{\mathbf{b}}_{\mathbf{z}} \qquad (6.14)
\end{aligned}$$

If the body frame is aligned with the principal axes of the body and the origin coincides with its centre of mass, assuming there are no products of inertia, then the angular momentum of the body is:

$$\begin{aligned}\mathbf{H} &= H_x\hat{\mathbf{b}}_\mathbf{x} + H_y\hat{\mathbf{b}}_\mathbf{y} + H_z\hat{\mathbf{b}}_\mathbf{z} \\ &= I_{xx}\omega_x\hat{\mathbf{b}}_\mathbf{x} + I_{yy}\omega_y\hat{\mathbf{b}}_\mathbf{y} + I_{zz}\omega_z\hat{\mathbf{b}}_\mathbf{z} \qquad (6.15)\end{aligned}$$

This can be differentiated using Euler's Moment Equation to give the dynamic equation of rotational motion in vector form, which makes no assumptions about the inertia matrix [76]:

$$\mathbf{T} = I\dot{\boldsymbol{\omega}} + \boldsymbol{\omega}\times I\boldsymbol{\omega} \qquad (6.16)$$

where $\mathbf{T}$ is expressed in the inertial frame $\mathbf{N}$:

$$\mathbf{T} = T_x\hat{\mathbf{n}}_\mathbf{x} + T_y\hat{\mathbf{n}}_\mathbf{y} + T_z\hat{\mathbf{n}}_\mathbf{z} \qquad (6.17)$$

Rearranging we have:

$$\dot{\boldsymbol{\omega}} = I^{-1}(\mathbf{T} - \boldsymbol{\omega}\times I\boldsymbol{\omega}) \qquad (6.18)$$

6.1.4 Kinematic Differential Equations of Motion

The orientation of the body frame with respect to the inertial frame is specified by the Euler angles ϕ, θ and ψ. Using a 3-2-1 sequence we can define the rotation matrix $\mathbf{R}$ as described in Appendix C.1:

$$\mathbf{R} = \mathbf{R_1}(\phi)\mathbf{R_2}(\theta)\mathbf{R_3}(\psi) \qquad (6.19)$$

The Euler angles are related to the angular velocities by the kinematic differential equations of motion [12]:

$$\begin{bmatrix}\dot{\phi}\\ \dot{\theta}\\ \dot{\psi}\end{bmatrix} = \frac{1}{c\theta}\begin{bmatrix} c\theta & s\phi s\theta & c\phi s\theta \\ 0 & c\phi c\theta & -s\phi c\theta \\ 0 & s\phi & c\phi\end{bmatrix}\begin{bmatrix}\omega_x\\ \omega_y\\ \omega_z\end{bmatrix} \qquad (6.20)$$

where $c\theta = \cos\theta$ and $s\phi = \sin\phi$

Many authors do not include the kinematic differential equations of motion in their models of the rotational dynamics of a shaft or rotor [18][25][77][78]. The kinematic differential equations of motion are however always included in the rotational dynamics of motion of spacecraft [11][12]. In a spinning shaft or rotor the range of angles tilted through is small and small angle approximations can be used to show that Equation 6.20 simplifies to $\begin{bmatrix}\dot{\phi} & \dot{\theta} & \dot{\psi}\end{bmatrix}^T = \begin{bmatrix}\omega_x & \omega_y & \omega_z\end{bmatrix}^T$. Therefore the kinematic differential equations of motion can be omitted from the motion of the 3Dwheel if the tilt range is small enough that the small angle approximations are valid.

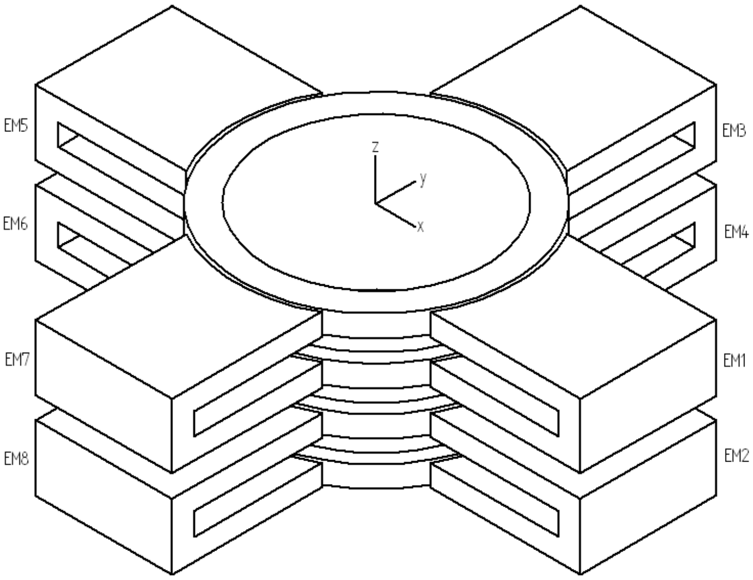

Figure 6.2: The arrangement and numbering of the electromagnets around the wheel

6.1.5 Kinematic Mapping Equations

The mapping to convert the forces produced by the electromagnets to the 3-axis torque and force exerted on the rotor is given by the kinematic mapping equations. Figure 6.2 shows the co-ordinate system and numbering of the electromagnets. x, y and z represent the wheel's inertial reference frame, which is fixed to the stator. Electromagnets 1 to 8 produce an attractive reluctance force, f_1 to f_8, in the radial direction. The passive forces in the axial direction are ignored because of their low magnitude compared to the active component as described in Section 3.2.3. The total force produced in the inertial reference frame is given by:

$$\begin{bmatrix} F_x \\ F_y \\ F_z \end{bmatrix} = \begin{bmatrix} 1 & 1 & 0 & 0 & -1 & -1 & 0 & 0 \\ 0 & 0 & 1 & 1 & 0 & 0 & -1 & -1 \\ 0 & 0 & 0 & 0 & 0 & 0 & 0 & 0 \end{bmatrix} \begin{bmatrix} f_1 \\ f_2 \\ f_3 \\ f_4 \\ f_5 \\ f_6 \\ f_7 \\ f_8 \end{bmatrix} \tag{6.21}$$

The torque about each of the inertial axes can similarly be calculated as:

$$\begin{bmatrix} T_x \\ T_y \\ T_z \end{bmatrix} = r_T \begin{bmatrix} 0 & 0 & -1 & 1 & 0 & 0 & 1 & -1 \\ 1 & -1 & 0 & 0 & -1 & 1 & 0 & 0 \\ 0 & 0 & 0 & 0 & 0 & 0 & 0 & 0 \end{bmatrix} \begin{bmatrix} f_1 \\ f_2 \\ f_3 \\ f_4 \\ f_5 \\ f_6 \\ f_7 \\ f_8 \end{bmatrix} \tag{6.22}$$

where r_T is the length of the moment that the torques act about, as described in Section 4.4.2.

6.1.6 System Summary

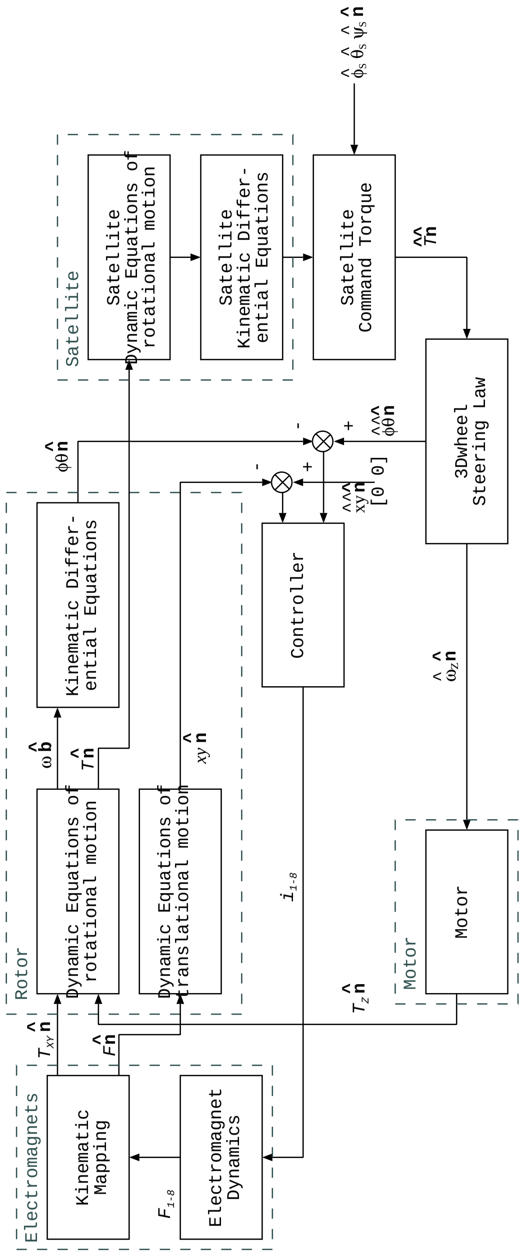

Figure 6.3: A block diagram of the 3Dwheel dynamics when mounted on a spacecraft.

Figure 6.3 shows the components of the motion of the 3Dwheel when mounted on a spacecraft. $\hat{\mathbf{n}}$ indicates a vector quantity in the inertial frame and $\hat{\mathbf{b}}$ indicates a vector quantity in the body frame. F_{1-8} and i_{1-8} are the eight electromagnet forces and currents respectively. $\hat{\phi}_s\hat{\theta}_s\hat{\psi}_s\hat{\mathbf{n}}$ is the desired spacecraft attitude. $\hat{T}\hat{\mathbf{n}}$ is the desired torque output from the 3Dwheel and $\hat{\omega}_z\hat{\mathbf{n}}$ is the desired spin rate of the rotor, $\omega\hat{\mathbf{n}}$ is the attitude rate of the rotor and $\phi\theta\hat{\mathbf{n}}$ is the attitude of the rotor, while $\hat{\phi}\hat{\theta}\hat{\mathbf{n}}$ is the desired rotor attitude.

The area enclosed by a dashed grey line is a piece of hardware that has dynamics that have to be simulated by a model in a Simulink simulation. The remaining items are always implemented in software for both a simulation and in the hardware in the laboratory or on a spacecraft.

The rotor's dynamic equations of rotational and translational motion and its kinematic differential equations of motion are all described in this Chapter. The rotational motion is given by Equation 6.18, translational motion by Equation 6.1 and the kinematic differential equations by Equation 6.20.

The electromagnet dynamics implement the reluctance force equation and the electromagnet kinematic mapping block implements Equations 6.21 and 6.22. The motor dynamics can be simulated using Equation 6.33.

The satellite dynamic blocks consisting of the dynamic equations of rotational motion and kinematic differential equations are given in Appendix C, as is the satellite command torque. The 3Dwheel steering law block implements Equation 6.36.

6.1.7 Air Gap Width

As the rotor moves the width of the air gap between each electromagnet and the rotor will vary. As the reluctance force generated by each electromagnet is inversely proportional to the square of the air gap width it is important to be able to calculate the air gap width at each electromagnet for an accurate simulation of the dynamics of the system and also for the derivation of the controller.

Non-Linear

Electromagnet n has its stator pole face fixed in the inertial reference frame at $[\begin{array}{ccc} x_{sn} & y_{sn} & z_{sn} \end{array}]^T$ and the corresponding point on the rotor moves around. The corresponding rotor point has a position $[\begin{array}{ccc} x_{rn} & y_{rn} & z_{rn} \end{array}]^T$ when the rotor is in its central position. The rotation matrices describing the position of a point after a rotation are given in Appendix C.1; because of the symmetry of rotor about the z-axis only rotations $\mathbf{R_x}(\alpha_x)$ and $\mathbf{R_y}(\alpha_y)$ need to be considered. The translation that the rotor had undergone is given by $[\begin{array}{ccc} x & y & z \end{array}]^T$ and so the width $\boldsymbol{\gamma_n}$ of the air gap between the rotor and electromagnet n is given by:

$$\boldsymbol{\gamma_n} = \left| \begin{bmatrix} x_{sn} \\ y_{sn} \\ z_{sn} \end{bmatrix} - \left(\mathbf{R_x}(\alpha_x)\mathbf{R_y}(\alpha_y) \begin{bmatrix} x_{rn} \\ y_{rn} \\ z_{rn} \end{bmatrix} + \begin{bmatrix} x \\ y \\ z \end{bmatrix} \right) \right| \tag{6.23}$$

For electromagnets on the x-axis the first component of $\boldsymbol{\gamma_n}$ provides the air gap width and the second component for electromagnets on the y-axis.

The radius of the rotor is r_r, the height of the rotor is η and the width of the air gap with the rotor in its central position is γ_0. The position of the rotor and stator in each air gap is defined in Table 6.1.

Electromagnet	Stator Position	Rotor Position
1	$[r_r + \gamma_0, 0, \eta/2]$	$[r_r, 0, \eta/2]$
2	$[r_r + \gamma_0, 0, -\eta/2]$	$[r_r, 0, -\eta/2]$
3	$[0, r_r + \gamma_0, \eta/2]$	$[0, r_r, \eta/2]$
4	$[0, r_r + \gamma_0, -\eta/2]$	$[0, r_r, -\eta/2]$
5	$[-r_r - \gamma_0, 0, \eta/2]$	$[-r_r, 0, \eta/2]$
6	$[-r_r - \gamma_0, 0, -\eta/2]$	$[-r_r, 0, -r_z]$
7	$[0, -r_r - \gamma_0, \eta/2]$	$[0, -r_r, \eta/2]$
8	$[0, -r_r - \gamma_0, -\eta/2]$	$[0, -r_r, -\eta/2]$

Table 6.1: The co-ordinates of each electromagnet's rotor and stator poles.

Linearised

When generating the linearised controller, a linear form of Equation 6.23 is required. For electromagnets one and two as the rotor moves in the positive x direction then the width of their air gaps will decrease and the width of the air gaps for electromagnets five and six will increase:

$$\begin{aligned} \triangle\gamma_1 &= \triangle\gamma_2 = -x \\ \triangle\gamma_5 &= \triangle\gamma_6 = x \end{aligned} \tag{6.24}$$

Similar values can be calculated for the remaining electromagnets along the y-axis.

Electromagnet one is at $[r_r, 0, \eta/2]^T$. Using the y-axis rotation matrix from Equation C.2 and assuming no translations about other axes, the air gap width of this electromagnet for rotations about the y-axis is:

$$\gamma_1 = (r_r + \gamma_0) - (r_r \cos\alpha_y + \eta/2 \sin\alpha_y) \tag{6.25}$$

Using small angle approximations this reduces to:

$$\gamma_1 = \gamma_0 - \eta/2\alpha_y \tag{6.26}$$

Performing similar rotations for the other electromagnets (or using symmetry) the linearised change in air gap width for all of the electromagnets can be found:

$$\begin{bmatrix} \triangle\gamma_1 \\ \triangle\gamma_2 \\ \triangle\gamma_3 \\ \triangle\gamma_4 \\ \triangle\gamma_5 \\ \triangle\gamma_6 \\ \triangle\gamma_7 \\ \triangle\gamma_8 \end{bmatrix} = \begin{bmatrix} -1 & 0 & 0 & -\eta/2 \\ -1 & 0 & 0 & \eta/2 \\ 0 & -1 & \eta/2 & 0 \\ 0 & -1 & -\eta/2 & 0 \\ 1 & 0 & 0 & \eta/2 \\ 1 & 0 & 0 & -\eta/2 \\ 0 & 1 & -\eta/2 & 0 \\ 0 & 1 & \eta/2 & 0 \end{bmatrix} \begin{bmatrix} x \\ y \\ \alpha_x \\ \alpha_y \end{bmatrix} \tag{6.27}$$

6.1.8 3-Axis Torque Output From the Wheel

The 3-axis output torque from the full wheel system $\mathbf{T}$ is the sum of the gyroscopic output torque from tilting the wheel $\mathbf{T_T}$ and the conventional torque from changing the angular velocity of the spinning wheel $\mathbf{T_C}$. Because the rotor is tilted through a small range of angles, we can use small angle approximations to say that there is no component of the gyroscopic torque about the z-axis and the conventional acceleration torque only has a component about the z-axis.

The output torque from tilting the rotor is generated by the same physical process as in a CMG. Incorporating the small angle approximations mentioned above, it is given by:

$$\mathbf{T_T} = \begin{bmatrix} \dot{\alpha}_x \\ \dot{\alpha}_y \\ 0 \end{bmatrix} \times \mathbf{h_0}(\phi, \theta, \dot{\alpha}_z) \tag{6.28}$$

where $\mathbf{h_0}$ is the angular momentum of the spinning rotor, and is a function of the rotor spin rate about the z-axis and the angle of the rotor about the x and y axes. The angular momentum when the rotor is not tilted is:

$$\mathbf{H_0}(\dot{\alpha}_z) = \mathbf{I} \begin{bmatrix} 0 \\ 0 \\ \dot{\alpha}_z \end{bmatrix} \tag{6.29}$$

The rotation matrix to rotate $\mathbf{H_0}(\dot{\alpha}_z)$ about the y-axis and then the x-axis can be calculated by:

$$\begin{aligned} \mathbf{R_{xy}} &= \begin{bmatrix} 1 & 0 & 0 \\ 0 & \mathrm{c}\phi & -\mathrm{s}\phi \\ 0 & \mathrm{s}\phi & \mathrm{c}\phi \end{bmatrix} \begin{bmatrix} \mathrm{c}\theta & 0 & \mathrm{s}\theta \\ 0 & 1 & 0 \\ -\mathrm{s}\theta & 0 & \mathrm{c}\theta \end{bmatrix} \\ &= \begin{bmatrix} \mathrm{c}\theta & 0 & \mathrm{s}\theta \\ \mathrm{s}\phi\mathrm{s}\theta & \mathrm{c}\phi & -\mathrm{s}\phi\mathrm{c}\theta \\ -\mathrm{c}\phi\mathrm{s}\theta & \mathrm{s}\phi & \mathrm{c}\phi\mathrm{c}\theta \end{bmatrix} \end{aligned} \tag{6.30}$$

Therefore the output torque from tilting the rotor is given by:

$$\mathbf{T_T} = \begin{bmatrix} \dot{\alpha}_x \\ \dot{\alpha}_y \\ 0 \end{bmatrix} \times \mathbf{R_{xy}I} \begin{bmatrix} 0 \\ 0 \\ \dot{\alpha}_z \end{bmatrix} \tag{6.31}$$

The output torque about the z-axis from the acceleration of the rotor is given by:

$$\mathbf{T_C} = I_{zz} \begin{bmatrix} 0 \\ 0 \\ \ddot{\alpha}_z \end{bmatrix} \tag{6.32}$$

The output torque from the tilting magnetically-levitated momentum-wheel is the sum of the torques from tilting and accelerating the rotor $\mathbf{T} = \mathbf{T_T} + \mathbf{T_C}$.

The dynamics of the brushless DC motor spinning the rotor are approximated in the Laplace domain by:

$$\dot{\Omega}_z(s) = \frac{sI_{drive}(s)}{sK_l + K_D} \tag{6.33}$$

where I_{drive} is the drive current to the motor, and the inertia and damping gains K_l and K_D are taken for a typical brushless DC motor used in the laboratory, with values 1.07×10^{-2} and 0.1 respectively [79].

6.1.9 Torque Command

Appendix C describes two steering laws that generate a demand torque $\hat{\mathbf{T}} = \begin{bmatrix} \hat{T}_x & \hat{T}_y & \hat{T}_z \end{bmatrix}^T$ that the 3Dwheel is required to generate. This demand needs to be converted from a torque to tilt demands about the x and y-axes. These torque commands then form the desired input to the closed loop controllers.

The gyroscopic torque generated by tilting the wheel is given by Equation 6.31. Multiplying this out and assuming that the inertia matrix **I** is diagonal with no product of inertia terms:

$$\mathbf{T_T} = \begin{bmatrix} \dot{\alpha}_y \cos\alpha_x \cos\alpha_y I_{zz}\dot{\alpha}_z \\ -\dot{\alpha}_x \cos\alpha_x \cos\alpha_y I_{zz}\dot{\alpha}_z \\ (-\dot{\alpha}_y \sin\alpha_y - \dot{\alpha}_x \sin\alpha_x \cos\alpha_y) I_{zz}\dot{\alpha}_z \end{bmatrix} \tag{6.34}$$

Ignoring the term about the z-axis, which will be controlled by a separate controller, this can be rewritten:

$$\mathbf{T_T} = \begin{bmatrix} 0 & \cos\alpha_x \cos\alpha_y I_{zz}\dot{\alpha}_z & 0 \\ -\cos\alpha_x \cos\alpha_y I_{zz}\dot{\alpha}_z & 0 & 0 \\ 0 & 0 & 0 \end{bmatrix} \begin{bmatrix} \dot{\alpha}_x \\ \dot{\alpha}_y \\ 0 \end{bmatrix} \tag{6.35}$$

This can be inverted to give the rotor tilt commands that can be fed to the electromagnet controllers:

$$\begin{bmatrix} \hat{\dot{\alpha}}_x \\ \hat{\dot{\alpha}}_y \end{bmatrix} = \begin{bmatrix} 0 & -1/(\cos\alpha_x \cos\alpha_y I_{zz}\dot{\alpha}_z) \\ 1/(\cos\alpha_x \cos\alpha_y I_{zz}\dot{\alpha}_z) & 0 \end{bmatrix} \begin{bmatrix} \hat{T}_x \\ \hat{T}_y \end{bmatrix} \tag{6.36}$$

The motor's speed input can be simply generated by a simple proportional controller from $\hat{T}_z$. The proportional gain in the simulation was found by experimentation.

6.1.10 Linearised Model

The translational and rotational dynamics mean that a non-linear model is required to accurately model the levitated spinning rotor. However, for the derivation of some of the controllers in the next Chapter it is convenient to linearise the model about its operating point.

The simplest model assumes that there is no coupling between any translation or rotation axis. From Equation 6.1 there is no coupling between the translational axes. By treating the gyroscopic term in Equation 6.16 as a disturbance then the rotational axes can be considered to be decoupled from each other and from the translational axes. Therefore a separate model can be generated for each actively controlled translation and rotation axis.

The reluctance force generated by an electromagnet, ignoring the minus sign that is usually included to indicate that it is an attractive force, is:

$$F_R = \frac{\mu_0 N^2 \varepsilon l i^2}{4\gamma^2} \tag{6.37}$$

This equation can be linearised by taking the first order Taylor series expansion:

$$\begin{aligned} F_R &= \frac{\mu_0 N^2 \epsilon l i_0^2}{4\gamma_0^2} + \frac{\mu_0 N^2 \epsilon l i_0}{2\gamma_0^2}\triangle i - \frac{\mu_0 N^2 \epsilon l i_0^2}{2\gamma_0^3}\triangle\gamma \\ &= f_0 + K_i\triangle i - K_\gamma\triangle\gamma \end{aligned} \tag{6.38}$$

where K_i is the force-current constant and K_γ is the force-displacement constant.

The total translational force along the x-axis is:

$$f_x = f_1 + f_2 - f_5 - f_6 \tag{6.39}$$

Substituting in the Taylor series expansion and the linearised air gap widths:

$$\begin{aligned} f_x = & \quad f_0 + K_i\triangle i_x + K_\gamma\triangle x \\ & + \; f_0 + K_i\triangle i_x + K_\gamma\triangle x \\ & - \; f_0 + K_i\triangle i_x + K_\gamma\triangle x \\ & - \; f_0 + K_i\triangle i_x + K_\gamma\triangle x \\ = & \quad 4K_i\triangle i_x + 4K_\gamma\triangle x \end{aligned} \tag{6.40}$$

Applying Newton's second law and rearranging we have:

$$\begin{aligned} f_x &= M\ddot{x} \\ \ddot{x} &= \frac{4}{M}(K_i \triangle i_x + 4K_\gamma \triangle x) \end{aligned} \tag{6.41}$$

Taking the Laplace transform:

$$\begin{aligned} s^2 X(s) &= \frac{4}{M}(K_i i_x(s) + 4K_\gamma X(s)) \\ X(s)(s^2 - \frac{4K_\gamma}{M}) &= \frac{4K_i i_x(s)}{M} \end{aligned} \tag{6.42}$$

The transfer function for translation along the x-axis is therefore:

$$G_x(s) = \frac{X(s)}{i_x(s)} = \frac{4K_i/M}{s^2 - 4K_\gamma/M} \tag{6.43}$$

For rotations about the y-axis, the torque acting on the rotor is given by:

$$T_y = r_T(f_1 + f_6 - f_2 - f_5) \tag{6.44}$$

where r_T is the length of the lever arm that the torques act through as discussed in Section 4.4.2. Substituting in the Taylor series expansion and the linearised air gap widths:

$$\begin{aligned} T_y = \quad r_T(&\quad f_0 + K_i \triangle i_{\alpha y} + K_\gamma \eta/2 \triangle \alpha_y \\ + &\quad f_0 + K_i \triangle i_{\alpha y} + K_\gamma \eta/2 \triangle \alpha_y \\ - &\quad f_0 + K_i \triangle i_{\alpha y} + K_\gamma \eta/2 \triangle \alpha_y \\ - &\quad f_0 + K_i \triangle i_{\alpha y} + K_\gamma \eta/2 \triangle \alpha_y) \\ = \qquad &\quad 4r_T(K_i \triangle i_{\alpha y} + K_\gamma \eta/2 \triangle \alpha_y) \end{aligned} \tag{6.45}$$

The dynamic equation of rotational motion (Equation 6.18) ignoring gyroscopic coupling and only considering rotations about the y-axis is:

$$T_y = I_{yy} \ddot{\alpha}_y \tag{6.46}$$

Substituting this into Equation 6.45 and taking the Laplace transform:

$$s^2 A_y(s) = \frac{4\eta_T K_i i_{\alpha y}(s)}{I_{yy}} + \frac{4r_T^2 K_\gamma A_y(s)}{I_{yy}} \tag{6.47}$$

The transfer function for rotations around the y-axis is therefore:

$$G_{\alpha y}(s) = \frac{A_y(s)}{i_{\alpha y}(s)} = \frac{4r_T K_i / I_{yy}}{s^2 - 4r_T^2 K_\gamma / I_{yy}} \tag{6.48}$$

The values used to generate the linearised model are shown in Table 6.2. Figure 6.4 shows the bode plot of the translation and rotation transfer functions. The translation transfer function has a magnitude of -57.1 dB at DC and a 3 dB frequency of 34.2 rads^{-1}. The rotation transfer function has a DC magnitude of -21.2 dB and a 3 dB frequency of 15.7 rads^{-1} . Because they are double integrators they have a constant phase of -180° and their magnitude decreases at a rate of -40 dB per decade.

N	100 turns
ε	8.0 mm
l	50.0 mm
γ_0	1.4 mm
i_0	3.0 A
M	1.301 kg
I_{yy}	0.001594 kgm^2
r_T	16 mm

Table 6.2: The values used to generate the linearised model.

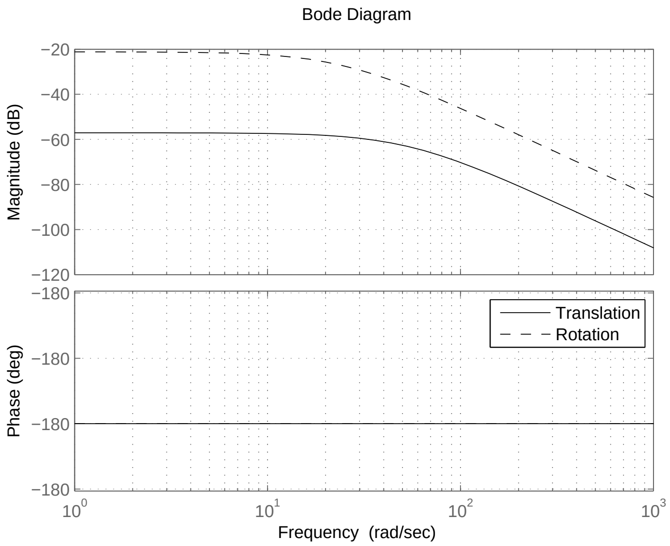

Figure 6.4: The linearised rotation and translation transfer functions.

6.1.11 Non-Linear Model

The linearised model that has just been generated is useful during the generation of the controllers. To accurately model the complete behaviour of the wheel a non-linear model is required. An accurate model is required to test that the controllers can cope with the hardware's non-linear behaviour and to see how the controllers perform away from the operating point that they were linearised about.

The non-linear model of the wheel was generated in the Simulink block diagram programming language. Simulink allows a system to be modelled in a hierarchical system of graphical drawings. Each level of the hierarchy introduces more detail until the basic mathematics of a block are represented by algebraic blocks or equations written in the Matlab programming language. Simulink allows the model to be solved using either fixed step discrete or continuous Ordinary Differential Equation (ODE) solvers. Results can be viewed graphically or the chosen variables saved for later analysis and plotting.

Wheel Non-linear Dynamics

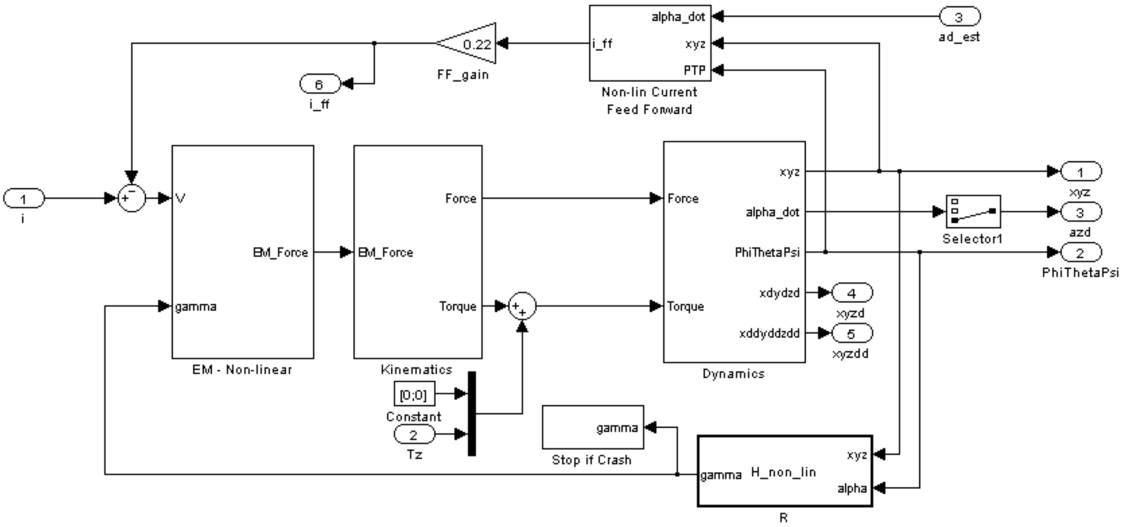

Figure 6.5: The top-level model of the wheel's non-linear dynamics.

Figure 6.5 shows the top-level block of the wheel's non-linear dynamics. The inputs and outputs are listed in Table 6.3 and the sub-blocks in Table 6.4.

Label	*Dimensions*	*Description*
i	$[8 \times 1]$	Electromagnet currents
Tz	$[1 \times 1]$	Motor torque
ad_est	$[3 \times 1]$	Estimated angular rates
xyz	$[3 \times 1]$	Translational position
PhiThetaPsi	$[3 \times 1]$	Rotational position in the inertial reference frame
azd	$[1 \times 1]$	Wheel's angular velocity about the z-axis in the body frame
xyzd	$[3 \times 1]$	Translational velocity
xyzdd	$[3 \times 1]$	Translational acceleration
i_ff	$[8 \times 1]$	Feed Forward Currents

Table 6.3: The inputs and outputs to the wheel's non-linear dynamics block.

Label	*Description*
EM - Non-linear	Electromagnet non-linear dynamics
Kinematics	Mapping from electromagnet forces to inertial force and torque
Dynamics	Wheel non-linear dynamics
Non-lin Current Feed Forward	Feed forward calculation
H_non_lin	Air gap width calculation

Table 6.4: The sub-blocks in the wheel's non-linear dynamics block.

The "H_non_lin" block is an embedded Matlab function that implements Equation 6.23. The "Stop if Crash" block stops the simulation if the rotor collides with the stator electromagnets. This is said to have happened if the following logical expression is true:

$$\gamma_0 \leq |\gamma_n - \gamma_0| \tag{6.49}$$

This is equivalent to saying that if an air gap moves further from its central position than one air gap width then a collision will have occurred.

Electromagnet Non-linear Dynamics

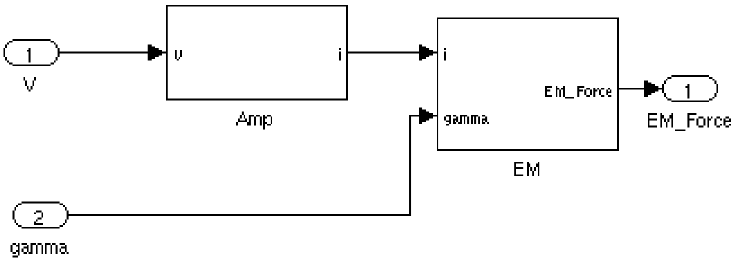

Figure 6.6: The electromagnet non-linear dynamics block implementing Equation 3.4.

Figure 6.5 shows the electromagnets non-linear dynamics block. The inputs and outputs are listed in Table 6.5.

Label	*Dimensions*	*Description*
V	$[8 \times 1]$	Controller output command
gamma	$[8 \times 1]$	Electromagnets air gap widths
EM_Force	$[8 \times 1]$	The horizontal attractive reluctance force generated by each electromagnet

Table 6.5: The inputs and outputs to the electromagnets' non-linear dynamics block.

The input to this block is the voltages generated by the controllers. The Amp sub-block takes these voltages and converts them to a current. Because of the linearity and low noise of the amplifiers used, this conversion has been represented by a gain of one. The EM sub-block implements the reluctance force equation:

$$F_R = \frac{\mu_0 N^2 \varepsilon l i^2}{4\gamma^2} \tag{6.50}$$

The air gap input to this block is the actual air gap width at each of the eight electromagnets. The force output is the attractive reluctance force generated by each electromagnet; the kinematic mapping equations are required to map these forces into the wheel's inertial reference frame.

Kinematic Mapping

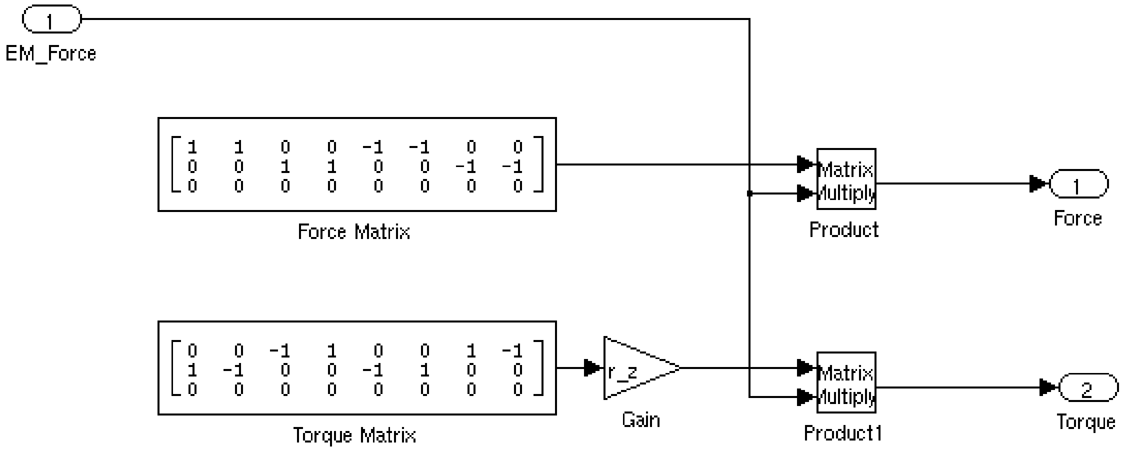

Figure 6.7: The kinematic mapping block implementing Equations 6.21 and 6.22.

Figure 6.7 shows the kinematic mapping block. The inputs and outputs are listed in Table 6.6.

Label	*Dimensions*	*Description*
EM_Force	$[8 \times 1]$	The horizontal attractive reluctance force generated by each electromagnet
Force	$[3 \times 1]$	The force acting on the rotor in the inertial reference frame
Torque	$[3 \times 1]$	The torque acting on the rotor in the inertial reference frame

Table 6.6: The inputs and outputs to the kinematic mapping block.

The kinematic mapping block maps the eight attractive forces produced by the eight electromagnets into the total force acting on rotor along the three axes of the inertial reference frame using Equation 6.21 and also into the three torques acting about the inertial reference frame's axes using Equation 6.22.

Non-Linear Dynamics

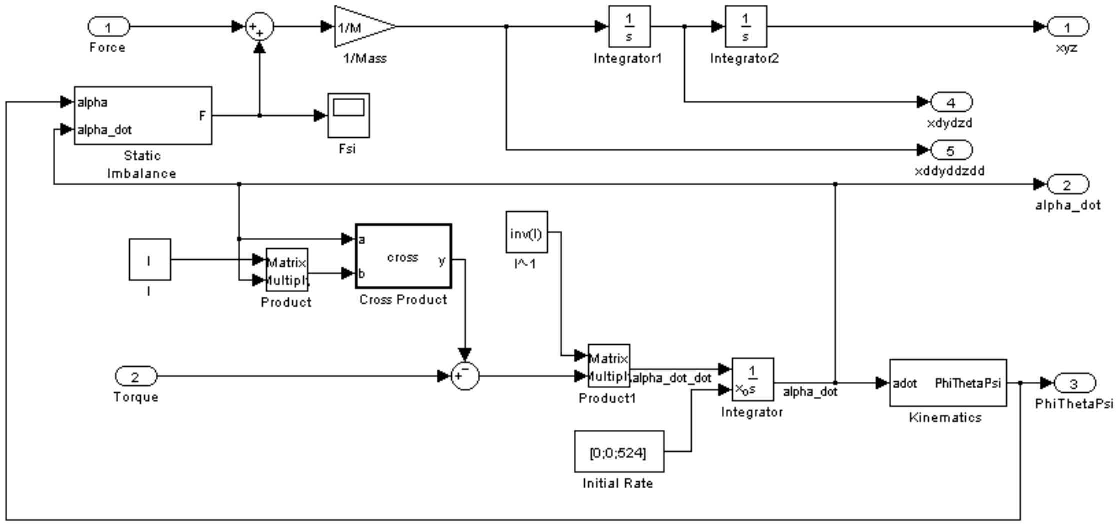

Figure 6.8: The non-linear dynamics block implementing Equations 6.1 and 6.18.

Figure 6.8 shows the non-linear dynamics block. The inputs and outputs are listed in Table 6.7.

Label	*Dimensions*	*Description*
Force	$[3 \times 1]$	The force acting on the rotor in the inertial reference frame
Torque	$[3 \times 1]$	The torque acting on the rotor in the inertial reference frame
xyz	$[3 \times 1]$	The translational position of the rotor
xdydzd	$[3 \times 1]$	The translational rate of the rotor
xddyddzdd	$[3 \times 1]$	The translational acceleration of the rotor
PhiThetaPsi	$[3 \times 1]$	The rotational position of the rotor in the inertial frame
alpha_dot	$[3 \times 1]$	The rotational rate of the rotor

Table 6.7: The inputs and outputs to the non-linear dynamics block.

The non-linear dynamics block implements the dynamic equations of translational and rotational motion, Equations 6.1 and 6.18 respectively. The translational acceleration is integrated twice to calculate the velocity and position of the rotor. The rotational acceleration is integrated once to give the rate, which passes through the kinematic differential equations of motion block to give the rotational position of the rotor in the inertial frame. The initial rotational rate of the wheel at the start of the acceleration is specified in this block. All other initial rates and positions are assumed to be zero.

The rotational rate and position is passed to the static imbalance block; the theory of which is explained in Section 6.2. The static imbalance disturbance force calculated is summed with the force exerted on the rotor by the electromagnets.

The translational and rotational rates are only passed out of this block to allow them to be monitored conveniently. The output of the equivalent hardware is only xyz and PhiThetaPsi.

Kinematic Differential Equations of Motion

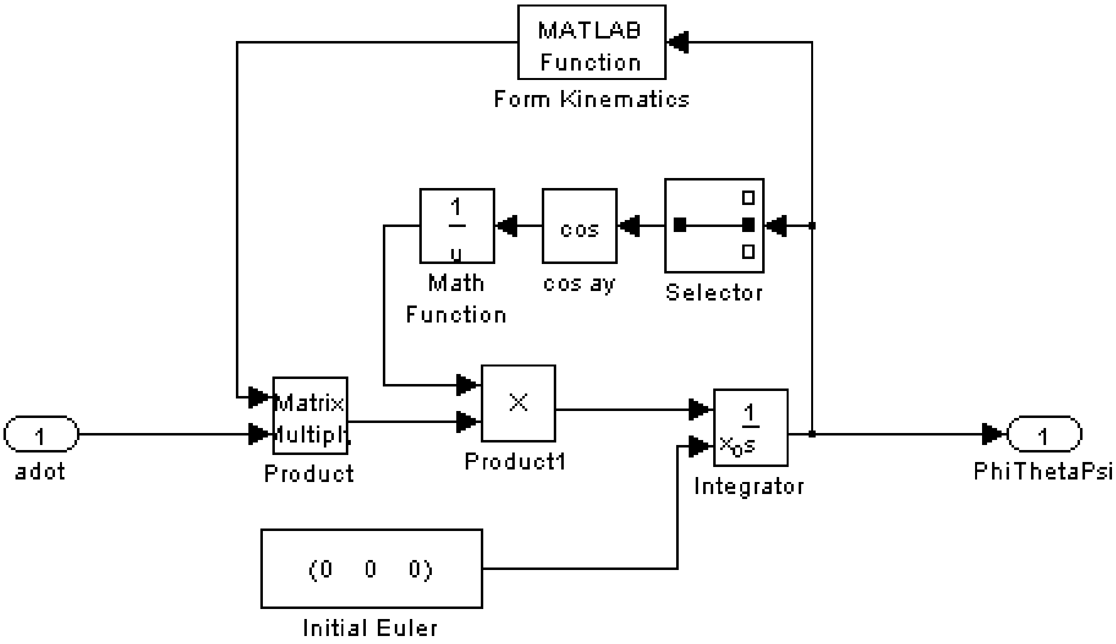

Figure 6.9: The kinematic differential equations of motion block implementing Equation 6.20.

Figure 6.9 shows the kinematic differential equations of motion block. The inputs and outputs are listed in Table 6.8.

Label	*Dimensions*	*Description*
adot	$[3 \times 1]$	The rotational rate of the rotor
PhiThetaPsi	$[3 \times 1]$	The rotational position of the rotor in the inertial frame

Table 6.8: The inputs and outputs to the kinematic differential equations of motion block.

The kinematic differential equations of motion block implements Equation 6.20. The “Form Kinematics” MATLAB Function forms the 3×3 matrix. The rotor is assumed to start from a central position.

Feed Forward

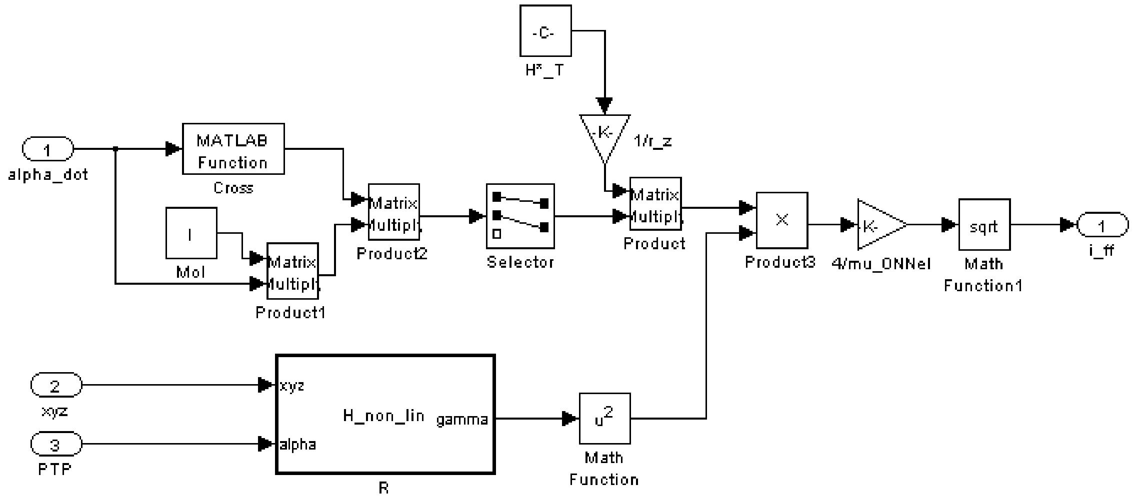

Figure 6.10: The non-linear feed forward block implementing Section 8.2.1 of this thesis.

Figure 6.10 shows the non-linear feed forward block. The inputs and outputs are listed in Table 6.9.

Label	*Dimensions*	*Description*
alpha_dot	$[3 \times 1]$	The rotational rate of the rotor
xyz	$[3 \times 1]$	The translational position of the rotor in the inertial frame
PTP	$[3 \times 1]$	ϕ, θ and ψ, the rotational position of the rotor in the inertial frame
PhiThetaPsi	$[3 \times 1]$	The rotational position of the rotor in the inertial frame

Table 6.9: The inputs and outputs to the non-linear feed forward block.

The non-linear feed forward block calculates the currents to compensate for gyroscopic cross-coupling as described in Section 8.2.1. The H sub-block calculates the air gap width at each electromagnet. The H*_T constant contains the pseudo-inverse of Equation 6.22 to map the three torques to eight currents. The constant was only defined as an 8×2 matrix hence the need for the selector block. The rest of the maths implements the reluctance force equation, Equation 6.50.

Static Imbalance

Figure 6.10 shows the static imbalance block. The inputs and outputs are listed in Table 6.10.

Label	*Dimensions*	*Description*
alpha_dot	$[3 \times 1]$	The rotational rate of the rotor
alpha	$[3 \times 1]$	The rotational position of the rotor in the inertial frame
F	$[3 \times 1]$	The disturbance force on the rotor due to its static mass imbalance

Table 6.10: The inputs and outputs to the static imbalance block.

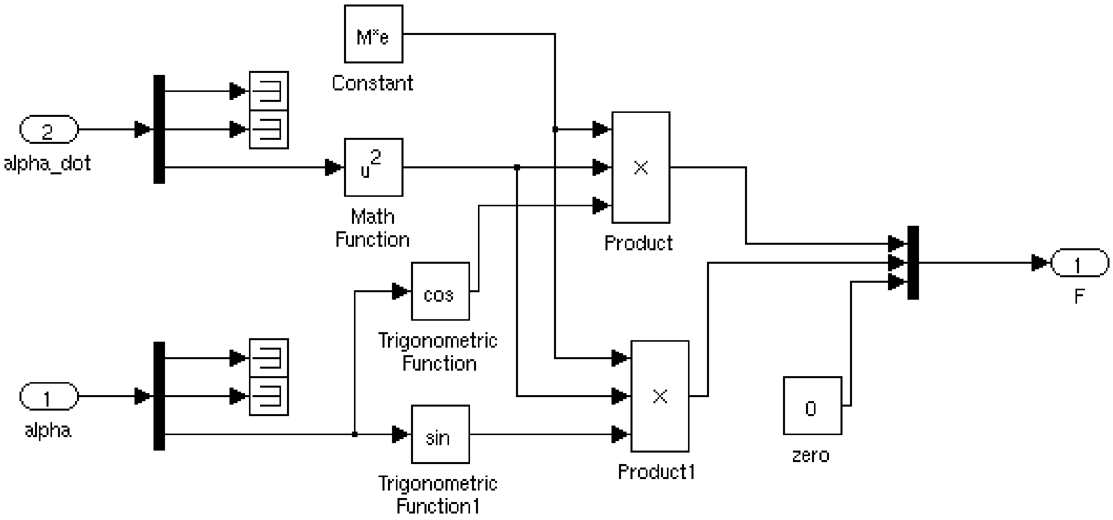

Figure 6.11: The static imbalance block implementing Equation 6.54.

The static imbalance block calculates the static balance disturbance force acting on the rotor using Equation 6.54. The magnitude of the imbalance Me is stored as a constant in the model's initialisation call-back function.

6.2 Rotor Imbalance

An ideal rotor has its mass evenly distributed about it and a diagonal inertia matrix. In reality rotors will not be perfectly balanced. This imbalance can have a static or a couple component. Most rotors will have a dynamic imbalance, which has both a static and couple component.

6.2.1 Static Imbalance

A static imbalance is where the centre of mass of the rotor is offset from the centre of rotation. It can be approximated by the addition of a single point mass.

The equations of motion for a simple point mass rotor can be written as:

$$\begin{aligned} M\ddot{x} + k_s x &= f_x(t) \\ M\ddot{y} + k_s y &= f_y(t) \end{aligned} \tag{6.51}$$

Where k_s is the spring constant of the bearing. In a static imbalance the centre of mass is located a distance e metres from the centre of rotation, the mass of the wheel is M kg and the wheel is rotating about the z-axis at a rate of Ω rads^{-1} then the equations of motion can be written as below if there are no external forces acting on the wheel [80]:

$$\begin{aligned} \frac{d^2}{dt^2} M(x + e\cos(\dot{\alpha}_z t)) + k_s x &= 0 \\ \frac{d^2}{dt^2} M(y + e\sin(\dot{\alpha}_z t)) + k_s y &= 0 \end{aligned} \tag{6.52}$$

Which can be written as:

$$\begin{aligned} M\ddot{x} + k_s x &= Me\dot{\alpha}_z^2 \cos(\dot{\alpha}_z t) \\ M\ddot{y} + k_s y &= Me\dot{\alpha}_z^2 \sin(\dot{\alpha}_z t) \end{aligned} \tag{6.53}$$

Where the terms on the right-hand side are the disturbance force due to the static imbalance of mass in the wheel. The force on the wheel due to the static imbalance F_{SI} is:

$$F_{SI} = \begin{bmatrix} Me\dot{\alpha}_z^2 \cos(\dot{\alpha}_z t) \\ Me\dot{\alpha}_z^2 \sin(\dot{\alpha}_z t) \\ 0 \end{bmatrix} \tag{6.54}$$

6.2.2 Couple Imbalance

With the couple imbalance, the principal axes of inertia are at an angle χ radians from the plane of the wheel. From [77], the resulting turning force on the wheel is given by the torque T_{CI} and given the difference in moments of inertia $I_{diff} = I_{xx} - I_{zz} = I_{yy} - I_{zz}$ can be calculated similarly as:

$$T_{CI} = \begin{bmatrix} -\chi I_{diff}\dot{\alpha}_z^2 \sin(\dot{\alpha}_z t) \\ \chi I_{diff}\dot{\alpha}_z^2 \cos(\dot{\alpha}_z t) \\ 0 \end{bmatrix} \tag{6.55}$$

Alternatively, when the rotational dynamics are written in vector form and the static imbalance is included in the I_{xz} or I_{yz} term of the inertia matrix then the cross product term of the rotational dynamics will include the disturbance torque from the couple imbalance:

$$\mathbf{T} = \mathbf{I}\dot{\boldsymbol{\omega}} + \boldsymbol{\omega} \times \mathbf{I}\boldsymbol{\omega} \tag{6.56}$$

When the inertia matrix $\mathbf{I}$ is diagonal with the couple imbalance represented by an I_{xz} term then multiplying out the gyroscopic component gives:

$$\begin{aligned} \mathbf{I} &= \begin{bmatrix} I_{xx} & 0 & I_{xz} \\ 0 & I_{yy} & 0 \\ I_{xz} & 0 & I_{zz} \end{bmatrix} \\ \dot{\boldsymbol{\alpha}} \times \mathbf{I}\dot{\boldsymbol{\alpha}} &= \begin{bmatrix} \dot{\alpha}_x\dot{\alpha}_y I_{xz} - \dot{\alpha}_y\dot{\alpha}_z I_{yy} + \dot{\alpha}_y\dot{\alpha}_z I_{zz} \\ \dot{\alpha}_x\dot{\alpha}_z I_{xx} - \dot{\alpha}_x^2 I_{xz} + \dot{\alpha}_z^2 I_{xz} - \dot{\alpha}_x\dot{\alpha}_z I_{zz} \\ \dot{\alpha}_x\dot{\alpha}_y I_{yy} - \dot{\alpha}_x\dot{\alpha}_y I_{xx} - \dot{\alpha}_y\dot{\alpha}_z I_{xz} \end{bmatrix} \end{aligned} \tag{6.57}$$

The $\dot{\alpha}_z^2 I_{xz}$ term is the disturbance due to the couple imbalance. When integrated as part of the wheel's dynamic equations it will give sinusoidal terms about the x and y axes. The $\dot{\alpha}_z^2 I_{xz}$ term has been shown to be equal to the $\chi I_{diff}\dot{\alpha}_z^2$ term in Equation 6.55, when the small angle approximation is replaced by $\chi \equiv \sin(\chi)$, and I_{xz} is calculated from a CAD model of the rotor rotated by the angle χ.

6.2.3 Imbalance Estimation

The static and couple imbalance of a rotor would normally be estimated and corrected to within a given tolerance on a balancing machine. No balancing machine was available at the University's workshop and neither time nor funds were available for the rotor to be balanced at an external company. The following method was devised to estimate the static imbalance of the rotor.

The dynamic equations of translational motion of the rotor incorporating the static imbalance and control force from the electromagnets, but assuming that the spring constant $k_s = 0$ are:

$$\begin{aligned} M\ddot{x} &= Me\dot{\alpha}_z^2\cos(\alpha_z+\alpha_e)+F_{emx} \\ M\ddot{y} &= Me\dot{\alpha}_z^2\sin(\alpha_z+\alpha_e)+F_{emy} \end{aligned} \tag{6.58}$$

Which can be rearranged to:

$$\begin{aligned} \left(\ddot{x}-\frac{F_{emx}}{M}\right) &= e\dot{\alpha}_z^2\cos(\alpha_z+\alpha_e) \\ \left(\ddot{y}-\frac{F_{emy}}{M}\right) &= e\dot{\alpha}_z^2\sin(\alpha_z+\alpha_e) \end{aligned} \tag{6.59}$$

$\ddot{x}$ and $\ddot{y}$ need to be calculated. The sensors measure x and y and the Linear Kalman filter can be used to estimate $\dot{x}$ and $\dot{y}$. A high-pass filter of the form:

$$G_{HPF}(s)=\frac{\frac{1}{\omega_{HPF}}s}{\frac{1}{\omega_{HPF}}s+1} \tag{6.60}$$

where ω_{HPF} is greater than the rotation rate of the wheel $\dot{\alpha}_z$ can be used to differentiate $\dot{x}$ and $\dot{y}$ to calculate the accelerations $\ddot{x}$ and $\ddot{y}$. The transfer function of the above high-pass filter when $\omega_{HPF}=150$ rads^{-1} is shown in Figure 6.12, which was used in the following example when the wheel was rotating at 500 rpm (or 52.4 rads^{-1}). The 3 dB frequency of the filter is at 150 rads^{-1} and so at 52.4 rads^{-1} the filter is acting as a differentiator. However, it is not perfect and has a phase of 70.7° at 52.4 rads^{-1}, compared with 90° for an ideal differentiator. The forces generated by the electromagnets and the mass of the rotor are known and so the left hand side of Equation 6.59 can be calculated. $\dot{\alpha}_z$ is also known and so the offset distance e between the centre of geometry and the centre of mass can be found from the amplitude of the sine wave.

There are then several options to calculate the phase position α_e of the centre of mass. Initially it was found by converting the sine wave to a square wave and xor-ing it with $\cos(\alpha_z)$. The resulting signal is a logical high when the two inputs to the xor are different. The proportion of a cycle that the xor output is high is related to α_e. This proportion can be found by low pass filtering the output of the xor. A more refined approach is to replace $\cos(\alpha_z)$ with $\cos(\alpha_z+\alpha_e')$ and to vary α_e' until the output of the xor is logic zero at all times. This was implemented in Simulink by low pass filtering the output of the xor and using a PI controller to generate α_e', as shown in Figure 6.13.

The method works well in the non-linear simulation of the 3Dwheel. When fed with a simulated input signal with a rotation rate of 52 rads^{-1}, but with a phase shift of $10°$, the PI controller converges to within 5% of the correct answer within 1.5 seconds as shown in Figure 6.14. Unfortunately this method could not be used on the engineering model of the wheel due to the noise in the y-axis translation eddy current sensor as described in Section 7.2.3.

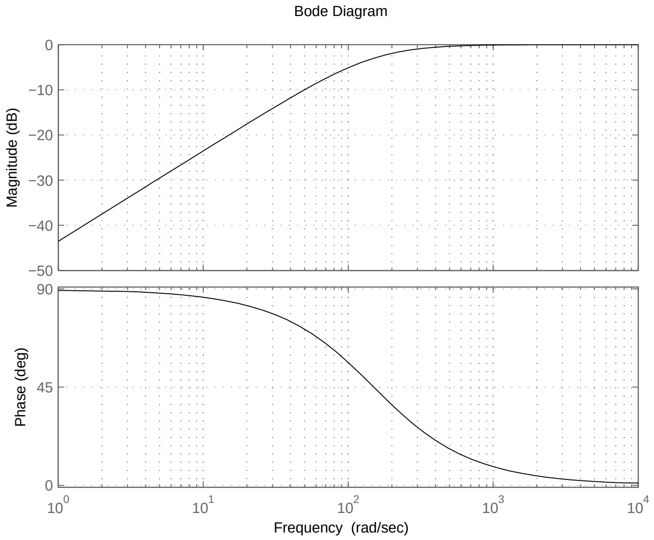

Figure 6.12: Transfer function of a high-pass filter with a cut-off frequency of 150 rads^{-1}.

6.2.4 Imbalance Compensation

As described by [31] it is not necessary or even beneficial to spin a rotor about its geometrical centre. If there is a static imbalance then doing so results in a disturbance force that will be transmitted to the spacecraft if the bearings are stiff enough. Allowing the rotor to spin about its centre of mass and principal axes of inertia will eliminate the disturbance due to the imbalance, [48][49][50] all suggest methods to do this. An alternative approach to estimating a rotor's mass imbalance has been presented in the preceding Section. The rotor must be balanced sufficiently well that the centre of mass is close enough to the geometrical centre that the rotor will not collide with the stator when spinning around the centre of mass and tilting.

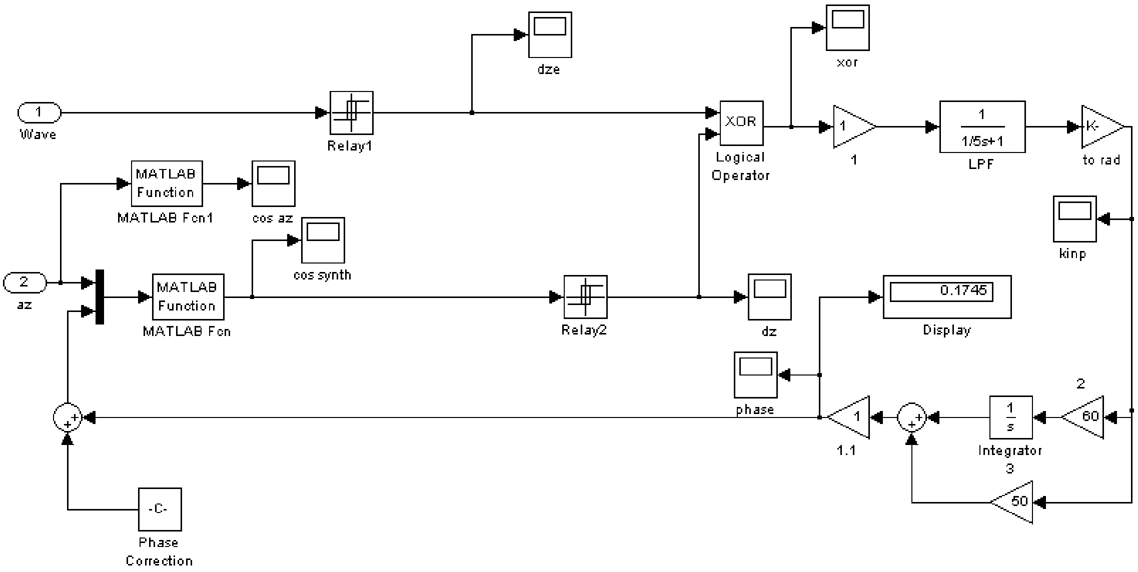

Figure 6.13: The Simulink model used to calculate α_e.

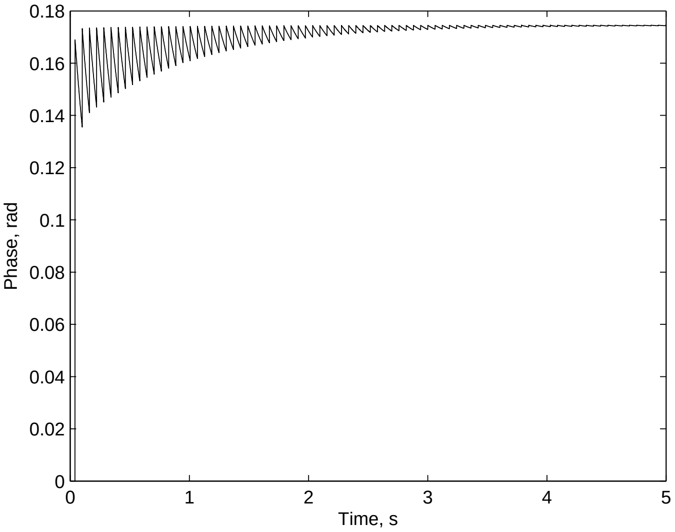

Figure 6.14: The PI controller converging to the correct phase difference.

6.3 Estimation

6.3.1 Kalman Filter

The rate of translation is required to be known if the static mass imbalance of the rotor is to be estimated or counteracted. Differentiating the positions from the eddy current sensors would differentiate the position and the noise from the sensors. A better solution is to use a Kalman Filter, which tracks the underlying translation rate and filters the noise at each sample.

To form the Kalman Filter a state space model is built with the state variables:

$$\mathbf{q} = \begin{bmatrix} q_1 \\ q_2 \\ q_3 \\ q_4 \end{bmatrix} = \begin{bmatrix} x \\ y \\ \dot{x} \\ \dot{y} \end{bmatrix} \tag{6.61}$$

The outputs are:

$$\mathbf{p} = \begin{bmatrix} x \\ y \end{bmatrix} \tag{6.62}$$

And the inputs are:

$$\mathbf{u} = \begin{bmatrix} F_x \\ F_y \end{bmatrix} \tag{6.63}$$

where F are the forces that the electromagnets are commanded to generate by the controller. From the translational dynamics of the rotor:

$$\dot{\mathbf{q}} = \begin{bmatrix} q_3 \\ q_4 \\ 0 \\ 0 \end{bmatrix} + \begin{bmatrix} 0 \\ 0 \\ M^{-1}F_x \\ M^{-1}F_y \end{bmatrix} \tag{6.64}$$

The complete state space model has the form:

$$\begin{aligned} \dot{\mathbf{q}} &= \mathbf{A}\mathbf{q} + \mathbf{B}\mathbf{u} \\ \mathbf{p} &= \mathbf{C}\mathbf{q} \end{aligned} \tag{6.65}$$

Therefore:

$$\begin{aligned}
\mathbf{A} &= \begin{bmatrix} 0 & 0 & 1 & 0 \\ 0 & 0 & 0 & 1 \\ 0 & 0 & 0 & 0 \\ 0 & 0 & 0 & 0 \end{bmatrix} \qquad (6.66) \\
\mathbf{B} &= \begin{bmatrix} 0 & 0 \\ 0 & 0 \\ M^{-1} & 0 \\ 0 & M^{-1} \end{bmatrix} \\
\mathbf{C} &= \begin{bmatrix} 1 & 0 & 0 & 0 \\ 0 & 1 & 0 & 0 \end{bmatrix}
\end{aligned}$$

The iterative procedure for implementing the Kalman estimator is [81]:

1. Form the state transition matrix:

$$\mathbf{\Phi}(t_k) = e^{\mathbf{AT}} \tag{6.67}$$

where $\mathbf{T}$ is the sampling period in seconds.

2. Predict the covariance $\bar{\mathbf{P}}$ and the state variable $\bar{\mathbf{q}}$ [58]:

$$\begin{aligned}
\bar{\mathbf{P}}_{k+1} &= \mathbf{\Phi}(t_k)\tilde{\mathbf{P}}_k\mathbf{\Phi}(t_k)^T + \mathbf{Q} \qquad (6.68) \\
\bar{\mathbf{q}}_{k+1} &= e^{\mathbf{AT}}\tilde{\mathbf{q}}_k + \int_0^T e^{\mathbf{A}\tau} d\tau \mathbf{B}\mathbf{u}_k \qquad (6.69)
\end{aligned}$$

where $\mathbf{Q}$ is an estimate of the noise and is a 4×4 diagonal matrix, with each of the values on the diagonal initially being 10^{-4}.

3. Calculate the Kalman gain:

$$\mathbf{K}_{k+1} = \bar{\mathbf{P}}_{k+1}\mathbf{C}^T(\mathbf{C}\bar{\mathbf{P}}_{k+1}\mathbf{C}^T + \mathbf{W})^{-1} \tag{6.70}$$

where $\mathbf{W}$ is an estimate of the measurement noise and is a 2×2 diagonal matrix, with each of the values on the diagonal initially being 10^{-4}.

4. Update the state estimate:

$$\tilde{\mathbf{q}}_{k+1} = \bar{\mathbf{q}}_{k+1} + \mathbf{K}_{k+1}(\mathbf{y}_{k+1} - \mathbf{C}\bar{\mathbf{q}}_{k+1}) \tag{6.71}$$

5. Update the error covariance estimate:

$$\tilde{\mathbf{P}}_{k+1} = \bar{\mathbf{P}}_{k+1} - \mathbf{K}_{k+1}\mathbf{C}\bar{\mathbf{P}}_{k+1} \tag{6.72}$$

This iterative process can be implemented as a block diagram as shown in Figure 6.15.

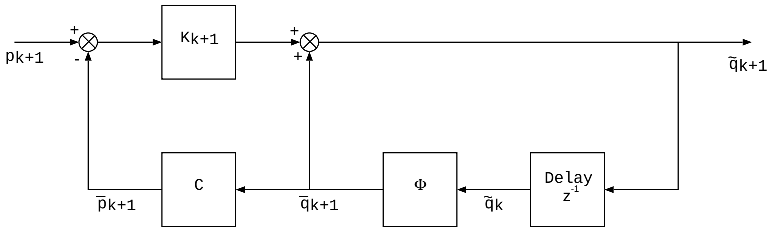

Figure 6.15: The implementation of the Kalman estimator in block diagram form.

6.3.2 Extended Kalman Filter

For linear systems the Kalman Filter introduced above uses the state transition matrix $\mathbf{\Phi}(t_k)$ to propagate the state and the covariance to the next time interval. For non-linear problems either the Linearised Kalman Filter or the Extended Kalman Filter are required. The Linearised Kalman Filter uses a linearised form of the system's dynamics to propagate a small deviation in the state variables to the next time period. For "highly" non-linear systems the Linearised Kalman Filter can diverge from the true state. The Extended Kalman Filter (EKF) uses a hybrid architecture with a continuous integration of the non-linear dynamics for the state propagation. The discrete computation of the covariance is retained. The Extended Kalman Filter is necessary to calculate the rate of rotation of the rotor.

The state $\mathbf{q}$ is:

$$\mathbf{q} = \left[\begin{array}{ccccc} \phi & \theta & \dot{\alpha}_x & \dot{\alpha}_y & \dot{\alpha}_z \end{array} \right]^T \tag{6.73}$$

The measured values $\mathbf{p}$ are:

$$\mathbf{p} = \left[\begin{array}{ccc} \phi & \theta & \dot{\alpha}_z \end{array} \right]^T \tag{6.74}$$

The inputs to the system $\mathbf{u}$ are:

$$\mathbf{u} = \left[\begin{array}{ccc} T_x & T_y & T_z \end{array} \right]^T = \mathbf{T} \tag{6.75}$$

which can be found from the controller output currents, the air gap widths and the kinematic mapping equations.

The dynamic equation of rotational motion is given by:

$$\ddot{\boldsymbol{\alpha}} = \mathbf{I}^{-1}(\mathbf{T} - \dot{\boldsymbol{\alpha}} \times \mathbf{I}\dot{\boldsymbol{\alpha}}) \tag{6.76}$$

The update function $f(\mathbf{q}, t)$ is given by:

$$\begin{aligned} f(\mathbf{q}, t) &= \dot{\mathbf{q}} \\ &= \left[\begin{array}{ccccc} \dot{\phi} & \dot{\theta} & \ddot{\alpha}_x & \ddot{\alpha}_y & \ddot{\alpha}_z \end{array} \right]^T \end{aligned} \tag{6.77}$$

Equation 6.76 provides rows 3 to 5 of Equation 6.77. The kinematic differential equations of motion provide rows 1 and 2:

$$\begin{bmatrix} \dot{\phi} \\ \dot{\theta} \\ \dot{\psi} \end{bmatrix} = \frac{1}{c\theta} \begin{bmatrix} c\theta & s\phi s\theta & c\phi s\theta \\ 0 & c\phi c\theta & -s\phi c\theta \\ 0 & s\phi & c\phi \end{bmatrix} \begin{bmatrix} \dot{\alpha}_x \\ \dot{\alpha}_y \\ \dot{\alpha}_z \end{bmatrix} \tag{6.78}$$

The iterative procedure for each time step of the Extended Kalman Filter is [82]:

1. Propagate the state:

$$\bar{\mathbf{q}}_{k+1} = \tilde{\mathbf{q}}_k + \int_{t_k}^{t_{k+1}} f(\tilde{\mathbf{q}}_k, \tau) d\tau \tag{6.79}$$

where in the Simulink implementation of the Filter, the integration is performed with a first order Euler integrator. To find the curve $y(x)$ given the function $y' = y'(x, y)$ the following integral is evaluated given that the starting value $y_0 = y(x_0)$ is known:

$$y(x_0 + d) = y(x_0) + \int_{x_0}^{x_0+d} y' dx \tag{6.80}$$

For the first order Euler method the integral is replaced by the area of a rectangle [83]:

$$y(x_0 + d) \approx y(x_o) + dy'(x_0, y_0) \tag{6.81}$$

2. Linearise around the last estimate:

$$\mathbf{A} = \left. \frac{\partial f(\mathbf{q}, t)}{\partial \mathbf{q}} \right|_{\mathbf{q}=\tilde{\mathbf{q}}_k} \tag{6.82}$$

A can be formed by analytically differentiating f with respect to $\mathbf{q}$ in advance and then substituting in the values of $\tilde{\mathbf{q}}_k$ at every time step.

3. Derive the state transition matrix by numerical integration:

$$\dot{\mathbf{\Phi}}(t_{k+1}, t_k) = \mathbf{A}\mathbf{\Phi}(t_{k+1}, t_k) \tag{6.83}$$

Therefore:

$$\mathbf{\Phi}(t_0, t_0) = I \tag{6.84}$$

and:

$$\mathbf{\Phi}(t_{k+1}, t_k) \approx I + \mathbf{A}\triangle t + \frac{1}{2}\mathbf{A}^2 \triangle t^2 + \ldots \tag{6.85}$$

where I is the identity matrix.

4. Propagate the covariance:

$$\bar{\mathbf{P}}_{k+1} = \mathbf{\Phi}(t_{k+1}, t_k)\tilde{\mathbf{P}}\mathbf{\Phi}(t_{k+1}, t_k)^T + \mathbf{Q} \tag{6.86}$$

where $\mathbf{Q}$ is an estimate of the noise and is a 5×5 diagonal matrix, with each of the values on the diagonal initially being 10^{-4}.

5. Calculate the Kalman gain:

$$\mathbf{K}_{k+1} = \bar{\mathbf{P}}_{k+1}\mathbf{C}_{k+1}^T(\mathbf{C}_{k+1}\bar{\mathbf{P}}_{k+1}\mathbf{C}_{k+1}^T + \mathbf{W}_{k+1})^{-1} \tag{6.87}$$

where $\mathbf{W}$ is an estimate of the noise and is a 3×3 diagonal matrix, with each of the values on the diagonal initially being 10^{-4}.

6. Update the state estimate:

$$\tilde{\mathbf{q}}_{k+1} = \bar{\mathbf{q}}_{k+1} + \mathbf{K}_{k+1}(\mathbf{y}_{k+1} - \mathbf{C}_{k+1}\bar{\mathbf{q}}_{k+1}) \tag{6.88}$$

7. Update the error covariance estimate:

$$\tilde{\mathbf{P}}_{k+1} = \bar{\mathbf{P}}_{k+1} - \mathbf{K}_{k+1}\mathbf{C}_{k+1}\bar{\mathbf{P}}_{k+1} \tag{6.89}$$

6.3.3 Kalman Filter Tuning

To obtain the best performance from the linear and extended Kalman filters, the noise estimates $\mathbf{Q}$ and $\mathbf{W}$ need to be tuned. Convergence of the filter can be measured by looking at the diagonal terms in the covariance matrix; smaller terms show a good convergence of the estimated value. The linear Kalman filter is relatively simple. Because the x and y axes have the same dynamics, there are only three different values in $\mathbf{Q}$ and $\mathbf{W}$ that need to be chosen. It was found to be relatively simple to modify one value at a time and view its effect on the covariance. The final values chosen were:

$$\mathbf{Q_{lin}} = \begin{bmatrix} 10^{-8} & 0 & 0 & 0 \\ 0 & 10^{-8} & 0 & 0 \\ 0 & 0 & 10^{-4} & 0 \\ 0 & 0 & 0 & 10^{-4} \end{bmatrix}, \mathbf{W_{lin}} = \begin{bmatrix} 10^{-8} & 0 \\ 0 & 10^{-8} \end{bmatrix} \tag{6.90}$$

There is less symmetry in the EKF noise matrices; five values need to be chosen. It was attempted to tune them by hand, but the values were interdependent and so a good final solution could not be found. Values that allowed the filter to converge when presented with simulation data were found, but the filter failed to converge when implemented in hardware with real world noise and dynamics. An alternative method to find $\mathbf{Q}$ and $\mathbf{W}$ was developed.

The hardware was run using a tuned controller and currents, positions and spin rate data were recorded for 10 seconds. The kinematic mapping equation was used to calculate the torque applied to the rotor from the recorded currents. A Simulink implementation of the EKF was taken. The recorded values of ϕ, θ and $\dot{\alpha}_z$ and torque were applied to the implementation. The model was run repeatedly with each of the diagonal elements of the five unique members of $\mathbf{Q}$ and $\mathbf{W}$ being tried with values 10^{-1}, 10^{-2}, 10^{-4}, 10^{-6} and 10^{-8}, requiring $5^5 = 3125$ simulations of the EKF. The covariance matrix was recorded at the end of each simulation and the set of $\mathbf{Q}$ and $\mathbf{W}$ elements that produced the smallest diagonal variance entries in the covariance matrix were chosen to initialise the EKF with. The final chosen values were:

$$\mathbf{Q_{EKF}} = \begin{bmatrix} 10^{-8} & 0 & 0 & 0 & 0 \\ 0 & 10^{-8} & 0 & 0 & 0 \\ 0 & 0 & 10^{-4} & 0 & 0 \\ 0 & 0 & 0 & 10^{-4} & 0 \\ 0 & 0 & 0 & 0 & 10^{-6} \end{bmatrix}, \mathbf{W_{EKF}} = \begin{bmatrix} 10^{-8} & 0 & 0 \\ 0 & 10^{-8} & 0 \\ 0 & 0 & 10^{-8} \end{bmatrix} \tag{6.91}$$

This brute force approach to tuning the filter took only several hours on a modern PC. It is similar to a Monte Carlo search, which could be used to further refine the choice of values for $\mathbf{Q}$ and $\mathbf{W}$.

6.4 Conclusions

Linearised and non-linear analytical models of the 3Dwheel's dynamic translational and rotational motion have been derived. The models show that the rotor's motion will be unstable in open-loop. Results from these models are therefore presented in the next Chapter after closed-loop controllers to stabilise the rotor's levitation and motion have been derived.

Real world rotors will not have their mass distributed evenly throughout them and so will exhibit mass imbalance. The two types of mass imbalance have been discussed here and their effect on the rotor's motion described. A technique to estimate a rotor's static imbalance has been presented here.

The sensors used to measure the rotor's position provide only the position. It is often necessary to know the rotor's translational or rotational rate. Differentiating the position output by the sensors will also differentiate the noise. A better technique is to use estimation techniques to calculate the rates based upon knowledge of the rotor's dynamics. Linear and Extended Kalman filters have been presented to calculate the rotor's translational and dynamic rates respectively. A technique to tune the Kalman filter for the dynamics of the hardware has been presented.

Chapter 7

Levitation Stabilisation and Results

In the previous Chapters a complex model of the interaction between the electromagnets and the rotor dynamics was developed. In order to stabilise the levitation of the rotor and make the 3Dwheel operate a feedback controller is required. Four different controllers will be presented here along with results from testing them with the non-linear simulation and on the 3Dwheel hardware in the laboratory. The controllers allowed the hardware to be successfully levitated and generate 3-axis output torques.

Chapter 3 described the magnetic behaviour of the 3Dwheel and the forces that the electromagnets exert on the rotor. Chapter 6 described the dynamic motion of the rotor when these forces acted upon it. This Chapter brings these together, to derive the controllers necessary to calculate the currents required through each electromagnet to make it move in the desired manner. Current control is necessary as it is the current in the reluctance force equation that determines the force generated by an electromagnet.

7.1 Decoupled Lead Lag Controller

The decoupled lead lag controller is the simplest of the controllers developed for the 3Dwheel. Lead lag controllers or compensators use a combination of proportional, derivative and integral terms to achieve the desired frequency response. A lead lag controller was chosen as it was the control technique that there was the most existing familiarity with.

Separate single-input single-output lead lag controllers are developed for both translation and rotation axes. The kinematic mapping equations are then used to convert the translation and rotation current demands into the current through each electromagnet coil.

7.1.1 Theory

From the linearised transfer function for translational motion, Equation 6.43, substituting $s = j\omega$:

$$\begin{aligned} G_x(j\omega) &= \frac{4K_i/M}{(j\omega)^2 - 4K_\gamma/M} \\ &= \frac{4K_i/M}{-\omega^2 - 4K_\gamma/M} \\ &= -\frac{4K_i/M}{\omega^2 + 4K_\gamma/M} \end{aligned} \tag{7.1}$$

The magnitude of this function is:

$$\begin{aligned} |G_x(j\omega)| &= \sqrt{\mathrm{Re}^2 + \mathrm{Im}^2} \\ &= \sqrt{\left(\frac{4K_i/M}{-\omega^2 - 4K_\gamma/M}\right)^2} \\ &= \frac{4K_i/M}{\omega^2 + 4K_\gamma/M} \end{aligned} \tag{7.2}$$

Using a lead-lag compensator with a cross-over frequency ω_c of 100 rads^{-1} and a phase margin of 55°. Assume a constant gain across all frequencies so that $K_x(j\omega) = K_x$ then:

$$\begin{aligned} |K_x G_x(j\omega = \omega_c)| &= K_x \frac{4K_i/M}{\omega_c^2 + 4K_\gamma M} = 1 \\ K_x &= \frac{\omega_c^2 + 4K_\gamma/M}{4K_i/M} \end{aligned} \tag{7.3}$$

A lead compensator of the form below is added to improve the phase margin:

$$K_{Lx} = \frac{1}{\beta} \frac{s + \omega_L}{s + \omega_L/\beta} \tag{7.4}$$

where $\beta = 0.1$ is known to give 55° of phase margin. The corner frequency ω_L is computed from the cross-over frequency to give the maximum phase lead at the cross-over frequency $\omega_L = \sqrt{\beta}\omega_c$. The lead compensator contributes to a gain loss of $1/\sqrt{\beta}$ and so the previously calculated value of K is multiplied by $\sqrt{\beta}$ to compensate for this:

$$K_{Lx} = \frac{K_x\sqrt{\beta}}{\beta} \frac{s + \omega_L}{s + \omega_L/\beta} \tag{7.5}$$

A lag term is added to add integral action to the controller to remove steady state error:

$$K_{int}(s) = \frac{s + \omega_{lag}}{s} \tag{7.6}$$

where ω_{lag} is the corner frequency of the lag component in rads^{-1}.

Similarly for the rotation controller:

$$\begin{aligned} G_{\alpha y}(j\omega) &= \frac{4r_T K_i/I_{yy}}{(j\omega)^2 - 4r_T^2 K_\gamma/I_{yy}} \\ &= \frac{4r_T K_i/I_{yy}}{-\omega^2 - 4r_T^2 K_\gamma/I_{yy}} \\ &= -\frac{4r_T K_i/I_{yy}}{\omega^2 + 4r_T^2 K_\gamma/I_{yy}} \end{aligned} \tag{7.7}$$

$$\begin{aligned} |G_{\alpha y}(j\omega)| &= \sqrt{\mathrm{Re}^2 + \mathrm{Im}^2} \\ &= \frac{4r_T K_i/I_{yy}}{\omega^2 + 4r_T^2 K_\gamma/I_{yy}} \end{aligned} \tag{7.8}$$

$$\begin{aligned} |K_{\alpha y} G_{\alpha y}(j\omega = \omega_c)| &= K_{\alpha y} \frac{4r_T K_i/I_{yy}}{\omega_c^2 + 4r_T^2 K_\gamma/I_{yy}} = 1 \\ K_{\alpha y} &= \frac{\omega_c^2 + 4r_T^2 K_\gamma/I_{yy}}{4r_T K_i/I_{yy}} \end{aligned} \tag{7.9}$$

Controller Discretization

For implementation in software on the real-time operating system a discrete controller is required with a fixed time sampling period. Matlab provides functions to discretize continuous systems with a choice of several different algorithms. Figure 7.1 shows a continuous controller and the same controller discretized using the Tustin [84] and First Order Hold [85] methods, both with a sampling period of 1.0 ms. The Tustin method had given good results on a previous project and was used initially. At higher bias currents it tended to result in an unstable system. Looking at the phase of the two methods it can be seen that the First Order Hold method more closely matches the continuous controller at frequencies approaching the Nyquist frequency. Controllers discretized with the First Order Hold method proved the most stable when used with the experimental hardware.

The discrete controller was implemented as a discrete state space controller. Figure 7.2 shows the controller form used, which implements the discrete state space equations:

$$\begin{aligned} \mathbf{q}(k+1) &= \mathbf{A}\mathbf{q}(k) + \mathbf{B}\mathbf{u}(k) \\ \mathbf{p}(k) &= \mathbf{C}\mathbf{q}(k) + \mathbf{D}\mathbf{u}(k) \end{aligned} \tag{7.10}$$

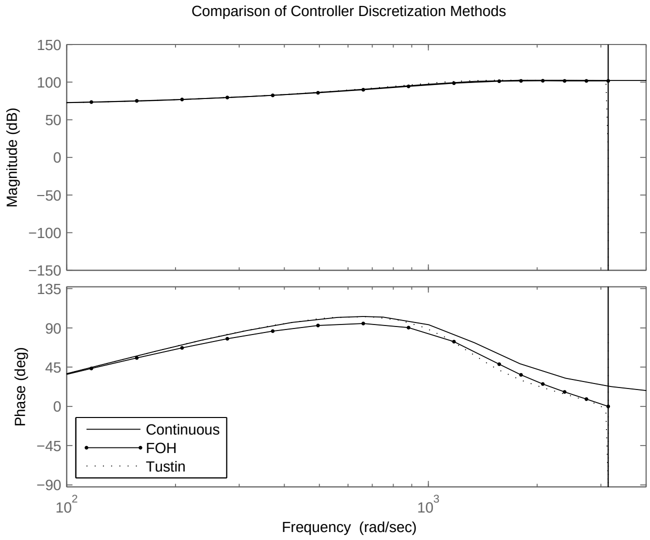

Figure 7.1: A comparison of the Tustin and First Order Hold (FOH) discretization methods with the continuous controller.

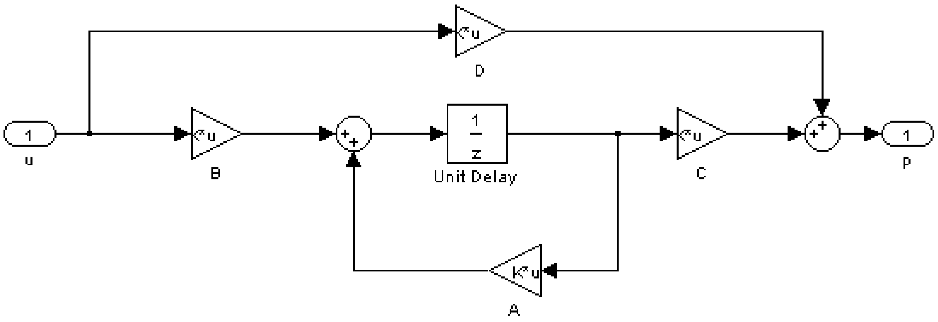

Figure 7.2: The implementation of the controller in Simulink in a discrete state space form.

Controller Implementation

The two translation, two rotation current demands calculated by the controllers and the bias current are converted to eight current demands by combining the kinematic mapping equations, Equations 6.21 and 6.22, and taking the pseudo-inverse:

$$\begin{bmatrix} \hat{i}_1 \\ \hat{i}_2 \\ \hat{i}_3 \\ \hat{i}_4 \\ \hat{i}_5 \\ \hat{i}_6 \\ \hat{i}_7 \\ \hat{i}_8 \end{bmatrix} = \begin{bmatrix} 1 & 0 & 0 & 1 & 1 \\ 1 & 0 & 0 & -1 & 1 \\ 0 & 1 & -1 & 0 & 1 \\ 0 & 1 & 1 & 0 & 1 \\ -1 & 0 & 0 & -1 & 1 \\ -1 & 0 & 0 & 1 & 1 \\ 0 & -1 & 1 & 0 & 1 \\ 0 & -1 & -1 & 0 & 1 \end{bmatrix} \begin{bmatrix} \hat{i}_x \\ \hat{i}_y \\ \hat{i}_{\alpha x} \\ \hat{i}_{\alpha y} \\ i_0 \end{bmatrix} \tag{7.11}$$

Where $\hat{i_x}$ and $\hat{i_y}$ are the demanded currents along the two translation axes, $\hat{i_{\alpha x}}$ and $\hat{i_{\alpha y}}$ are the demanded currents about the two rotation axes and i_0 is the bias current.

7.1.2 Simulation Results

N	100 turns
ε	8.0 mm
l	50.0 mm
γ_0	1.4 mm
i_0	3.0 A
M	1.301 kg
I_{yy}	0.001594 kgm^2
r_T	16 mm
K_i	1.28 NA^{-1}
K_γ	916.0 Nm^{-1}
β	0.01
ω_c	100 rads^{-1}

Table 7.1: The values used to generate the lead-lag controller for the 3Dwheel hardware.

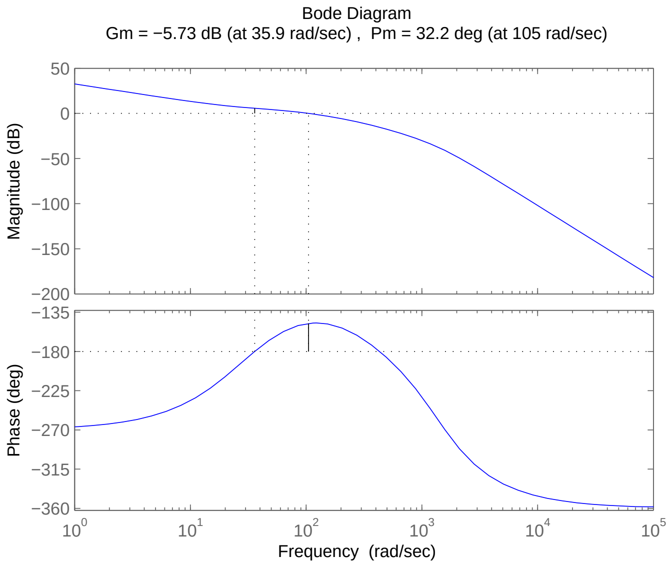

Figure 7.3: The frequency response of the linearised decoupled translation model, controller and electromagnet dynamics.

The controller was implemented using the values given in Table 7.1. ω_c and β were tuned manually for best performance. Figure 7.3 shows the frequency response of the linearised translational dynamics, decoupled lead-lag translation controller and second order electromagnet dynamics. Figure 7.4 shows the equivalent for rotational motion. The translational system has a cross-over frequency of 32° at 105 rads^{-1} and the rotational system 32° at 104 rads^{-1}. Figure 7.5 shows the rotor being tilted through 30 mrad in a non-linear simulation by this lead

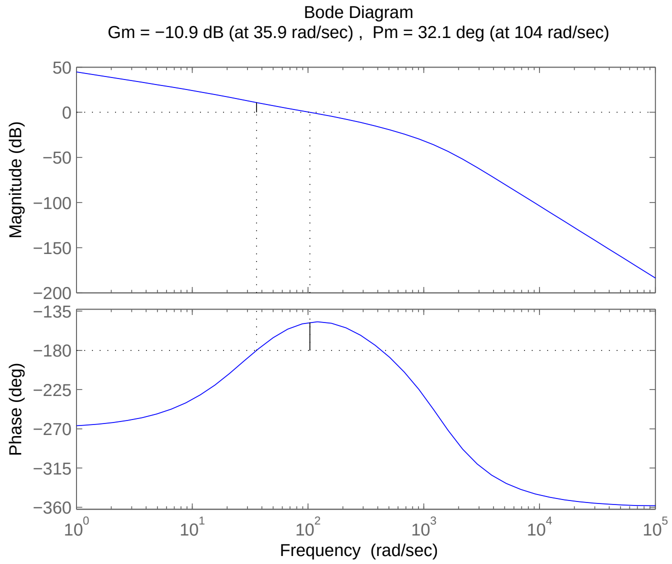

Figure 7.4: The frequency response of the linearised decoupled rotational model, controller and electromagnet dynamics.

lag controller. The controller had been designed for a linearised system dynamics but was here being tested on a non-linear model. The controller was tuned for the dynamics of the hardware rather than the non-linear simulation. When it was observed that this lead lag controller could stabilise the non-linear simulation, effort was concentrated on testing the controller with the engineering model hardware, hence the 31% overshoot in Figure 7.5. Development work was stopped on the simulation of the system when the controllers were capable of levitating the hardware.

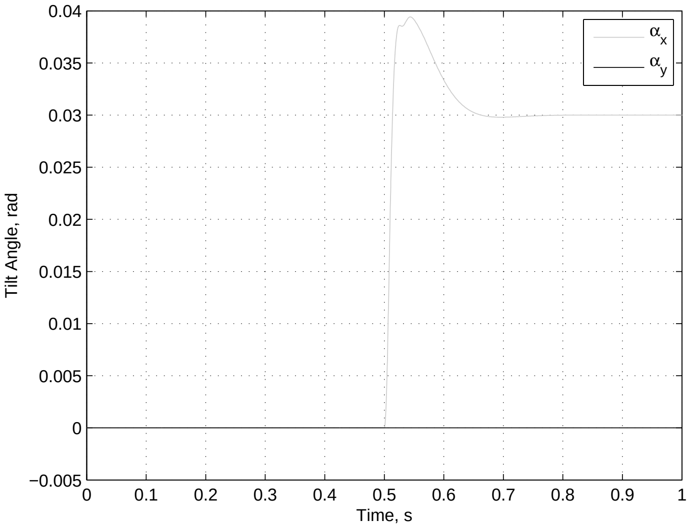

Figure 7.5: The decoupled lead lag controller tilting the rotor through 30 mrad in a non-linear simulation.

7.1.3 Experimental Results

An iterative procedure of changing the controller values of β, ω_c and ω_{lag} and then the loop gains in the translation and rotation loops to stabilise the system, before trying new controller values was used to obtain the most stable levitation of the 3Dwheel. The initial values used were those from the simulation.

When there was stable levitation the Digital Signal Analyser (DSA) tool was used to measure the frequency response of the translation and rotation loops. Initially $\omega_c = 100$ rads^{-1} and the phase margin at the cross-over frequency of around 270 rads^{-1} was low. ω_c was increased to 270 rads^{-1} to maximise the phase margin at the cross-over frequency. Finally, the loop gains were modified to give the maximum phase margin at the cross-over frequency.

The transfer function of the anti-aliasing filters is given by:

$$G_{AA} = \frac{1}{R_1Cs+1}\frac{1}{R_2Cs+1} \tag{7.12}$$

where the resistor and capacitor values were the ones fitted to the system at the time: $C =$ 100 nF, $R_1 = R_2 = 3.3$ kΩ to give a cut-ff frequency of 3030 rads^{-1}. The electromagnet dynamics were initially assumed to be:

$$G_{EM} = \frac{1}{Ls+R_{EM}} \tag{7.13}$$

The resistance and inductance of the wound electromagnets were measured and the average of the eight was found to be $R_{EM} = 0.906$ Ω and $L = 2.755$ mH.

The frequency response of system of the mechanical and electrical plant dynamics, anti-aliasing filter and the controller were compared with the response measured by DSA. An additional low-pass filter with a cut-off of $\omega_{LPF} = 600$ rads^{-1} was needed to obtain a close match:

$$G_{LPF}(s) = \frac{-1}{s/\omega_{LPF}+1} \tag{7.14}$$

The source of this low pass filter is unknown. It was found that the simulated response could be matched more closely, and with less effort, to the measured response by replacing the electromagnet dynamics and low pass filter with a single second order filter:

$$G_{match} = \frac{K_{match}}{\omega_n^{-2}s^2+(2\zeta/\omega_n)s+1} \tag{7.15}$$

The best match was given by $\omega_n = 1400$ rads^{-1}, $K_{match} = 1$ and $\zeta = 0.78$.

The final values used in the controller are shown in Table 7.2. Figures 7.6 and 7.7 show the final frequency responses of the hardware in the laboratory. The theoretical response was the loop response generated by the product of the mechanical part shown in Equation 6.43, together with the transfer functions of the anti-aliasing filters and the electromagnet part. The translation controller has a phase margin of 7° at the crossover frequency of 465 rads^{-1} and the rotation controller has a phase margin of 35° at the crossover frequency of 213 rads^{-1}. The translation controller's poor phase margin is due to its flat gain response; the cross-over frequency cannot be easily moved to the peak of the phase because of the flat magnitude. The 7° of phase margin for the translation controller means that the translation axis will only just be stable and external disturbances may cause stable levitation of the rotor to be lost.

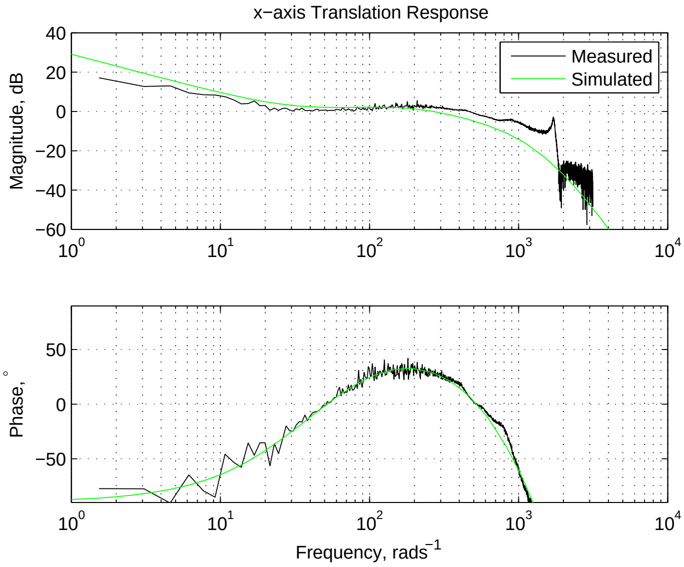

Figure 7.6: The measured (black) and theoretical (green) frequency response of the x-axis translation system with the decoupled lead-lag controller and the engineering model hardware.

β	0.06
ω_c	270 rads^{-1}
ω_{lag}	270 rads^{-1}

Table 7.2: The controller values used in the decoupled lead-lag compensator for implementation on the hardware.

The noise in translation was around 1-bit of the analogue input card, about 2.4 μm, as shown in Figure 7.8. The bias current used at this point was 1.0 A. The rotor had a tendency to oscillate axially when disturbed. Increasing the bias current to 2.4 A increased the passive axial stiffness of the electromagnets and prevented these oscillations. However, the increase in bias current, increased the gain of the system and the noise in the translation direction increased to greater than 10 μm as shown in Figure 7.9. However, the performance of the system at both bias currents is good with the rotor being able to be levitated with a high precision and with low noise.

To improve the noise performance, the cut-off frequency of anti-aliasing filter at the output of the PC was dropped from 3030 rads^{-1} to 455 rads^{-1} by changing R_2 to 22 kΩ. A first order RC low pass filter has $45°$ of phase loss at its cut-off frequency. Bringing the cut-off frequency closer to the system's cross-over frequency decreases the phase margin at the cross-over frequency. In this case the phase loss from the anti-aliasing filter makes the system with the decoupled first-order lead lag compensator unstable because of its low phase margin at its

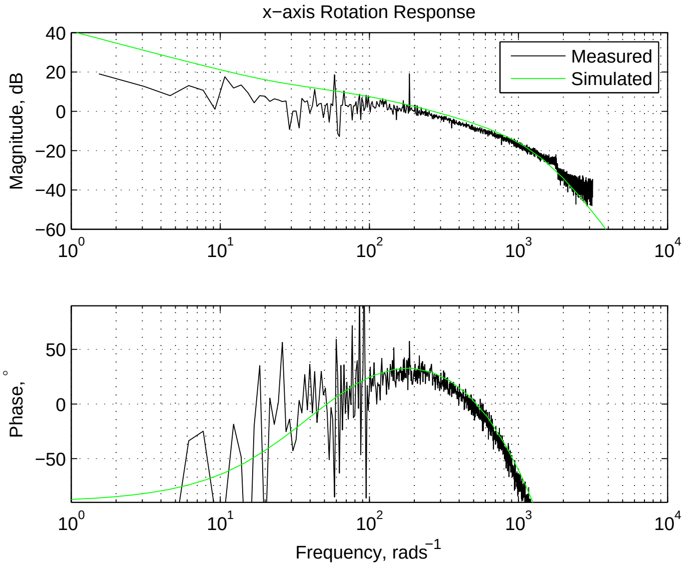

Figure 7.7: The measured (black) and theoretical (green) frequency response of the x-axis rotation system with the decoupled lead-lag controller and the engineering model hardware.

cross-over frequency. Tuning a second-order lead lag controller by hand is difficult. It was therefore decided to automatically generate the decoupled controller using the $H\infty$ method to generate enough phase margin at the system's cross-over frequency to have a stable system. The decoupled $H\infty$ controller is discussed in the next Section.

7.1.4 Conclusions

The simplest form of controller used on the 3Dwheel, the decoupled lead lag controller, was able to stably levitate the 3Dwheel hardware's rotor. The lead lag controller was a first order controller, which offered limited possibilities to shape the system's frequency response. The translation axis of the system had a very flat frequency response which only allowed a phase margin of 7° at the crossover frequency and so was unlikely to stay stable under large external disturbances. It was therefore decided to use a second order decoupled controller that was tuned using the $H\infty$ method rather than the first order lead lag controller.

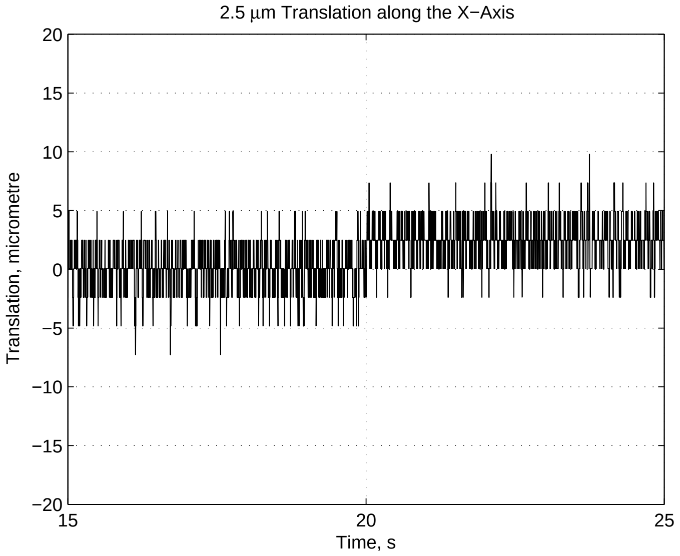

Figure 7.8: The response of the hardware to a 2.5 μm translation step command along the x-axis using a bias current of 1.0 A.

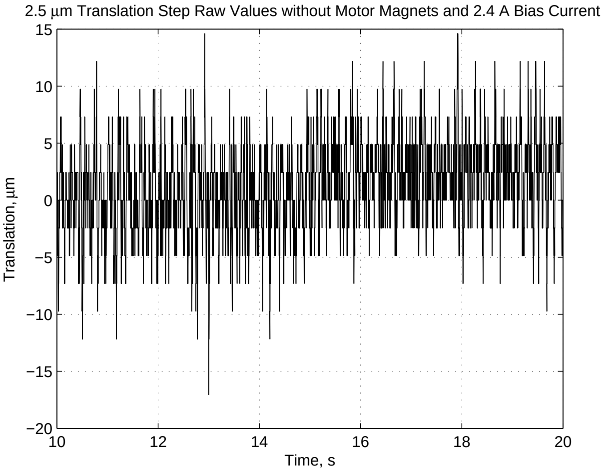

Figure 7.9: The response of the hardware to a 2.5 μm translation step command along the x-axis using a bias current of 2.4 A.

7.2 H∞ Decoupled Controller

The decoupled controllers generated so far have the benefit of simplifying the control problem; as there is no coupling between translational and rotational motion, then using a multi-variable controller would add additional complexity to the problem. The decoupled controllers allow the loop gains of each channel to be manually tuned if there is any uncertainty in the plant dynamics. However decoupled controllers make it difficult to compensate for coupling between axes, such as in the rotational dynamics, which have been treated as a disturbance so far.

The H∞ sensitivity minimisation technique can be used to automatically tune the decoupled controllers. Controllers with a higher order possible with the lead lag method can easily be generated with H∞ sensitivity minimisation, while keeping the simplicity of the decoupled controller.

7.2.1 Theory

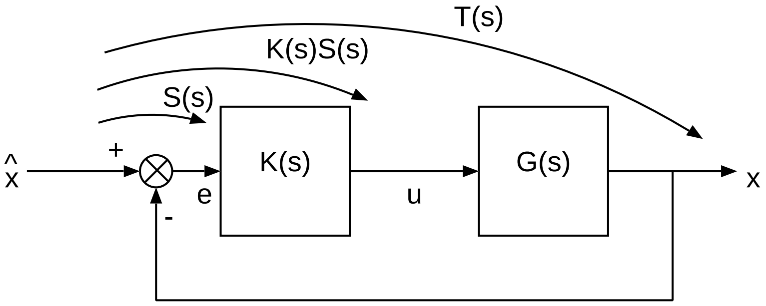

Figure 7.10: The plant and controller structure.

Figure 7.10 shows a simple closed loop system. $G(s)$ contains the plant dynamics expressed in the Laplace domain and $K(s)$ is the controller. The measured output x is negatively feed back to calculate the error e from the desired output $\hat{x}$. The sensitivity transfer function is defined as:

$$S(s) = \frac{e}{\hat{x}} \tag{7.16}$$

The loop transfer function $L(s)$ is defined as:

$$L(s) = K(s)G(s) \tag{7.17}$$

The complimentary transfer function $T(s)$ is then:

$$T(s) = \frac{L(s)}{1 + L(s)} = L(s)S(s) \tag{7.18}$$

where the sensitivity transfer function can also be written as:

$$S(s) = \frac{1}{1 + L(s)} \tag{7.19}$$

The sensitivity transfer function describes the system's rejection of disturbances and the complimentary transfer function its ability to track the input.

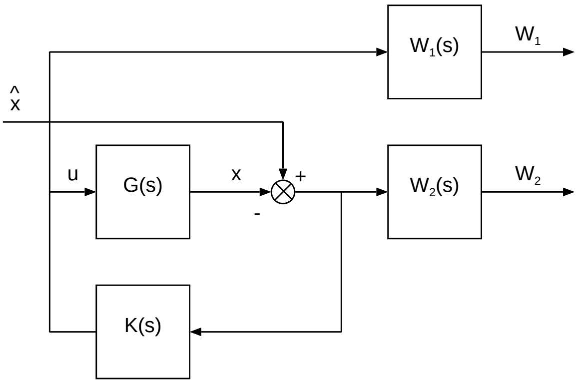

Figure 7.11: The decoupled H∞ controller synthesis structure.

Figure 7.11 shows the structure used to synthesize the decoupled H∞ controllers [86]. W_1 is a weighting function that limits the controller action. The W_2 weighting function determines the system's sensitivity transfer function.

The H∞ method tries to minimise the controller down onto the weighting functions:

$$\left\| \begin{array}{c} W_2 S(s) \\ W_1 K(s) S(s) \end{array} \right\|_{\infty} \tag{7.20}$$

The H∞ synthesis tool indicates the achieved H∞ cost γ. γ can be converted to decibels using: $20\log_{10}(\gamma)$. The value in decibels indicates the overshoot above 0 dB of the sensitivity transfer function in the generated system over the requested sensitivity transfer function. Hence the γ value provides an indication of how successful the controller synthesis was.

7.2.2 Implementation

The mechanical plant dynamics from Equations 6.43 and 6.48 were combined with the electromagnet dynamics in Equation 7.15 and the anti-aliasing filter dynamics from Equation 7.12. An H∞ controller to levitate the 3Dwheel hardware was then synthesised for this using weighting functions:

$$W_1 = 10^{-5} \tag{7.21}$$

$$W_2 = \frac{s + 50}{s + 10^{-4}} \tag{7.22}$$

The values of the weighting functions were tuned manually to give the best performance from the hardware in the laboratory. The bias current was set to 2.4 A and after tuning the loop gain, the rotor was stably levitated. The DSA tool was then run and a good match between the measured loop response and the theoretical model was achieved when the electromagnet dynamics were $\omega_n = 3600$ rads^{-1}, $K_{match} = 1$ and $\zeta = 0.8$ for translation and $\omega_n = 600$ rads^{-1}, $K_{match} = 1$ and $\zeta = 0.8$ for rotation . The controller was synthesised again for these plant dynamics. The frequency responses are shown in Figures 7.12 and 7.13. When choosing the second-order electromagnet parameters the aim was to achieve a good match between the phase rather than the magnitude of the measured and theoretical frequency responses. Effort was concentrated on the rotation controller where both the phase and magnitude matched, while still giving a good match on the phase of the translation controller. The phase responses match well. The match between the magnitude responses is poor, particularly at low frequencies. The translation controller has a phase margin of 34° at a crossover frequency of 385 rads^{-1} and the rotation controller has a phase margin of 41° at a frequency of 121 rads^{-1}. These compare with 32° of phase margin for both the rotation and translation lead lag controllers in simulation, demonstrating that the second order controller generated by the decoupled H∞ has an improved performance.

The final synthesised translation controller is:

$$\begin{aligned} K_x(s) = {} & \frac{89749359200(s+3030)(s+454.5)}{(s+6.94\times10^5)(s+3352)(s+0.0001)} \cdots \\ & \cdots \frac{(s+127.4)(s+16.04)(s^2+5760s+1.296\times10^7)}{(s^2+1424s+1.96\times10^6)(s^2+5890s+1.369\times10^7)} \end{aligned} \tag{7.23}$$

and rotation:

$$\begin{aligned} K_\alpha(s) = {} & \frac{2245995927(s+3030)(s+454.5)}{(s+4.11\times10^4)(s+4733)(s+0.0001)} \cdots \\ & \cdots \frac{(s+58.2)(s+16.5)(s^2+5760s+1.296\times10^7)}{(s^2+1530s+8.079\times10^6)(s^2+6977s+2.031\times10^7)} \end{aligned} \tag{7.24}$$

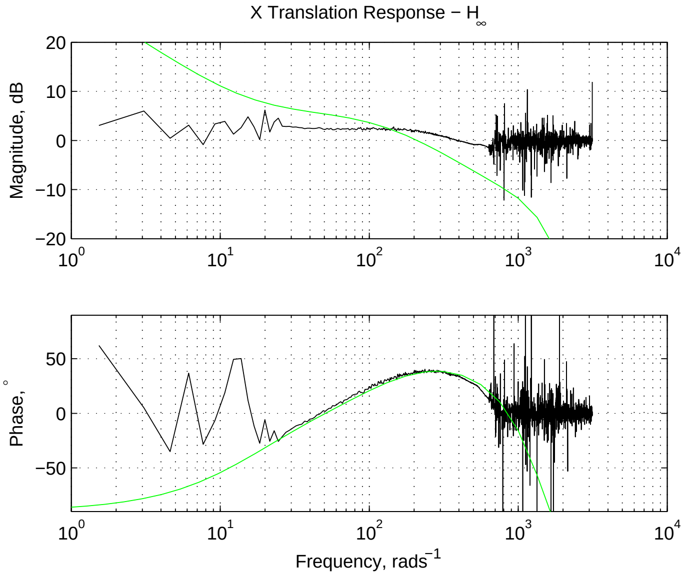

Figure 7.12: The measured (black) and theoretical (green) frequency response of the x-axis translation system with the decoupled H∞ controller.

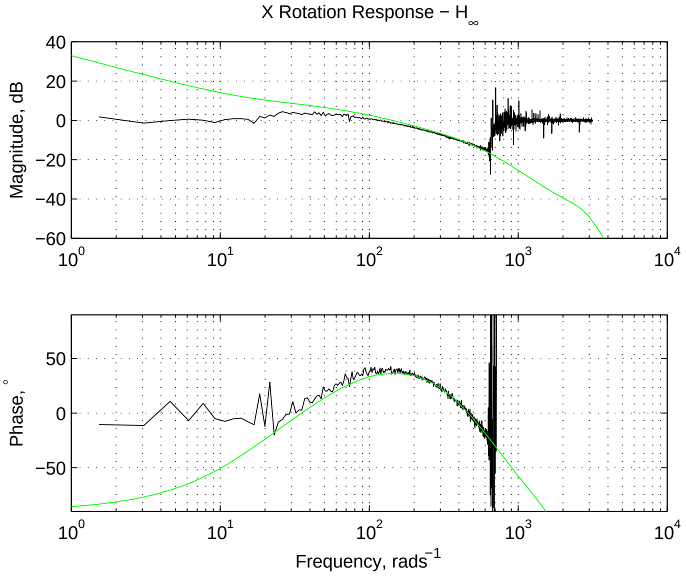

Figure 7.13: The measured (black) and theoretical (green) frequency response of the x-axis rotation system with the decoupled H∞ controller.

7.2.3 Results

Figures 7.14 and 7.15 show the sensitivity transfer functions for translations along and rotations about the x-axis for the decoupled H∞ controller with the linearised model, including the second-order dynamics and anti-aliasing filters that were used to create the controller. For the translation controller synthesis $\gamma = 1.6348$, and $\gamma = 1.1934$ for the rotational motion's controller. These γ values are much less than the gamma values achieved when synthesising other H∞ controllers later in the thesis. The low γ values show that the controller is easily synthesisable and the performance should be as desired.

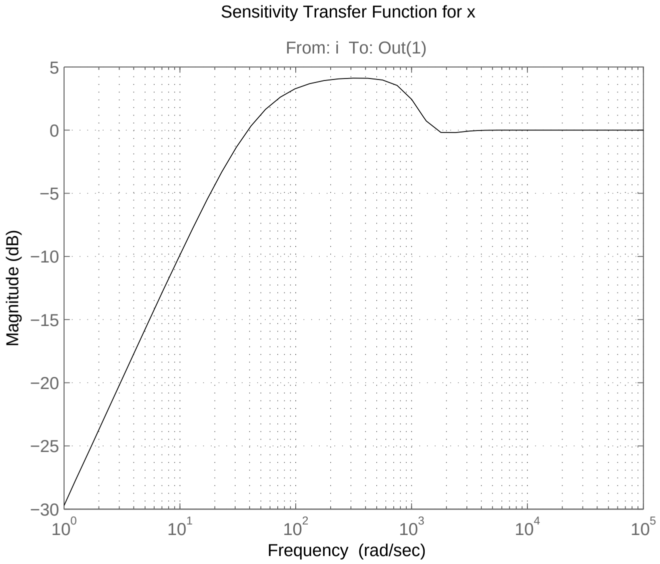

Figure 7.14: The sensitivity transfer function for translation along the x-axis with the decoupled H∞ controller.

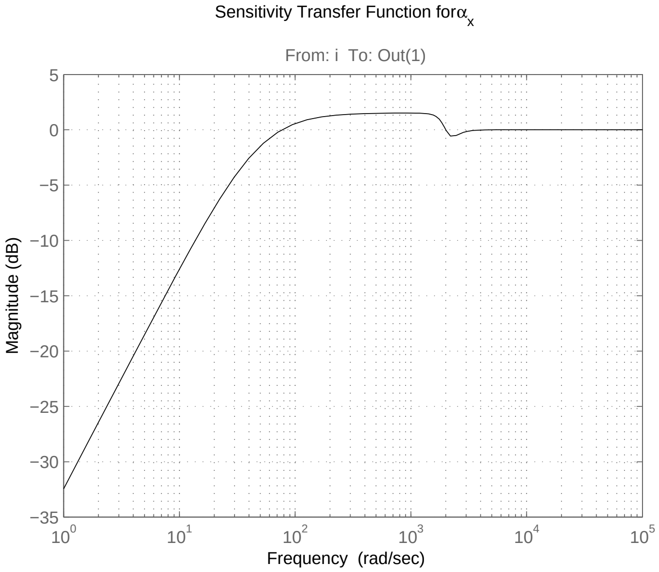

Figure 7.15: The sensitivity transfer function for rotation about the x-axis with the decoupled H∞ controller.

Accuracy

Figure 7.16 shows the distribution of the wheel position while the 3Dwheel engineering model's rotor is being levitated but is not rotating during control by the H∞ decoupled controller. The desired position is maintained to three sigma within 11.6 μm. Figure 7.17 shows the distribution of wheel positions with the same controller, but with the wheel rotating at 500 rpm. While rotating at this angular velocity the position is maintained to three sigma of the desired position within 290 μm.

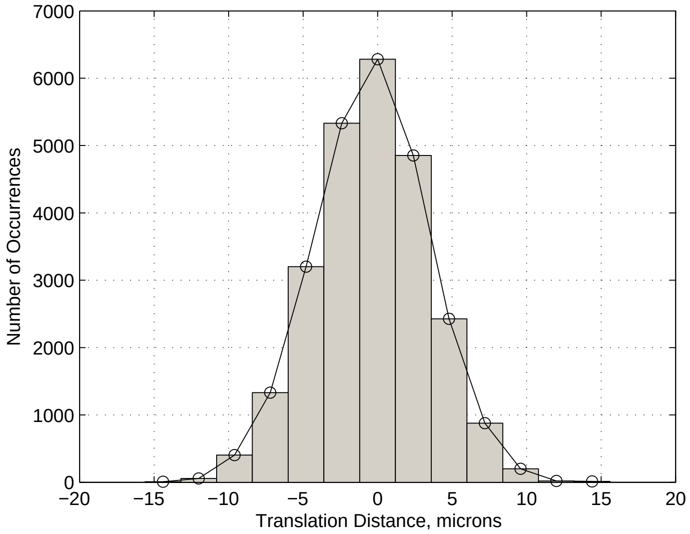

Figure 7.16: The distribution of the wheel positions from the central position during non-rotating levitation with the H∞ decoupled controller with the 3Dwheel hardware.

Figure 7.18 shows the rotor's position along the x and y axes while spinning at around 500 rpm in the laboratory. The sine wave disturbance on the x-axis is due to the mass imbalance of the rotor and occurs at the rotor's spin rate. There should be a similar disturbance on the y-axis. Due to an error, the positions of the bolts securing the aluminium liner to the steel rotor additional holes were drilled in the aluminium liner at a similar height to the y-axis translation eddy current sensor. To minimise the effect of the additional holes, they were filled with aluminium pegs and the surface finish smoothed on the lathe. However, a small disturbance can still be seen in the y-axis translation data. There are four of these holes around the aluminium liner. Figure 7.19 shows an FFT of the y-axis translation data when the rotor was accurately measured as spinning at 560 rpm (9.3 Hz) using a Testo 470 optical RPM measurement device, accurate to ±0.02%. Because of the four holes, their disturbance appears as a 37.3 Hz peak in the FFT data, with even and odd higher order harmonics.

The periodic disturbance due to mass imbalance visible in Figure 7.18 explains the shape of the histogram in Figure 7.17. The rotor's position moves periodically between two extreme vales as a result of the controller not fully damping the rotor's static mass imbalance.

Figure 7.20 shows the translational position of the hardware rotor along the x-axis when at 15.0 seconds there is a demand for a step of 2.5 μm along the x-axis. Also shown is the rotational motion about the x and y-axes over the same time period. The analogue input card in

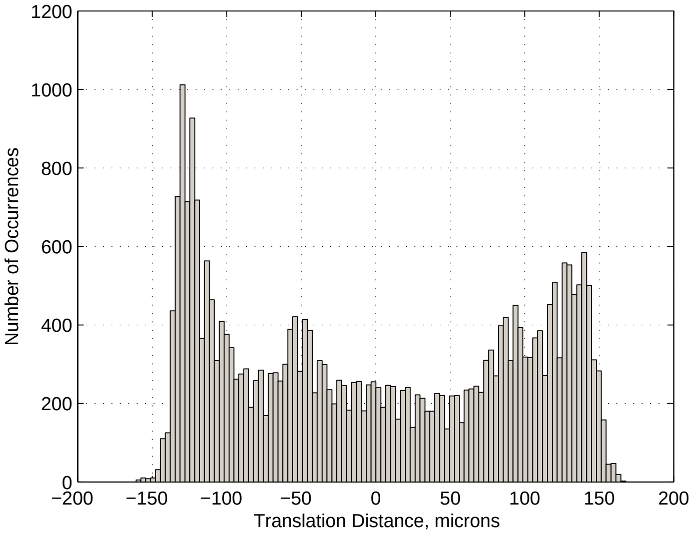

Figure 7.17: The distribution of the wheel positions from the central position while rotating at 500 rpm with the H∞ decoupled controller with the 3Dwheel hardware.

the controlling PC has a resolution 12-bit, with 1-bit corresponding to 2.4 μm. The rotor is moving from the desired position no more than 4-bits demonstrating the low noise and controllability of the system. If the resolution of the input cards is increased then the accuracy of the positional control should increase because of the low levels of noise in the rest of the system. Figure 7.20 also shows that the controllers are able to decouple translational motion from rotational motion.

Tilt Range

Figure 7.33 shows the extent that the decoupled H∞ controller can tilt the engineering model of the 3Dwheel through. The maximum angle before becoming unstable is 0.05 radians (2.9°). The air gap is sized to allow the rotor to tilt through a maximum of $\pm 3°$, therefore when tilted by 2.9° two of the air gaps are 44 μm wide.

Tilting Torque

Figure 7.22 shows the hardware's rotor tilting through 0.03 radians (1.7°) while it is not spinning. It tilts through 0.0297 radians in 0.058 seconds. This is a tilt rate of 0.512 rads^{-1}. If the wheel was spinning at 5000 rpm it would have an angular momentum of 1.22 Nms. This tilt would therefore generate a torque of 0.62 Nm. The tilt command in this case was a step command filtered through a low pass filter with a 3 dB frequency of 17 rads^{-1}.

Figure 7.23 shows the 3Dwheel's rotor tilting through 0.03 radians while spinning at 496 rpm in the laboratory. It tilts through 0.0301 radians in 0.054 s at a rate of 0.558 rads^{-1}. This generates a peak torque of 0.067 Nm at 496 rpm, or would generate a torque of 0.680 Nm if

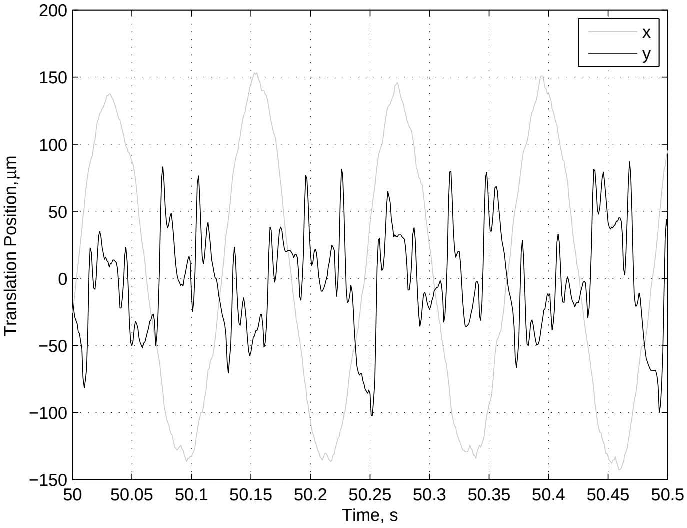

Figure 7.18: The rotor’s translational position while spinning at around 500 rpm.

this tilt rate could be sustained while the wheel was rotating at 5000 rpm. The demand was again low pass filtered by a first order filter with a 3 dB frequency of 17 rads^{-1}. This frequency was chosen to give the fastest response with an acceptable overshoot (17% in this case, but controllable by altering the filter’s corner frequency). Figure 7.24 shows the torque generated by this tilt.

The periodic disturbance in α_y that is particularly noticeable after the tilt has a frequency of 55.1 rads^{-1}. This is the same as the spin rate of the rotor. There is a 90° phase difference between the two axes. This disturbance is due to the component of the rotor’s angular velocity from spinning that is now about the x-axis. The disturbance is then gyroscopically coupled about the y-axis and is discussed in Section 8.2.

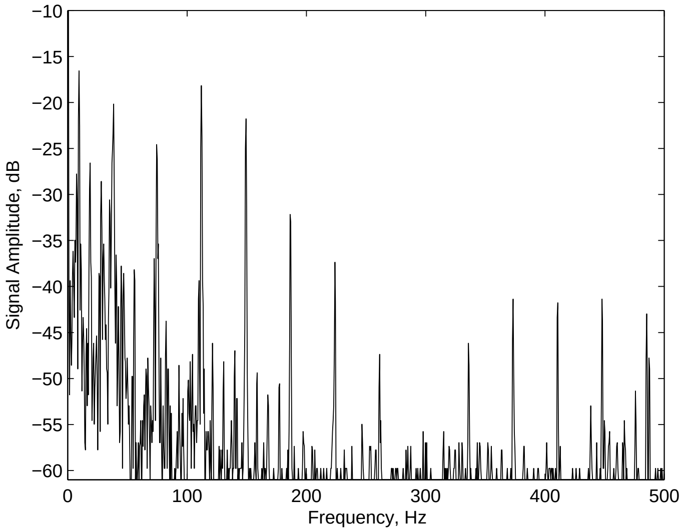

Figure 7.19: The frequency spectrum of the y-axis eddy current sensor voltage with the rotor spinning at 560 rpm.

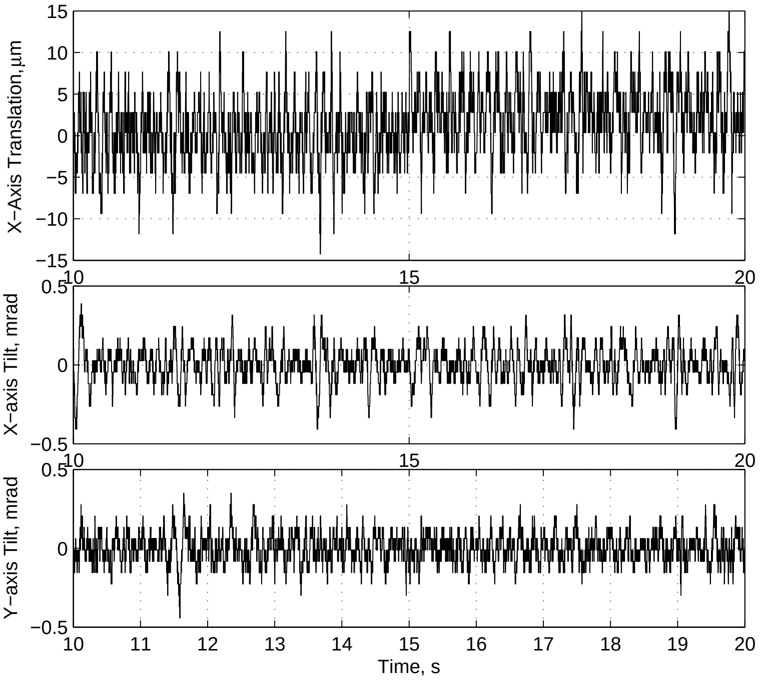

Figure 7.20: A 2.5 μm translation demanded along the x-axis at 15.0 seconds. There is no coupling visible in the rotational data.

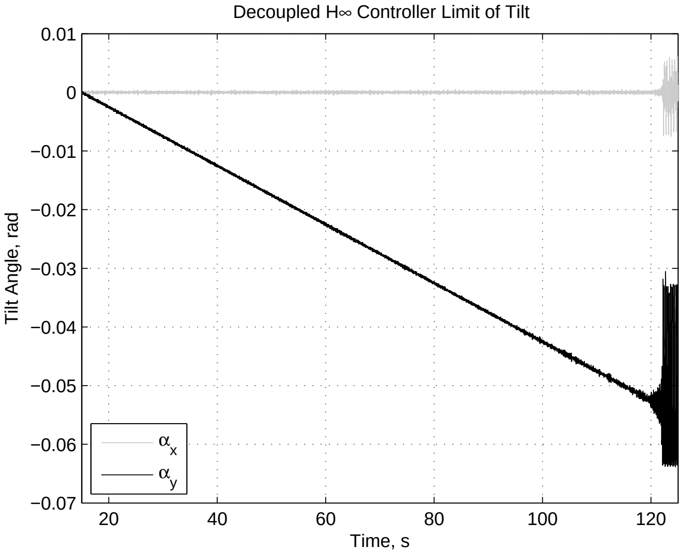

Figure 7.21: The H∞ decoupled controller's tilt range.

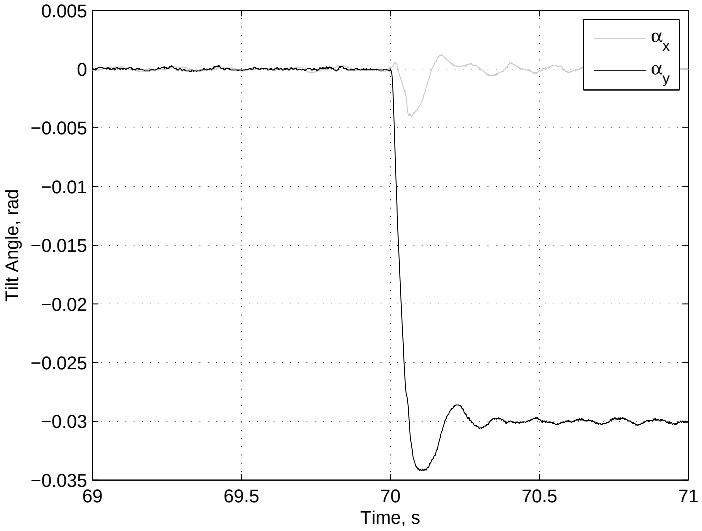

Figure 7.22: Tilting the wheel through 0.03 rad while not spinning.

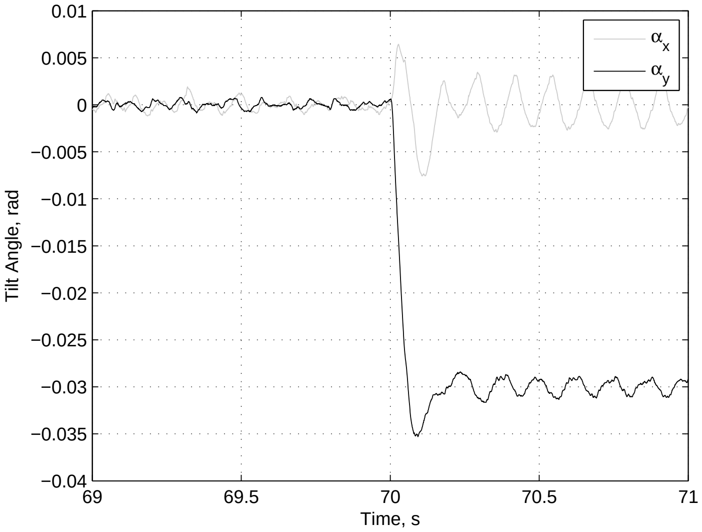

Figure 7.23: Tilting the wheel through 0.03 rad while spinning at 496 rpm.

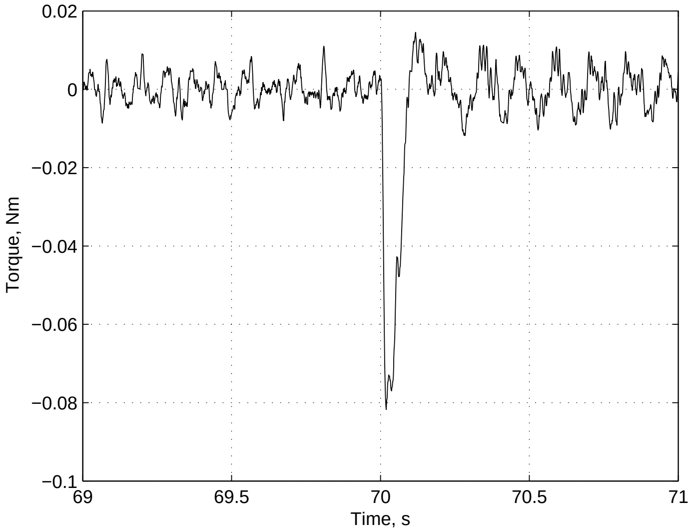

Figure 7.24: The torque generated while tilting the wheel through 0.03 radians and spinning at 496 rpm.

7.3 H∞ Multi-Variable Controller

Rather than assuming that the motion along or about each axis was decoupled from other axes it was desired to make a multi-variable controller where the two translation axes and two rotation axes were simultaneously controlled by a single controller. The controller would have knowledge of the coupling between axes and would handle this coupling. Using the H∞ technique to generate this controller is a natural extension of the work performed so far.

7.3.1 Theory

The following assumptions were made: 1. the kinematic differential equations of motion have been omitted, 2. the air gap equations were linearised, which is valid for the small tilt angles encountered here, 3. the $\omega \times I\omega$ term in the equations of rotational motion had been removed using feedback linearisation.

The kinematic differential equations of motion were assumed to have no effect because they greatly simplify the state space model. For small tilt angles about the x and y-axes, small angle approximations can be used so that $\left[\begin{array}{ccc} \dot{\phi} & \dot{\theta} & \dot{\psi} \end{array}\right]^T = \left[\begin{array}{ccc} \omega_x & \omega_y & \omega_z \end{array}\right]^T$. The tilt range of the 3Dwheel is $\pm 3^\circ$ and so the small angle approximations are valid and the kinematic differential equations of motion can be assumed to have no effect and can be omitted.

It is first necessary to build a state-space model that the H∞ controller synthesis tool then uses to generate the multi-variable controller. The model states $\mathbf{q}$ defined for the state-space model are:

$$\mathbf{q} = \left[\begin{array}{cccccccc} \dot{x} & x & \dot{y} & y & \dot{\alpha}_x & \alpha_x & \dot{\alpha}_y & \alpha_y \end{array}\right]^T \tag{7.25}$$

The input vector $\mathbf{u}$ is:

$$\mathbf{u} = \left[\begin{array}{cccccccc} i_1 & i_2 & i_3 & i_4 & i_5 & i_6 & i_7 & i_8 \end{array}\right]^T \tag{7.26}$$

The output vector $\mathbf{p}$ is:

$$\mathbf{p} = \left[\begin{array}{cccc} x & y & \alpha_x & \alpha_y \end{array}\right]^T \tag{7.27}$$

The constant terms in the reluctance force equation are separated out:

$$\begin{aligned} F_R &= \frac{\mu_0 N^2 \varepsilon l i^2}{4\gamma^2} \\ &= K_{em}\frac{i^2}{\gamma^2} \end{aligned} \tag{7.28}$$

The reluctance force can then be defined for each electromagnet, i.e.:

$$f_n = K_{em}\frac{i_n^2}{\gamma_n^2} \tag{7.29}$$

where each of the eight air gaps is calculated using the linearised air gap equations using Equation 6.27 with the addition of the default air gap width γ_0. For example:

$$\gamma_1 = \gamma_0 - x - \gamma/2\alpha_y \tag{7.30}$$

The entire state space model is given by the two equations:

$$\begin{aligned} \dot{\mathbf{q}} &= \mathbf{Aq} + \mathbf{Bu} \\ \mathbf{p} &= \mathbf{Cq} \end{aligned} \tag{7.31}$$

The translation dynamic response in the inertial frame is given by Newton's Second Law:

$$\begin{bmatrix} \ddot{x} \\ \ddot{y} \\ \ddot{z} \end{bmatrix} = M^{-1}\mathbf{F} \tag{7.32}$$

The total force is given by the kinematic mapping equations:

$$\begin{bmatrix} F_x \\ F_y \end{bmatrix} = r_z \begin{bmatrix} 1 & 1 & 0 & 0 & -1 & -1 & 0 & 0 \\ 0 & 0 & 1 & 1 & 0 & 0 & -1 & -1 \end{bmatrix} \begin{bmatrix} f_1 \\ f_2 \\ f_3 \\ f_4 \\ f_5 \\ f_6 \\ f_7 \\ f_8 \end{bmatrix} \tag{7.33}$$

The rotation dynamic response in the inertial frame, assuming the gyroscopic term has been removed using feedback linearisation (see Section 8.2.1) is given by:

$$\begin{bmatrix} \ddot{\alpha}_x \\ \ddot{\alpha}_y \\ \ddot{\alpha}_z \end{bmatrix} = \mathbf{I}^{-1}\mathbf{T} \tag{7.34}$$

$$\begin{bmatrix} T_x \\ T_y \end{bmatrix} = r_z \begin{bmatrix} 0 & 0 & -1 & 1 & 0 & 0 & 1 & -1 \\ 1 & -1 & 0 & 0 & -1 & 1 & 0 & 0 \end{bmatrix} \begin{bmatrix} f_1 \\ f_2 \\ f_3 \\ f_4 \\ f_5 \\ f_6 \\ f_7 \\ f_8 \end{bmatrix} \tag{7.35}$$

$\dot{\mathbf{q}}$ can be written by the non-linear vector:

$$\dot{\mathbf{q}} = \begin{bmatrix} -\frac{\frac{K_{em}\,{i_5}^2}{(\gamma_0+x+\alpha_y\,r_z)^2}+\frac{K_{em}\,{i_6}^2}{(\gamma_0+x-\alpha_y\,r_z)^2}-\frac{K_{em}\,{i_1}^2}{(x-\gamma_0+\alpha_y\,r_z)^2}-\frac{K_{em}\,{i_2}^2}{(\gamma_0-x+\alpha_y\,r_z)^2}}{M} \\ \dot{x} \\ -\frac{\frac{K_{em}\,{i_7}^2}{(\gamma_0+y-\alpha_x\,r_z)^2}+\frac{K_{em}\,{i_8}^2}{(\gamma_0+y+\alpha_x\,r_z)^2}-\frac{K_{em}\,{i_3}^2}{(\gamma_0-y+\alpha_x\,r_z)^2}-\frac{K_{em}\,{i_4}^2}{(y-\gamma_0+\alpha_x\,r_z)^2}}{M} \\ \dot{y} \\ \frac{r_z\left(\frac{K_{em}\,i7^2}{(\gamma_0+y-\alpha_x\,r_z)^2}-\frac{K_{em}\,{i_8}^2}{(\gamma_0+y+\alpha_x\,r_z)^2}-\frac{K_{em}\,{i_3}^2}{(\gamma_0-y+\alpha_x\,r_z)^2}+\frac{K_{em}\,{i_4}^2}{(y-\gamma_0+\alpha_x\,r_z)^2}\right)}{I_{xx}} \\ \dot{\alpha}_x \\ -\frac{r_z\left(\frac{K_{em}\,{i_5}^2}{(\gamma_0+x+\alpha_y\,r_z)^2}-\frac{K_{em}\,{i_6}^2}{(\gamma_0+x-\alpha_y\,r_z)^2}-\frac{K_{em}\,{i_1}^2}{(x-\gamma_0+\alpha_y\,r_z)^2}+\frac{K_{em}\,{i_2}^2}{(\gamma_0-x+\alpha_y\,r_z)^2}\right)}{I_{yy}} \\ \dot{\alpha}_y \end{bmatrix} \tag{7.36}$$

The $\mathbf{A}$ and $\mathbf{B}$ matrices in the state space model (Equation 7.31) can be calculated by taking the Jacobian of $\dot{\mathbf{q}}$:

$$\mathbf{A} = \begin{bmatrix} \frac{\partial \dot{\mathbf{q}}_1}{\partial \mathbf{q}_1} & \cdots & \frac{\partial \dot{\mathbf{q}}_1}{\partial \mathbf{q}_8} \\ \vdots & \ddots & \vdots \\ \frac{\partial \dot{\mathbf{q}}_8}{\partial \mathbf{q}_1} & \cdots & \frac{\partial \dot{\mathbf{q}}_8}{\partial \mathbf{q}_8} \end{bmatrix} \tag{7.37}$$

$$\mathbf{B} = \begin{bmatrix} \frac{\partial \dot{\mathbf{q}}_1}{\partial \mathbf{u}_1} & \cdots & \frac{\partial \dot{\mathbf{q}}_1}{\partial \mathbf{u}_8} \\ \vdots & \ddots & \vdots \\ \frac{\partial \dot{\mathbf{q}}_8}{\partial \mathbf{u}_1} & \cdots & \frac{\partial \dot{\mathbf{q}}_8}{\partial \mathbf{u}_8} \end{bmatrix} \tag{7.38}$$

The $\mathbf{C}$ matrix to calculate the output variables from the states is:

$$\mathbf{C} = \begin{bmatrix} 0 & 1 & 0 & 0 & 0 & 0 & 0 & 0 \\ 0 & 0 & 0 & 1 & 0 & 0 & 0 & 0 \\ 0 & 0 & 0 & 0 & 0 & 1 & 0 & 0 \\ 0 & 0 & 0 & 0 & 0 & 0 & 0 & 1 \end{bmatrix} \tag{7.39}$$

The anti-aliasing filters and second order electromagnet dynamics were implemented as transfer functions. Matlab model creation functions were used to append an anti-aliasing filter and second-order dynamics to each of the state-space model's current inputs and an anti-aliasing filter to each output. An H∞ controller was then generated for this system using the synthesis structure shown in Figure 7.11 with the difference that $\hat{x}$ is now a 4 element vector $\hat{\mathbf{x}} = [\ \hat{x}\ \ \hat{y}\ \ \hat{\alpha}_x\ \ \hat{\alpha}_y\ ]^T$ and i is an eight element vector consisting of the current through each electromagnet. Similarly the weighting functions W_1 and W_2 are 8×8 and 4×4 respectively diagonal matrices of the single-input single-output weighting functions:

$$\begin{aligned} W_{1TF}(s) &= 10^{-5} \\ W_{2TF}(s) &= \frac{s+150}{s+10^{-4}} \end{aligned} \tag{7.40}$$

These weighting function values were found through experimentation to give the best performance from the hardware.

7.3.2 Results

Figures 7.27 and 7.28 show the sensitivity transfer functions. The γ cost achieved by the controller synthesis was 2.3358. This is significantly larger than the γ achieved for the decoupled H∞ controllers and results in a 7.4 dB overshoot of the sensitivity transfer function. However, Figures 7.25 and 7.26 show the theoretical loop transfer functions for translation along and rotation about the x-axis respectively for the state-space model with anti-aliasing filter and second-order dynamics and the multi-variable H∞ controller. The phase margin for translational motion was 30° at a crossover frequency of 219 rads^{-1} and 47° at 175 rads^{-1} for rotational motion. The predicted phase margin is greater than the decoupled H∞ controller's phase margin and so this controller should be more stable.

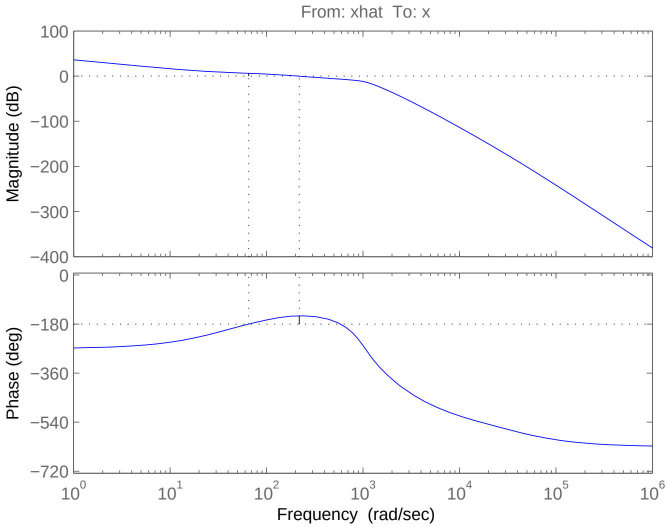

Figure 7.25: The loop transfer function for translation along the x-axis with the H∞ multi-variable controller.

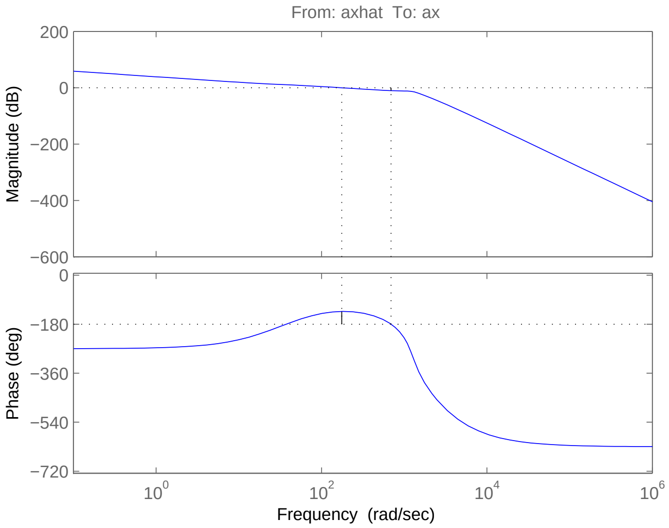

Figure 7.26: The loop transfer function for rotation about the x-axis with the H∞ multi-variable controller.

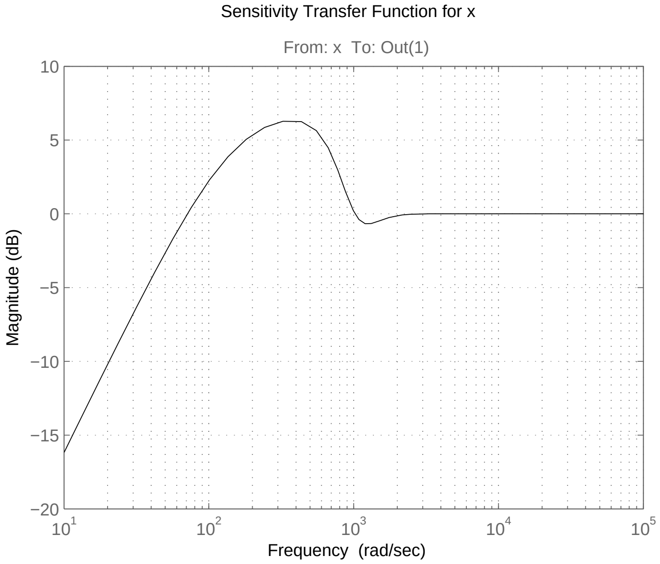

Figure 7.27: The sensitivity transfer function for translation along the x-axis with the H∞ multi-variable controller.

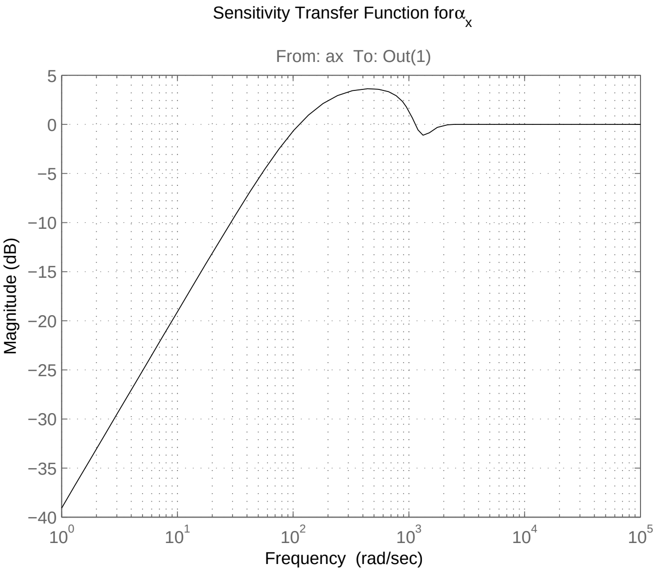

Figure 7.28: The sensitivity transfer function for rotation about the x-axis with the H∞ multi-variable controller.

System Frequency Response

Figure 7.29 shows the laboratory measured and theoretical frequency responses of the controller and hardware for translation along an axis with the H∞ multi-variable controller. Figure 7.30 shows the equivalent for rotation. The measured frequency has a phase margin for translational motion of 43° at a crossover frequency of 226 rads^{-1} and 55° at 126 rads^{-1} for rotational motion. This is an improvement of 9° and 14° for translation and rotation respectively compared with the decoupled H∞ controller. This improved phase margin should result in greater stability and rejection of disturbances.

There is a poor match between the theoretical (from which the controller was synthesised) and measured frequency response. The measured response has a greater phase margin than the theoretical H∞ controller. If more time was available the state space model, and the second order dynamics and anti-aliasing filter dynamics appended to it would be carefully investigated and refined to give a better match between the measured and theoretical responses, which would improve the stability and performance of the levitation of the 3Dwheel.

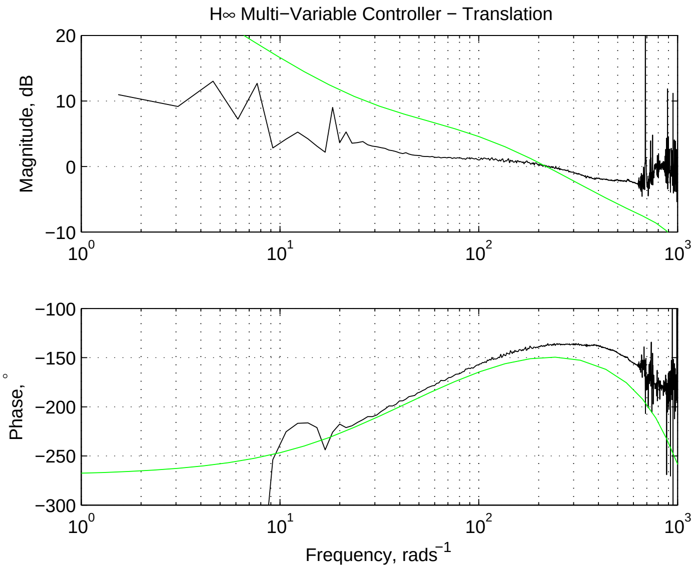

Figure 7.29: The final measured (black) and theoretical (green) frequency responses of the x-axis translation system with the H∞ multi-variable controller and the engineering model hardware in the laboratory.

Accuracy

Figure 7.31 shows the distribution of the wheel positions while the rotor is being levitated but not rotating during control by the H∞ multi-variable controller in the laboratory. The desired position is maintained to three sigma within 13.0 μm. Figure 7.32 shows the distribution of wheel positions with the same controller, but with the wheel rotating at 500 rpm. While rotating at this angular velocity the position is maintained to three sigma of the desired position within 446 μm.

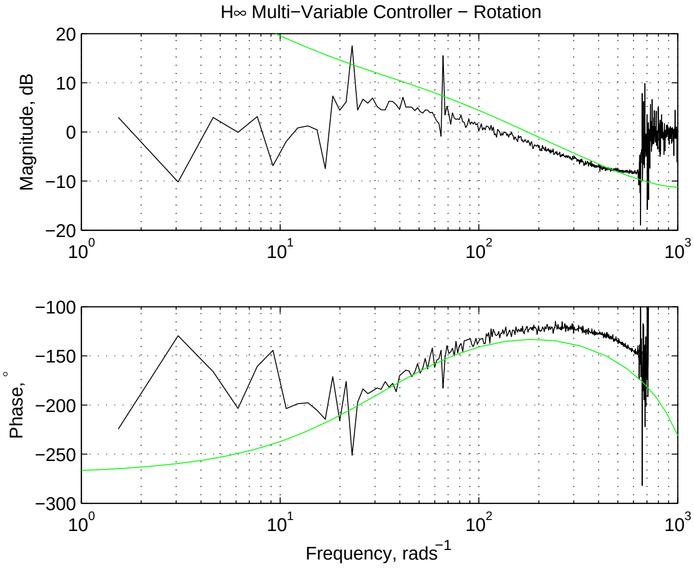

Figure 7.30: The final measured (black) and theoretical (green) frequency responses of the x-axis rotation system with the H∞ multi-variable controller and the engineering model hardware in the laboratory.

Tilt Range

Figure 7.33 shows the extent that the H∞ multi-variable controller can tilt the engineering model hardware of the 3Dwheel through. The maximum angle before becoming unstable is 0.03 radians (1.7°), although after 0.02 radians (1.1°) the rotor is visibly less stable about both the tilting y-axis and the stationary x-axis. The tilting range is linked to the ability of the controller to operate away from its point of linearisation. The multi-variable controller has a range of half of what the H∞ decoupled controller is capable of in this respect.

Tilting Torque

Figure 7.34 shows the rotor being tilted through 0.015 radians by the multi-variable H∞ controller while it is not rotating in the laboratory. The average tilt rate is 0.18 rads^{-1} sustained over 81 ms, which would generate a gyroscopic torque of 0.21 Nm if the wheel was spinning at 5000 rpm. Figure 7.35 shows the wheel being tilted through 0.015 radians by the multi-variable H∞ controller while the wheel is spinning at a demanded rate of 500 rpm. This is a tilt rate of 0.24 rads^{-1}, which generates a peak torque of 29 mNm at 500 rpm. The wheel was tilted through a smaller angle than it was with the H∞ decoupled controller because the range of the multi-variable H∞ controller is less than the decoupled one as discussed in the Tilt Range Section earlier. A 17 rads^{-1} low pass filter was again used to pre-filter the demand. The oscillation after the tilt is due to the component of the spin rate about the x-axis, which is gyroscopically coupled about the y-axis as discussed in Section 8.2. The tilt rate is slower than that produced by the decoupled H∞ controller. Because of the poor match between the multi-variable model and hardware it is not clear whether this is due to the response of the synthesised controller or multi-variable controllers in general.

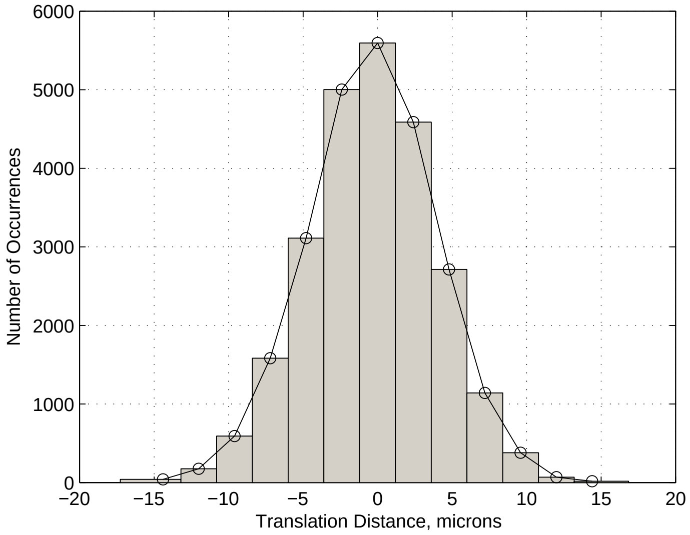

Figure 7.31: The distribution of the wheel positions of the hardware from the central position while not rotating with the H∞ multi-variable controller.

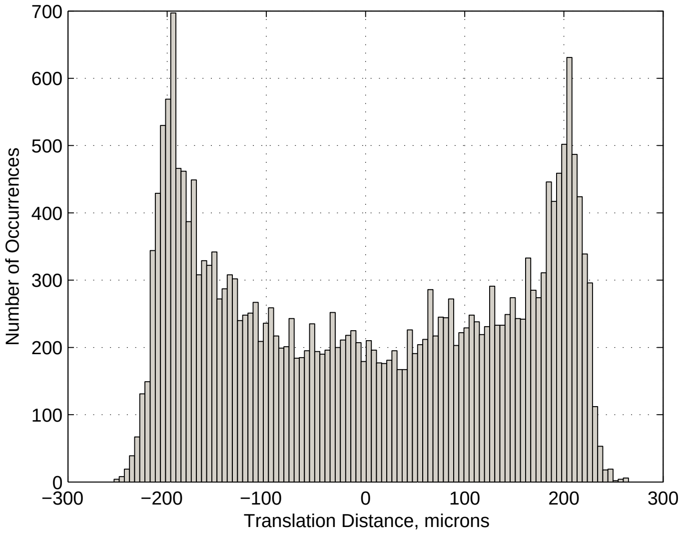

Figure 7.32: The distribution of the wheel positions of the hardware from the central position while rotating at 500 rpm with the H∞ multi-variable controller.

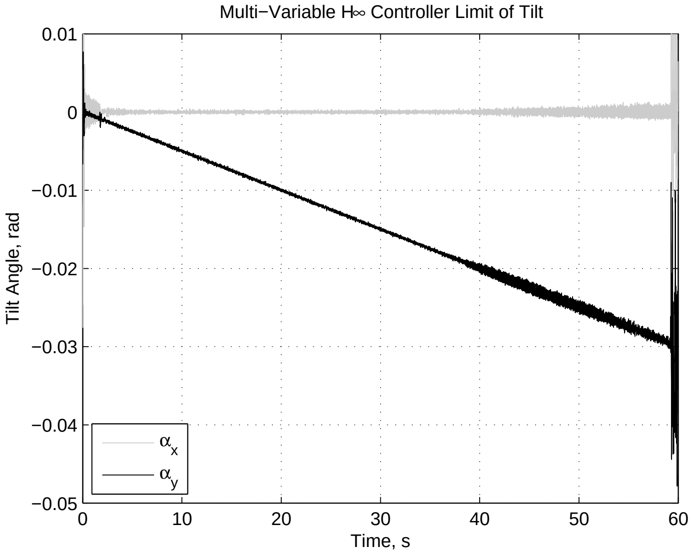

Figure 7.33: The H∞ multi-variable controller's tilt range.

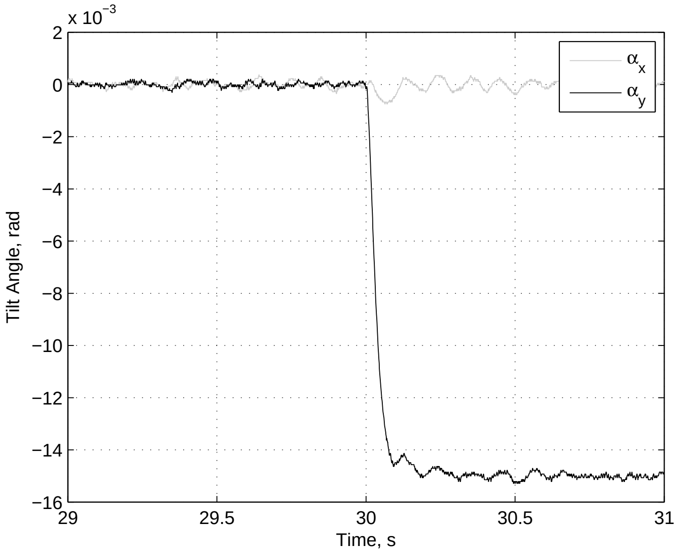

Figure 7.34: Tilting the wheel through 0.015 rad while not spinning using the multi-variable H∞ Controller.

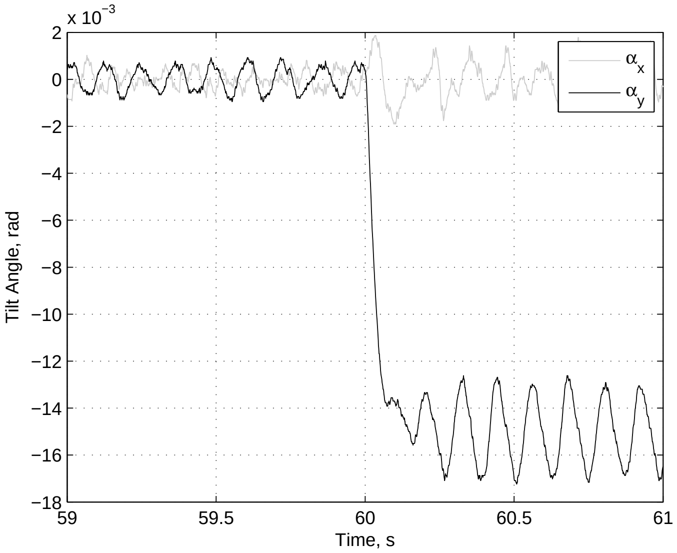

Figure 7.35: Tilting the wheel through 0.015 rad while spinning at 500 rpm using the multivariable H∞ Controller.

7.4 State Feedback Controller

An alternative method to control a system is the state feedback method, where internal states are fed-back to the controller. Estimation methods such as Kalman filters are required to calculate states that are not directly observable. To develop a state feedback for the 3Dwheel a state space model was constructed. The states $\mathbf{q}$ are:

$$\mathbf{q} = \left[\begin{array}{cccccccccc} x & y & \dot{x} & \dot{y} & \phi & \theta & \psi & \dot{\alpha}_x & \dot{\alpha}_y & \dot{\alpha}_z \end{array}\right]^T \tag{7.41}$$

The inputs $\mathbf{u}$ to the system are:

$$\mathbf{u} = \left[\begin{array}{ccccccccc} i_1 & i_2 & i_3 & i_4 & i_5 & i_6 & i_7 & i_8 & T_z \end{array}\right]^T \tag{7.42}$$

The state space rate vector $\dot{\mathbf{q}}$ is:

$$\dot{\mathbf{q}} = \left[\begin{array}{cccccccccc} \dot{x} & \dot{y} & \ddot{x} & \ddot{y} & \dot{\phi} & \dot{\theta} & \dot{\psi} & \ddot{\alpha}_x & \ddot{\alpha}_y & \ddot{\alpha}_z \end{array}\right]^T \tag{7.43}$$

$\ddot{x}$ and $\ddot{y}$ can be calculated from the dynamics of translational motion, Equation 6.1, with the non-linear reluctance force equation; Equation 7.29 was used to calculate the forces produced by the eight electromagnets. The air gaps were calculated by the linearised equation, Equation 7.30. The kinematic mapping equation, Equation 7.33, is used to map the force from each electromagnet to forces along the principal axes in the inertial frame.

Similarly, $\ddot{\alpha}_x$, $\ddot{\alpha}_y$ and $\ddot{\alpha}_z$ are given by the dynamics of rotational motion, Equation 6.18, but linearised using feedback linearisation to remove the $\boldsymbol{\omega} \times I\boldsymbol{\omega}$ term. The mapping from the eight electromagnet forces to torques in the inertial frame are given by Equation 7.35.

$\dot{\phi}$, $\dot{\theta}$ and $\dot{\psi}$ are given by the kinematic differential equations of motion, Equation 6.20.

The $\mathbf{A}$ and $\mathbf{B}$ matrices of the state space model are calculated by finding the Jacobian of $\dot{\mathbf{q}}$ with respect to $\mathbf{q}$ and $\mathbf{u}$ similarly to the multi-variable H∞ controller.

The pole placement technique was then used to generate a controller to stabilise the system. In pole placement the desired feedback system's poles are specified along with the $\mathbf{A}$ and $\mathbf{B}$ matrices of the plant. The pole placement algorithm then devises a controller that results in the specified close loop poles. The Matlab Control Systems Toolbox `place` function was used to generate the controller. The requested poles are shown in Table 7.3. They are all in the left hand plane because the system needs to be stable.

The controller generated is in the form of a matrix $\mathbf{K}$ that is multiplied by the state variables $\mathbf{q}$. The matrix $\mathbf{K}$ generated is shown in Equation 7.44:

State Variable	Pole
x	$-200 + 10\jmath$
y	$-200 - 10\jmath$
$\dot{x}$	$-210 + 10\jmath$
$\dot{y}$	$-210 - 10\jmath$
ϕ	$-205 + 5\jmath$
θ	$-205 - 5\jmath$
ψ	$-205 + 10\jmath$
$\dot{\alpha}_x$	$-205 - 10\jmath$
$\dot{\alpha}_y$	$-210 + 5\jmath$
$\dot{\alpha}_z$	$-210 - 5\jmath$

Table 7.3: The closed loop poles requested from the pole placement tool.

$$\mathbf{K} = \begin{bmatrix} 11443 & 123.29 & 104.28 & 0.59309 & -279.18 & 776.73 & 77.51 & -1.1654 & 7.8258 & 0.37408 \\ 11423 & 80.067 & 104.19 & 0.3841 & -135.58 & -932.66 & 68.028 & -0.86506 & -8.3683 & 0.32343 \\ -185.82 & 11536 & -0.89287 & 104.74 & -698.09 & -148.24 & -15.695 & -7.3166 & -0.54153 & -0.13866 \\ -158.23 & 11530 & -0.75932 & 104.7 & 984.22 & -7.1721 & -23.094 & 8.7473 & -0.24378 & -0.17377 \\ -11443 & -123.29 & -104.28 & -0.59309 & 279.18 & -776.73 & -77.51 & 1.1654 & -7.8258 & -0.37408 \\ -11423 & -80.067 & -104.19 & -0.3841 & 135.58 & 932.66 & -68.028 & 0.86506 & 8.3683 & -0.32343 \\ 185.82 & -11536 & 0.89287 & -104.74 & 698.09 & 148.24 & 15.695 & 7.3166 & 0.54153 & 0.13866 \\ 158.23 & -11530 & 0.75932 & -104.7 & -984.22 & 7.1721 & 23.094 & -8.7473 & 0.24378 & 0.17377 \\ 1.9459 & -0.18503 & 0.0092612 & -0.00060196 & -0.36918 & 2.4792 & 95.992 & -0.0014924 & 0.011715 & 0.94397 \end{bmatrix} \tag{7.44}$$

The controller generated does not contain an integral component and so the system can contain steady state errors. Integration can be added by taking the translational and rotational position in the states, x, y, α_x and α_y and subtracting them from the desired positions. These position errors are then integrated, converted to eight currents using the pseudo-inverse of the kinematic mapping equations and multiplied by an integration gain. These currents are then added to the output of the multiplication of the controller matrix. The implementation of the integration in the Simulink model is shown in Figure 7.36.

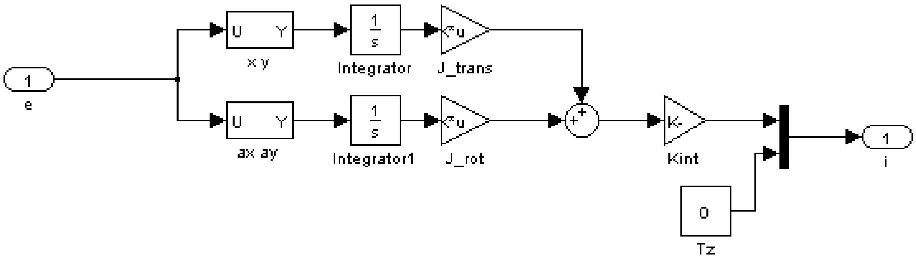

Figure 7.36: The Simulink implementation of integration in the state feedback controller.

Because the rates in the states $\mathbf{q}$ cannot be observed directly it is necessary to use the linear and extended Kalman filters to calculate the rates from the observed positions when constructing the state vector. Figure 7.37 shows the implementation of the state feedback controller in Simulink. The “Full Dynamics” block contains the two Kalman filters and either the complete non-linear model of the wheel or the i/o blocks to connect the engineering model of the wheel. The “Sine Wave” and “trans” blocks are used in testing to form the desired state $\hat{\mathbf{q}}$. $\hat{\psi}$ in $\hat{\mathbf{q}}$ is the desired angular position of the rotor about the z-axis, which is constantly changing as the rotor spins. It is formed by integrating $\dot{\alpha}_z$. The current states $\mathbf{q}$ are subtracted from the desired states $\hat{\mathbf{q}}$ to give the error $\mathbf{e}$. $\mathbf{e}$ is multiplied by the control matrix $\mathbf{K}$ and also passed to the integration block. The two sets of currents calculated are summed and added to a bias current before being applied to the 3Dwheel.

The state feedback controller worked in simulation, although it could be difficult for the software to solve as algebraic loops can exist in the model. When the anti-aliasing filter and electromagnet dynamics were added to the state space model the pole placement function was not able to achieve the desired pole locations and a controller could not be generated. Time was not available for further development work.

Figure 7.38 shows a simulation of the state feedback and decoupled H∞ controllers tilting the rotor through 0.5°. The state feedback has a 40% faster response with 29% less overshoot. Figure 7.39 shows the frequency response for the x-axis translations in simulation. The cross-over frequency is around 31 rads^{-1}.

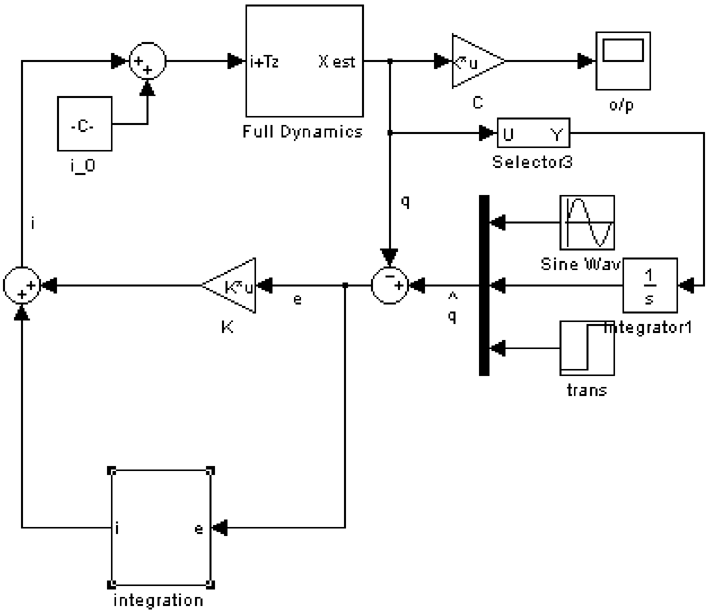

Figure 7.37: The Simulink implementation of the state feedback controller.

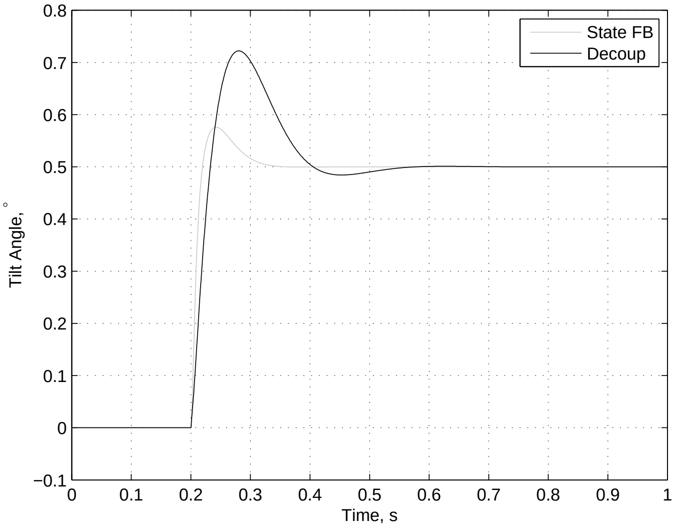

Figure 7.38: Simulation results comparing the state feedback and decoupled H∞ controllers tilting the rotor $0.5°$ about the x-axis.

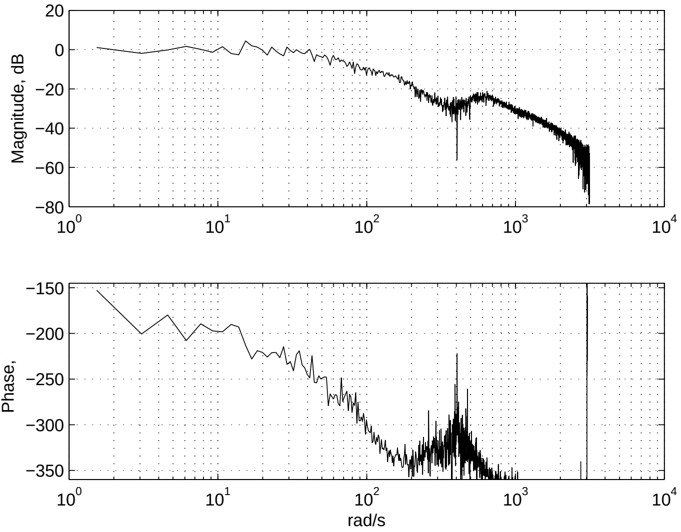

Figure 7.39: A Digital Signal Analyser (DSA) measurement of the frequency response of the x-axis translation of the state feedback controller in simulation.

7.5 Conclusions

Four different basic control techniques have been developed to stabilise the levitation of a tilting magnetically levitated momentum wheel. Three of these techniques have been successfully controlling the 3Dwheel hardware in the laboratory. In order of complexity these techniques are the decoupled lead-lag controller, the decoupled H∞ controller, the multi-variable H∞ controller and the state feedback controller.

	Decoupled	Multi-var.
Trans. Cross-over	385 rads^{-1}	226 rads^{-1}
Trans. Phase Margin	34°	43°
Rot. Cross-over	121 rads^{-1}	126 rads^{-1}
Rot. Phase Margin	41°	55°

Table 7.4: Comparison between the decoupled and multi-variable H∞ controllers for translational and rotational motion.

Table 7.4 compares the measured performance of two of these controllers with the hardware. The multi-variable controller has a greater phase margin and so can be expected to be more stable. Its lower cross-over frequency means a lower gain at high frequencies and so should have the best noise performance. When levitating the hardware while the wheel was stationary and rotating there were no observable differences in the stability or noise performance of the two controllers. However, the tilt range results show that the decoupled controller is more stable. Each decoupled controller implementation required loop gains in the translation and rotation control loops to be manually tuned for optimum stability. There is a mismatch in the magnitude of the frequency response of the hardware, which has not been measured accurately enough, even with the help of the DSA tool. This gain mismatch can easily be compensated in the lab with the decoupled controllers but not with the more complex multi-variable controllers. If the gain is not precisely known with the multi-variable controllers then the cross-over frequency will not be at the frequency that gives the greatest possible phase margin and hence the poorer stability of the multi-variable controller.

As shown in Table 7.4 the more complicated controllers such as the H∞ multi-variable controller offer the potential of a more desirable response than simpler controllers such as the decoupled controllers. Complex controllers such as the H∞ multi-variable and the state feedback are synthesised by algorithms that require a precise model of the plant dynamics. If there is any uncertainty in the plant dynamics then the performance of these complex controllers is adversely affected. The decoupled controllers have the advantage of being easily modifiable by hand to achieve the optimum performance when there is uncertainty in the plant dynamics.

All of the controllers when properly tuned are able to begin levitating the rotor with the rotor at rest in any initial position. During initial testing additional support and damping of the rotor had to be provided by holding the rotor with fingers to initially levitate the rotor.

The quantization of the position is visible in Figure 7.8, showing that the system is low-noise and can be controlled with a high precision. The precision of this engineering model is limited by the resolution of the data acquisition card. The rotor's position has been controlled to within 3 sigma of the desired value in 11.6 μm.

The rotor became uncontrollable when spinning at angular velocities above around 1000 rpm (105 rads^{-1}). At the highest spin rates the rotor oscillated. The rotor had not been balanced and so had a unknown and potentially large static and couple imbalance. It is believed that the imbalance is causing these oscillations and limiting the engineering model's spin rate.

Chapter 8

Additional Control Techniques and Results

In the previous Chapter four different controllers were introduced. Three of them were successfully demonstrated controlling the levitation and motion of the 3Dwheel hardware in the laboratory. In this Chapter additional experimental results demonstrate the 3Dwheel's ability to generate a conventional torque about its spin axis, the power consumption of the engineering model and finally there is a discussion of feed-forward compensation to stabilise the levitation at high spin rates.

The Chapter concludes with simulation results demonstrating how the now proven 3Dwheel can be used to control the attitude of the TopSat small satellite. The 3 axis attitude control of TopSat is demonstrated using only a single 3Dwheel.

8.1 Conventional Torque

Although work has concentrated on the development of the tilting momentum wheel, the 3Dwheel is still capable of generating a torque about its spin axis in the same manner as a conventional momentum wheel. Figure 8.1 shows the angular velocity and angular acceleration of the 3Dwheel's hardware rotor as it is accelerated to 86 rads^{-1} (821 rpm), using the decoupled H∞ controller for levitation in the laboratory. Figure 8.2 shows the torque generated about the spin axis during this acceleration. The generated torque is over 20 mNm for the majority of the acceleration, which is comparable to similarly sized satellite momentum wheels, and the peak torque is 37 mNm.

To generate the maximum torque in these tests, maximum acceleration was achieved by running the motor without closed loop control, hence the variable acceleration rate and output torque in Figures 8.1 and 8.2. Modifying the PI controller to control acceleration rather than velocity, and increasing the message rate over the I^{2}C interface would allow the output torque to be smoothly controlled.

The motor fitted to the 3Dwheel is not optimised for this application. A custom designed motor may be able to generate a greater torque, or the same torque but with an improved power consumption.

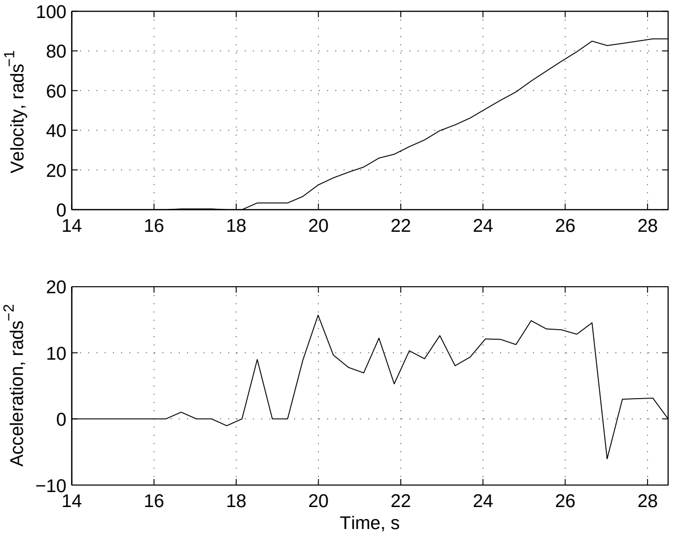

Figure 8.1: The angular velocity and angular acceleration of the rotor hardware as it is accelerated to 820 rpm in the laboratory.

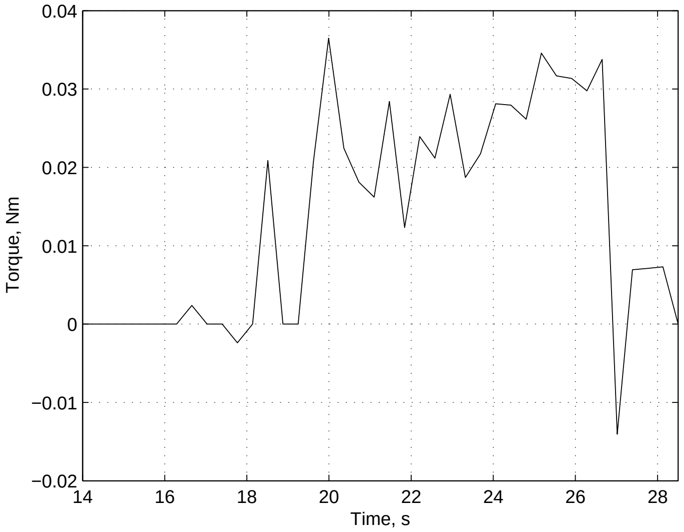

Figure 8.2: The torque generated about the spin axis by the acceleration of the rotor hardware.

8.2 Cross Coupling

The $\boldsymbol{\omega}\times\mathbf{I}\boldsymbol{\omega}$ term in the dynamics of rotational motion can couple the motion about one axis to the other axes. This term is also responsible for the generation of the gyroscopic torque when tilting the wheel. The rotor was not balanced during manufacture. Its inertia matrix was found from the CAD model of the outer steel part, the two parts of the aluminium liner and the permanent magnet. The magnet ring from the brushless DC motor, the permanent magnet for calculating the spin rate of the rotor were not included in the matrix nor were the screws and adhesive connecting the parts. Because the CAD model assumes that the material has a uniform density and because the parts are symmetrical then there are no off diagonal terms in the rotor's inertia matrix:

$$\mathbf{I} = \begin{bmatrix} 0.001594 & 0 & 0 \\ 0 & 0.001594 & 0 \\ 0 & 0 & 0.002326 \end{bmatrix} \tag{8.1}$$

where each term has units kgm^2. SSTL's microsat momentum wheel is balanced so that its couple imbalance (the product of inertia terms) is better than 2.0×10^{-8} kgm^2 [87].

The product of inertia terms will have a very limited effect if they are only in the I_{xy} term because of the low angular velocity about the x and y axes compared with the rate about the z-axis. For example in Figure 7.23 while potentially generating 680 mNm of torque the rotor was tilted about the x-axis at 0.558 rads^{-1} compared with a spin rate of 524 rads^{-1} about the z-axis. Therefore the I_{xz} and I_{yz} terms need to be minimised during balancing.

Simulating the rotor dynamics in open loop the product of inertia terms I_{xz} and I_{zx} were set to -2×10^{-8} kgm^2 while the rotor was initially spinning around the z-axis at 524 rads^{-1} and stationary about the other axes. Figure 8.3 shows the rotational rates about the x and y axes as a result of the I_{xz} and I_{zx} terms. The magnitude of the rate is independent of the spin rate of the rotor and is determined by the magnitude of the products of inertia.

When the spinning rotor is tilted there will be a component of the rotor's angular velocity in the x or y-axes. For a rotor spinning at 524 rads^{-1} a 1° tilt about the y-axis will result in a angular velocity component about the x-axis of $524\sin(1^\circ) = 9.1$ rads^{-1}. Figure 8.4 shows the disturbance in the rotation rates about the x and y-axes when simulated open loop with a diagonal rotation matrix. Due to the large magnitude of the rates compared with off diagonal products of inertia the magnitude of rate disturbance can be assumed to be proportional to the component of the rate about the x or y-axis.

Figures 7.23 and 7.35 show the periodic disturbance in the hardware rotor's tilt angle after being tilted with the H∞ decoupled and multi-variable controllers. This disturbance is due to the component of the rotor's angular velocity in the x or y-axes. It is important that controllers are able to overcome this disturbance to minimise noise generated on the platform. The disturbance occurs at the frequency that the rotor is spinning with, which is likely to be greater than the bandwidth of the controller.

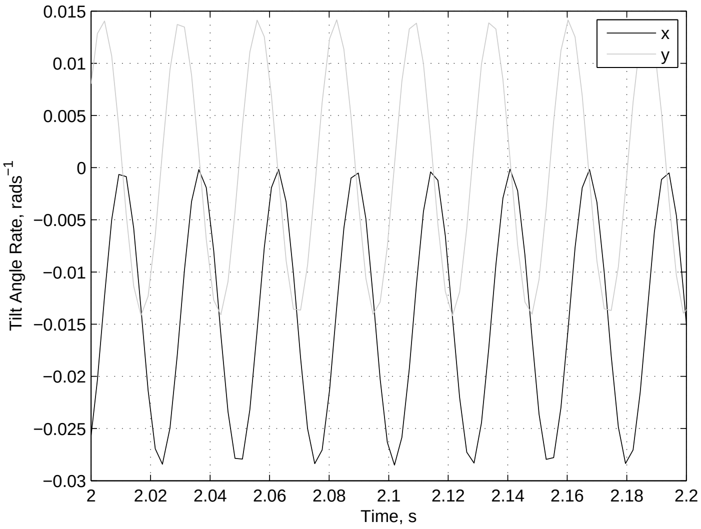

Figure 8.3: The rotor's attitude rates with a product of inertia $I_{xz} = I_{zx} = -2 \times 10^{-8}$ kgm^2 spinning at 524 rads^{-1}.

8.2.1 Feed Forward Compensation

Because the $\boldsymbol{\omega} \times \mathbf{I}\boldsymbol{\omega}$ term in the dynamics of rotational motion generates a disturbance with a frequency component at the same frequency as the rotor's spin rate, which is likely to be greater than the bandwidth of the controller, a control strategy to counteract this disturbance needs to be designed. The proposed solution is to use the existing H∞ decoupled or multivariable controllers to control the rotor's position but to add a feed forward term that directly counteracts the $\boldsymbol{\omega} \times \mathbf{I}\boldsymbol{\omega}$ disturbance. This term will be calculated directly by algebra and so its maximum frequency will be determined by the frequency of the real time operating system. Because the eddy current sensors only measure the rotor's position, the extended Kalman filter (EKF) described in Section 6.3.2 has to be used to calculate the rate $\boldsymbol{\omega}$. Figure 8.5 shows the proposed controller structure. This technique is also called feedback linearisation as the feed-back term linearises the rotational dynamic equations of motion.

$\boldsymbol{\omega} \times \mathbf{I}\boldsymbol{\omega}$ generates a torque, which must be converted to a current to be applied to the electromagnets. The kinematic mapping from electromagnet output force to torque is given by Equation 6.22. This matrix can be inverted using the Moore-Penrose pseudoinverse [88]:

$$\mathbf{H}^{+} = \mathbf{H}^{T}(\mathbf{H}\mathbf{H}^{T})^{-1} \tag{8.2}$$

If the r_T gain term is added later the inverse is given by:

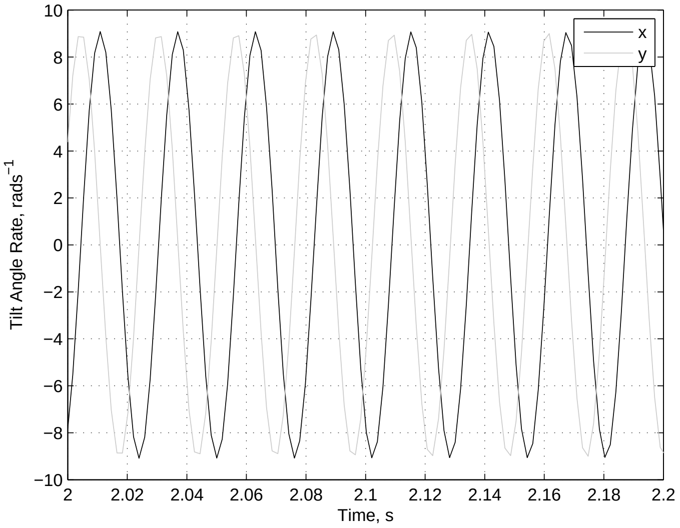

Figure 8.4: The rotor's attitude rates while spinning at 524 rads^{-1} but tilted about the y-axis by 1°.

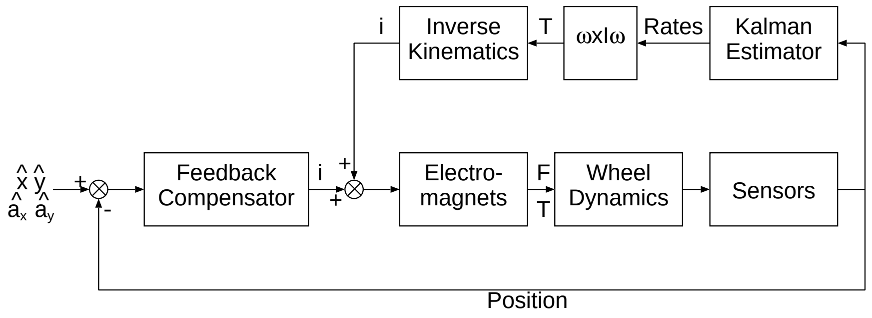

Figure 8.5: The proposed controller structure incorporating the Kalman filter and feed forward term.

$$\begin{bmatrix} 0 & \frac{1}{4} \\ 0 & -\frac{1}{4} \\ -\frac{1}{4} & 0 \\ \frac{1}{4} & 0 \\ 0 & -\frac{1}{4} \\ 0 & \frac{1}{4} \\ \frac{1}{4} & 0 \\ -\frac{1}{4} & 0 \end{bmatrix} \tag{8.3}$$

Two approaches were taken to convert the forces f_1 to f_8 generated by the pseudo inverse into eight currents. As the linearised reluctance force equation (Equation 6.38) is used in the generation of the decoupled controllers then the feed forward currents should be calculated using $i_n = f_n/K_i$. The alternative of rearranging the standard non-linear reluctance force equation (Equation 3.4) to give the current in terms of force was also tried.

Because the rotor had not been balanced, its inertia matrix was unknown and it was not able to stabilise the hardware with a feed forward term as there was too great a disparity between the model that the EKF and feed forward term were built around. Therefore, simulation results will be presented here.

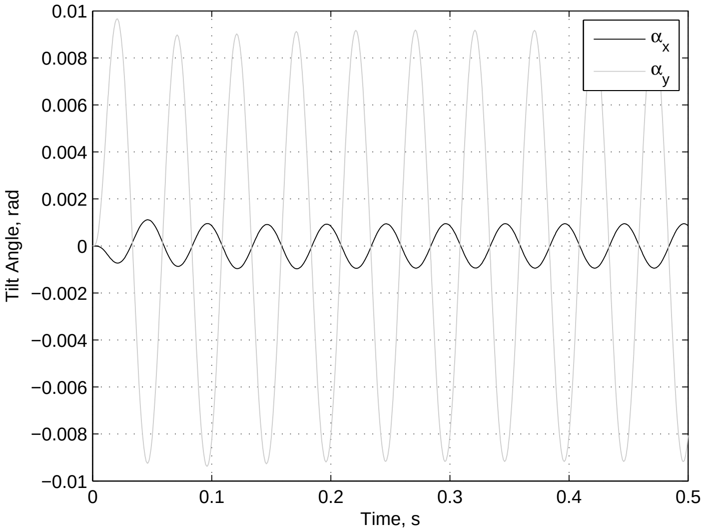

Figure 8.6: The wheel tilt angles in a simulation with no feed forward control.

Figure 8.6 shows the results from a simulation with the wheel spinning at 52 rads^{-1} and with a tilt demand on the rotor of a sine wave with peak amplitude of 0.01 radians at 20 Hz. There is no feed forward term in this model. The inertia matrix contains the product of inertia $I_{xz} = I_{zx} = -2 \times 10^{-8}$ kgm^2. Due to the $\boldsymbol{\omega} \times \mathbf{I}\boldsymbol{\omega}$ term there is coupling between the axes. Because the coupling is below the bandwidth of the controller some of the coupled disturbance has been damped by the controller.

Figure 8.7 shows the results from the same simulation but with a feed forward term. The rates $\boldsymbol{\omega}$ used in the term are taken directly from the output of the dynamic equations of motion. This is not possible when implemented with the 3Dwheel hardware as the sensors can only measure positions and not rates. The feed forward value was applied to the model by converting to linearised currents. This was repeated for currents calculated non-linearly and with the EKF calculating the rates. The results are presented in Table 8.1. Using the feed forward term reduced the cross coupled rotational disturbance in all cases. Calculating the current using the non-linear reluctance force equation gave a better performance than by using the linearised form. When the rates were calculated using the EKF the performance was not as good as in the physically unrealisable case of taking them directly from the model. Further work to improve the tuning of the EKF may result in an improvement of the 4 dB increase in cross-coupling rejection that this simulation suggested is possible.

To illustrate the benefits of the feed forward term Figure 8.8 shows the currents generated by the decoupled H∞ rotation controllers with no feed forward term present when being demanded to tilt the rotor at 20 Hz about the y-axis. Figure 8.9 shows the same currents but with the feed forward term present. There is a 17.0 dB drop in current about the x-axis because the

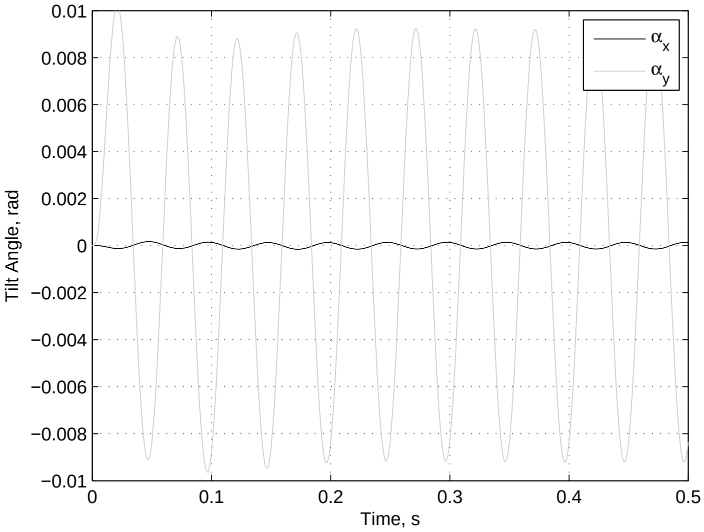

Figure 8.7: The wheel tilt angles in a simulation with the tilt rates taken directly from the equations of motion and the feed forward applied as linearised currents.

Method	Peak Magnitude of gyroscopic disturbance about the x-axis
No feed forward	1.0 mrad
Act. rates via lin. i	0.15 mrad
Est. rates via lin. i	0.35 mrad
Act. rates via non-lin. i	0.05 mrad
Est. rates via non-lin. i	0.25 mrad

Table 8.1: The performance of the various feed forward implementations.

feed forward term is damping the cross coupled motion. The feed forward term has the benefit of being implemented algebraically and so does not have the bandwidth limitation that the compensators do at high rotor spin rates.

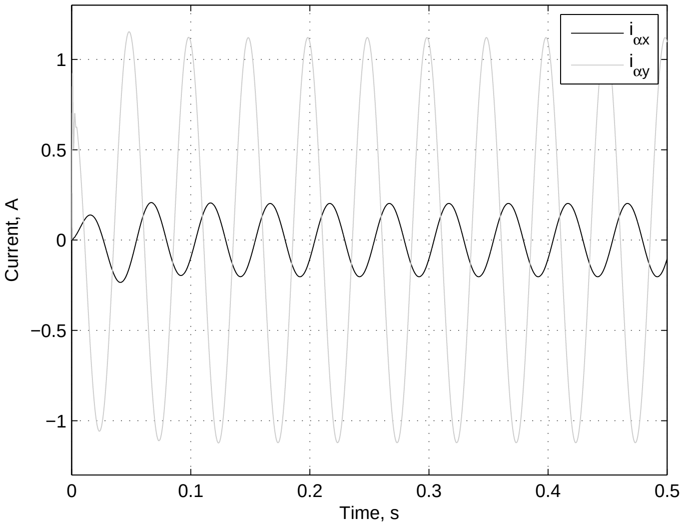

Figure 8.8: The rotation controller currents in a simulation with no feed forward term.

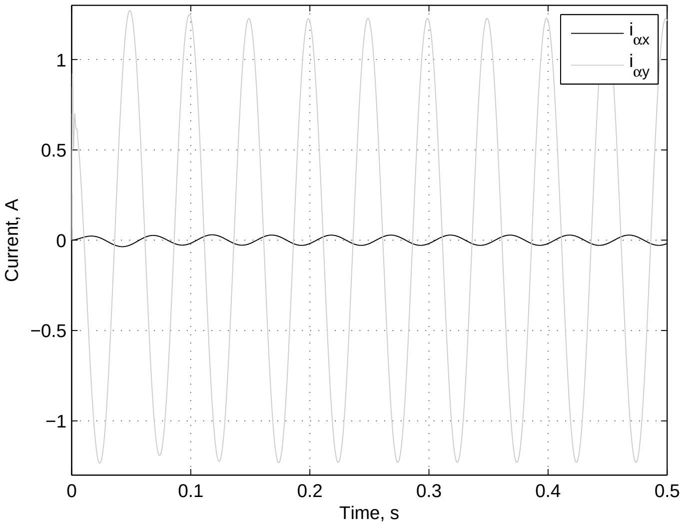

Figure 8.9: The rotation controller currents in a simulation with the tilt rates taken directly from the equations of motion.

8.3 Power Consumption

The engineering model of the 3Dwheel was developed to prove the 3Dwheel concept of a tilting magnetically-levitated momentum-wheel; no effort was made to minimise its power consumption. Power consumption is however an important consideration for the development of a flight ready 3Dwheel. The power consumption of the 3Dwheel engineering model's components is given in Table 8.2. The bias current through each electromagnet was 2.4 A during these measurements. One option to improve the power consumption is to change from the electromagnetic to the electrodynamic principle and have the bias flux generated by permanent magnets rather than the electromagnets, as described in Section 3.3.1. The Control Only value in Table 8.2 refers to the component of the current required to control the position of the rotor and not any bias flux as shown in Figure 8.10 and discussed later, additionally the rotor is assumed to be perfectly balanced.

5 × Eddy Current Sensors	0.22 A at 18.0 V = 4.0 W
8 × Current Amplifiers Quiescent	1.4 A at 28.0 V = 39 W
8 × Current Amplifiers Levitating	20.0 A at 28.0 V = 560 W
8 × Current Amplifiers Control Only	2.8 A at 28.0 V = 78 W
Brushless Motor at >20 mNm	0.24 A at 18.0 V = 4.3 W

Table 8.2: The power consumption of the hardware system components.

Section 7.1 describes how the currents from the four controllers are combined in the decoupled controllers to form the current demands for each of the eight electromagnets. Figure 8.10 shows the sum of the magnitudes of the eight electromagnet currents generated by the control currents (the two translation and two control currents) from the $H\infty$ decoupled controller while levitating the rotor while it was not spinning. The magnitude of the control currents was used because the control currents are negative at times, but still require power to generate them. The mean total current over 34.0 seconds was 2.8 A, the power supplies are fed from a 28 V supply giving an average power consumption of 78 W. Figure 8.11 shows the same data but with the rotor spinning at 500 rpm. The mean current this time was 3.5 A over 30.0 seconds, giving an average power consumption of 98 W for all components. Unfortunately it was not possible to record data from the $H\infty$ multi-variable controller to make a comparison against as its greater complexity did not leave enough time for recording the data during each period of the real-time operating system.

The bias current chosen for each controller determines the wheel's power consumption. A bias current of 2.4 A was used as this was the lowest current that generated enough stiffness for stable levitation. The bias current i_0 is a component of the plant dynamics and so the controller must be updated when the bias current is changed.

Providing a bias current of 2.4 A to eight electromagnets results in a power consumption of 538 W, which explains the high power consumption in Table 8.2. Although using the electromagnetic principle results in the possibility of generating larger forces compared with providing bias flux from permanent magnets, the additional stiffness comes with a penalty in the form of power consumption. To minimise the power consumption of the 3Dwheel as much flux as possible should come from permanent magnets.

Existing magnetically-levitated momentum-wheels have power consumptions ranging from

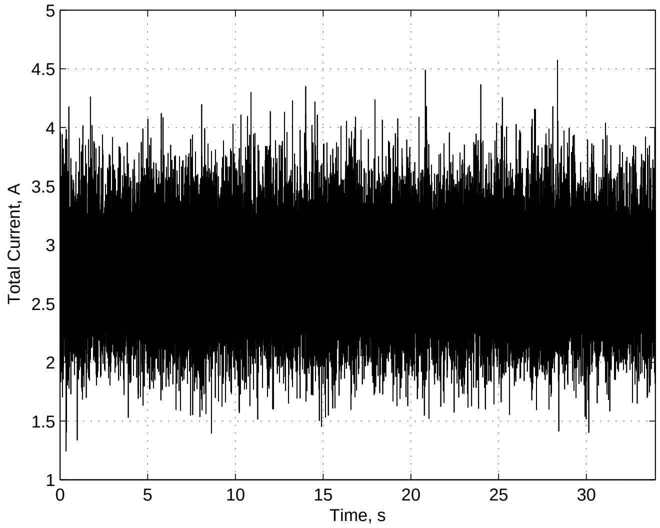

Figure 8.10: The magnitude of the total controlled current, excluding bias current, for the H∞ decoupled controller to levitate the rotor while it was not spinning.

2.5 W [14] to 23 W [31] for suspension. With total power consumption including the motor while generating its maximum torque ranging up to 37 W [17] and even 190 W [24] for magnetically levitated wheels on the large SPOT satellites.

The power consumption of the 3Dwheel has two components translational and rotational. In other non-tilting momentum wheels rotational motion is passively controlled resulting in a lower power consumption. The 3Dwheel requires larger air gaps than other wheels to allow the rotor to tilt. To generate the same force, current is proportional to the air gap width, resulting in the 3Dwheel's increased power consumption. Existing wheels have air gap widths of between 0.6 mm [17] and 1.0 mm [23], while the 3Dwheel's is 1.4 mm.

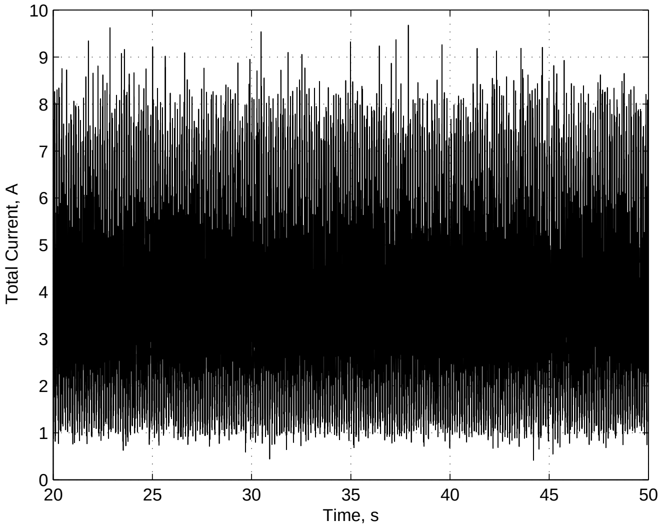

Figure 8.11: The magnitude of the total controlled current, excluding bias current, for the H∞ decoupled controller to levitate the rotor while it was spinning at 500 rpm.

8.4 3Dwheel on a Satellite

The 3Dwheel hardware has been successfully demonstrated providing a 3 axis output torque in the laboratory. This final section shows how the 3Dwheel's proven ability can be applied on a satellite to provide attitude control of the TopSat satellite. It will be shown that a single 3Dwheel can provide 3-axis attitude control of a small satellite. Figure 6.3 gave an overview of the system showing the 3Dwheel fitted to a spacecraft.

For these simulations the dynamic model of the 3Dwheel was added to the dynamic model of a spacecraft, which is described in Appendix C. The inertia matrix from Surrey Satellite Technology Limited's 2005 TopSat small satellite was used in the satellite model; this matrix is [89]:

$$\mathbf{I_{sat}} = \begin{bmatrix} I_{xx} & I_{xy} & I_{xz} \\ I_{yx} & I_{yy} & I_{yz} \\ I_{zx} & I_{zy} & I_{zz} \end{bmatrix} = \begin{bmatrix} 12.053 & -0.1635 & 0.2715 \\ -0.1635 & 10.386 & -0.879 \\ 0.2715 & -0.879 & 8.398 \end{bmatrix} \tag{8.4}$$

Where closed loop control was used then Sidi's control torque command was used as described in Appendix C. The spacecraft's attitude was fed back around the control loop using quaternions rather than Euler angles to avoid singularities. The control torque command was generated by Equation C.14. The desired rotor tilt rates were calculated from Equation 6.36. The calculated desired rates were then integrated to give the desired rotor angles that were fed to the decoupled H∞ levitation controller.

8.4.1 Satellite Reorientation

TopSat is a typical modern small satellite. It has a Time Delay Integration imaging mode, where the satellite pitches during image acquisition to maintain the camera pointing at one spot on the ground, improving the image resolution [1]. TopSat also has a requirement to be able to roll up to $\pm 30^\circ$ off track to image areas that are off to the side of its ground track. Coupled with the requirement to be able to counteract disturbances such as gravity gradient, aerodynamic, solar radiation and magnetic field disturbance, a three axis attitude control system is required. Three conventional momentum wheels are required to build an attitude control system that can generate an output torque about all three axes of the satellite, although a pyramidal configuration of four wheels may be used to provide redundancy. A single 3Dwheel could be used instead of three conventional wheels to fulfil TopSat's attitude actuation requirements. With its spin axis aligned with the satellite's pitch axis it can pitch the satellite by operating conventionally and accelerating or decelerating the rotor. It can also use its gyroscopic torque output to roll the satellite for off track imaging when required and to remove any disturbances about the yaw axis.

Figure 8.12 shows the 3Dwheel rolling the TopSat small satellite through 29.3° in 45 seconds using its gyroscopic torque output while the rotor was spinning at a constant rate of 10,000 rpm. The rotor was tilted from its central position by $+2.8^\circ$ in 1 second generating a torque of 120 mNm and then returned to its central position at the end of the manoeuvre to stop the satellite from turning. This was achieved using open loop control of the desired wheel tilt angle. For implementation on a spacecraft then a form of closed loop control would be required

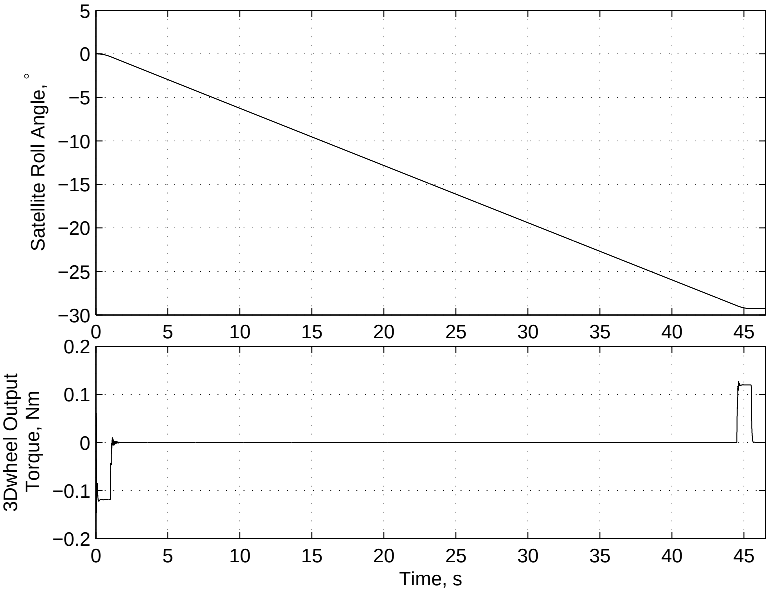

Figure 8.12: The 3Dwheel turning the TopSat small satellite through a roll angle of $29.3°$ using its gyroscopic torque output.

to ensure that the rotation rate of the spacecraft is zero at the end of the manoeuvre. To turn the satellite at a higher rate then the rotor can be spun faster, which is likely to be possible due to the lack of touching parts.

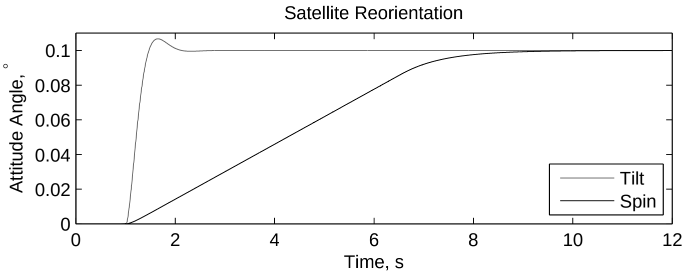

Figure 8.13: The satellite's attitude when reorientating using a tilting momentum wheel (tilt in the legend) and a conventional momentum wheel (spin in the legend).

Figure 8.13 shows the attitude of the model TopSat spacecraft in a simulation when it was reorientated through 0.1° by tilting the momentum wheel and also by conventionally accelerating the spinning rotor. This manoeuvre was performed under closed loop control of TopSat. Because of the larger output torque available from tilting the wheel, this reorientation can be performed almost five times faster than is possible by operating the wheel conventionally. The axis of the output torque when tilting the wheel is not fixed and so this torque can be generated about any axis normal to the wheel's spin axis. The large torque and high bandwidth makes the 3Dwheel ideal for spacecraft rendezvous and docking or remote servicing missions.

8.4.2 Disturbance Damping

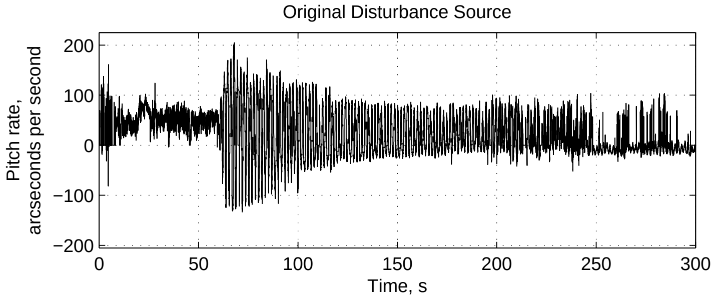

Figure 8.14: The attitude rate observed on the UK-DMC satellite while it was suffering from a high frequency disturbance [7].

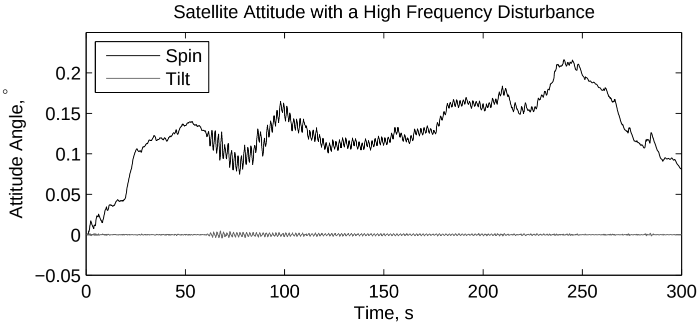

Figure 8.15: The satellite's attitude when applied with the high frequency disturbance shown in Figure 8.14, with the disturbance being damped by a tilting momentum wheel (tilt in the legend) and a conventional momentum wheel (spin in the legend).

A disturbance in the attitude rates of the UK-DMC spacecraft had been identified through image processing [7]. With a frequency of 0.6 Hz the disturbance was too high for the conventional momentum wheels on UK-DMC to damp. The effect of the disturbance is visible in the attitude rate shown in Figure 8.14. This angular rate data was differentiated to give an angular acceleration and then multiplied by UK-DMC's moment of inertia about that axis to give the torque that caused the disturbance. This torque was then applied to the TopSat model using closed loop control and its attitude is shown in Figure 8.15 when the disturbance is damped by the momentum wheel operating conventionally and when tilting.

The magnitude of the attitude disturbance is over twenty times less when damped with a tilting momentum wheel than when it is damped by a momentum wheel operating conventionally. This improvement in performance is due to the 3Dwheel's improved bandwidth.

8.4.3 Frequency Response

Figure 8.16 shows the frequency response measured using the DSA tool of the attitude control system of the simulated TopSat satellite with the 3Dwheel generating a gyroscopic torque by tilting and a conventional momentum wheel. With the 3Dwheel fitted the cross-over frequency

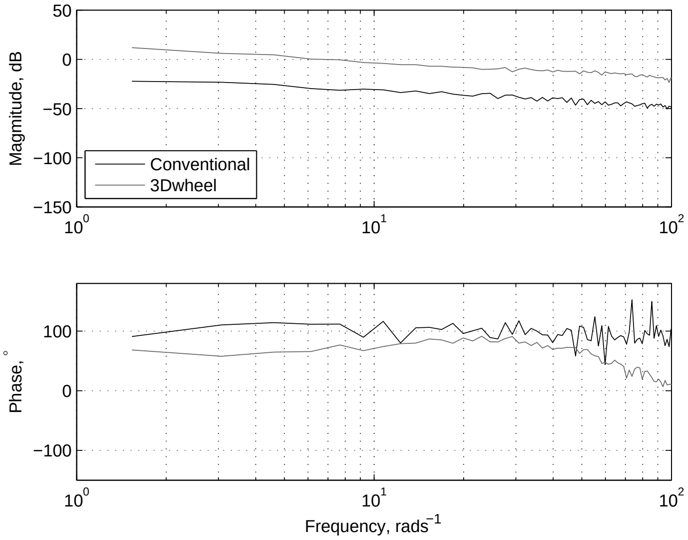

Figure 8.16: The frequency response of the simulation of the 3Dwheel generating a gyroscopic torque by tilting and a conventional momentum wheel on the TopSat satellite measured using the DSA tool.

of the attitude control system is 6.7 rads^{-1}. The satellite model used closed loop control with quaternion feedback. The cross-over frequency and hence bandwidth of the system fitted with the conventional momentum wheel was too low be measured with the DSA tool. Interpolating the measured response it appears to be around two orders of magnitude less than the 3Dwheel's. Conventional wheels are satisfactory for satellite reorientations or for damping disturbances that have a period equivalent to the orbital period such as gravity gradient or solar radiation disturbance, but cannot damp microvibrations.

8.5 Conclusions

The 3Dwheel can generate a torque about its spin axis in exactly the same way as a conventional momentum wheel. The addition of the ability to tilt does not affect its ability to generate this conventional torque. Because of lack of mechanical bearings and friction then the bandwidth of this conventional torque may be increased, although this theory had not been tested. The rotor could also be be spun faster increasing its angular momentum.

Because the 3Dwheel engineering model's rotor was not balanced its inertia matrix and particularly the products of inertia were not known. This resulted in the feedback linearisation technique not being tested on the hardware and the performance of the multi-variable controllers at removing cross-coupling not being investigated.

When tilted there is a component of the spinning rotor's angular velocity about the other axes. This creates a periodic disturbance about the x and y-axes. The frequency of this disturbance will be greater than the controller's bandwidth for high spin rates. Feed forward compensation has been suggested in this thesis as a solution to this problem. Because the rotor's static imbalance and inertia matrix were unknown feed forward compensation could not be successfully tested with the 3Dwheel hardware. If the feed forward term is not able to damp all of the disturbance generated when the spinning rotor is tilted then the range of angles that the rotor tilts through may have to be limited, limiting the time duration that the tilting torque can be generated for.

With all of the 3Dwheel's bias flux being provided by the electromagnets it has a high power consumption, with 335 W being required for bias flux. To improve the power consumption the 3Dwheel must be changed from using the electromagnetic to the electrodynamic principle with some of the bias flux being generated by permanent magnets. While spinning at 500 rpm, 98 W was required for active control of the spinning rotor, which is four times greater than any existing magnetically levitated momentum wheel. This increase is due to the 3Dwheel requiring power to actively control translational and rotational degrees of freedom. In non-tilting designs the rotational motion is passively controlled. The width of the electromagnets' air gaps in the 3Dwheel is greater than in non-tilting wheels to allow room for the rotor to move. The air gap width and hence power consumption can be reduced by limiting the range of angles that the rotor can be tilted through. The controllers derived were not optimised for power consumption. The power consumption may be reduced slightly by optimising the controllers. A complete multi-parameter optimisation of the 3Dwheel could be performed to choose the optimal design in terms of torque output, tilt range and power consumption. This increase in power consumption is a penalty that occurs if the benefits of a tilting momentum wheel are required.

The demonstrated performance of the 3Dwheel has also been shown to be ideal for use on a spacecraft. The gyroscopic output torque can be used to reorientate a typical small satellite. The conventional torque output about the wheel's spin axis is no different from existing momentum wheels'. The high bandwidth of the gyroscopic output has been demonstrated to be ideal for damping high frequency disturbances on a satellite. The ability to generate a greater torque than a conventional momentum wheel and its greater bandwidth also makes it ideal for applications such as spacecraft rendezvous or robotic servicing. The 3Dwheel's reduced mass and volume compared to a set of conventional wheels gives further reason to use it.

Chapter 9

Conclusions

A tilting magnetically levitated momentum wheel called the 3Dwheel has been modelled, designed, built and successfully demonstrated.

Chapter 2 presented the 3Dwheel concept developed for this thesis and explained how it compared with existing attitude control actuators. The torque output envelope about all three principal axes of a spacecraft was demonstrated. The existing literature was reviewed demonstrating that the 3Dwheel concept is both novel and practical.

Chapter 3 examined the theory behind magnetism. This knowledge allows the materials used to build the laboratory model of the 3Dwheel to be chosen. The forces generated by an electromagnet were then derived and the concept of stiffness introduced. The basic geometry of an electromagnet was then presented.

Chapter 4 presented the three electromagnet geometries developed for this thesis. Analytical and finite element models of each of these geometries were developed using the knowledge developed in Chapter 3. The effect on the electromagnet's properties of changing each of the dimensions of the electromagnet were investigated. Careful magnet design is required to ensure that the 3Dwheel's rotor is controllable at all rotor positions and this was demonstrated.

Chapter 5 built on the knowledge and results generated in the previous two Chapters to present the two pieces of hardware that were designed and developed during this thesis to demonstrate in the laboratory the theoretical and simulation results. The design process developed and presented in this Chapter for the engineering model of the 3Dwheel that was successfully levitated and demonstrated in the laboratory can also be applied to future tilting magnetically levitated momentum wheels, such as a flight-ready version of the 3Dwheel. Some additional mechanical components that were not required for the engineering model were discussed along with suggestions as to how they can be designed and built. Together with the existing practical demonstration of the 3Dwheel they show that the 3Dwheel concept is suitable for a flight on a spacecraft.

Chapter 6 developed a linearised and non-linear model of the 3Dwheel's dynamics of motion. These models are required to evaluate the performance of the 3Dwheel, and to develop and test controllers to stabilise its levitation and motion. There was also a discussion on how a real rotor's imbalance affects its motion and a technique to measure this imbalance was developed.

Kalman Filters to estimate the rotor's rate of rotational motion were developed along with a technique to tune the Kalman Filters using experimental data.

Chapter 7 describes the four controllers that were developed for this thesis to control the levitation and motion of the 3Dwheel. Results from simulations and from the successful operation of the 3Dwheel in the laboratory were presented allowing a comparison of the controllers to be made.

Chapter 8 presented additional results from the evaluation of the 3Dwheel hardware. Its ability to generate a conventional torque about its spin axis and its power consumption were measured. Now that the 3Dwheel hardware had been successfully demonstrated in the laboratory, simulations were presented showing how its gyroscopic output torque can be used to reorientate the TopSat small satellite, thus providing 3-axis attitude control from a single actuator.

9.1 Summary

The 3Dwheel concept has been successfully demonstrated in simulation and in the laboratory. Four degrees of freedom in the 3Dwheel are actively controlled allowing the rotor to be tilted or gimballed, generating a gyroscopic output torque. The tilt axis can be steered to be anywhere in the plane normal to the rotor's spin axis. A single 3Dwheel can therefore generate an output torque about all three principal axes of a spacecraft.

The magnetic bearings used in the 3Dwheel are based on the electromagnetic principle, while existing magnetically levitated momentum wheels have used the electrodynamic principle. The rotor's position can be controlled with a high accuracy while being levitated; the translational position of the rotor can be maintained to three sigma of the desired position within 11.6 μm. A maximum tilt rate of 0.558 rads^{-1} has been achieved with the wheel spinning at 496 rpm, generating a gyroscopic output torque of 0.067 Nm. This tilt rate would generate a torque of 0.68 Nm at 5000 rpm. Use of the 3Dwheel to provide 3-axis control of a satellite's attitude has been demonstrated in simulation.

The magnetically levitated momentum wheel solves many of the problems that designers of momentum wheels for small satellites face. There is no contact between moving parts and so no wear and hence an increased lifetime. Some existing momentum wheels are operated at low spin rates to minimise wear. With the 3Dwheel having no wear the full angular velocity range of the wheel can be used generating larger torques, or providing greater gyroscopic stability. The reduced levels of friction allow the wheel to have a greater bandwidth.

The 3Dwheel's rotation axes cross-over frequency is in the order of 120 rads^{-1}, with the translation axes having a cross-over two or three times greater. When fitted to the TopSat satellite in simulation, the 3Dwheel has a bandwidth two orders of magnitude greater than a conventional momentum wheel. This improved bandwidth makes the 3Dwheel ideal for damping microvibrations on imaging satellites, improving their image quality, or for high bandwidth small angle manoeuvres, such as in spacecraft rendezvous and docking. For satellite reorientations the conventional torque generated by accelerating the magnetically levitated rotor is more suitable.

The rotor in the engineering model of the 3Dwheel was not balanced. At higher spin rates the rotor's static and couple imbalance generated a large disturbance on the rotor limiting the maximum rate that the rotor could be spun at. This prevented the feed forward compensation technique from being tested.

When the spinning rotor is tilted there is a component of the rotor's spinning angular velocity about the x and y-axes generating a disturbance. This disturbance has the same frequency as the rotor's spin rate, which may be greater than the bandwidth of the controller. If this disturbance cannot satisfactorily be damped using techniques such as feed forward compensation then the range of angles that the rotor tilts through will have to be limited.

The power consumption of the engineering model of the 3Dwheel is high for several reasons. Because it uses the electromagnetic principle, the bias flux that is required for the stiffness of the wheel must be generated by the electromagnets. The advantage of the electromagnetic principle compared with the electrodynamic principle is the ability to generate larger forces and hence have a greater stiffness, if required. The electrodynamic approach has a linear relationship between force and current that aided the design of controllers in the past. This project has shown that modern control techniques and implementations can overcome the electromagnetic principle's non-linear force-current relationship. However, the reduced power consumption of the electrodynamic principle means that it should be preferred over the electromagnetic principle for magnetically levitated momentum wheels on spacecraft.

Ignoring the component of the power-consumption required to generate the bias flux, the 3Dwheel still has a power consumption four times greater than other magnetically levitated momentum wheels. This is due to the 3Dwheel's increased air gap widths to allow for the motion of the rotor while tilting. The current drawn is proportional to the air gap width while generating a constant force. An increase in power consumption is a penalty that must be accepted if the 3Dwheel's benefits of a 3-axis high-bandwidth output torque are required.

Three conventional momentum wheels are required for 3-axis attitude control of a spacecraft. These can be replaced with a single 3Dwheel providing mass and volume savings. The mass and volume savings still exist if two 3Dwheels are used for redundancy. There is a penalty in terms of increased power consumption though.

It has been shown in simulation that a single 3Dwheel can reorientate a small satellite using its gyroscopic torque output. Additionally, the 3Dwheel can generate an output torque about its spin axis by accelerating the rotor as well as a conventional wheel can.

9.2 Novelty

This project is novel because:

- a magnetically levitated momentum wheel using the electromagnetic principle sized for a small satellite has been designed, built and demonstrated in the laboratory;
- the wheel hardware has been tilted through 2.9° in the laboratory, which is a factor of three greater than other designs. The robustness of this wheel's controller allows stable levitation throughout this tilt range;
- the tilt range means that this is the first tilting momentum wheel that is capable of generating a controllable torque about all three axes that can reorientate a small satellite;

- the design of a tilting magnetically levitated momentum wheel that has been built and successfully demonstrated is described and discussed providing a scalable design methodology for such a wheel;
- the performance and benefits of including the ability to tilt the rotor in a magnetically levitated momentum wheel have been examined.

9.3 Future Work

This project and the engineering model of the 3Dwheel have demonstrated that the tilting magnetically levitated momentum wheel concept works. The following items need to be further developed to produce a flight ready 3Dwheel for use on a spacecraft:

- modification of the mechanical design by the inclusion of permanent magnet bias flux and a revised controller design to use the electrodynamic principle to minimise the power consumption;
- a revised mechanical design to place the electromagnets and sensors in the centre of the rotor to minimise the volume of the design;
- optimise the magnet and rotor design to produce an optimal design in terms of power, mass, volume and torque capability;
- develop controllers to use the 3Dwheel to perform large angle slew manoeuvres;
- development of embedded controller hardware that is low volume and low power consumption to replace the PC based control system implemented in the engineering model of the 3Dwheel. Such controllers are commonly used in modern digital electronics using Digital Signal Processing (DSP) Integrated Circuits (ICs) or microprocessors. Development systems are available from most manufacturers to speed the design process. Some attention must be paid to ensuring that the electronics is radiation hardened and tolerant of the space environment. In low earth orbit, where the small satellites that are the most likely to use the 3Dwheel concept fly, radiation hardened Field Programmable Gate Array ICs are available on which DSPs and microprocessors can be easily implemented;
- replacement of the linear current amplifier with a more power efficient switching class-D amplifier;
- design touch down bearings and a launch lock mechanism. Various ideas for these items are discussed in Section 5.3.

9.4 Publications and Awards

- Jon Seddon, Alexandre Pechev, *3Dwheel - A Single Actuator Providing 3-Axis Control of Satellites*. AIAA Journal of Spacecraft and Rockets, 49(3):553-556, 2012

- Jon Seddon, Alexandre Pechev, *3Dwheel: 3-axis low-noise, high-bandwidth attitude actuation from a single momentum wheel using magnetic bearings*. In Proceedings of 23rd Annual AIAA/USU Conference on Small Satellites, Utah, USA, 10-13 August, 2009
- Jon Seddon, Alexandre Pechev, *A low-noise, high-bandwidth magnetically-levitated momentum-wheel for 3-axis attitude control from a single wheel*. In Proceedings of 13th European Space Mechanisms and Tribology Symposium (ESMATS), Vienna, Austria, 23-25 September, 2009
- Royal Aeronautical Society Aerospace Speakers' Travel Grant for attendance at the Utah Small Satellite conference.
- Royal Academy of Engineering International Travel Grant for attendance at the ESMATS conference.

Appendix A

Derivation of the Reluctance Force Equation

The approaches taken by Molenaar [64] and Demarest [63] are used here. The dimensions used in this derivation are shown in Figure A.1. ε is the width of the electromagnet poles and l is the depth of the poles, both in metres. γ is the air-gap width - the separation between the rotor and the stator, also in metres. i is the current flowing through the coil in amperes and N is the number of turns in a coil. γ_{rotor} and γ_{stator} are the distances in metres that the magnetic flux flows through the iron of the rotor and stator respectively.

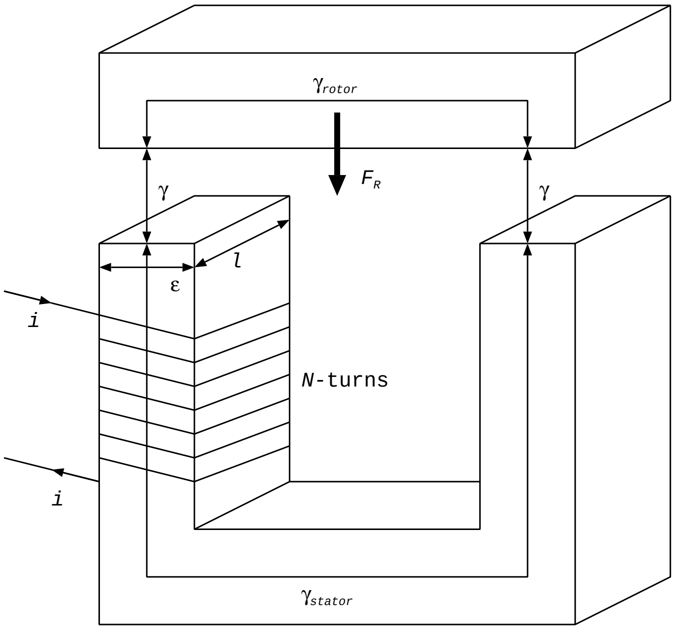

Figure A.1: The dimensions used in calculating an electromagnet's reluctance force.

Assuming that the permeability of the rotor and stator are large and that the air-gap width is small then:

- there is no fringing in the air-gaps - flux flows in a straight line through the air-gap;

- there is no leakage flux.

The cross-section area A_{EM} of the circuit is given by:

$$A_{EM} = \varepsilon l \tag{A.1}$$

Because of the assumptions made the magnetic field $\mathbf{B}$ will be nearly uniform throughout a cross section of this magnetic circuit. The magnetic flux Φ can then be found by integrating over a cross section of the circuit:

$$\Phi = \int_{A_{EM}} \mathbf{B} \cdot \mathbf{dA_{EM}} = BA_{EM} \tag{A.2}$$

where B is the magnetic flux density in tesla. The relationship between the magnetic flux and the current flowing in the coils can be found by evaluating Ampere's Law clockwise around the magnetic circuit $\sum \gamma$, which includes γ twice, γ_{rotor} and γ_{stator}:

$$\oint_{\sum \gamma} \mathbf{H} \cdot \mathbf{d}\boldsymbol{\gamma} = \oint_{\sum \gamma} \frac{1}{\mu} \mathbf{B} \cdot \mathbf{d}\boldsymbol{\gamma} = Ni \tag{A.3}$$

where $\mathbf{H}$ is the magnetic field strength and μ is the permeability of the appropriate material - iron or air. The lines of flux have been assumed to be parallel to $\sum \gamma$ and so $\mathbf{B} \cdot \mathbf{d}\boldsymbol{\gamma}$ can be replaced with $Bd\gamma$. B is also a constant and so we can simplify to:

$$B \oint_{\sum \gamma} \frac{1}{\mu} d\gamma = B \left(\frac{\gamma_{rotor} + \gamma_{stator}}{\mu_{iron}} + \frac{2\gamma}{\mu_{air}} \right) = Ni \tag{A.4}$$

Because:

$$B = \frac{\Phi}{area} \tag{A.5}$$

We can write:

$$\Phi = \frac{Ni}{\dfrac{\gamma_{rotor} + \gamma_{stator}}{\varepsilon l \mu_{iron}} + \dfrac{2\gamma}{\varepsilon l \mu_{air}}} \tag{A.6}$$

However, $\mu_{iron} \gg \mu_{air}$ and in a vacuum $\mu_{air} \approx \mu_0$, so we can approximate Φ to:

$$\Phi = \frac{Ni}{\dfrac{2\gamma}{\varepsilon l \mu_0}} = \frac{Ni\varepsilon l \mu_0}{2\gamma} \tag{A.7}$$

From Demarest [63], the magnetic energy W_R of this reluctance circuit is:

$$W_R = \frac{1}{2}\int_V \mathbf{B}\cdot\mathbf{H}dv \tag{A.8}$$

Where V is the surrounding volume of the magnetic circuit. Again, because $\mu_{iron} \gg \mu_{air}$, we need only consider the airgap, and $B = \Phi/S = \mu_0 H$ so:

$$W_R = \frac{1}{2}\frac{\Phi^2}{\mu_0(\varepsilon l)^2}2\gamma\varepsilon l = \frac{\Phi^2\gamma}{\mu_0\varepsilon l} = \frac{\mu_0\varepsilon l N^2 i^2}{4\gamma} \tag{A.9}$$

From Demarest [63], the reluctance force F_R is given by:

$$\mathbf{F_R} = \boldsymbol{\nabla}\mathbf{W_R}|_{constant\ i} \tag{A.10}$$

And so:

$$F_R = \frac{\delta W_R}{\delta\gamma} = -\frac{\mu_0 N^2\varepsilon l i^2}{4\gamma^2} \tag{A.11}$$

Appendix B

Tools and Techniques

B.1 Digital Signal Analyser (DSA)

The Digital Signal Analyser tool is a Matlab/Simulink tool that allows the frequency response of a closed loop system to be identified. It works by injecting a source signal into the system and then recording the system's response. A modified version of the Matlab Empirical Transfer Function Estimate is used to compute the ratio of the output Fast Fourier Transform (FFT) to the input source's FFT, generating the frequency response of the closed loop system. The frequency response is generally displayed as a bode plot, but Nyquist and Nichols plots can also be generated. The source signal can be chosen to be either a swept sine wave or white noise. The start and stop frequencies and the duration of the simulation must be specified for the swept sine wave. The amplitude of the source must be specified for both types of signal.

The DSA tool was used in both simulations and also for hardware in the loop testing with the engineering model hardware. The bode plot generated was generally saved and then the frequency response of models of the plant system could be over plotted. The parameters of the model were varied until the model's response gives a good match against the measured response.

The signal source and simulation duration need to be carefully chosen to get the best performance from the DSA tool. A white noise source was generally preferred because at certain frequencies the system's response to a swept sine wave would cause the system to become unstable. The amplitude of the source needs to be greater than the noise levels in the system to allow a response to be measured. The greater the length of time that the simulation can be run for, particularly with a white noise source, then the more data points will be present at each frequency for the FFT improving the measured response's signal to noise ratio.

B.2 Finite Element Analysis (FEA)

Finite Element Analysis (FEA) simulations allow the properties of a system to be modelled. They are often used to calculate the stress, temperature, fluid dynamics or magnetism of a system. For this project, magneto-static simulations were used to look at the properties of the magnetic bearings.

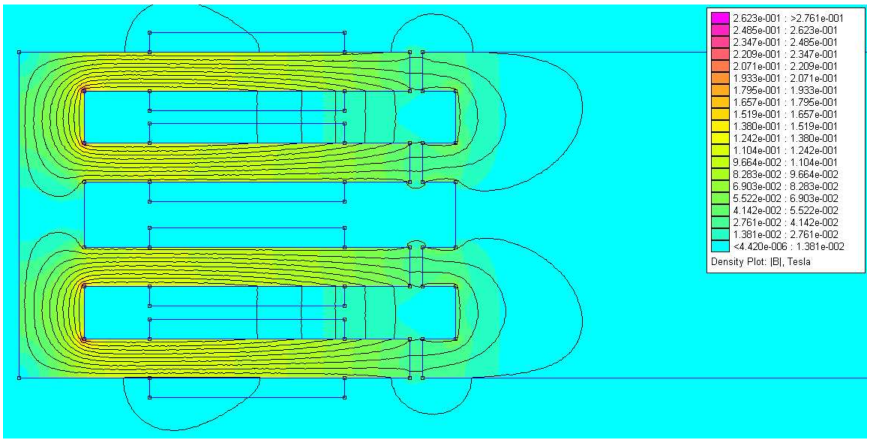

Figure B.1: A two dimensional magnetostatic finite element simulation of two electromagnets from an early design for the wheel.

There are four stages in the solution of a problem using FEA [90]:

1. Discretization of the problem into a finite number of smaller elements.
2. Deriving equations governing the behaviour of a typical element.
3. Assembling all of the elements in the problem into a matrix.
4. Solving the matrix obtained from Step 3.

FEA simulations were used in this project to check the magnitude of the flux densities in materials, to ensure that materials were not saturated, and to calculate the forces exerted by the magnetic fields. There are several methods that can be used to calculate the force, the most commonly used in this project was the Weighted Stress Tensor Method, which was implemented by the FEA software.

FEA simulations allow the properties and behaviour of a circuit to be easily and rapidly viewed. A numerical model is still required for the development of the controller, but FEA simulations save considerable amounts of time when designing the initial geometry of a system. FEA simulations are also useful to check that the numerical model has been developed correctly.

FEA software packages can solve either two-dimensional (2D) or three-dimensional (3D) problems. Several packages were used in this project. FEMM [91] is a freeware 2D program that was very easy to use and was used for the majority of the project. It also features a scripting facility that allows a design to be repeatedly analysed with components at different orientations, or at different currents. Figure B.1 shows the results of a 2D simulation in FEMM of the design shown in Figure 4.22.

Maxwell 3D [92] is a commercial package by Ansoft, now Ansys Inc., that was used to confirm that the assumptions made when simplifying the 3D designs to 2D to simulate in FEMM were valid. Figure B.2 shows the results of simulating two of the 3Dwheel's electromagnets in 3D using Maxwell.

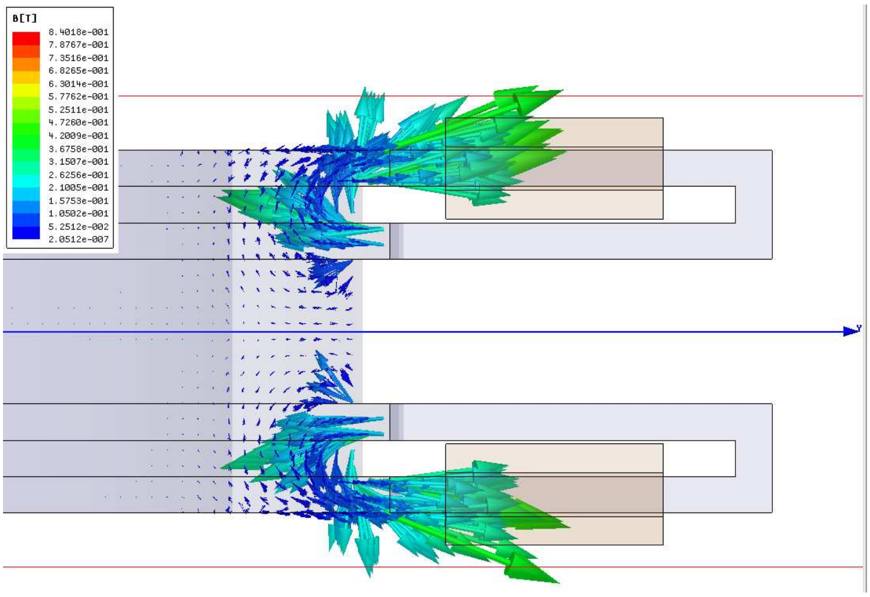

Figure B.2: A three dimensional magnetostatic finite element simulation of two electromagnets from the 3Dwheel. The direction of the arrows indicates the direction of the magnetic flux and the size of the arrows, the magnitude of the flux.

Appendix C

Satellite Dynamic Model

This Appendix describes the dynamic model of the Horyu small satellite developed by Jon Seddon during an exchange visit to Kyushu Institute of Technology, Kitakyushu, Japan during a four month break from the PhD in 2006/7. This dynamic model was reused with TopSat's inertia matrix for testing of the 3Dwheel.

C.1 Rotation Matrices

In an inertial reference frame, a point $\begin{bmatrix} x & y & z \end{bmatrix}^T$ that is rotated about the x-axis by an angle α_x will have a position $\begin{bmatrix} x' & y' & z' \end{bmatrix}^T$ after the rotation [12]:

$$\begin{aligned} \begin{bmatrix} x' \\ y' \\ z' \end{bmatrix} &= \begin{bmatrix} 1 & 0 & 0 \\ 0 & \cos\alpha_x & -\sin\alpha_x \\ 0 & \sin\alpha_x & \cos\alpha_x \end{bmatrix} \begin{bmatrix} x \\ y \\ z \end{bmatrix} \\ &= \mathbf{R_x}(\alpha_x) \begin{bmatrix} x \\ y \\ z \end{bmatrix} \end{aligned} \tag{C.1}$$

Similar equations can be written for rotations through an angle α_y about the inertial y-axis and α_z about the inertial z-axis:

$$\begin{aligned} \begin{bmatrix} x' \\ y' \\ z' \end{bmatrix} &= \begin{bmatrix} \cos\alpha_y & 0 & \sin\alpha_y \\ 0 & 1 & 0 \\ -\sin\alpha_y & 0 & \cos\alpha_y \end{bmatrix} \begin{bmatrix} x \\ y \\ z \end{bmatrix} \\ &= \mathbf{R_y}(\alpha_y) \begin{bmatrix} x \\ y \\ z \end{bmatrix} \end{aligned} \tag{C.2}$$

$$\begin{aligned}\begin{bmatrix} x' \\ y' \\ z' \end{bmatrix} &= \begin{bmatrix} \cos\alpha_z & -\sin\alpha_z & 0 \\ \sin\alpha_z & \cos\alpha_z & 0 \\ 0 & 0 & 1 \end{bmatrix} \begin{bmatrix} x \\ y \\ z \end{bmatrix} \\ &= \mathbf{R_z}(\alpha_z) \begin{bmatrix} x \\ y \\ z \end{bmatrix} \end{aligned} \tag{C.3}$$

C.2 Coordinate Systems

Three coordinate systems are in use [11]:

- the inertial equatorial axis frame with its origin at the centre of the Earth and assumed to be stationary with respect to the stars;
- the orbit reference frame that moves with the centre of mass of the satellite around the orbit. The z-axis points towards the centre of mass of the Earth, the x-axis is in the plane of the orbit, perpendicular to the z-axis and in the direction of velocity of the satellite and the y-axis is normal to the plane of the orbit and completes the right-handed axis system;
- the body frame of the satellite is the third frame. It is centred on the centre of mass of the satellite. The angles between this frame and reference frame define the satellite's attitude.

These coordinate systems are illustrated in Figure C.1.

C.3 Rotations

Several rates of rotation are defined [11]:

- $\boldsymbol{\omega}_{\mathbf{BI}}$ - the rotation of the body frame in the inertial frame;
- $\boldsymbol{\omega}_{\mathbf{BR}}$ - the angular velocity of the body frame relative to the reference frame;
- $\boldsymbol{\omega}_{\mathbf{RI}}$ - the angular velocity of the reference frame relative to the inertial frame;
- $\boldsymbol{\omega}_{\mathbf{RIB}}$ - the velocity $\boldsymbol{\omega}_{\mathbf{RI}}$ expressed in the body frame.

These rotations are related through the equation:

$$\boldsymbol{\omega}_{\mathbf{BI}} = \boldsymbol{\omega}_{\mathbf{BR}} + \boldsymbol{\omega}_{\mathbf{RIB}} \tag{C.4}$$

Because the orbit of the satellite is not a perfect circle then $\boldsymbol{\omega}_{\mathbf{RI}}$ is not a constant. The position of the satellite in its orbit and its velocity can be calculated from an orbit propagation model. Therefore the attitude model for Horyu ignores $\boldsymbol{\omega}_{\mathbf{RI}}$ and just models the motion of the body frame with respect to the reference frame.

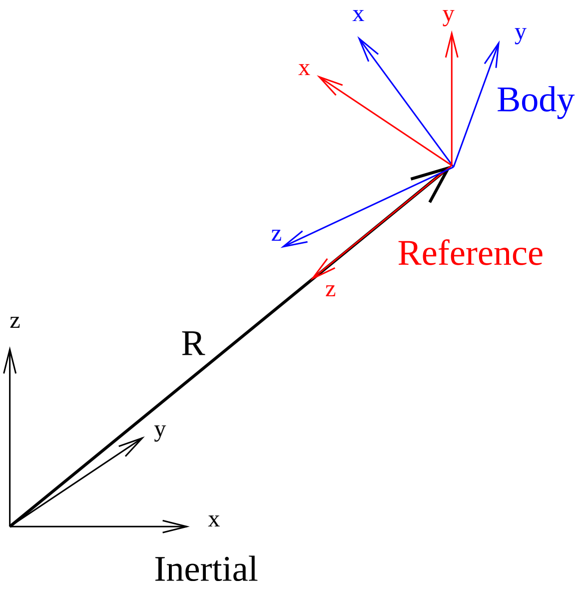

Figure C.1: The three coordinate systems used. **R** is the vector representing the satellite's position in the inertial frame.

C.4 Direction Cosine Matrix

The direction cosine matrix (DCM) is a 3 × 3 matrix and maps vectors from one reference frame to another.

The direction cosine matrix $\mathbf{A_{IR}}$ to convert from the inertial frame to the reference frame is formed by:

$$\mathbf{A_{IR}} = \begin{bmatrix} \hat{x}_{refx} & \hat{x}_{refy} & \hat{x}_{refz} \\ \hat{y}_{refx} & \hat{y}_{refy} & \hat{y}_{refz} \\ \hat{z}_{refx} & \hat{z}_{refy} & \hat{z}_{refz} \end{bmatrix} \tag{C.5}$$

Where $\hat{\mathbf{x}}_{\mathbf{ref}}$ is the unit vector along the x-axis of the reference frame, expressed in the inertial frame.

The vector $\mathbf{a_I}$, which is in the inertial frame, can be converted to the vector $\mathbf{a_R}$ in the reference frame by:

$$\mathbf{a_R} = \mathbf{A_{IR}} \mathbf{a_I} \tag{C.6}$$

A vector in the reference frame can be converted to the inertial frame by multiplying by $\mathbf{A_{IR}}^T$.

C.5 Euler Angle Representation

The attitude of the satellite can also be represented using Euler angles, which show the angles that the body frame must be rotated through to get to the reference frame. The order that the axes are rotated in is important; the same order must be used throughout the project.

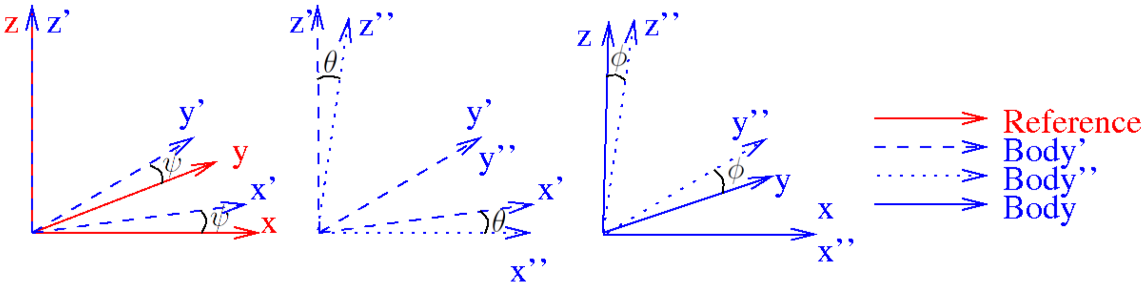

Figure C.2: The formation of the the 3-2-1 Euler angle representation. First the Reference frame is rotated by the angle ψ about its z-axis to form the intermediate Body' axis. Body' is then rotated by the angle θ about its y-axis to form the intermediate Body" axis. Finally Body" is rotated by the angle ϕ about its x-axis to form the Body axis.

For this project the Euler rotation order of 3-2-1, or yaw-pitch-roll will be used. From [12] the Euler angles can be found from the quaternions by equating terms in the direction cosine matrix for the Euler angles with the equivalent term in the quaternion direction cosine matrix. Roll is given by phi ϕ, pitch by theta θ and yaw by psi ψ:

$$\begin{aligned}\phi &= \arcsin\left(\frac{2(q_2q_3 + q_1q_4)}{\cos(\arcsin(-2(q_1q_3 - q_2q_4)))}\right) \\ \theta &= \arcsin(-2(q_1q_3 - q_2q_4)) \\ \psi &= \arcsin\left(\frac{2(q_1q_2 + q_3q_4)}{\cos(\arcsin(-2(q_1q_3 - q_2q_4)))}\right)\end{aligned} \tag{C.7}$$

This order of rotations is shown in Figure C.2. Euler angles are prone to singularities as shown in Figure C.3. With the 3-2-1 rotation order the singularity occurs at $\theta = 90°$. A different order of rotations can sometimes be used to avoid a known singularity, or a simulation can be stopped before it reaches a known singularity. Alternatively the quaternion representation can be used, which does not suffer from singularities.

C.6 Quaternion Representation

Quaternions use four quantities to represent the three degrees of freedom in an attitude rotation with redundancy. Quaternions are therefore able to avoid singularities. The attitude of a satellite can be difficult to visualise using quaternions and so the Euler angles are useful for this.

If quaternions are used to describe the attitude of the body frame in the reference frame, the direction cosine matrix to convert a vector from the reference frame to the body frame is:

$$\mathbf{A_{RB}}(\mathbf{q}) = \begin{bmatrix} 1 - 2(q_2^2 + q_3^2) & 2\,(q_1q_2 + q_3q_4) & 2\,(q_1q_3 - q_2q_4) \\ 2\,(q_1q_2 - q_3q_4) & 1 - 2(q_1^2 + q_3^2)2 & 2\,(q_2q_3 + q_1q_4) \\ 2\,(q_1q_3 + q_2q_4) & 2\,(q_2q_3 - q_1q_4) & 1 - 2(q_1^2 + q_2^2) \end{bmatrix} \tag{C.8}$$

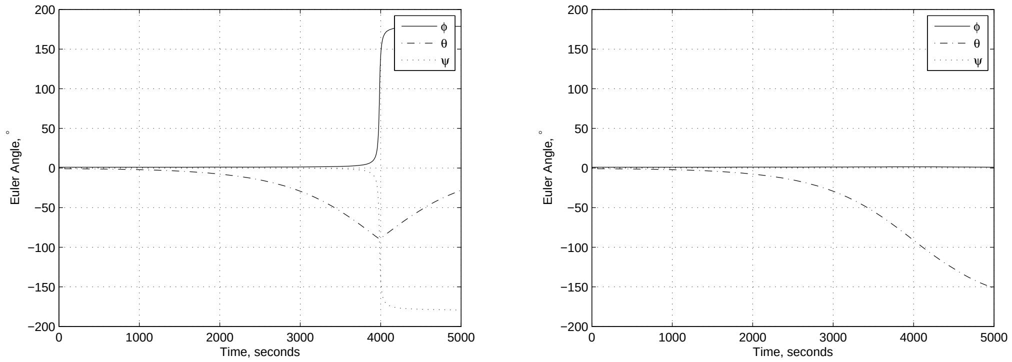

(a) The satellite body dynamics calculated using Euler Angles and suffering from a singularity

(b) The satellite body dynamics calculated using quaternions and not suffering from a singularity

Figure C.3: The effect of a singularity occurring in the body dynamics.

In this project q_4 has been used as the scalar component of the quaternion as in [11] and [12]. In other texts q_1 is used as the scalar component; care must be taken to be consistent throughout the project.

C.7 Equations of Motion

From Euler's moment equation [76]:

$$\dot{\mathbf{h}}_{\mathbf{I}} = \dot{\mathbf{h}}_{\mathbf{B}} + \boldsymbol{\omega} \times \mathbf{h}_{\mathbf{B}} \tag{C.9}$$

Where $\dot{\mathbf{h}}_I$ is the rate of change of angular momentum,(i.e. the torque), in the inertial frame and $\dot{\mathbf{h}}_B$ is the rate of change of angular velocity in the body frame. $\boldsymbol{\omega}$ is the angular velocity of the body in the inertial frame and $\mathbf{h}_{\mathbf{B}}$ is the angular momentum in the body frame. If momentum wheels are used then $\mathbf{h}_{\mathbf{B}}$ will be the sum of the satellite angular momentum and the wheel angular momentum.

From Equation C.9 the attitude dynamic equation of motion for Horyu, assuming magneto-torquers are the only attitude control actuators used, can be written as:

$$\mathbf{T}_{\mathbf{c}} + \mathbf{T}_{\mathbf{d}} = \mathbf{I}\dot{\boldsymbol{\omega}} + \boldsymbol{\omega} \times \mathbf{I}\boldsymbol{\omega} \tag{C.10}$$

Where $\mathbf{T}_{\mathbf{c}}$ is the control torque in the inertial frame generated by the magneto-torquers. $\mathbf{T}_{\mathbf{d}}$ is the disturbance torque on Horyu, expressed in the inertial frame. The gravity gradient disturbance torque $\mathbf{G}$ is ignored in this project. $\mathbf{I}$ is the inertia matrix of the satellite. The relationship between these terms is shown in Figure C.4.

Equation C.10 can then be rearranged to give:

$$\dot{\boldsymbol{\omega}} = \mathbf{I}^{-1}\left(\mathbf{T}_{\mathbf{c}} + \mathbf{G} - \boldsymbol{\omega} \times \mathbf{I}\boldsymbol{\omega}\right) \tag{C.11}$$

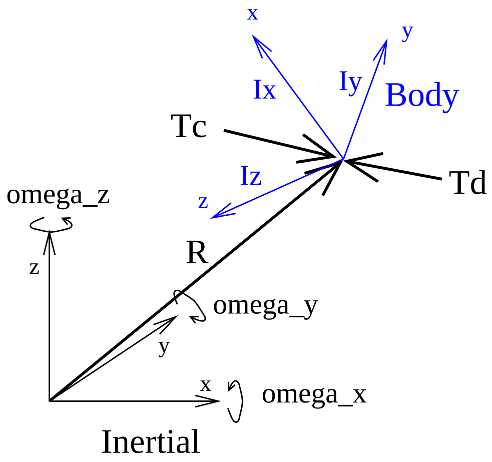

Figure C.4: The relationship between the terms in Horyu's equation of motion - Equation C.10.

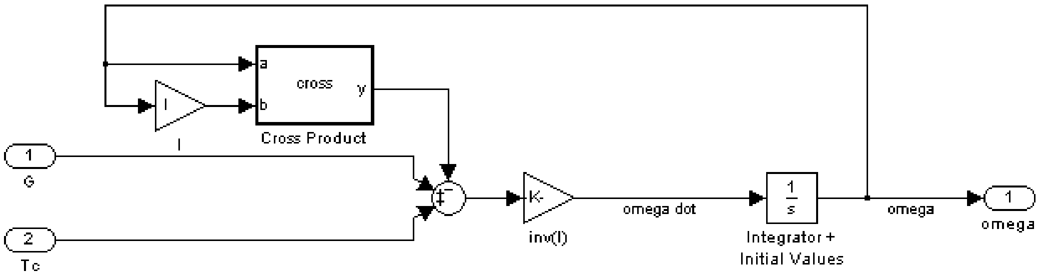

Figure C.5: The equation of motion implemented in Simulink to give the satellite's body dynamics.

The output of Equation C.11 can be integrated to give the rotation rate of the body frame in the inertial frame. The rotation rate at the start of the model can be specified in the integral. The implementation of this is shown in Figure C.5, but with the inertia matrix **I** replaced by the 3×1 vector of principal inertia terms. When the matrix **I** is known from the CAD model, the vector **I** gain block can be replaced by the matrix multiplication of **I** and $\boldsymbol{\omega}$.

C.8 Kinematics

The kinematic differential equations represent the time dependent relationship between the body frame and the reference frame. To avoid problems with singularities this relationship is most easily defined using quaternions [12]:

$$\dot{\mathbf{q}} = \begin{bmatrix} \dot{q}_1 \\ \dot{q}_2 \\ \dot{q}_3 \\ \dot{q}_4 \end{bmatrix} = \frac{1}{2} \begin{bmatrix} q_4 & -q_3 & q_2 & q_1 \\ q_3 & q_4 & -q_1 & q_2 \\ -q_2 & q_1 & q_4 & q_3 \\ -q_1 & -q_2 & -q_3 & q_4 \end{bmatrix} \begin{bmatrix} \omega_1 \\ \omega_2 \\ \omega_3 \\ 0 \end{bmatrix} \tag{C.12}$$

$\dot{\mathbf{q}}$ is more easily integrated than the alternative direction cosine matrix representation and so is often used on-board satellites.

C.9 Control Torque Command

C.9.1 Sidi's Approach

From Sidi [11], $\mathbf{q_E}$ is the attitude error quaternion, $\mathbf{q_T}$ is the target attitude quaternion and $\mathbf{q}$ is the current attitude quaternion:

$$\mathbf{q_E} = \begin{bmatrix} q_{E1} \\ q_{E2} \\ q_{E3} \\ q_{E4} \end{bmatrix} = \begin{bmatrix} q_{T4} & q_{T3} & -q_{T2} & q_{T1} \\ -q_{T3} & q_{T4} & q_{T1} & q_{T2} \\ q_{T2} & -q_{T1} & q_{T4} & q_{T3} \\ -q_{T1} & -q_{T2} & -q_{T3} & q_{T4} \end{bmatrix} \begin{bmatrix} -q_1 \\ -q_2 \\ -q_3 \\ q_4 \end{bmatrix} \tag{C.13}$$

The command torque inputs to the magneto-torquers can then be defined as:

$$\begin{aligned} T_{cx} &= 2K_x q_{E1} q_{E4} - K_{xd} p \\ T_{cy} &= 2K_y q_{E2} q_{E4} - K_{yd} q \\ T_{cz} &= 2K_z q_{E3} q_{E4} - K_{zd} r \end{aligned} \tag{C.14}$$

Where $\boldsymbol{\omega_{BR}} = \begin{bmatrix} p & q & r \end{bmatrix}^T$ is the satellite body angular velocity in the orbit reference frame, and $\mathbf{K}$ and $\mathbf{K_d}$ are the gain constants of the controller.

C.9.2 Wie's Approach

From Wie [12], $\mathbf{q_E}$ is the attitude error quaternion, $\mathbf{q_T}$ is the target attitude quaternion and $\mathbf{q}$ is the current attitude quaternion:

$$\mathbf{q_E} = \begin{bmatrix} q_{E1} \\ q_{E2} \\ q_{E3} \\ q_{E4} \end{bmatrix} = \begin{bmatrix} q_{T4} & q_{T3} & -q_{T2} & -q_{T1} \\ -q_{T3} & q_{T4} & q_{T1} & -q_{T2} \\ q_{T2} & -q_{T1} & q_{T4} & -q_{T3} \\ q_{T1} & q_{T2} & q_{T3} & q_{T4} \end{bmatrix} \begin{bmatrix} q_1 \\ q_2 \\ q_3 \\ q_4 \end{bmatrix} \tag{C.15}$$

If the quaternion desired is $\begin{bmatrix} 0 & 0 & 0 & +1 \end{bmatrix}^T$ then the command torque inputs to the magneto-torquers can be defined as:

$$\mathbf{T_c} = -\mathbf{K}\mathbf{q_E} - \mathbf{C}\boldsymbol{\omega} \tag{C.16}$$

Where $\mathbf{K} = k\mathbf{D}$, and k is a scalar constant. $\mathbf{C}$ and $\mathbf{D}$ are the matrices:

$$\mathbf{C} = \begin{bmatrix} c_1 & 0 & 0 \\ 0 & c_2 & 0 \\ 0 & 0 & c_3 \end{bmatrix} \tag{C.17}$$

$$\mathbf{D} = \begin{bmatrix} 1 & 0 & 0 & 0 \\ 0 & 1 & 0 & 0 \\ 0 & 0 & 1 & 0 \end{bmatrix} \tag{C.18}$$

Where c_1, c_2 and c_3 are scalar contstants chosen using control theory to give the controller its desired properties. $\boldsymbol{\omega}$ is the body-frame angular velocity in the reference frame.

Wie proposes several other controllers in Section 7.3.1 of his book.

Appendix D

Tilting Beam Design

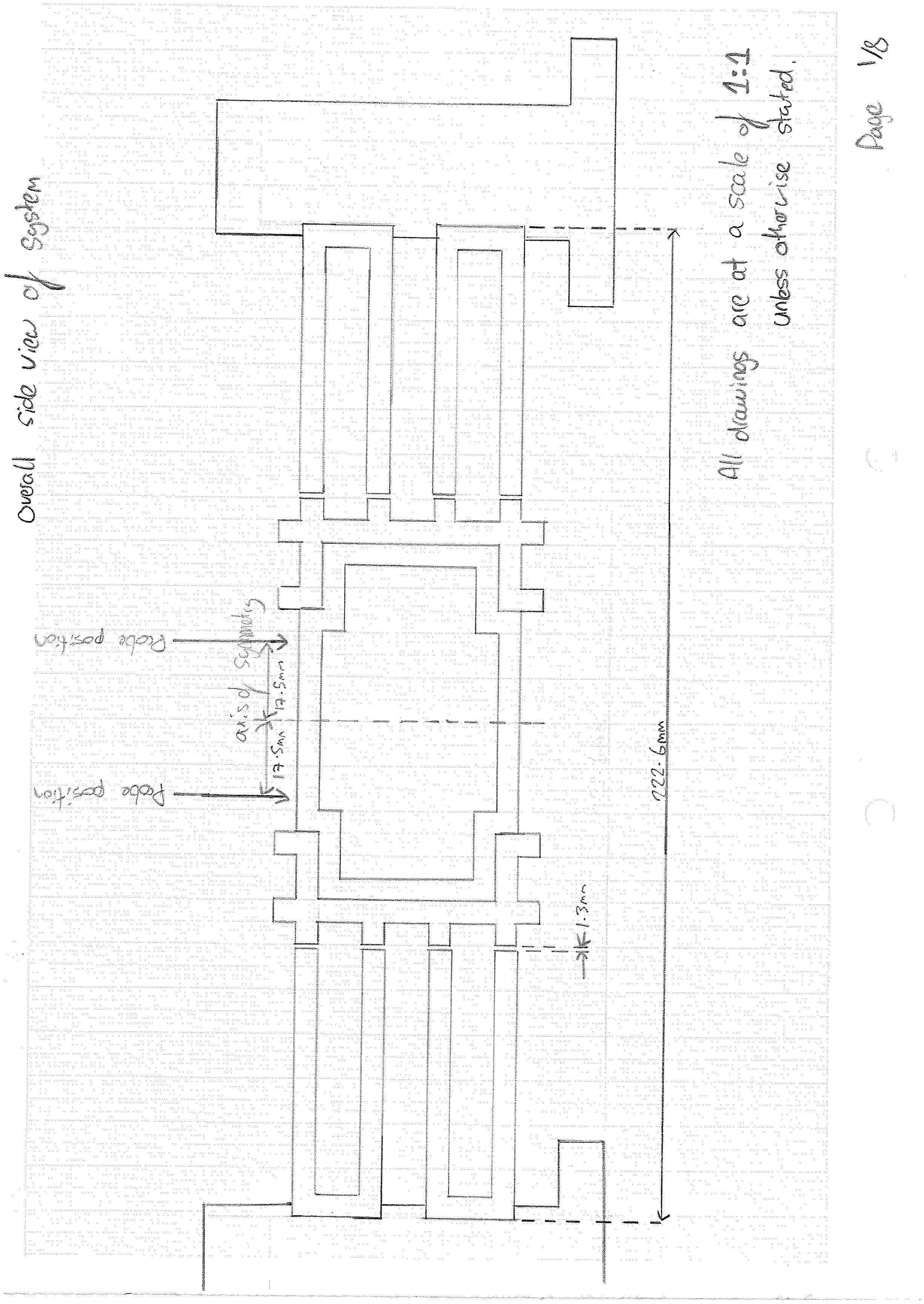
Overall side view of system
All drawings are at a scale of 1:1
unless otherwise stated.
Page 1/8
Probe position
Probe position
axis of symmetry
17.5mm
17.5mm
222.6mm
1.3mm

Beam End Pieces x 2

Made from steel

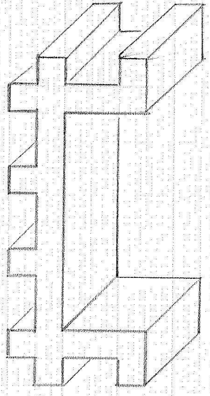

Side view

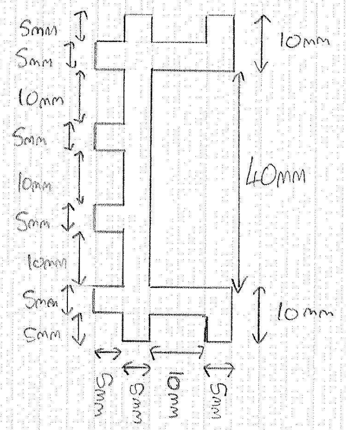

Top view

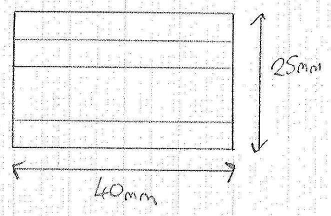

Beam Central Frame x1 Aluminium

Side View:

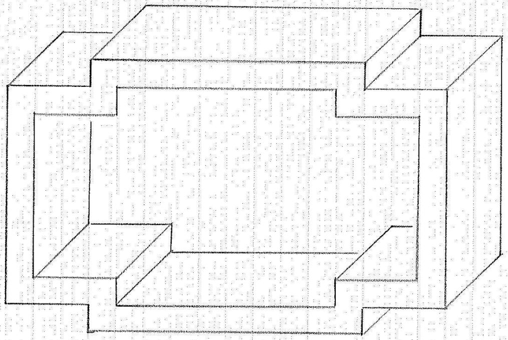

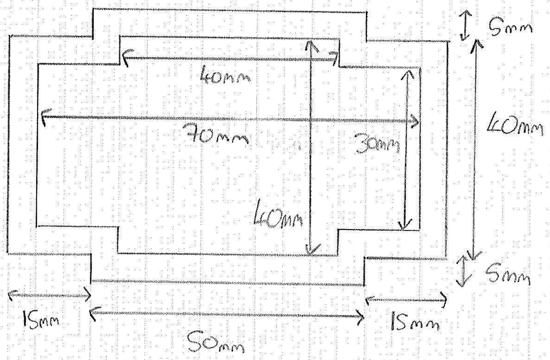

Top View

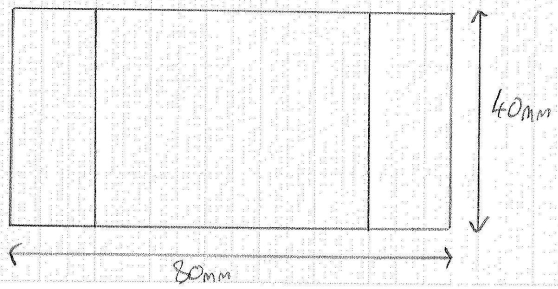

Page 3/8

Electromagnets x 4 Laminated Steel.

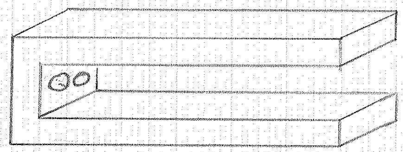

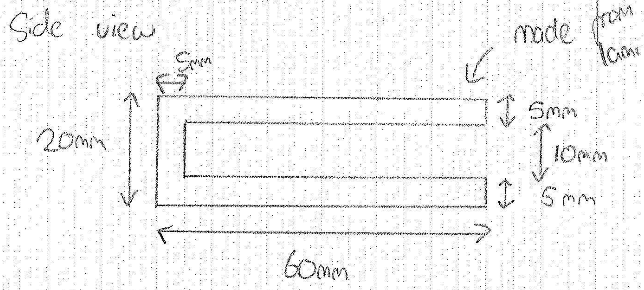

made from laminated steel laminations going into page

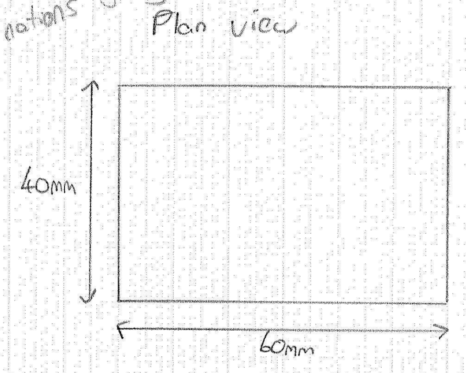

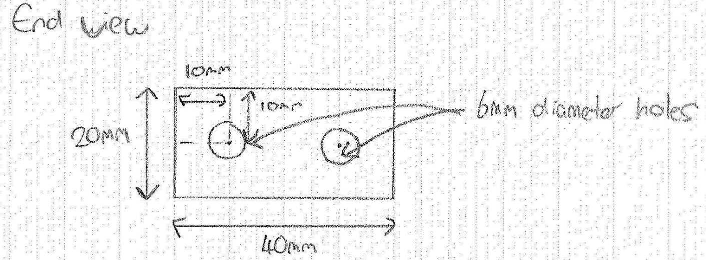

M6 nuts will be used between the poles

So that the poles stop them from rotating

Page 4/8

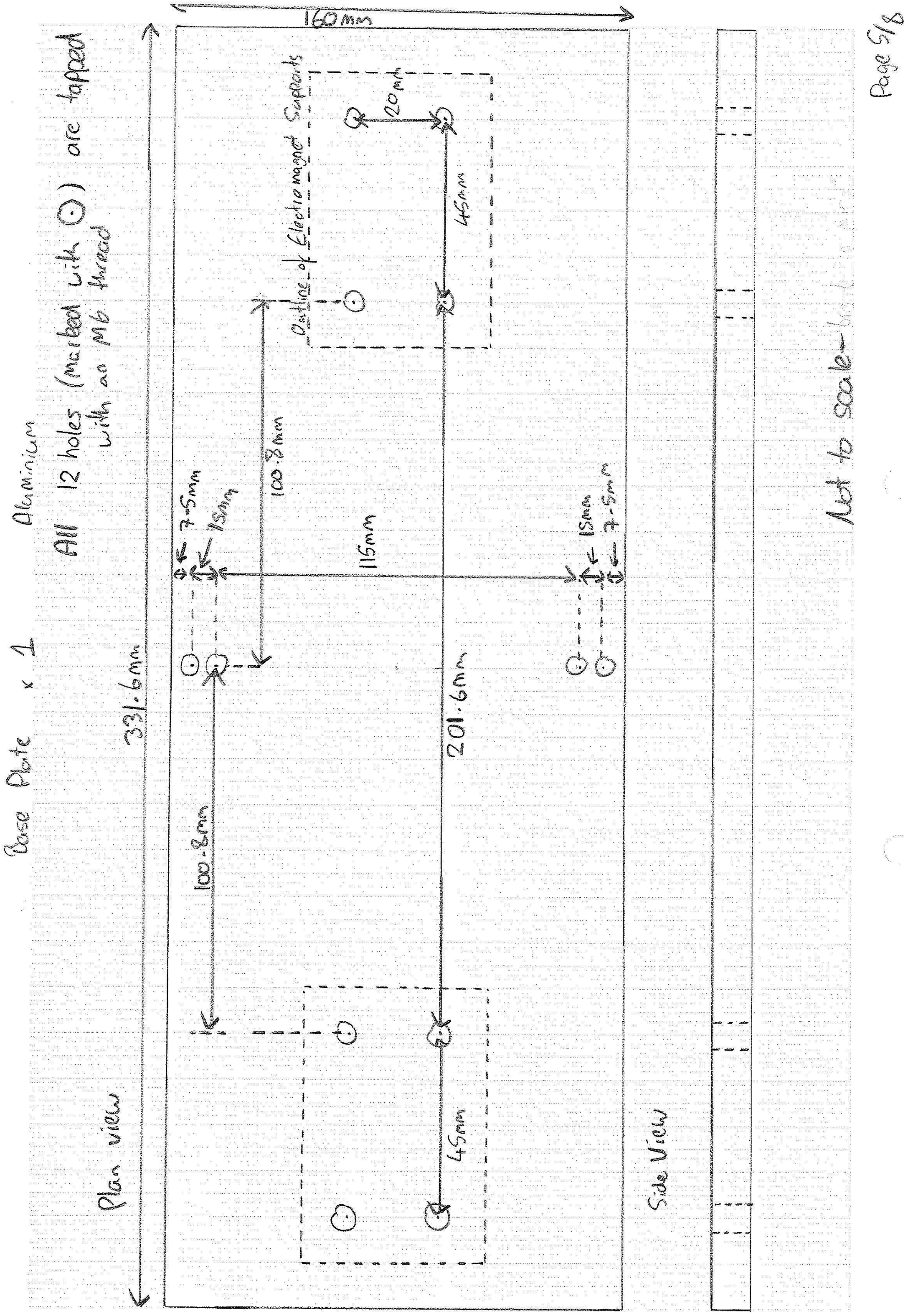
Base Plate x 1
Aluminium
All 12 holes (marked with ⊙) are tapped with an M6 thread
Plan view
Side View
160mm
331.6mm
Outline of Electromagnet Supports
20mm
45mm
100.8mm
100.8mm
7.5mm
15mm
115mm
15mm
7.5mm
201.6mm
100.8mm
45mm
Not to scale
Page 5/8

Electromagnet Supports x2 Aluminium

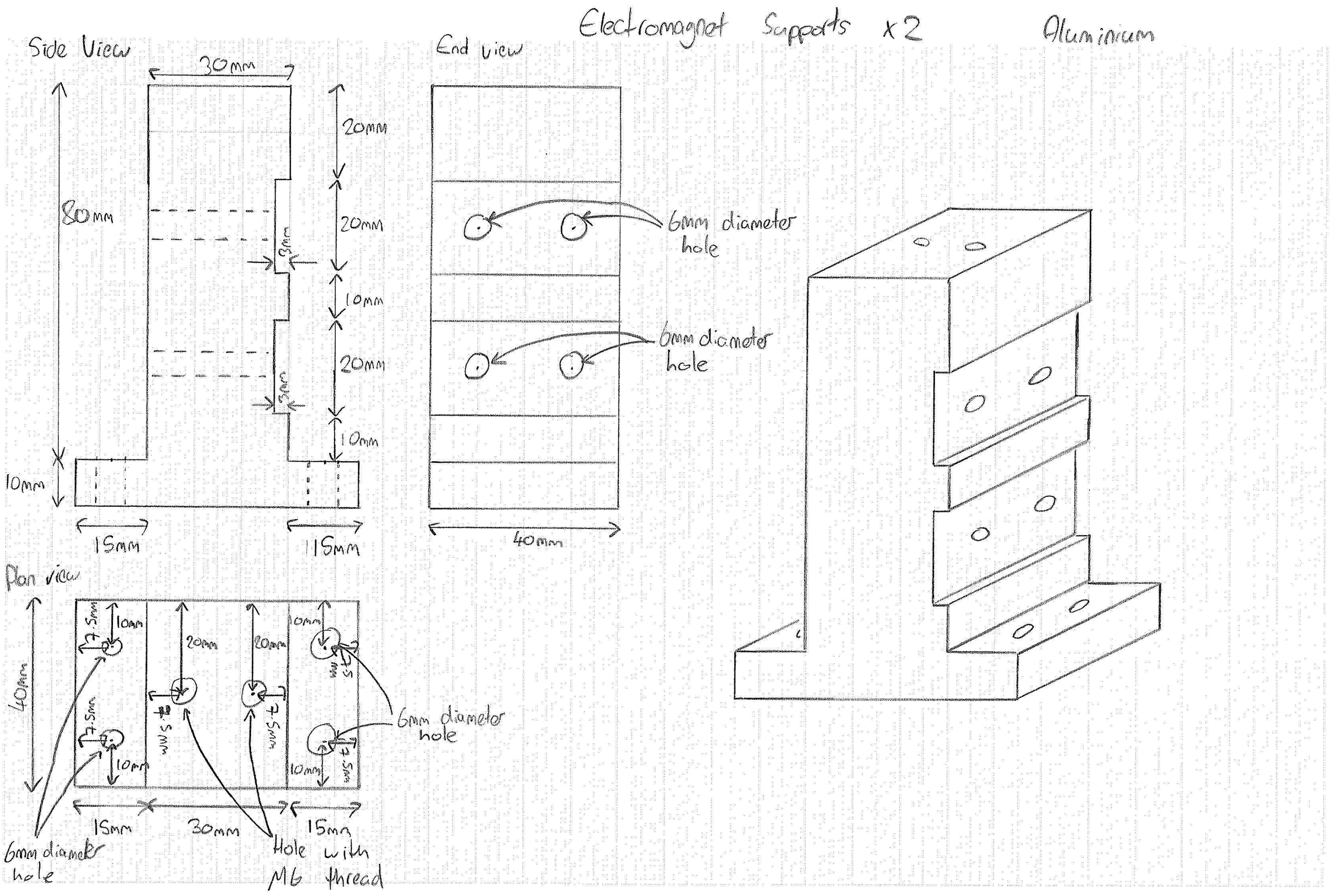

Page 6/8

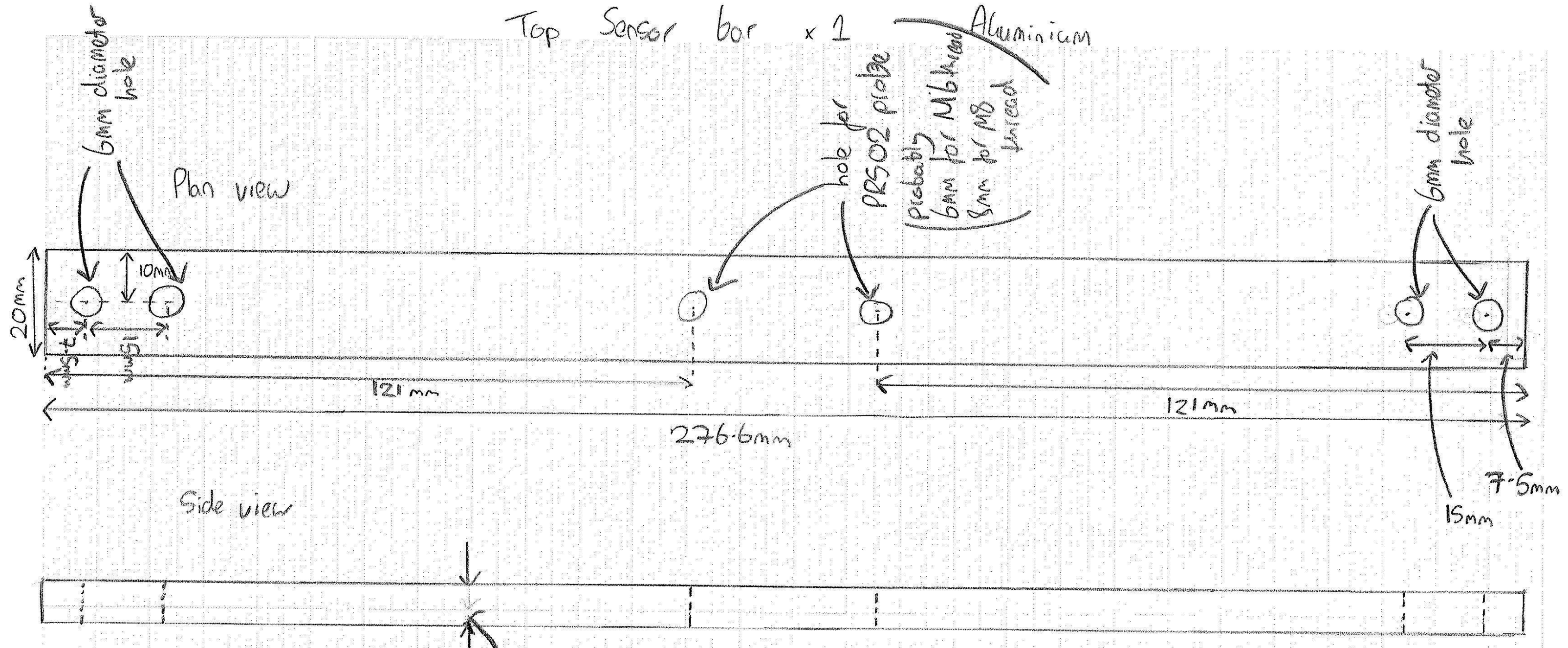

Thickness dependent upon materials available - only requirement being that it doesn't bend under the weight of the probes. - a minimum of 8mm is suggested
Please check with Dr Pecher or Jon Seddon

Page 7/8

Middle Sensor Bar x 1 Aluminium

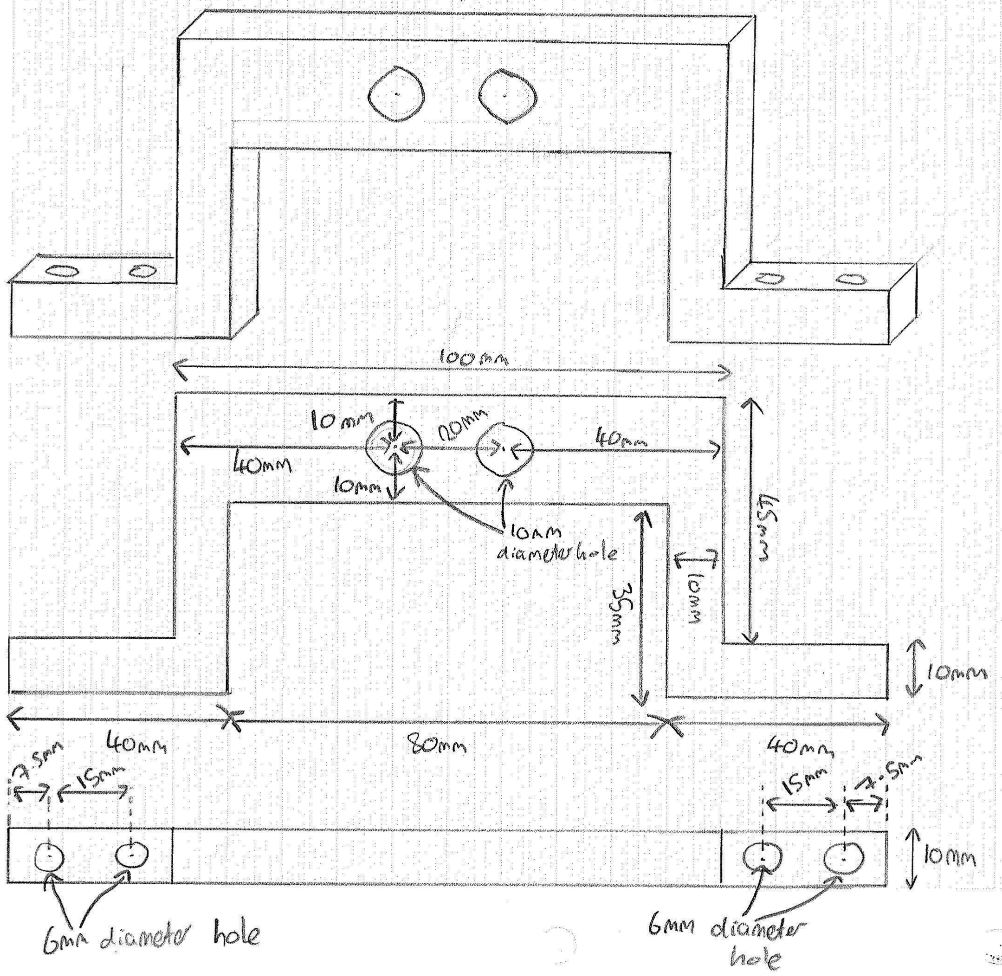

Note the 80mm wide hole in the beam allows the rotor to be slid to either side to allow the sensors to be fitted to each hole

Page 8/8

Appendix E

3Dwheel Design

REVISION HISTORY			
REV	DESCRIPTION	DATE	APPROVED

3Dwheel

List of Drawings:

Complete System
Wheel Assembly
Sensor Support Assembly
Rotor
Rotor Centre Top Piece
Rotor Centre Bottom Piece
Baseplate
Electromagnet and Axial-Sensor-Bracket Support
Electromagnet
Axial Sensor Support
Top Radial Sensor Support
Radial Sensor Support Connector
Bottom Radial Sensor Support
Permanent Magnet Holder

Please contact Jon Seddon on extension 3411 with any questions, or email j.seddon@surrey.ac.uk.

Alternatively contact Dr Alexandre Pechev on extension 3417 or a.pechev@surrey.ac.uk

	NAME	DATE
DRAWN	Jon Seddon	11/20/08
CHECKED		
ENG APPR		
MGR APPR		

UNLESS OTHERWISE SPECIFIED
DIMENSIONS ARE IN MILLIMETERS
ANGLES ±X.X°
2 PL ±X.XX 3 PL ±X.XXX

SURREY SPACE CENTRE
University of Surrey

TITLE
List of Drawings

SIZE	DWG NO	REV
A3		

FILE NAME: ListOfDrawings.dft

SCALE:	WEIGHT:	SHEET 1 OF 1

REVISION HISTORY

REV	DESCRIPTION	DATE	APPROVED

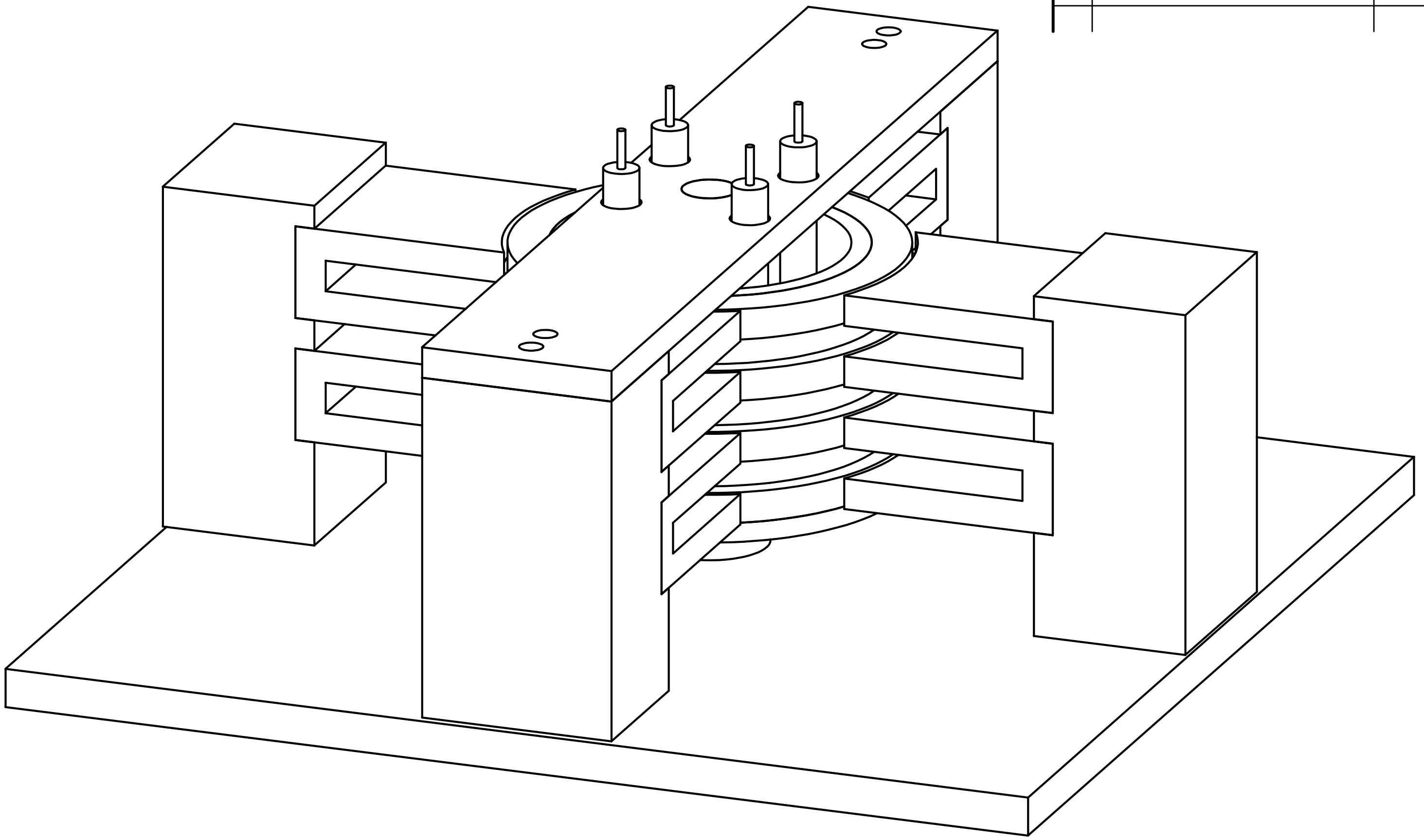

	NAME	DATE
DRAWN	Jon Seddon	11/18/08
CHECKED		
ENG APPR		
MGR APPR		

UNLESS OTHERWISE SPECIFIED
DIMENSIONS ARE IN MILLIMETERS
ANGLES ±X.X°
2 PL ±X.XX 3 PL ±X.XXX

SURREY
SPACE CENTRE

University of
Surrey

TITLE
Complete System

SIZE	DWG NO	REV
A3		

FILE NAME: complete_assembly.dft

SCALE:	WEIGHT:	SHEET 1 OF 1

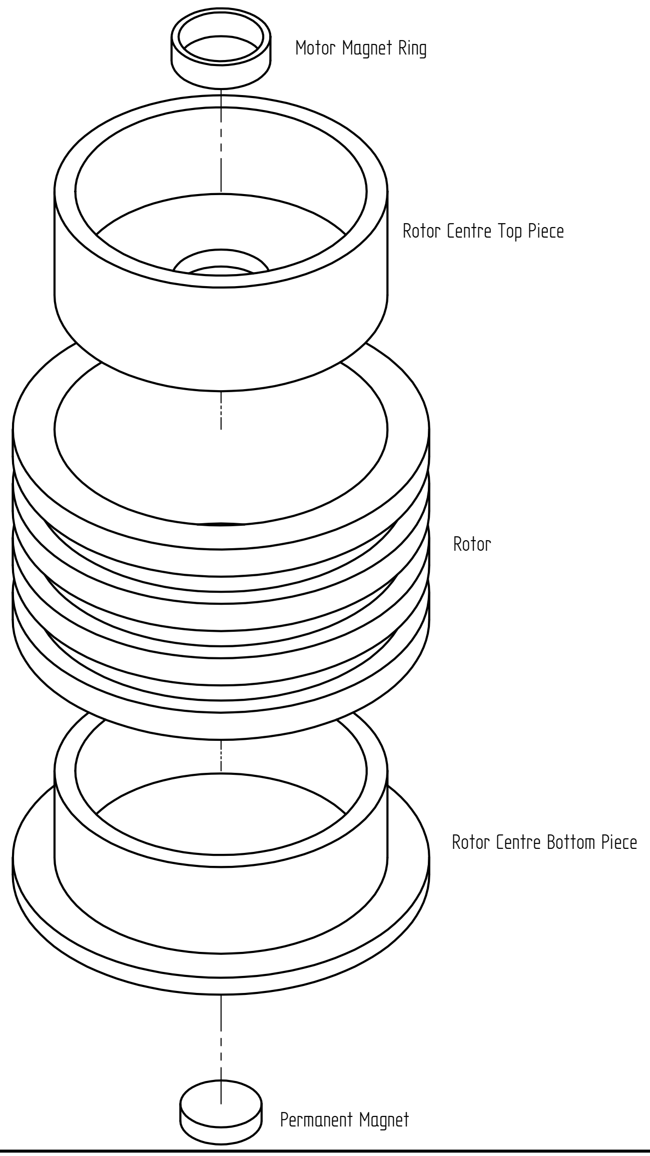

REVISION HISTORY

REV	DESCRIPTION	DATE	APPROVED

	NAME	DATE
DRAWN	Jon Seddon	11/17/08
CHECKED		
ENG APPR		
MGR APPR		

UNLESS OTHERWISE SPECIFIED
DIMENSIONS ARE IN MILLIMETERS
ANGLES ±X.X°
2 PL ±X.XX 3 PL ±X.XXX

SURREY SPACE CENTRE
University of Surrey

TITLE
Wheel Assembly

SIZE	DWG NO	REV
A3		

FILE NAME: wheel_assembly.dft

SCALE:	WEIGHT:	SHEET 1 OF 1

REVISION HISTORY			
REV	DESCRIPTION	DATE	APPROVED

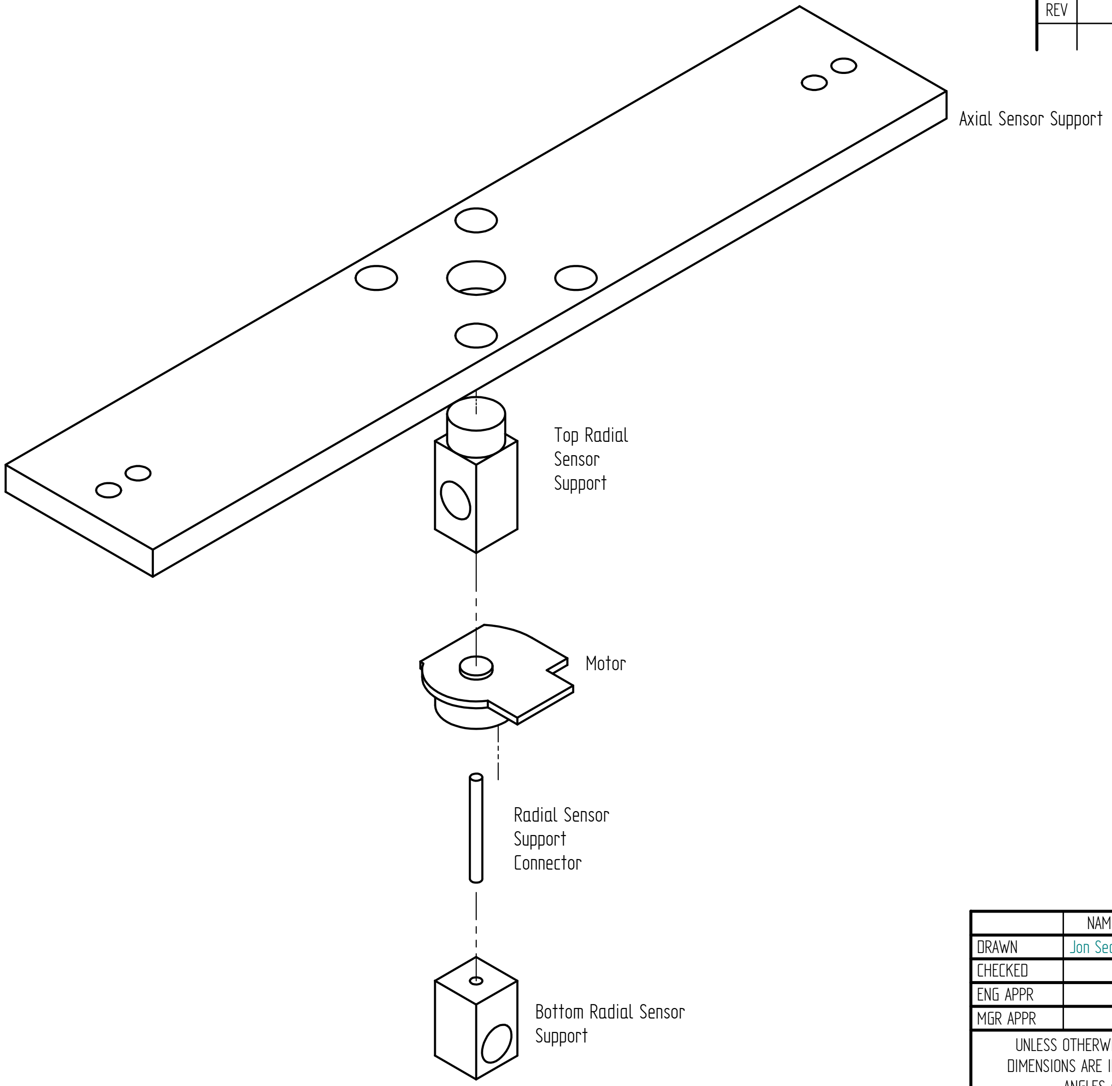

	NAME	DATE
DRAWN	Jon Seddon	11/18/08
CHECKED		
ENG APPR		
MGR APPR		

UNLESS OTHERWISE SPECIFIED
DIMENSIONS ARE IN MILLIMETERS
ANGLES ±X.X°
2 PL ±X.XX 3 PL ±X.XXX

University of Surrey

TITLE
Sensor Support Assembly

SIZE A3	DWG NO	REV

FILE NAME: bracket_assembly.dft

SCALE:	WEIGHT:	SHEET 1 OF 1

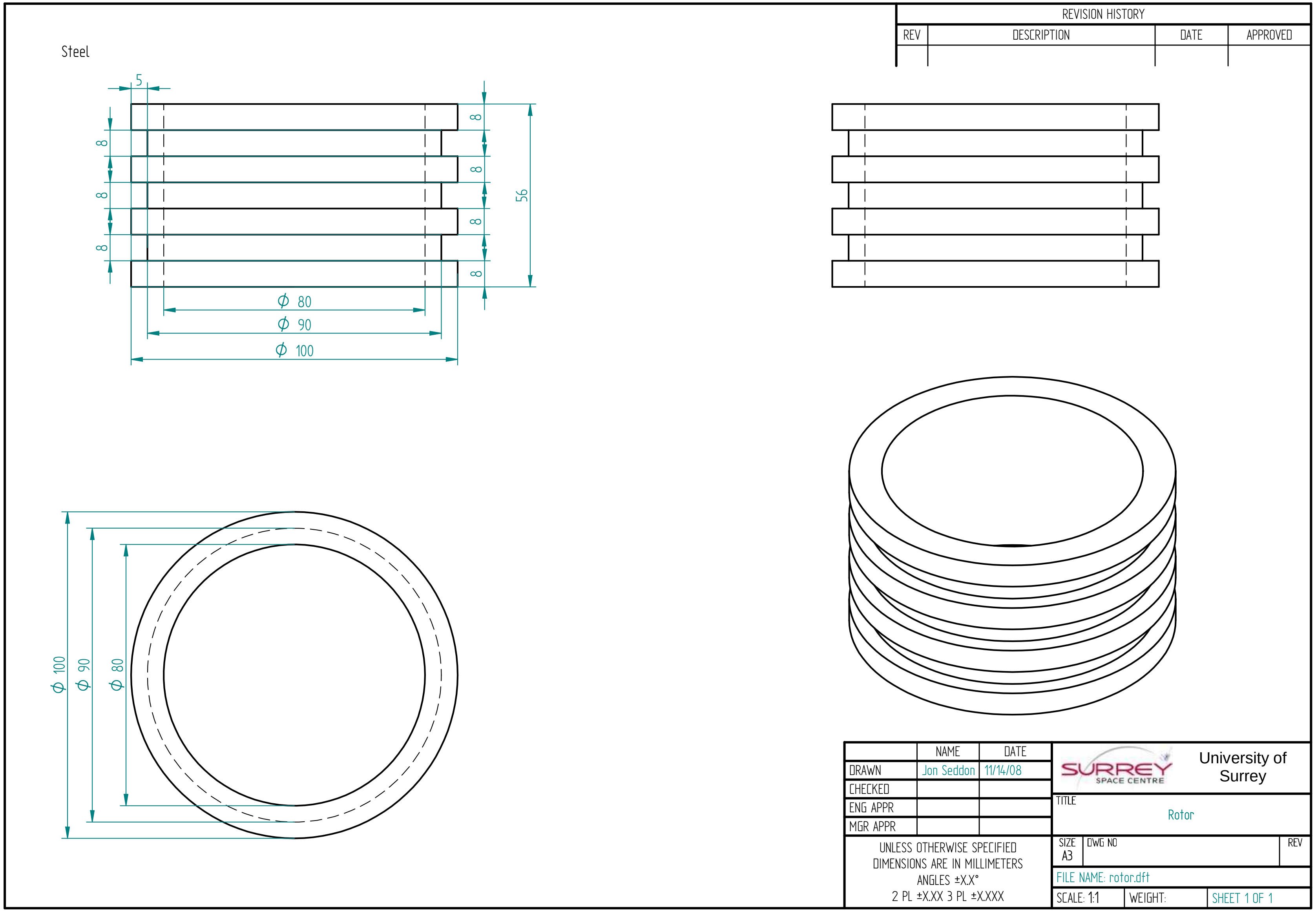
Steel
5
8
8
8
8
8
8
8
56
ϕ 80
ϕ 90
ϕ 100
ϕ 100
ϕ 90
ϕ 80
REVISION HISTORY
REV
DESCRIPTION
DATE
APPROVED
NAME
DATE
DRAWN
Jon Seddon
11/14/08
CHECKED
ENG APPR
MGR APPR
UNLESS OTHERWISE SPECIFIED
DIMENSIONS ARE IN MILLIMETERS
ANGLES ±X.X°
2 PL ±X.XX 3 PL ±X.XXX
SURREY SPACE CENTRE
University of Surrey
TITLE
Rotor
SIZE
A3
DWG NO
REV
FILE NAME: rotor.dft
SCALE: 1:1
WEIGHT:
SHEET 1 OF 1

REVISION HISTORY

REV	DESCRIPTION	DATE	APPROVED
2	Modifications to use improved motor	8/9/09	

Aluminium

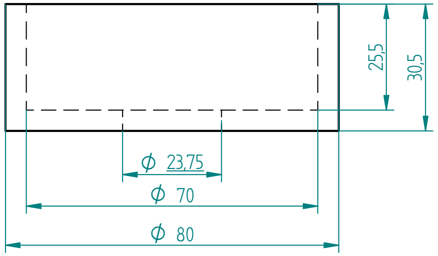

Modification: enlarge 23.75 mm hole to 25.5 mm to accept larger motor rotor.

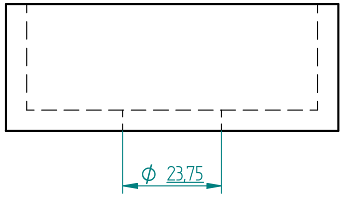

Note: internal 23.75mm diameter hole will have motor magnet ring glued inside it.

This top piece wil be secured to the rotor via screws going through the sidewall of this piece into the rotor. The screws need to be within the top 4mm of the open end of this piece to not interfere with the position sensors.

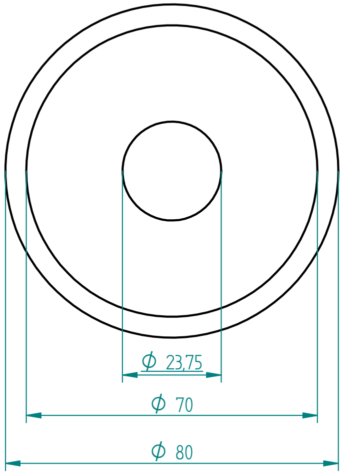

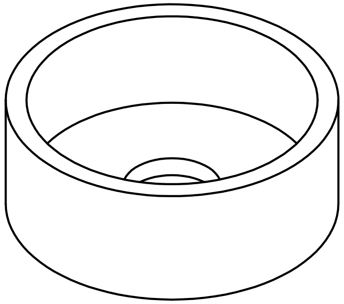

Secured to steel Rotor via screws in its side

	NAME	DATE
DRAWN	eep2js	09/08/09
CHECKED		
ENG APPR		
MGR APPR		

UNLESS OTHERWISE SPECIFIED
DIMENSIONS ARE IN MILLIMETERS
ANGLES ±X.X°
2 PL ±X.XX 3 PL ±X.XXX

SURREY SPACE CENTRE
University of Surrey

TITLE
Rotor Centre Top Piece

SIZE A3 | DWG NO | REV

FILE NAME: AL_Rev2.dft

SCALE: 1:1 | WEIGHT: | SHEET 1 OF 1

REVISION HISTORY			
REV	DESCRIPTION	DATE	APPROVED

Aluminium

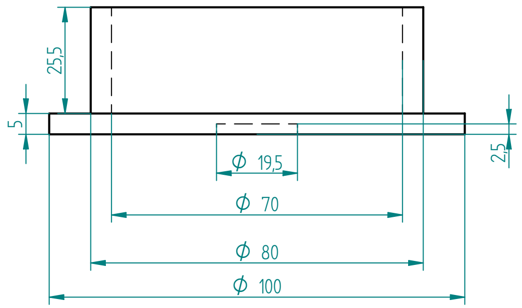

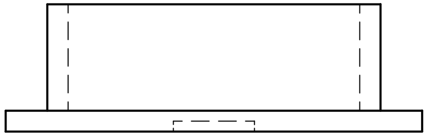

Centre 19.5 mm diameter cut-out
to have permanent magnet glued
inside.

Screws will go through bottom
flange into steel rotor

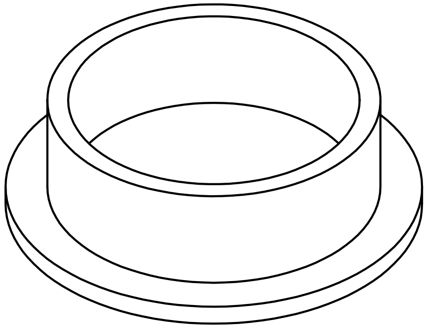

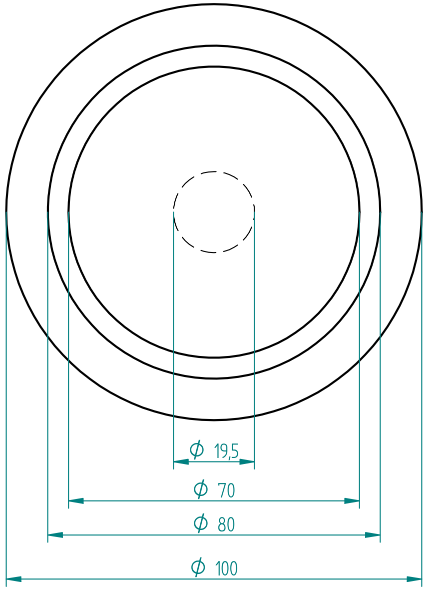

	NAME	DATE
DRAWN	Jon Seddon	11/14/08
CHECKED		
ENG APPR		
MGR APPR		

UNLESS OTHERWISE SPECIFIED
DIMENSIONS ARE IN MILLIMETERS
ANGLES ±X.X°
2 PL ±X.XX 3 PL ±X.XXX

SURREY SPACE CENTRE
University of Surrey

TITLE
Rotor Centre Bottom Piece

SIZE	DWG NO	REV
A3		

FILE NAME: AlPM2.dft

SCALE: 1:1 WEIGHT: SHEET 1 OF 1

Aluminium

REVISION HISTORY			
REV	DESCRIPTION	DATE	APPROVED

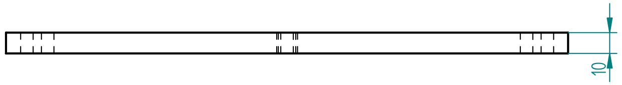

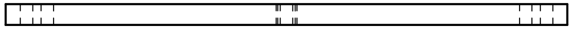

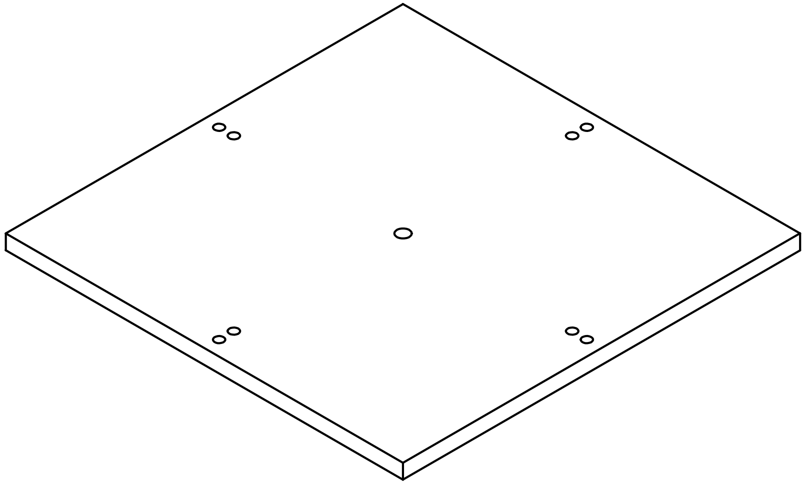

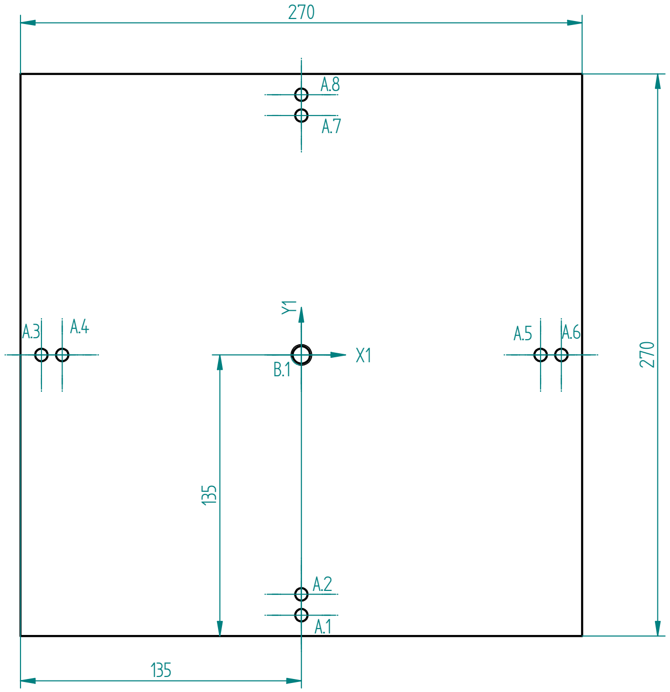

Hole Table				
Hole	X	Y	Size	Note
A.1	0	-125	Φ 6	
A.2	0	-115	Φ 6	
A.3	-125	0	Φ 6	
A.4	-115	0	Φ 6	
A.5	115	0	Φ 6	
A.6	125	0	Φ 6	
A.7	0	115	Φ 6	
A.8	0	125	Φ 6	
B.1	0	0	Φ 10	M10 Thread

	NAME	DATE
DRAWN	Jon Seddon	11/20/08
CHECKED		
ENG APPR		
MGR APPR		

UNLESS OTHERWISE SPECIFIED
DIMENSIONS ARE IN MILLIMETERS
ANGLES ±X.X°
2 PL ±X.XX 3 PL ±X.XXX

SURREY SPACE CENTRE
University of Surrey

TITLE
Baseplate

SIZE A3
DWG NO
REV

FILE NAME: BasePlate.dft

SCALE: 1:2
WEIGHT:
SHEET 1 OF 1

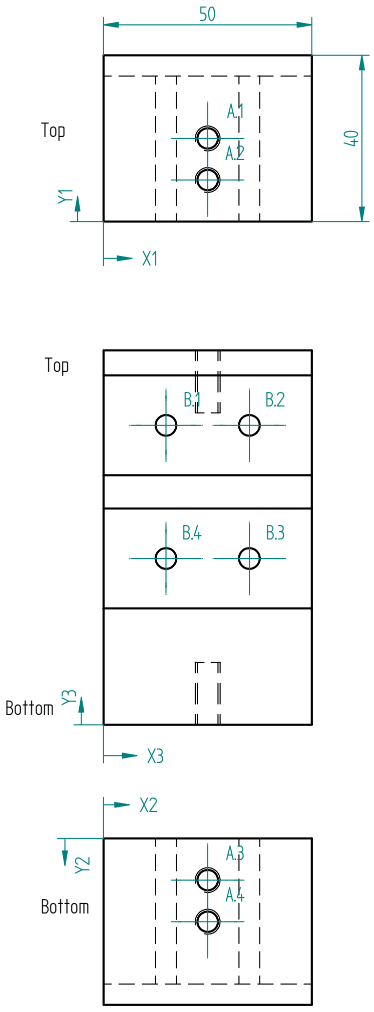

Aluminium
Quantity: 4, 2 with the threaded holes in
the top and 2 without

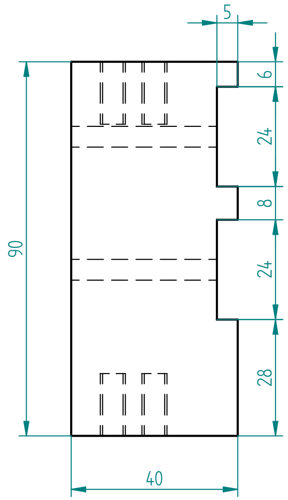

REVISION HISTORY

REV	DESCRIPTION	DATE	APPROVED

Hole Table

Hole	X	Y	Size	Note
A.1	25	20	Φ 6	M6 Thread 15mm Deep
A.2	25	10	Φ 6	M6 Thread 15mm Deep
A.3	25	-10	Φ 6	M6 Thread 15mm Deep
A.4	25	-20	Φ 6	M6 Thread 15mm Deep
B.1	15	72	Φ 5	
B.2	35	72	Φ 5	
B.3	35	40	Φ 5	
B.4	15	40	Φ 5	

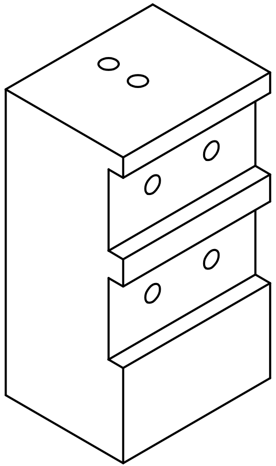

	NAME	DATE
DRAWN	Jon Seddon	11/19/08
CHECKED		
ENG APPR		
MGR APPR		

UNLESS OTHERWISE SPECIFIED
DIMENSIONS ARE IN MILLIMETERS
ANGLES ±X.X°
2 PL ±X.XX 3 PL ±X.XXX

SURREY SPACE CENTRE
University of Surrey

TITLE
Electromagnet and Axial-Sensor-Bracket Support

SIZE A3 DWG NO REV

FILE NAME: SupEM_Py_ver2.dft

SCALE: 1:1 WEIGHT: SHEET 1 OF 1

REVISION HISTORY

REV	DESCRIPTION	DATE	APPROVED
1	Initial piece extened to 57mm long to aid the spark erosion process	18/12/2008	

Laminated Steel
Quantity: 8

Notes: Steel to be made into a u-shape 50x24x57mm without the curved face by Photofab Ltd. Curved edge to be cut by spark erosion at Multispark Ltd and mounting holes to be drilled at the Faculty Workshop at the University.

Laminations made from multiple sheets of this u-shaped plane

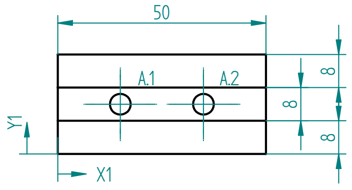

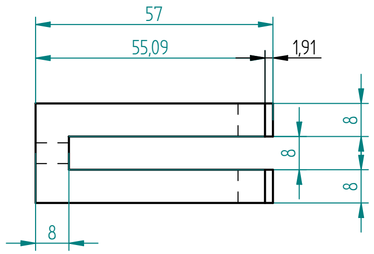

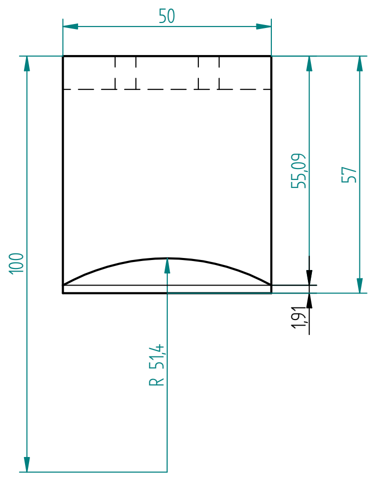

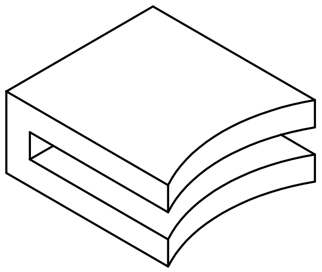

Hole Table

Hole	X	Y	Size
A.1	15	12	ϕ 5
A.2	35	12	ϕ 5

	NAME	DATE
DRAWN	Jon Seddon	11/14/08
CHECKED		
ENG APPR		
MGR APPR		

UNLESS OTHERWISE SPECIFIED
DIMENSIONS ARE IN MILLIMETERS
ANGLES ±X.X°
2 PL ±X.XX 3 PL ±X.XXX

SURREY SPACE CENTRE
University of Surrey

TITLE
Electromagnet

SIZE A3 | DWG NO | REV 1

FILE NAME: EMBotPy.dft

SCALE: 1:1 | WEIGHT: | SHEET 1 OF 1

REVISION HISTORY			
REV	DESCRIPTION	DATE	APPROVED

Aluminium

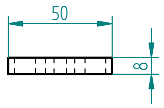

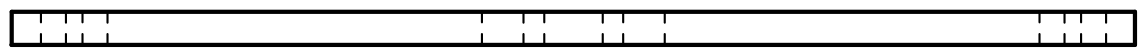

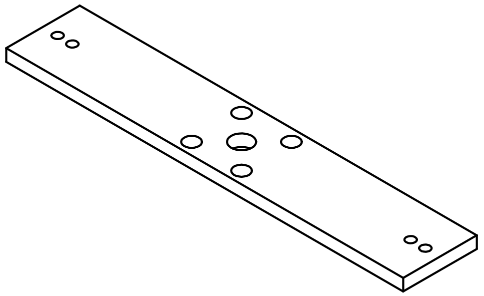

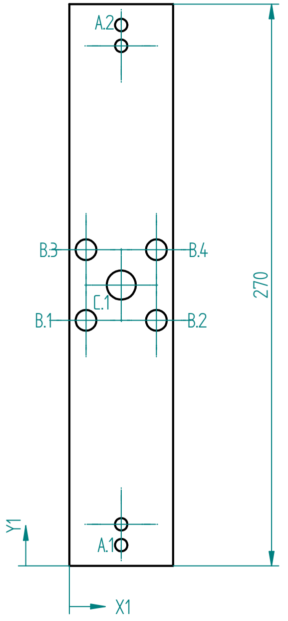

Hole Table			
Hole	X	Y	Size
A.1	25	20	Φ 6
A.2	25	250	Φ 6
B.1	8,03	118,03	Φ 10
B.2	41,97	118,03	Φ 10
B.3	8,03	151,97	Φ 10
B.4	41,97	151,97	Φ 10
C.1	25	135	Φ 14

Note 1: the Top Radial Sensor Support will be secured into the 14mm diameter C1 hole via grub screws through the side of this piece. If 18mm is too far to place grub screws through then the Top Radial Sensor Support will need to be extended upwards and a collar made to secure it to this Axial Sensor Support. There will be a torque on the Top Radial Sensor Support of ~20mNm and so the grub screws/collar must be capable of containing this torque.

.

Note 2: the positions for the 10mm diameter holes were calculated automatically. The positions should be rounded to the nearest millimetre.

	NAME	DATE
DRAWN	Jon Seddon	11/18/08
CHECKED		
ENG APPR		
MGR APPR		

UNLESS OTHERWISE SPECIFIED
DIMENSIONS ARE IN MILLIMETERS
ANGLES ±X.X°
2 PL ±X.XX 3 PL ±X.XXX

SURREY SPACE CENTRE

University of Surrey

TITLE
Axial Sensor Support

SIZE A3
DWG NO
REV

FILE NAME: SupAxSens.dft

SCALE: 1:1
WEIGHT:
SHEET 1 OF 1

REVISION HISTORY			
REV	DESCRIPTION	DATE	APPROVED
2	Modifications to use larger motor	8/9/09	

Aluminium

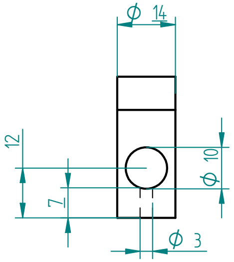

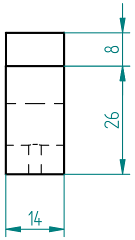

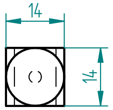

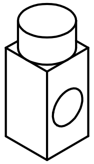

Modification: extend the 14 mm diameter circular top section into the square section by 5mm to allow the sensors to be moved upwards. THe circular section should now be 13 mm long. Extend the flat face on this circular section similarly by 5mm. Remove 3 mm from the bottom of the square section so that this is now 4 mm in length rather than the existing 7 mm. Drill and tap a new grub screw, on the opposite side to the existing one, 2 mm from the new end so that it is in the centre of the new square section.

Note 1: this piece will be secured into the Axial Sensor Support's 14mm diameter hole via grub screws through the side of the Axial Sensor Support. If 18mm is too far to place grub screws through then the 14mm diameter round section of this piece will need to be extended upwards and a collar made to secure it to the Axial Sensor Support. There will be a torque on the Top Radial Sensor Support of ~20mNm and so the grub screws/collar must be capable of containing this torque.

Note 2: The Radial Sensor Support Connector will slot into the 3mm diameter hole of this piece. It will be secured via a grub screw that is not shown on this drawing.

Note 3: The motor will attach to this piece via a bracket that has not been drawn yet.

	NAME	DATE
DRAWN	eep2js	09/08/09
CHECKED		
ENG APPR		
MGR APPR		

UNLESS OTHERWISE SPECIFIED
DIMENSIONS ARE IN MILLIMETERS
ANGLES ±X.X°
2 PL ±X.XX 3 PL ±X.XXX

SURREY SPACE CENTRE
University of Surrey

TITLE
Top Radial Sensor Support

SIZE	DWG NO	REV
A3		

FILE NAME: SupRadSens_Rev2.dft

SCALE: 1:1	WEIGHT:	SHEET 1 OF 1

REVISION HISTORY			
REV	DESCRIPTION	DATE	APPROVED

Aluminium

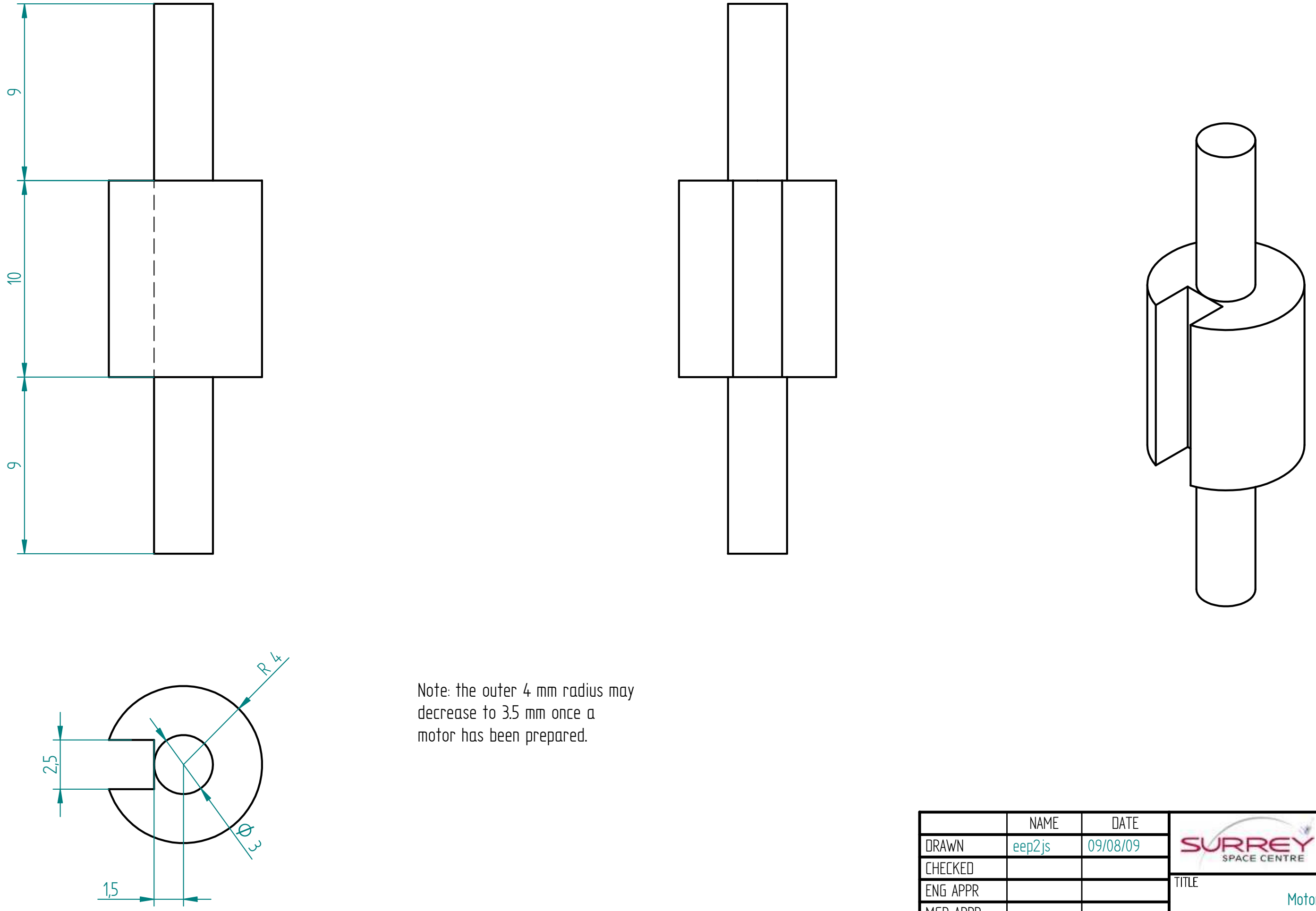

Note: the outer 4 mm radius may decrease to 3.5 mm once a motor has been prepared.

	NAME	DATE
DRAWN	eep2js	09/08/09
CHECKED		
ENG APPR		
MGR APPR		

UNLESS OTHERWISE SPECIFIED
DIMENSIONS ARE IN MILLIMETERS
ANGLES ±X.X°
2 PL ±X.XX 3 PL ±X.XXX

SURREY SPACE CENTRE

University of Surrey

TITLE
Motor Holder

SIZE	DWG NO	REV
A3		

FILE NAME: MotorHolder.dft

SCALE 5:1: | WEIGHT: | SHEET 1 OF 1

REVISION HISTORY

REV	DESCRIPTION	DATE	APPROVED
2	Modified to accept larger motor	8/9/09	

Aluminium

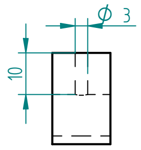

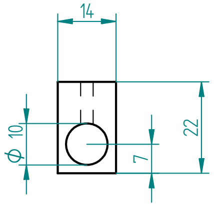

Modification: Remove 6 mm from the top square section so that there is now 4 mm of square section between the end of the piece and the edge of the 10 mm diameter hole. Drill and tap a new grub screw on the opposite face to the exisiting one, centered 2 mm from the end of the piece.

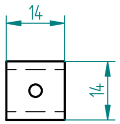

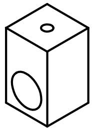

Note: The Radial Sensor Support Connector will slot into the 3mm diameter hole of this piece. It will be secured via a grub screw that has not be shown on this drawing.

	NAME	DATE
DRAWN	eep2js	09/08/09
CHECKED		
ENG APPR		
MGR APPR		

UNLESS OTHERWISE SPECIFIED
DIMENSIONS ARE IN MILLIMETERS
ANGLES ±X.X°
2 PL ±X.XX 3 PL ±X.XXX

SURREY SPACE CENTRE
University of Surrey

TITLE
Bottom Radial Sensor Support

SIZE	DWG NO	REV
A3		

FILE NAME: SupRadSens_Lower_Rev2.dft

SCALE: 1:1	WEIGHT:	SHEET 1 OF 1

REVISION HISTORY

REV	DESCRIPTION	DATE	APPROVED

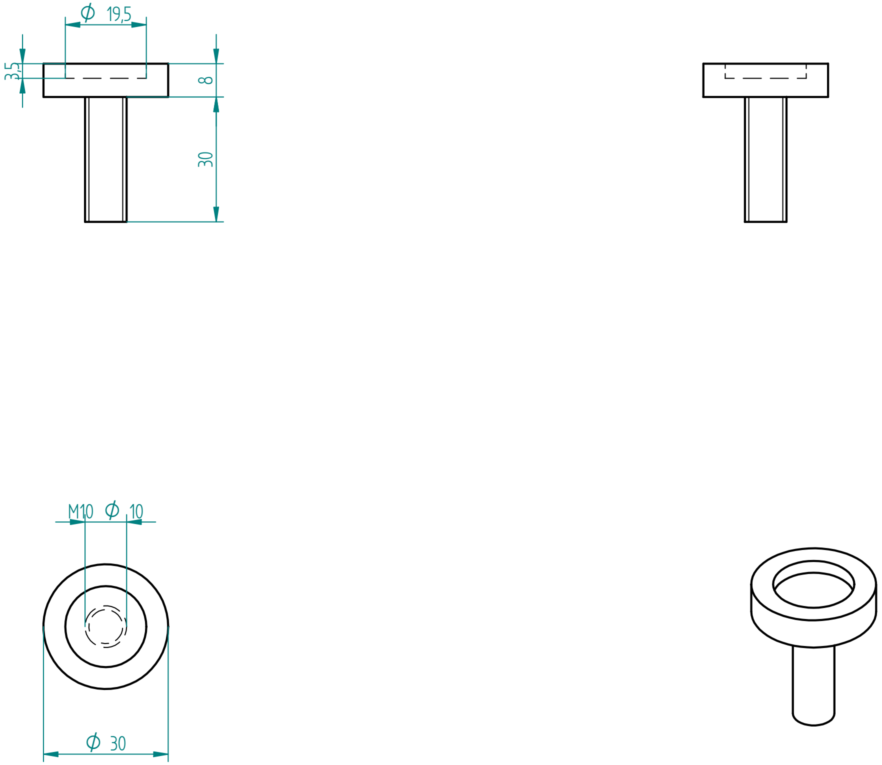

	NAME	DATE
DRAWN	Jon Seddon	11/19/08
CHECKED		
ENG APPR		
MGR APPR		

UNLESS OTHERWISE SPECIFIED
DIMENSIONS ARE IN MILLIMETERS
ANGLES ±X.X°
2 PL ±X.XX 3 PL ±X.XXX

SURREY SPACE CENTRE
University of Surrey

TITLE
Permanent Magnet Holder

SIZE A3
DWG NO
REV

FILE NAME: SupPMstator.dft

SCALE: 1:1
WEIGHT:
SHEET 1 OF 1

References

[1] D. Dungate, D. Liddle, A. Cropp, W. Levett, M. Price, and H. Steyn. Topsat imaging mode adcs design. In *5th ESA International Conference on Spacecraft Guidance, Navigation and Control Systems*, pages 493–496, Frascati, Italy, 2003.

[2] Surrey Satellite Technology Ltd. Magnetorquer - mtr-30. Data Sheet, 2011.

[3] Surrey Satellite Technology Ltd. Low power resistojet. Data Sheet, 2011.

[4] Surrey Satellite Technology Ltd. Xenon propulsion system. Data Sheet, 2008.

[5] Surrey Satellite Technology Ltd. Mini-satellite reaction wheel. Data Sheet, 2002.

[6] James R. Wertz and Wiley J. Larson. *Space mission analysis and design*. Microcosm Kluwer Academic, 3rd edition, 1999.

[7] David C. Bamber, Dr Philip L. Palmer, and Dr Stephen Mackin. Attitude determination through image registration model and test-case for novel attitude system in low earth orbit. In *AIAA/AAS Astrodynamics Specialists Conference*, pages 1–14, Keystone, Colorado, 2006. No. AIAA 2006-6157.

[8] WM Hosny and SJ Dodds. Analytical investigation of the torque capability of the reaction sphere. *Electric Power Components and Systems*, 25(2):181–197, 1997.

[9] E. Onillon, O. Chatelat, L. Rossini, L. Lisowski, S. Droz, and J. Moerschell. Reaction sphere for attitude control. In *13th European Space Mechanisms and Tribology Symposium 2009*, volume SP670, Vienna, Austria, 2009. ESA.

[10] Vladimir A Chobotov. *Spacecraft attitude dynamics and control*. Krieger, 1991.

[11] Marcel J Sidi. *Spacecraft dynamics and control : a practical engineering approach*. Cambridge University Press, 1997.

[12] Bong Wie. *Space vehicle dynamics and control*. American Institute of Aeronautics and Astronautics, 1998.

[13] Rockwell Collins. Teldix ball bearing momentum and reaction wheels. Data Sheet, 2006.

[14] Carl H. Henrikson, Joseph Lyman, and Philip A. Studer. Magnetically suspended momentum wheels for spacecraft stabilization. In *12th AIAA Aerospace Sciences Meeting*, pages 1–8, Washington D.C., 1974.

[15] P. Studer. A practical magnetic bearing. *IEEE Transactions on Magnetics*, 13(5):1155–1157, 1977. 0018-9464.

[16] R.S. Sindlinger. Magnetic bearing momentum wheels with magnetic gimballing capability for 3-axis active attitude control and energy storage. In *Attitude and Orbit Control Systems Conference*, volume ESA SP-128, pages 395–401, Noordwijk, 1977. European Space Agency.

[17] A. A. Robinson. A lightweight, low-cost, magnetic-bearing reaction wheel for satellite attitude-control applications. *ESA Journal*, 6:397–406, 1982.

[18] C. Murakami, Y. Ohkami, O. Okamoto, A. Nakajima, M. Inoue, J. Tsuchiya, K. Yabu-Uchi, S. Akishita, and T. Kida. A new type of magnetic gimballed momentum wheel and its application to attitude control in space. *Acta Astronautica*, 11(9):613–619, 1984.

[19] K. Tsuchiya, M. Inoue, S. Akishita, A. Nakajima, and Y. Ohkami. Anisotropic stiffness effect on stability of a magnetically suspended momentum wheel. *Journal of Guidance, Control, and Dynamics*, 14(2):330–336, 1991.

[20] V. Gondhalekar, J.R. Downer, D.B. Eisenhaure, R.L. Hockney, and B.G. Johnson. Low noise spacecraft attitude control systems. In *Proceedings of the 26th Intersociety Energy Conversion Engineering Conference*, volume 4, pages 244–249, Boston, MA, 1991. American Nuclear Society.

[21] J. P. Rowland. Magnetic bearing wheels for very high pointing accuracy satellite missions. In *International Symposium on Magnetic Suspension Technology*, volume 2, pages 857–872, Hampton Virginia, 1991. NASA.

[22] Alois Wittman. Tilting momentum wheel for spacecraft. Patent, 1992.

[23] Michael Scharfe, Karl Meinzer, and Ralf Zimmermann. Development of a magnetic-bearing momentum wheel for the amsat phase 3-d small satellite. In *International Symposium on Small Satellites*, Annecy, France, 1996. No. A97-23887.

[24] A. Samuel and B. Lechable. An overview on aerospatiale magnetic bearing products for spacecraft attitude control and for industry. In *3rd ESA International Conference on Spacecraft Guidance, Navigation and Control Systems*, pages 649–655, Noordwijk, Netherlands, 1997.

[25] Stefano Carabelli, Cristiana Delprete, and Giancarlo Genta. Rotor on active magnetic suspension. part i: Theoretical considerations. *European Journal of Mechanical and Environmental Engineering*, 43(3):123–128, 1998.

[26] Andrea Argondizza, Stefano Carabelli, Lorenzo Cardascia, and Cristiana Delprete. Rotor on active magnetic suspension - part ii: experimental characterization. *European Journal of Mechanical and Environmental Engineering*, 44(1):17–25, 1999.

[27] S. Carabelli, G. Genta, M. Silvagni, and A. Tonoli. Inertia wheel on low-noise active magnetic suspension. *Space Technology*, 23(2-3):105–117, 2003.

[28] Michael Scharfe, Thomas Roschke, Enrico Bindl, and Daniel Blonski. Design and development of a compact magnetic bearing momentum wheel for micro and small satellites. In *15th AIAA/USU Conference on Small Satellites*, pages 1–9, Utah, 2001. No. SSC01-IX-1.

[29] Michael Scharfe, Thomas Roschke, Enrico Bindl, Daniel Blonski, and Ren Seiler. The challenges of miniaturisation for a magnetic bearing wheel. In R. A. Harris, editor, *Proceedings of the 9th European Space Mechanisms and Tribology Symposium*, pages 17 – 24, Lige, Belgium, 2001.

[30] J. Zhou and K. J. Tseng. A disk-type bearingless motor for use as satellite momentum-reaction wheel. In *Proceedings of the Power Electronics Specialists Conference*, volume 4, pages 1971–1975, Cairns, Queensland, Australia, 2002. IEEE.

[31] U.J. Bichler. A magnetic bearing momentum wheel for high pointing accuracy and vibration sensitive space applications. In *Proceedings of the Annual Rocky Mountain Guidance and Control Conference*, pages 149–164, Keystone, Colorado, 1991.

[32] U.J. Bichler and T. Eckardt. A gimbaled low noise momentum wheel. In *The 27th Aerospace Mechanisms Symposium*, pages 181–196, NASA Ames Research Center, 1993. NASA.

[33] Bangcheng Han and Liu Bin. The influences of parameters on performance of hybrid axial magnetic bearing. In *Systems and Control in Aerospace and Astronautics, 2008. ISSCAA 2008. 2nd International Symposium on*, pages 1–6, 2008.

[34] Renuganth Varatharajoo. *Synergisms for Spacecraft Attitude Control System*. PhD thesis, Universitat Dresden, 2003.

[35] Mark Siebert, Ben Ebihara, Ralph Jansen, Robert L. Fusaro, Wilfredo Morales, Albert Kascak, and Andrew Kenny. A passive magnetic bearing flywheel. In *36th Intersociety Energy Conversion Engineering Conference*, volume 1, pages 125–132, Savannah, Georgia, 2002.

[36] M. Privat and A. da Costa. Pneumatic locking device for magnetic bearing reaction wheel. In R. A. Harris, editor, *ESA SP-524: European Space Mechanisms and Tribology Symposium*, pages 121 – 128, 2003.

[37] B. Gerlach, M. Ehinger, H. K. Raue, and R. Seiler. Gimballing magnetic bearing reaction wheel with digital controller. In B. Warmbein, editor, *11th European Space Mechanisms and Tribology Symposium, ESMATS 2005*, pages 35 – 40, Lucerne, Switzerland, 2005. ESA.

[38] P. E. Allaire, E. H. Maslen, R. R. Humphris, C. K. Sortore, and P. A. Studer. Low power magnetic bearing design for high speed rotating machinery. In *International Symposium on Magnetic Suspension Technology*, volume 1, pages 317–329, Hampton Virginia, 1991. NASA.

[39] M. Toyoshima and K. Araki. In-orbit measurements of short term attitude and vibrational environment on the engineering test satellite vi using laser communication equipment. *Optical Engineering*, 40:827, 2001.

[40] M. Privat. On-ground and in-orbit micro-vibrations measurement comparison. In *8th European Space Mechanisms and Tribology Symposium*, ESA SP-438, pages 181–186, Toulouse, 1999. ESA.

[41] D. Pang, J A Kirk, D K Anand, R G Johnson, and R B Zmood. Modelling and design for pm/em magnetic bearings. In *International Symposium on Magnetic Suspension Technology*, volume 1, pages 105–120, Hampton Virginia, 1991. NASA.

[42] Michel Zayadine. *Etude de Reglage en Position de la Sustentation Magnetique par Attraction*. PhD thesis, Ecole Polytechnique Federale de Lausanne, 1996.

[43] G. Walsh, C. Shay, K. Kefauver, and L. Hromada. High speed flywheel for leo satellites, 1998. Intelligent Control Engineering Laboratory, University of Maryland at College Park.

[44] Aldo DArrigo and Alfred Rufer. Integrated electromagnetic levitation and guidance system for the swissmetro project. In *International Conference on Magnetically Levitated Systems*, pages 263–268, Rio de Janeiro, Brazil, 2000.

[45] Brian T. Murphy, Hamid Ouroua, Matthew T. Caprio, and John D. Herbst. Permanent magnet bias, homopolar magnetic bearings for a 130 kw-hr composite flywheel. In *The 9th International Symposium on Magnetic Bearings*, pages 1–7, Lexingon, Kentucky, 2004.

[46] Thomas Lange. Optimal magnetic bearing control for high speed momentum wheels. In *AIAA Guidance and Control Conference*, pages 675–680, Gatlinburg, Tennessee, 1983. American Institute of Aeronautics and Astronautics.

[47] R. D. Williams, F. J. Keith, and P. E. Allaire. Digital control of active magnetic bearings. *Industrial Electronics, IEEE Transactions on*, 37(1):19–27, 1990. 0278-0046.

[48] T. Higuchi, T. Mizuno, and M. Tsukamoto. Digital control system for magnetic bearings with automatic balancing. In *2nd International Symposium on Magnetic Bearings*, pages 27–32, 1990.

[49] R. Herzog, P. Buhler, C. Gahler, and R. Larsonneur. Unbalance compensation using generalized notch filters in the multivariable feedback of magnetic bearings. *Control Systems Technology, IEEE Transactions on*, 4(5):580–586, 1996. 1063-6536.

[50] Lum Kai-Yew, V. T. Coppola, and D. S. Bernstein. Adaptive autocentering control for an active magnetic bearing supporting a rotor with unknown mass imbalance. *Control Systems Technology, IEEE Transactions on*, 4(5):587–597, 1996. 1063-6536.

[51] T. Namerikawa and M. Fujita. Modeling and robustness analysis of a magnetic suspension system considering structured uncertainties. *Decision and Control, 1997., Proceedings of the 36th IEEE Conference on*, 3:2559–2564, 1997.

[52] B. Shafai, S. Beale, P. Larocca, and E. Cusson. Magnetic bearing control systems and adaptive forced balancing. *Control Systems Magazine, IEEE*, 14(2):4–13, 1994. 0272-1708.

[53] D. L. Trumper, S. M. Olson, and P. K. Subrahmanyan. Linearizing control of magnetic suspension systems. *Control Systems Technology, IEEE Transactions on*, 5(4):427–438, 1997. 1063-6536.

[54] P. Tsiotras and E. Velenis. Low-bias control of ambs subject to saturation constraints. In *Control Applications, Proceedings of the 2000 IEEE International Conference on*, pages 138–143, Anchorage, USA, 2000.

[55] Jeffrey D. Lindlau and Carl R Knospe. Feedback linearization of an active magnetic bearing with voltagecontrol. *IEEE Transactions on Control Systems Technology*, 10(1):21–31, 2002.

[56] A. Lanzon and P. Tsiotras. A combined application of h-infinity loop shaping and mu-synthesis to control high-speed flywheels. *IEEE Transactions on Control Systems Technology*, 13(5):766–77, 2005.

[57] Richard C. Dorf and Robert H. Bishop. *Modern control systems*. Pearson Prentice Hall, 10th edition, 2005.

[58] John J. D'Azzo and Constantine H. Houpis. *Linear Control System Analysis and Design: Conventional and Modern 3rd Edition*. McGraw-Hill, London, 3rd edition, 1988.

[59] P.K. Sinha and A.N. Pechev. Nonlinear h-infinity controllers for electromagnetic suspension systems. *IEEE Transactions on Automatic Control*, 49(4):563–568, 2004.

[60] Congying Han. *Underactuated Attitude Control of Small Spacecraft*. PhD thesis, University of Surrey, 2011.

[61] Donald R. Askeland. *The Science and Engineering of Materials*. Chapman and Hall, 3rd edition, 1996.

[62] Zureks. B-h_loop.svg, 2006. http://en.wikipedia.org/wiki/File:B-H_loop.png.

[63] Kenneth R. Demarest. *Engineering Electromagnetics*. Prentice Hall, 1998.

[64] Lex Molenaar. *A novel Planar Magnetic Bearing and Motor Configuration applied in a Positioning Stage*. PhD thesis, Technische Universiteit Delft, 2000.

[65] David J. Richie. *Combined Attitude Control and Energy Storage for Small Satellites using Variable Speed Control Moment Gyroscopes*. PhD thesis, University of Surrey, 2008.

[66] D.J. Richie, V. Lappas, and Dr Philip L. Palmer. Sizing/optimization of a small satellite energy storage and attitude control system. *Journal of Spacecraft and Rockets*, 44(4):940–952, 2007.

[67] Cirrus Logic Inc. Apex sa60 amplifier, 2007. http://www.cirrus.com/en/products/sa60.html.

[68] School of Electronics Technical Services Unit and University of Surrey Physical Sciences. Producing wound components. http://info.ee.surrey.ac.uk/Workshop/advice/coils/, 2006.

[69] Sensonics Ltd. Senturion eddy current probes. Data Sheet, 2008.

[70] Geoff Matthews. Prs04 on a curved target. Personal Communication, 2010.

[71] Theo Konink and Gerard Kester. Multipurpose holddown and release mechanism (mhrm). In *13th European Space Mechanisms and Tribology Symposium*, Vienna, Austria, 2009. European Space Agency.

[72] P. Krulevitch, A. P. Lee, P. B. Ramsey, J. C. Trevino, J. Hamilton, and M. A. Northrup. Thin film shape memory alloy microactuators. *Microelectromechanical Systems, Journal of*, 5(4):270–282, 1996.

[73] Wonjun Tak, Minsoo Lee, and Byungkyu Kim. Shape memory alloy actuator based satellite separation device using plastic deformation. In *13th European Space Mechanisms and Tribology Symposium*, Vienna, Austria, 2009. European Space Agency.

[74] D. Boscher, S. Bourdarie, P. O'Brien, and T. Guild. Onera-desp library v4.2, 2004-2008.

[75] Larry M. Trase. The evaluation and implementation of a water containment system to support aerospace flywheel testing. In *37th Intersociety Energy Conversion Engineering Conference*, Washington DC, 2002.

[76] William Tyrrell Thomson. *Introduction to Space Dynamics*. Dover Publications, 1986.

[77] G. Genta. *Dynamics of Rotating Systems*. Springer, New York, 2005.

[78] Akira Chiba, Tadashi Fukao, Osamu Ichikawa, Masahide Oshima, Masatsugu Takemoto, and David G. Dorrell. *Magnetic bearings and bearingless drives*. Elsevier Newnes, 2005.

[79] Maxon Motor AG. Maxon motor catalogue, 2007.

[80] Izhak Bucher. Dynamics of rotating machinery lecture notes, 2002. Technion - Israel Institute of Technology.

[81] Howie M. Choset, Seth Hutchinson, Kevin M. Lynch, George Kantor, Wolfram Burgard, Lydia E. Kavraki, and Sebastian Thrun. *Principles of robot motion: theory, algorithms, and implementation*. MIT Press, 2005.

[82] R. Dhaouadi, N. Mohan, and L. Norum. Design and implementation of an extended kalman filter for the state estimation of a permanent magnet synchronous motor. *Power Electronics, IEEE Transactions on*, 6(3):491–497, 1991. 0885-8993.

[83] K Weltner, J Grosjean, P Schuster, and W.J. Weber. *Mathematics for engineers and scientists*. Stanley Thornes, 1986.

[84] Karl Astrom and Bjorn Wittenmark. *Computer Controlled Systems - Theory and Design, Third Edition*. Prentice Hall, 1997.

[85] Gene Franklin, David Powell, and Michael Workman. *Digital Control of Dynamic Systems, Second Edition*. Addison-Wesley, 1990.

[86] Alexandre Pechev. H-infinity sensitivity minimisation. Personal Communication, May 2008.

[87] Nigel Phillips. Momentum wheel mass imbalance. Personal Communication, March 2009.

[88] Adi. Ben-Israel and Thomas N.E. Greville. *Generalized Inverses: Theory and Applications*. Springer, 2nd edition, 2003.

[89] Yoshi Hashida. Topsat inertia matrix. Personal Communication, 2006.

[90] Matthew N.O. Sadiku. *Numerical Techniques in Electromagnetics*. CRC Press, 1992.

[91] David Meeker. Femm software package, 2006. http://www.femm.info/.

[92] Ansys Inc. Maxwell 3d software package, 2006. http://www.ansys.com/.